THE UNIVERSITY OF CHICAGO

COLLOIDAL SEMICONDUCTOR NANOCRYSTALS:

SURFACE CHEMISTRY, PHOTONICS, AND ELECTRONICS

A DISSERTATION SUBMITTED TO

THE FACULTY OF THE DIVISION OF THE PHYSICAL SCIENCES

IN CANDIDACY FOR THE DEGREE OF

DOCTOR OF PHILOSOPHY

DEPARTMENT OF CHEMISTRY

BY

IGOR FEDIN

CHICAGO, ILLINOIS

JUNE 2017

TABLE OF CONTENTS

LIST OF FIGURES

LIST OF TABLES

ACKNOWLEDGEMENTS

First and foremost, I would like to thank my research adviser, Professor Dmitri V. Talapin. From the very first day, anytime we had a conversation, he had a handful of keen, creative, and inspirational ideas. Anytime I struggled with a project, he gave me valuable tactic and strategic advice, and I returned to my bench, cheered up and cracking the problem from a new angle. He taught me planning scientific projects and that perfect balance between fundamental exploration and goal-oriented work. When it came to presenting results of my work in publications and at conferences, it was Dmitri who taught be the best strategies. I greatly acknowledge his hard work in finding the financial support for our group, so that I never hesitated to buy a chemical or a piece of equipment I needed. Finally, I am thankful to Dmitri for his great advice on my future career options.

I would like to thank my committee members, Professors Philippe Guyot-Sionnest and Gregory S. Engel, for their time and effort in reading my dissertation and their valuable comments on the presentation of my research. I appreciate Prof. Guyot-Sionnest's interest in the electrochemistry project and his valuable input. I thank Prof. Engel for his advice on my future career path.

I will always remember the warm welcome and introduction to the lab by the Talapin laboratory. It was Dr. Sandrine Ithurria-Lhullier who taught me the first synthesis of CdSe quantum dots. Dr. Dmitriy S. Dolzhnikov introduced me to electrochemistry. Dr. Jong-Soo Lee taught me electronic measurements. Dr. Sara M. Rupich introduced me to the laboratory

infrastructure and operations. Dr. Matthew G. Panthani was a great senior postdoc and group leader, and a bright personality. Dr. J. Matthew Kurley was a big help with machining. Later on, I learned some synthetic tricks about III – V semiconductors from Dr. Wenyong Liu and FET measurements from Dr. Jaeyoung Jang and Dr. Tae Kyu An. I will always remember the fun synthesis of *tris*(trimethylsilyl)arsine with Vishwas Srivastava and Dr. Hao Zhang under the supervision of Wenyong. My special thanks go to my group collaborators. Dr. Chunxing She and I had a long journey of nanoplatelets for amplified spontaneous emission and laser action. I have been lucky to be a part of Dr. Yuanyuan Wang's project on photo-patterning of semiconductors. Kavan Mulloy has been a great help with syntheses of nanoplatelets and preparation of samples. I would like to thank each and every member of the Talapin lab, current or former, Eric M. Janke, Patrick D. Cunningham, Margaret H. Hudson, Vladislav Kamysbayev, Dr. Abhijit Hazarika, Dr, Xinzheng Lan, Jia-Ahn Pan, Joshua Portner, Wooje Cho, Dr. Igor Coropceanu, Dr. Ke Gong, Dr. Michael A. Boles, Jake Russel, Dr. Danny Haubold, Dr. Jianwei Nai, Hannah Muir, João Batista Souza Junior, Vadim Tanygin, Leonardo Martins Amaral, Taha Ezzyat, Dr. Chengyang Jiang, Dr. Jae Sung Son, Fernando Castro, Travis Dietz, Dr. Jing Huang, Dr. Dae-Sung Chung, Dr. Angshuman Nag.

My work heavily relied on external collaborators and their facilities. Argonne National Laboratory has been vital for my research. I collaborated with Dr. Clare Rowland and Dr. Benjamin T. Diroll on a number of projects, using the laboratories of Dr. Richard D. Schaller and Dr. David Gosztola. I would also like to thank Prof. Matthew Pelton (UMBC) and Prof. Edo Waks (UMD) with their groups for interesting collaborative projects. I thank my current collaborators: Dr. Justin R. Caram and Katherine E. Shulenberger from the group of Prof.

Moungi G. Bawendi (MIT); Kemar Reid and Prof. Sandra J. Rosenthal (Vanderbilt); and Josef Haimerl and Prof. John Lupton (URegensburg).

I would like to thank the Deaprtment of Chemistry and James Franck Institute. I was honored to collaborate with Dr. Peter D. Dahlberg and Nicholas E. Williams on the ASE project in the laboratory of Prof. Engel. I thank Prof. Bozhi Tian for following up with me about my projects and his advice on my future career path. Transmission electron microscopy has been vital for my studies, and my thanks go to Prof. Jotham R. Austin and Dr. Yimei Chen. I appreciate the hard work of Dr. Justin E. Jureller and Dr. Qiti Guo making MRSEC facilities available for us. I would like to acknowledge the work of Tanya Shpigel, Dr. Vera Dragisich, Dr. Melinda Moore, and Dr. Meishan Zhao. My visitation host, Dr. Pavlo Zolotavin, convinced me to join this wonderful School. Dr. Justin R. Caram was a great mentor (called "bad influence" in our Department) during my first year.

Graduate school would not have been as bright without friends. I was lucky to make friends with every member of the Talapin Lab and will always remember our outings, especially kayaking down the Wisconsin River. A number of friends from my undergrad and master's stayed in touch with me and visited me here in Chicago. I would like to acknowledge J. Perry Corbett and his family, Dr. Oleksandr Koniev, Dr. Sergii Kolodych, Dr. Mykhailo Vybornyi, brothers Andriy and Egor Chertok, Dr. Elena Mikhalyova, and Dr. Denis Ganshevsky. I was lucky to meet new friends here in Chicago, and besides the Talapin Lab, would like to acknowledge Nataliia and Pavel Elkin; Polina Navotnaya; Dr. Julius Reyes; Jeremy L. Paige and his children, Tyren, Makhia, and Zion; Charles Hall.

I would like to acknowledge the University of Akron, where I did my M.S. program in Physics, my adviser, Prof. Sergei F. Lyuksyutov, and Profs. Jutta Luettmer-Strathmann, Robert

R. Mallik, and David S. Perry. I would like to acknowledge my undergraduate institution, Kiev National University, and my adviser, Dr. Marian V. Gorichko. Finally, I am much thankful to my high-school teacher of Chemistry, Natalia V. Druzhynina.

Finally, I owe my special gratitude to my family. I thank my parents, Vira and Oleg† Fedin, for what kind of person I am, where I am, and what my interests are. I thank my Mom for her love, support, and faith in me over these decades. Her visit to Chicago in March 2013 made my stay here warmer and sunnier. I thank my grandparents, Palagia and Alexander† Gomon, and Valentina† and Ivan† Fedin for their love. I gratefully acknowledge my uncles, Vitaliy Gomon and Viacheslav Fedin, with their families, my cousins, Inna, Evgen (and his family), Anna, and Dmitry, and my half-brother Alexey.

ABSTRACT

It has been 24 years since the first synthesis of colloidal CdSe quantum dots (QDs). Today, we can find them in consumer goods: we enjoy sharp colors on television displays, where improved QDs act as chromophores. Two decades of deliberate work has brought understanding of the chemical processes lying in the preparation and surface passivation of these materials. The community has learned to synthesize nanocrystals of pre-defined composition, covering the whole range of industrially important semiconductors, of various shapes, and of desired surface termination. Over these years, we have observed and understood important physical phenomena in these materials, *e.g.*, quantum confinement in quantum dots, exciton generation and splitting, charge hopping from one dot to another in an array, *etc*. With this understanding, for a number of systems, we can synthesize a material with pre-defined properties, for example, QDs with a desired bandgap width and position for photovoltaic applications, or QDs with a desired PL band position, stability, and environmental compatibility for biological imaging.

The two decades of research has raised even more questions. We would like to fully describe a given systems (*e.g.*, understand the complex exciton and multiexcitons dynamics in a QD), elicit maximum performance from the system (*e.g.*, 100% photoluminescence quantum yield and narrow spectral lines in QDs, or bulk carrier mobilities in solution-processed semiconductors), and even push the system beyond temporary conventional limits (*e.g.*, raising the efficiency of solar cell by multiexcitons generation in quantum dots). Ultimately, we would

like industry to take advantage of the ease and tunability of solution-processed semiconductors and introduce them in bigger classes of goods. For that, we will need to mature the field to the degree of existing industrial processes (*e.g.*, layer-by-layer deposition, polymer synthesis, *etc.*). In particular, we will need meters inserted into the system, monitoring its state *in situ*, providing feedback to the researcher, and manipulating it automatically. We will also need to bring the protocols to the levels where they can be commercialized, *i.e.*, not only bring all figures of merit to the extreme, but account for new aspects of the process like optimization of the atom conversion or minimization of waste.

In one direction of the present work, we explore the possibility of potentiometry and amperometry in quantitative characterization of ligand adsorption at the nanocrystal surface and develop a tool that enables us to controllably grow three monolayers of CdS over CdSe QDs. In another direction, we optimize the synthesis of colloidal quantum wells, CdSe and CdSe/CdS nanoplatelets, and observe superior photonic properties from them. Namely, we demonstrate record-low threshold of amplified spontaneous emission, high saturation gain, and suppressed Auger recombination. We demonstrate laser action at four different wavelengths, including the commercially unavailable 575 nm. We observe that perforation of nanoplatelets leads to colloidal particles of new topology: rings and double rings. Finally, we demonstrate the niche for solution-processed electronic materials: ease of synthesis and possibility of patterning.

We believe that our electrochemical probe will find its application in the commercial synthesis of bright core-shells. With more work, researchers will demonstrate electrically pumped lasing in CdSe/CdS nanoplatelets. Colloidal nanorings will be a cheap and convenient platform to topology-determined electronic properties of semiconductors. Finally, our contributions to electronic properties of InP QDs will be a step toward understanding InP.

INTRODUCTION

Semiconductors that we encounter in the form of colloidal nanocrystals (NCs) most frequently are those of the II – VI family (zinc, cadmium, and mercury chalcogenides: ZnE, CdE, and HgE, E = S, Se, Te),[1] the IV – VI family (lead chalcogenides, PbE),[2] and the III – V family (gallium and indium pnictides: GaPn, InPn, Pn = P, As, Sb).[3] A new class of materials, emerged rapidly in our field in the past years, is perovskite structures of the general formula $MPbX_3$, (M = caesium, methylammonium, or formamidinium).[4] Interestingly, ubiquitous in commercial electronics, silicon, germanium, and group IIIB nitrides are still considered unusual among colloidal NCs.

Synthesis of Colloidal Semiconductor Nanocrystals

The first protocols for colloidal semiconductor NCs, similar to layer-by-layer deposition techniques, used highly chemically reactive precursors, *e.g.*, dimethylcadmium ($Cd(CH_3)_2$), *bis*-trimethylsilyl (TMS) selenide ($[(CH_3)_3Si]_2Se$, also TMS_2Se,),[1] *etc*. The recipes have evolved and rely on combinations of more benign reactants of moderate and high reactivity. In a typical synthesis, we react a molecular metal precursor (metal carboxylates, phosphonates, covalent halides, *etc*.) with non-metal precursors (TMS-derivatives, trialkylphosphine derivatives, substituted thio- and selenoureas, *etc.*) in a non-polar solvent (high-boiling hydrocarbons, trialkylphosphines) in the presence of surfactants (carboxylates, phosphonates, amines, phosphines, *etc.*) at elevated temperatures (60 – 380^{o}C). For example, a synthesis of wurtzite

CdSe (w-CdSe) NCs from cadmium octadecylphosphonate and trioctylphosphine selenide (TOPSe) is given by the following simplified equation.

$$(m + x)\ Cd(C_{18}H_{37}PO(OH)O)_2 + 2m\ Oct_3PSe \rightarrow \underline{[CdSe]_m[Cd(C_{18}H_{37}PO(OH)O)_2]_x}$$
$$+ 2m\ Oct_3PO + 2m\ (C_{18}H_{37}PO(OH))_2O$$

NCs must obey charge neutrality; therefore, excess cadmium atoms are bound with negatively charged X-type ligands (phosphonates, carboxylates, hydroxyls, *etc*.). Atoms of Cd and Se in either wurtzite or zincblende crystal structure have for counter neighbors. To satisfy the coordination number of four, some surface cadmium atoms are also coordinated with neutral L-type ligands (amines, alkylphosphines, *etc*.). Satisfying coordination number for every surface atom, however, would cause much steric hindrance. Therefore, I shall use a general formula $[CdSe]_m[CdX_2L_{2-\delta}]_x$ for CdSe NCs.[5]

Spherical NCs range from 2 to 20 nm in diameter and contain between one hundred and one hundred thousand atoms. The size of the NCs is tuned during the synthesis through the choice of the precursors and the reaction temperature. Large NCs, desired for electronic applications, are usually prepared from a combination of highly reactive (for nucleation) and moderately reactive (for growth) precursors at high temperatures. Researchers engineer the shape of NCs by choosing particular precursors and/or surfactants. CdSe nanorods (NRs) grow because phosphonates block the growth of side facets.[6] A short-chain carboxylate, *e.g.*, acetate, is necessary for anisotropic growth of CdSe nanoplatelets (NPLs).[7] Colloidal NCs are dispersed in non-polar solvents (hexane, methylcyclohexane (MCH), toluene, chloroform, *etc*.). They are sterically stabilized with long-chain surfactants (X and L-type ligands).

The Color of Semiconductor NCs

Every bulk semiconductor has a valence band (the highest band of states filled with electrons at 0 K, analogue of HOMO in molecules) and a conduction band (the lowest band of electronic states empty at 0 K, analogue of LUMO in molecules). The energy space between the top of the valence band and the bottom of the conduction gap is the bandgap of a semiconductor. Electrons can be thermally or optically excited across the bandgap, resulting in an electron in the conduction band and a hole the valence band. If the semiconductor absorbs all visible light (has a bandgap smaller than 1.63 eV), it has a black color in the bulk.

Every electronic state is characterized by energy (E) and electron wave vector (quasi momentum, k). Electronic states map lines (bands of states) in (k, E) coordinates. In the vicinity of band edges, the bands can be assumed parabolic. In such case, the energy of a state in the conduction band is given by: $E = E_{\mathrm{c}} + \frac{\hbar^2 k^2}{2m_e}$, where E_{c} is the energy at the bottom of the conduction band and m_e is the effective mass of the electron in the semiconductor. The energy of a state in the valence band is given by: $E = E_{\mathrm{v}} - \frac{\hbar^2 k^2}{2m_h}$, where E_{v} is the energy at the top of the hole (valence) band and m_h is the effective mass of the hole in the band. CdSe, for example, has one electron band and three hole bands. For the bulk state, k is a quasi-continuous variable, so the bands are represented by quasi-continuous lines. In NCs, the spacing between two consecutive values of k is proportional to the inverse of the NC size, $\Delta k \propto 1/d$. Given that there is no state with $k = 0$ (which would have meant the wavefunction identically equals zero), the energy of the lowest-energy transition in NCs is higher than the bandgap energy, ΔE_0.

$$\Delta E = \Delta E_0 + \frac{\hbar^2 k_1^{\,2}}{2\mu}$$

μ is the reduced effective electron-hole mass in the equation, $\mu^{-1} = m_e^{-1} + m_h^{-1}$. The energy of the transition increases with the decrease in the NC size. The effect is more pronounced for semiconductors with smaller effective masses. Some semiconductors have degenerate hole bands as k tends to zero; in such case, the degeneracy is lifted in NCs and we observe two transitions: heavy hole – electron ($hh - e$) and light hole – electron ($lh - e$).

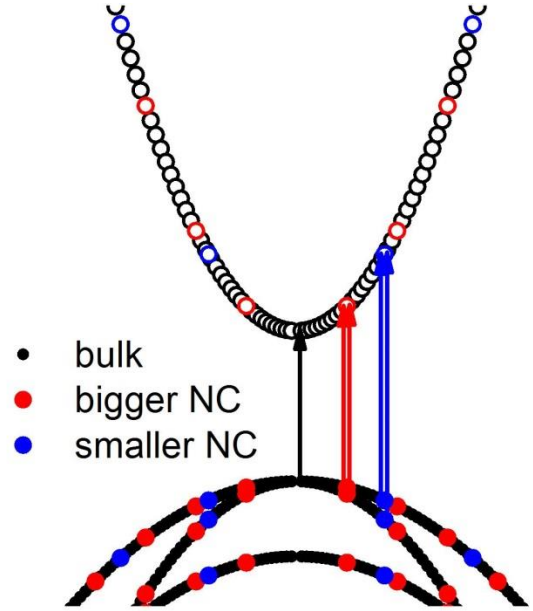

Figure 0.1. A schematic of size-dependent lowest energy transition in CdSe NCs. The diagram is plotted in $k - E$ axes.

Photoexcited electron and hole can create a bound state, called an exciton, just as electron and proton form a hydrogen atom. Hydrogen atom has a binding energy of 13.6 eV and a Bohr radius of a_0 = 0.0529 nm. Exciton Bohr radius increases with the increase of the dielectric constant of the medium and the decrease of the effective mass of the carriers: $a = a_0 \varepsilon / \mu$. In CdSe, for example, the exciton Bohr radius is 5.1 nm.[8] Exciton binding energy in the bulk decreases with the increase of the dielectric constant of the semiconductor and increase of effective carrier mass: $E = 13.6\,\text{eV} \cdot \mu / \varepsilon^2$. Stable excitons form only if the exciton binding

energy is bigger than the thermal energy at a given temperature (which is not the case for many bulk semiconductors at the room temperature). When the size of a NC is smaller than the exciton Bohr radius, the exciton is squeezed. This phenomenon is called quantum confinement. Spherical semiconductor NCs with quantum confinement are called quantum dots (QDs). The exciton binding energy increases in such case. Therefore, we observe peaks in absorption spectra of colloidal solutions of QDs.

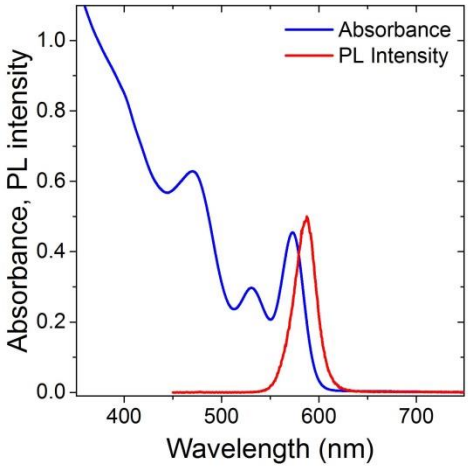

Figure 0.2. Typical absorption and PL spectra of a dilute colloidal solution of quantum dots (QDs), here zincblende CdSe QDs.

The energy of an optical transition probed by spectroscopy is smaller than the energy of the electronic transition by the amount of exciton binding energy. Bandgap energies measured by scanning tunneling spectroscopy (STS) or cyclic voltammetry (CV) are overestimated by the amount of charging energy.

The photoluminescence quantum yield (PL QY) of semiconductor NCs ranges from 0 to 100%. Surface atoms often have unsaturated coordination numbers, which results in lone electron pairs for non-metals and vacancies for metals. Therefore, surface atoms of the metal act as electron traps and surface atoms of the non-metal act as hole traps, impairing the PL QY. A shell of a wider-bandgap semiconductor grown around a QD improves the PL QY by confining

the carriers to the core and preventing them from trapping at the surface.[9] For example, growth of shells of $Cd_{1-x}Zn_xS$ shells over CdSe cores brings PL QYs to unity.

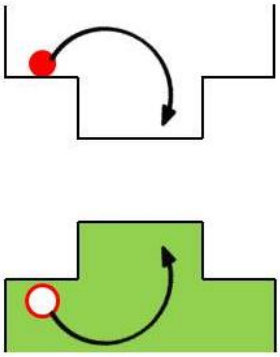

Figure 0.3. A schematic diagram of confining the carriers to the core in a wide-gap-shell core-shell structure.

All-Inorganic Semiconductor NCs for Electronic Applications

Electrons can be injected into the conduction band from external sources (electrodes or alkali metals), as well as holes can be injected into the valence balance band. Not only the width of the bandgap, but also its alignment with respect to vacuum matters. Just as some molecules are electrophiles (*e.g.*, $FeCl_3$), some semiconductors (*e.g.*, Fe_2O_3) have a low-lying bottom of the conduction band and are susceptible to electron injection (*n*-doping). Similar to nucleophilic molecules, some semiconductors (*e.g.*, CdTe, GaAs) have a high-lying top of the valence band and are thus susceptible to hole injection (*p*-doping). An externally injected carrier can hop from one QD to its neighbor. Therefore, charge transport occurs in arrays of QDs.

A colloidal solution of QDs is a convenient material for electronic devices. A film of a desired semiconductor can be deposited out of a concentrate colloidal solution.[10] The long-chain surfactants used for steric stabilization of NCs in non-polar solvents are electrically insulating and impede transport of charge carriers in the film. For that reason, a number of ligand stripping and ligand exchange protocols have been developed that result in NCs capped with small

charged inorganic ligands. These NCs are electrostatically stabilized in polar solvents, *e.g.*, hydrazine, DMF, formamide (FA), *N*-methylformamide (NMF), DMSO, *etc.* Films are then deposited and annealed. The NCs can sinter into a bulk material (II – VI and IV – VI semiconductors) or remain as an array of QDs (III – V semiconductors). The former case allows achieving solid-state compositions unavailable otherwise. Composition-matched ligands "solder" individual grains of the semiconductor in films.[11]

Motivation and Outline

Postsynthetic modifications of NCs, like the above mentioned core-shell growth and ligand exchange, or cation or anion exchange are performed without monitoring the system *in situ*. The field needs a technique or a tool that would provide us with real-time information about the system and allow us to automate the process. In Chapter one, we propose two electroanalytical techniques, potentiometry and amperometry, to monitor deposition of inorganic anions on QDs and NPLs.

CdSe NPLs is a relatively new class of materials with atomic precision along the defining dimension, high PL QY, and narrow spectral lines. In Chapter two, we explore the synthetic protocol to control the dimensions of the NPLs and improve the PL QY of CdSe/CdS NPL core-shells. We suspect that extended lateral dimensions of NPLs will increase the lifetime of multiexcitons. Therefore, we study amplified spontaneous emission and lasing from NPLs in Chapter three.

We notice that treatment of CdSe NPLs with selenium in oleylamine leads to their perforation and formation of CdSe nanorings and double rings. We track the perforation and propose a mechanism for it in Chapter four.

CdSe QDs are already in consumer goods, but commercial electronic devices from colloidal NCs are still under development. In chapter five, we discuss the niche for solution-processed electronic materials: ease of fabrication (InP) and possibility of patterning.

Different chapters of this dissertation present various numerical data. The precision and accuracy of our measurements are incorporated in the number significant figures and/or uncertainties. A stand-alone power of 10 means uncertainty in the exponent of 1, *e.g.*, a reported value of 10^{12} means the value lies between 10^{11} and 10^{13}. A number with one or more significant digits implies uncertainty of 1 in the last significant digit, *e.g.*, read 240 as 240 ± 10. In all other cases, uncertainties are listed together with the reported value. Data plotted as scatter typically contain error bars. When an error bar is smaller than the extent of the symbol denoting the corresponding data point, the bar is not shown and the extent of the symbol serves as a conservative estimate for it (*e.g.*, all data for potentiometry in polar media have error bars of the order of a few mV – invisible in the whole titration curve). For numerical values used for other calculations (calibration curves) we keep one or two digits beyond the significant.

CHAPTER ONE

ASSESMENT OF THE NANOCRYSTAL SURFACE WITH ELECTROCHEMISTRY

1.1. Postsynthetic Modifications of Colloidal NCs

Colloidal NCs are typically synthesized in non-polar solvents and capped with long-chain organic surfactants. These surfactants, or ligands, determine the shape of the NCs during the synthesis, provide steric colloidal stabilization in non-polar solvents, and cap surface dangling bonds. Such NCs are ready for a number of photonic or magnetic applications in which only PL or biocompatibilty is important but electrical conductivity is not necessary. Other applications require postsynthetic modifications of NCs: shell growth, ligand exchange or removal, and cation or anion exchange. Further improvement of the PL of semiconductor NCs requires an overgrowth of a shell of wider-bandgap semiconductor (*e.g.*, a shell of ZnS over ZnSe). Electronic applications require removal of the insulating long-chain organics with electrophilic agents (ligand stripping, *e.g.*, treatment of PbSe with $Me_3O^+BF_4^-$)[12] or exchange for short inorganic ligands (ligand exchange, *e.g.*, capping CdSe with $CdCl_3^-$).[13] Sometimes, a material cannot be synthesized directly in a desired crystal structure or shape, but can be obtained from another material *via* a cation exchange.[14] For example, NCs of thermodynamically unstable wurtzite InP are synthesized from Cu_3P,[15] or nanoplatelets (NPLs) of HgTe are prepared from NPLs of CdTe.[16] Recently, a partial anion exchange on perovskite $CsPbBr_3$ NCs yielded blue-emitting $CsPbBr_{3-x}Cl_x$ NCs.[17]

These postsynthetic modifications use either precisely calculated amounts of reactants or a big excess thereof. Successive ion-layer adsorption and reaction (SILAR)[18] – a way to grow luminescent CdSe/$Cd_{1-x}Zn_xS$ core-shells for quantum-dot displays – requires precise calculation of the amounts of the precursors calculation may be hard as it requires the exact knowledge of the total area of each type of facet and possible missing surface atoms. Excess precursors, however, will lead to undesired secondary nucleates; a lack of a precursor will lead to defects, detrimental for PL and charge transport. Another way of core-shell growth, colloidal atomic layer deposition (*c*-ALD),[19] ligand exchange, cation exchange use excess precursor (up to 10- or 100-fold to ensure completion), which is washed off afterwards. Such approach would be too wasteful at the industrial scale. Finally, the researcher does not always know whether the process is running as expected.

Monitoring the NC surface *in situ*, during NC growth or postsynthetic modifications, would be particularly valuable. Epitaxial deposition of GaAs, for example, employs reflection high-energy electron diffraction (RHEED) to count the number of deposited layers and even determine the completion of a particular layer deposition.[20] In the field of colloidal NCs, however, monitoring *in situ* is still under development. Few reported examples include *in situ* fluorescence[21] and UV-vis absorption spectroscopy[22], FTIR[23], NMR,[24] synchrotron SAXS and XANES.[25] These techniques require sophisticated equipment (as in synchrotron based SAXS and XANES) or lack easily interpretable relation between analytical signal and surface chemistry (as in optical spectroscopy). Spectra of aliquots help in the growth of luminescent core-shells, but may be troublesome in the case of IR materials, insulating shells (silica, CaF_2). A finer problem with absorption or PL spectroscopy as a monitoring tool is that the measured signal, the wavelength of the excitonic peak, levels off as the process approaches its completion. The signal

corresponding to 95%, 99%, or 99.9% completion will be nearly identical. We desire the exact opposite: a sharp transition at the completion as it happens in acid-base titrations. Therefore, the goal is to develop a tool that will allow us to monitor a postsynthetic modification of NCs, obtain real-time feedback from the system, and locate the point of completion.

Potentiometry meets the requirements and is established in acid-base, precipitation and complexation, and Red-Ox titrations. It is as a surface-sensitive, non-destructive, fast, and inexpensive technique to probe NC surface *in situ*.[26] Easy to set up and interpret, this approach can be used for on-line analyses during NC syntheses. The model system will be CdSe NCs – the most studied colloidal semiconductor NCs synthesized in two crystal structures, wurtzite (w-) and zinc blende (zb-), and a variety of shapes. Because potentiometry works in conductive media, we will first titrate electrostatically stabilized ligand-stripped CdSe QDs with sulfide in polar solvents.

1.2. Potentiometric Titrations of "Bare" CdSe QDs with Sulfide in a Polar Solvent

1.2.1. Synthesis of the material

We synthesized w-CdSe QDs by an injection of trioctylphosphine selenide (TOPSe) into a solution of cadmium oleate ($Cd(C_{17}H_{33}COO)_2$) in the presence of trioctylphosphine (TOP), trioctylphosphine oxide (TOPO), oleic acid (OA), and oleylamine (OAm) in a non-polar solvent 1-octadecene (ODE) at temperatures between 270°C and 300°C. This way, we produced Cd-rich QDs with the diameter between 3 and 5 nm and a reasonable monodispersity.[27]

$$(n+x)\ Cd(C_{17}H_{33}COO)_2 + n\ TOPSe + (2-\delta)x\ L \rightarrow \underline{[CdSe]_n[Cd(C_{17}H_{33}COO)_2L_{2-\delta}]_x}$$

$$+ n\ TOPO + n\ (C_{17}H_{33}COO)_2O$$

OAm, TOP, or TOPO serve as L-type ligands, and oleate or hydroxide serve as X-type ligands. We removed organic ligands with a mild electrophilic agent trimethyloxonium tetrafluroborate, Me_3OBF_4.[12]

$$\underline{[CdSe]_n[Cd(C_{17}H_{33}COO)_2L_{2-\delta}]_x} + x(4-\delta)\ Me_3OBF_4 \rightarrow \underline{[CdSe]_n[Cd^{2+}\ldots 2BF_4^-]_x}$$

$$+ x(2-\delta)\ (LMe^+ + BF_4^-) + (4-\delta)x\ Me_2O$$

The resulting QDs were electrostatically stabilized in polar solvents like DMF or NMF; $Cd^{2+}\ldots 2BF_4^-$ denotes a diffuse layer. We titrated colloidal solutions of such "bare" CdSe QDs with 1.00×10^{-2} M K_2S in NMF.

1.2.2. Calibration of the electrochemical cell

The potentiometric cell consisted of two electrodes: a silver – silver sulfide working electrode ($Ag|Ag_2S$) and a silver – silver cryptate reference electrode ($Ag|AgCryp^+$, Cryp). The reference electrode was a cleaned silver wire immersed in a solution containing 0.10 M silver crypatate, a complex of silver with 2.2.2-cryptand (Cryp), and 0.10 M free cryptand, separated from the working solution with a vycor membrane. By forming a strong complex with Ag^+ ions ($K = 10^{10}$),[26] 2.2.2-cryptand (Cryp) not only pinned the potential of the reference electrode, but also protected Ag^+ from a rapid reduction by NMF. 0.10 M NBu_4ClO_4 in NMF served as an indifferent electrolyte, setting the ionic strength of the solution and defining thus the activities of all ions.

The measured signal was voltage – EMF of the electrochemical cell.

$$E_{\text{cell}} = E_{Ag_2S,S^{2-}/Ag} - E_{AgCryp^+,Cryp/Ag} = \left(E^0_{Ag_2S,S^{2-}/Ag} - \frac{k_B T}{2e}\ln a_{S^{2-}}\right) - \left(E^0_{AgCryp^+,Cryp/Ag} + \frac{k_B T}{e}\ln\frac{a_{AgCryp^+}}{a_{Cryp}}\right)$$

We relate activities to concentrations through activity coefficients $\{\gamma_i\}$.

$$E_{\text{cell}} = \left(E^0_{\text{Ag}_2\text{S},\text{S}^{2-}/\text{Ag}} - \frac{k_\text{B}T}{2e} \ln\left(\gamma_{\text{S}^{2-}} \left[\text{S}^{2-}\right]\right) \right) - \left(E^0_{\text{AgCryp}^+,\text{Cryp}/\text{Ag}} + \frac{k_\text{B}T}{e} \ln \frac{\gamma_{\text{AgCryp}^+} \left[\text{AgCryp}^+\right]}{\gamma_{\text{Cryp}} \left[\text{Cryp}\right]} \right)$$

The combination of high and equal concentrations of AgCryp^+ and Cryp acts as a buffer and ensures constancy of the potential of the reference electrode.

$$E_{\text{cell}} = \left(E^0_{\text{cell}} - \frac{k_\text{B}T}{e} \ln \frac{\gamma_{\text{S}^{2-}}^{1/2} \gamma_{\text{AgCryp}^+}}{\gamma_{\text{Cryp}}} - \frac{k_\text{B}T}{e} \ln \frac{\left[\text{AgCryp}^+\right]}{\left[\text{Cryp}\right]} \right) - \frac{k_\text{B}T}{2e} \ln\left[\text{S}^{2-}\right] = E^0 - s \cdot \log\left[\text{S}^{2-}\right]$$

The activity coefficients and the potential of the reference electrode are embedded in E^0. The Nernstian slope *s* equals 29.58 mV at 298.15 K for the doubly-charged S^{2-}. The first step was to calibrate the cell with respect to the concentration of sulfide.

NMF (HL) undergoes autoionization to form formylmethylammonium (H2L^+) and formylmethylamide (L^-), $2\text{HL} \leftrightarrow \text{H2L}^+ + \text{L}^-$, to a high degree, $\text{p}K_\text{w} = 11.4$.[28] We expect sulfide to undergo substantial solvolysis in NMF: $\text{S}^{2-} + \text{HL} \leftrightarrow \text{HS}^- + \text{L}^-$. It is possible to suppress the solvolysis of S^{2-} by adding some strong base to the solution, but in such case, L^- and the base will compete with S^{2-} for the NC surface, complicating the analysis. For this reason, we refrain from adding any external base and have to account for the solvolysis. We derive the relationship between the total concentration of all sulfide species, c_0, and the equilibrium concentration of free S^{2-}, $[\text{S}^{2-}]$.

$2\text{HL} \leftrightarrow \text{H}_2\text{L}^+ + \text{L}^-$ $\qquad K_\text{w} = \left[\text{H}_2\text{L}^+\right]\left[\text{L}^-\right]$

$\text{S}^{2-} + \text{HL} \leftrightarrow \text{HS}^- + \text{L}^-$ $\qquad K_{b1} = \dfrac{\left[\text{HS}^-\right]\left[\text{L}^-\right]}{\left[\text{S}^{2-}\right]}$

Charge balance: $\qquad \left[\text{K}^+\right] + \left[\text{H}_2\text{L}^+\right] = 2\left[\text{S}^{2-}\right] + \left[\text{HS}^-\right] + \left[\text{L}^-\right]$

Mass balance:

$$\left[\mathrm{K}^{+}\right] = 2c_0$$
$$\left[\mathrm{S}^{2-}\right] + \left[\mathrm{HS}^{-}\right] = c_0$$

We arrive at a cubic equation in $\left[\mathrm{S}^{2-}\right]$, or a quadratic equation in c_0:

$$K_{b1}\left[\mathrm{S}^{2-}\right]^3 + \left(K_w - 2K_{b1}c_0 - K_{b1}{}^2\right)\left[\mathrm{S}^{2-}\right]^2 + \left(K_{b1}c_0{}^2 - 2K_{\mathrm{w}}c_0\right)\left[\mathrm{S}^{2-}\right] + K_{\mathrm{w}}c_0{}^2 = 0$$

The electrode potential depends linearly upon [S^{2-}] through the Nernst equation: $E = E^0 - s \cdot \log\left[\mathrm{S}^{2-}\right]$; the ideal Nernstian slope, *s*, equals 29.58 mV at 298.15 K. We are interested in the dependence of the electrode potential on the total concentration of all sulfide species, c_0.

The electrode potential depended linearly on the concentration of free sulfide, [S^{2-}], at total sulfide concentrations, $c_0 \geq 10^{-5}\,\mathrm{M}$ (Figure 1.1 A). The slope of -36 mV was close to the Nernstian -29.58 mV. At concentrations below 10^{-5} M, the electrode potential deviated greatly: it took 50 nmol S^{2-} to adsorb and establish double electric layers at the electrode and other surfaces. We shall see that this amount is small and will serve as an error bar in routine titrations. We needed, however, to calibrate the electrode in this low-concentration range. While it is impossible to establish a reliable concentration of sulfide of 10^{-6} M by dissolving K_2S, it is very possible to achieve this or lower concentrations by having a precipitate of a sparingly soluble sulfide like CdS in equilibrium with ions of Cd^{2+} and S^{2-} in the solution by tuning the reliable concentration of Cd^{2+}. We titrated 55 μmol $Cd(NO_3)_2$ with 0.1 M K_2S to establish the behavior of the electrode in the low-sulfide range (Figure 1.1 B)

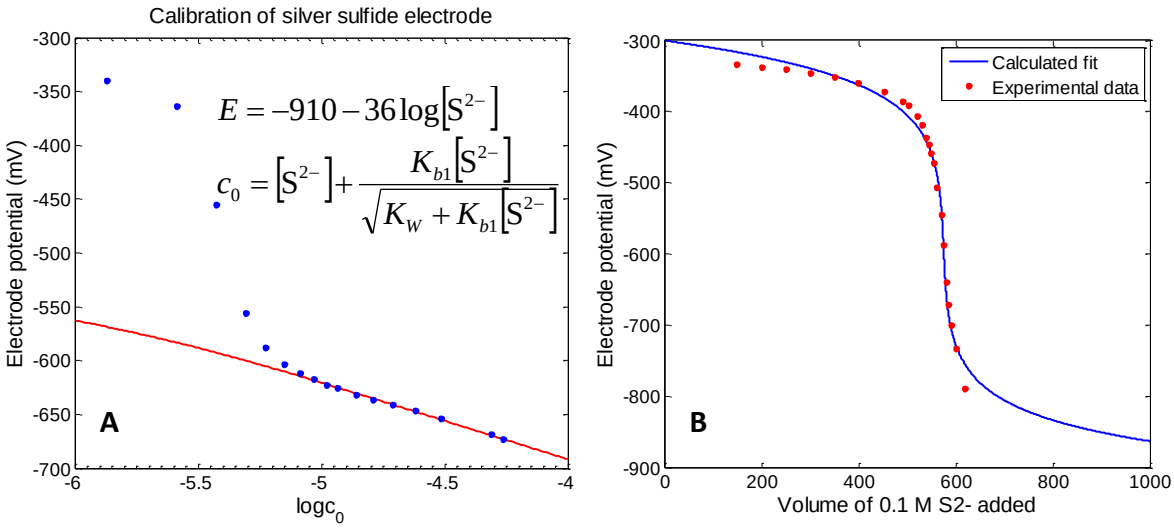

Figure 1.1. Calibration of the $Ag|Ag_2S$ electrode in two complementary ranges. (A) Calibration in the higher sulfide concentration range. (B) Calibration in the lower sulfide concentration regime: titration of a ~5 μmol aliquot of $Cd(NO_3)_2$ with 0.1 M K_2S.

1.2.3. Titration of a batch of CdSe QDs with K_2S

In a typical titration, we dispersed an aliquot of "bare" CdSe QDs in 5 ml of 0.10 M NBu_4ClO_4 in NMF and titrated it with 1.00×10^{-2} M K_2S. We were monitoring the cell potential (open circuit voltage) with Agilent 34410A multimeter with the internal impedance of 10 GΩ, interfaced with LabView. We injected the titrant with a syringe pump dropwise, with the droplet size 12 – 13 μl (Figure 1.2) We monitored the evolution of the potential after the injection of every droplet of the titrant and recorded the equilibrated value (typically 5 min after the injection). The evolution of the potential was useful for extracting the adsorption kinetics (Section 1.5).

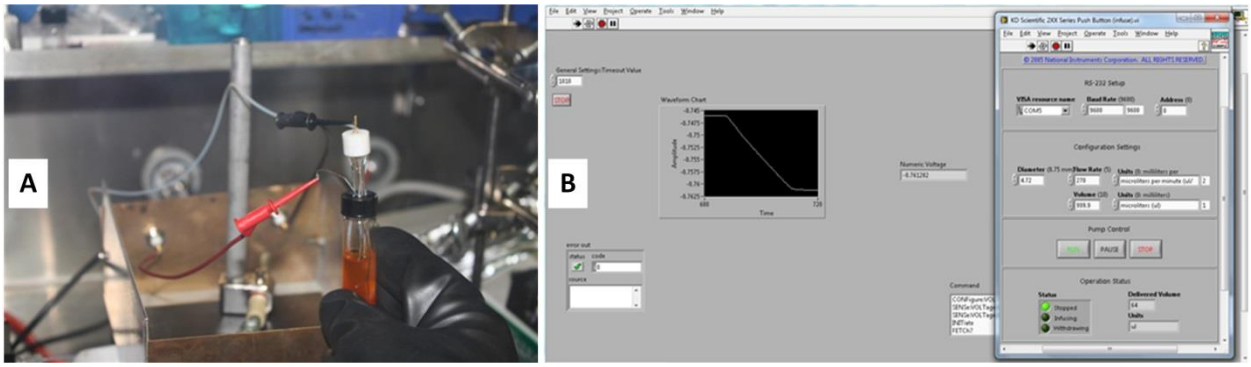

Figure 1.2. (A) A photograph of the experimental set-up. The vial is filled with a titrated solution of CdSe QDs in NMF. The red cable is contacting the home-made Ag|Ag_2S electrode. The black wire is contacting the reference electrode. The titrant is injected through a tube. The electrochemical cell is enclosed in a Faraday's cage during the measurement. (B) A screenshot of Labview interface controlling the injection of the titrant and measuring the cell potential.

The system started at low negative potentials (*ca*. -300 mV), indicative of low free sulfide concentrations. Half-way to the equivalence point, the system had the shallowest slope – similar to titrations of a weak acid with a strong base. The dramatic drop if the cell potential around the equivalence point was dramatic indicated a high affinity of sulfide to the QD surface. The cell potential remained at *ca.* -300 mV in a titration of CdSe QDs with indifferent $NaBF_4$.

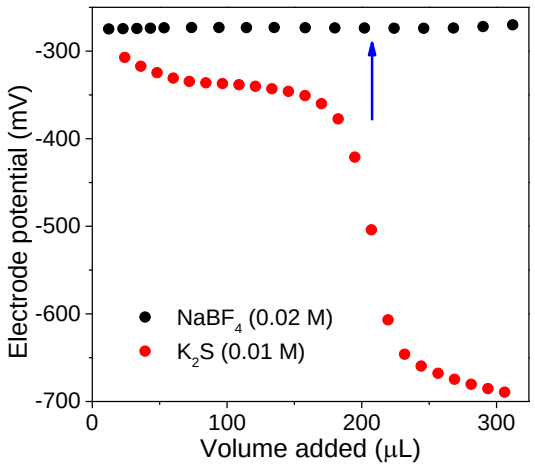

Figure 1.3. A typical titration curve for the titration of CdSe QDs with K_2S. As a blank experiment, a titration of an equal aliquot of QDs with indifferent $NaBF_4$.

In a titration of three aliquots of a particular batch of CdSe QDs, potentiometry proved as a feasible quantitative analysis technique.

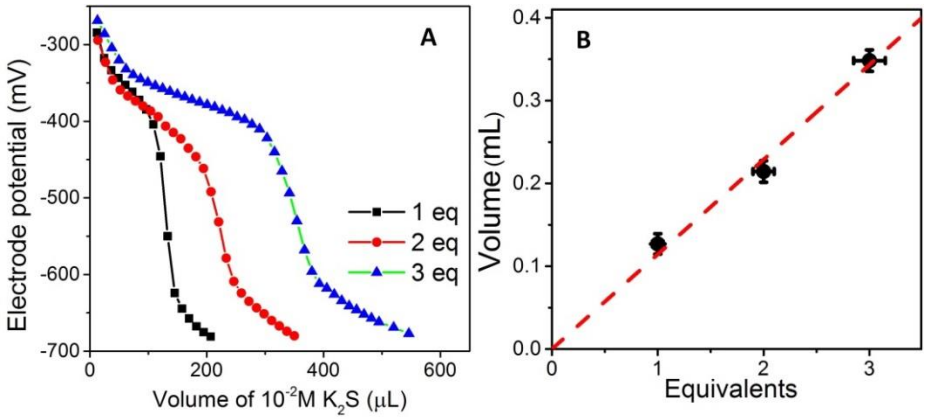

Figure 1.4. (A) Potentiometric titration of three aliquots of CdSe QDs. (B) The position of the equivalence point scales with the amount of QDs used for the titration. Adapted with permission from ref. 27. Copyright 2014, American Chemical Society.

Next, we titrated aliquots of $[CdSe]_n[Cd^{2+}\ldots 2BF_4^-]_x$ NCs of four different sizes. We varied the size by tuning the amount of TOPO, the reaction temperature, and the growth temperature. Smaller amounts of TOPO and higher reaction temperature yielded larger QDs, but at the expense of the size distribution (Figure 1.5A). The total mass of CdSe in each aliquot was identical, as follows from the equality of the absorbance at 350 nm, where excitonic features have disappeared and absorbance is proportional to the total number of CdSe "molecules."[29]

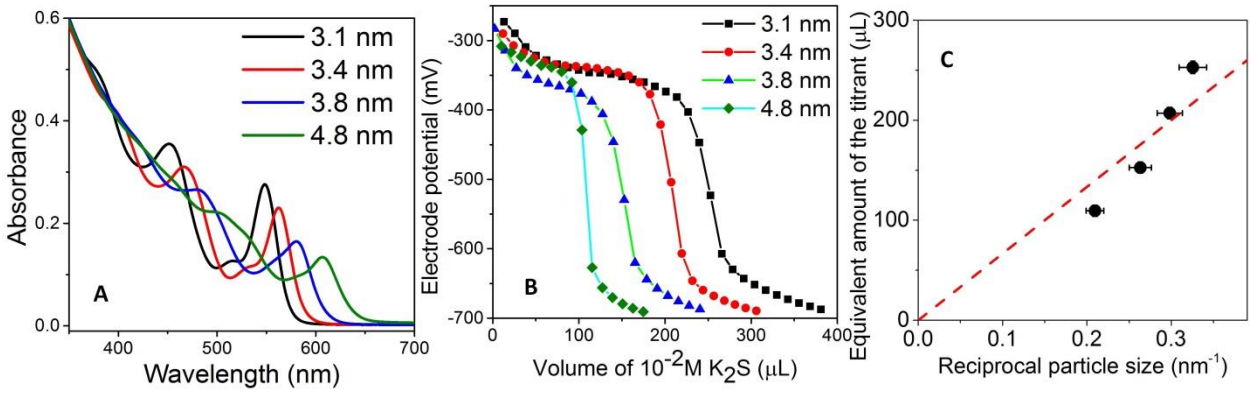

Figure 1.5. Titration of identical masses of "bare" CdSe QDs of four different sizes. Adapted with permission from ref. 27. Copyright 2014, American Chemical Society.

Smaller QDs took larger volumes of the titrant and *vice versa* (Figure 1.5A). This observation confirmed that smaller QDs have a larger total surface area. For a total mass of particles *m*, the total surface area is $A = N \cdot \pi d^2 = \frac{m}{\rho \cdot \frac{1}{6}\pi d^3} \cdot \pi d^2 = \frac{6m}{\rho d}$. In our case, the equivalent amount of the titrant deviated from the expected d^{-1} dependence upward for smaller dots. Multiple factors can be responsible for this observation. First, a QD is not a perfect sphere, and asphericity and thus surface-per-mass increase as the size of the QD decreases. Second, larger QDs terminate in stoichiometric facets, while smaller QDs terminate in Cd-rich facets, requiring higher amount of S^{2-} per unit area. Third, dynamic surface reconstructions during the titration may consume higher amounts of sulfide in smaller QDs. ICP revealed a stronger deviation from 1:1 composition in smaller NCs (Table 1). A similar behavior was described in the literature.[22]

Table 1.1. Stoichiometry of CdSe QDs of four different sizes measured by ICP.

QD size	Cd:Se ratio
3.1 nm	1.18 ± 0.10
3.4 nm	1.10 ± 0.08
3.8 nm	1.08 ± 0.07
4.8 nm	1.08 ± 0.10

It was necessary to cross-check potentiometry against another technique to make sure the jump in the potential of the electrode corresponded to the point of complete surface coverage. Electrokinetic potential (ζ-potential) gives us an idea of the NC surface charge. We observed a dramatic jump in ζ-potential 70% of the way to the equivalence point.

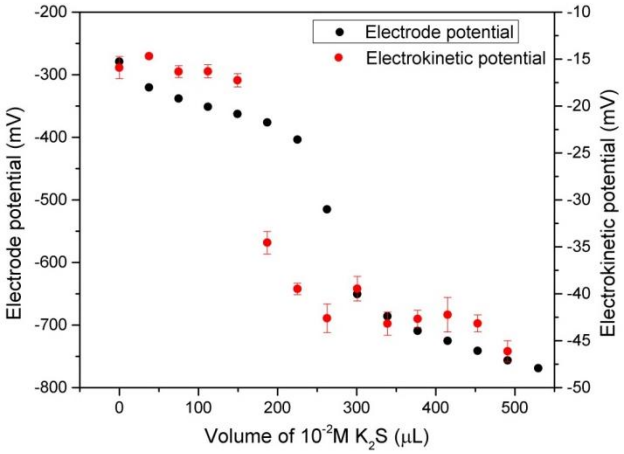

Figure 1.6. Variation of the electrokinetic potential of CdSe QDs along the titration with K_2S.

1.3. Potentiometric Titrations of CdSe/S^{2-} QDs with Cadmium Salts in a Polar Solvent

We prepared sulfide-capped CdSe QDs and NPLs by a two-phase ligand exchange with $(NH_4)_2S$ or K_2S. Four-monolayer CdSe NPLs, for example, undergo the following reaction.

$$\underline{[CdSe]_{4n}[Cd(OAc)_2]_n} + 2n\ (NH_4)_2S \rightarrow \underline{[CdSe]_{4n}[CdS]_n[S^{2-}\ldots 2\underline{NH_4^+}]_n} + 2n\ (NH_4^+ + OAc^-)$$

The resulting NCs, electrostatically stabilized in polar solvents like NMF or FA, carry a negative charge at the surface and are surrounded by a diffuse layer of cations.

The obvious cadmium-selective electrode is a piece of cadmium metal immersed in a solution containing Cd^{2+} ions. Such electrode is expected to obey the Nernst equation, $E = E^0 + s \cdot \log[Cd^{2+}]$, with s = 29.58 mV at T = 298.15 K. We cleaned a cadmium wire or plate in nitric acid - hydrogen peroxide – ethanol, 1:1:2 by volume. In calibrations, the electrode turned out to show the Nernstian slope only at high concentrations (Figure 1.6 A,B). To reduce the total area of the electrode exposed to the solution, we embedded a cadmium wire in epoxy or a ceramic tube, cut the resulting cylinder, and used the cross-section of the wire as the electrode. The slope was non-Nernstian and the response irreproducible (Figure 1.6 C). Finally, by analogy with the Ag|Ag_2S electrode, we coated a cleaned wire of cadmium with a thin layer of CdS; the

resulting electrode was sensitive to both Cd^{2+} and S^{2-} ions and showed a Nernstian slope in a calibration with Cd^{2+} (Figure 1.7 D). None of the electrodes worked in titrations.

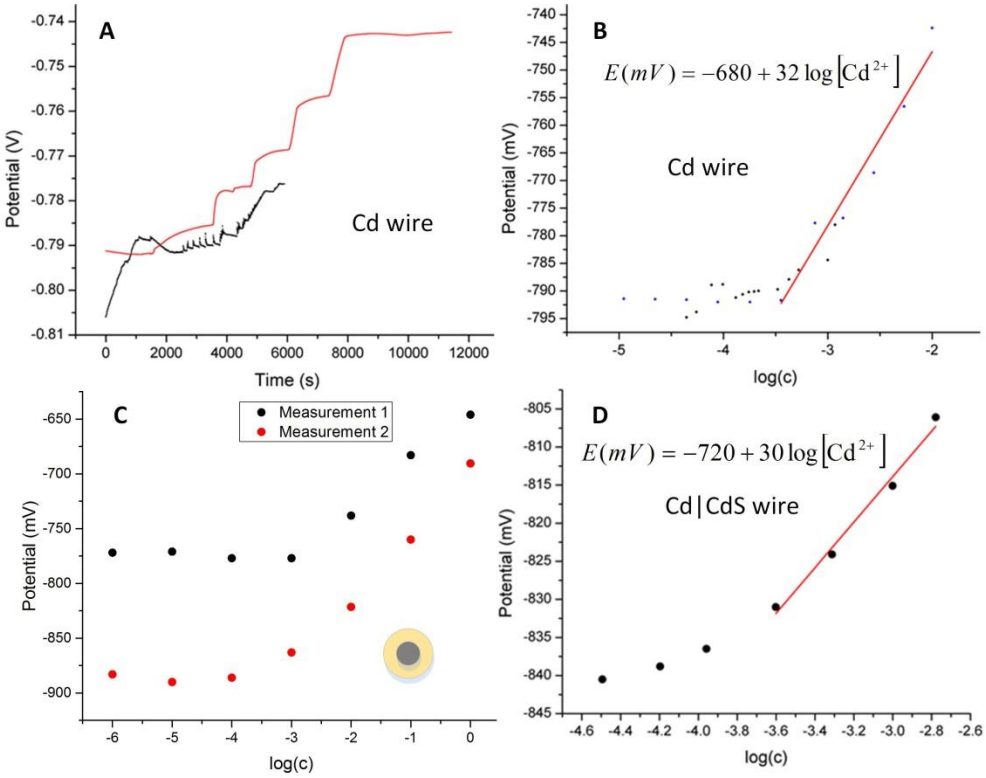

Figure 1.7. Calibration of home-made Cd-selective electrodes in NMF. (A) Response of a cadmium wire to injections of 1.0×10^{-2} M (black) and 1.0×10^{-1} M (black) solutions of $Cd(NO_3)_2$. (B) The corresponding calibration line. (C) Calibration of a cross-section of cadmium wire. (D) Calibration of a Cd|CdS wire.

We also acquired commercial Cd ion-sensitive electrodes – membrane electrodes in which the potential was determined by the ratio of the tested concentration, c_x, and the known concentration, c_0, of Cd^{2+} separated by a membrane. The potential of the cell is linear in log*c*.

$$E = E' + s \cdot \log {c_x}/{c_0} = E^0 + s \cdot \log c_x$$

We emptied the outer compartment filled with aqueous electrolyte and filled it with 0.10 M NBu_4ClO_4/NMF. The electrode showed the Nernstian slope in broader range of concentrations.

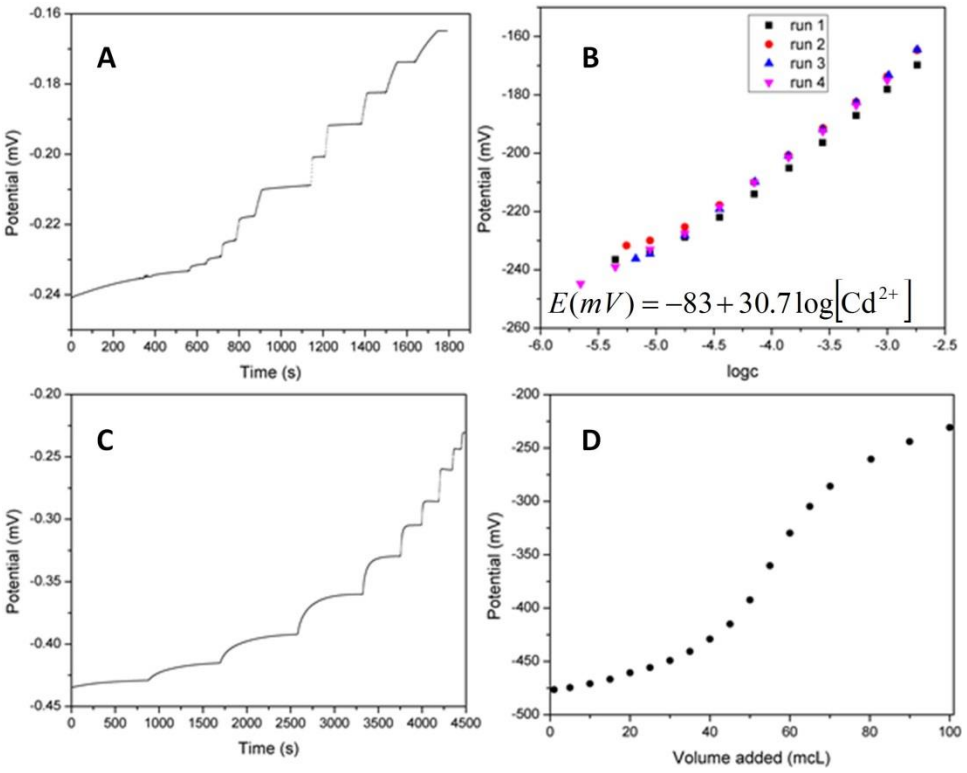

Figure 1.8. The response of a commercial electrode to injected amounts of 10^{-2} M $Cd(NO_3)_2$. (B) A series of calibration curves. (C) The response of the electrode in a titration of $CdSe/S^{2-}$ QDs with 0.01 M $Cd(NO_3)_2$ in NMF. (D) The corresponding titration curve.

A batch of sulfide-capped CdSe QDs yielded a typical titration curve with a clear equivalence point in a titration with $Cd(NO_3)_2$ monitored with the commercial electrode. Cleaning the electrode after titrations with Cd^{2+} was problematic because the NCs went through the isoelectric point and deposited at the electrode membrane. It was hard to reproduce the titration curve on a fresh batch of $CdSe/S^{2-}$ QDs. For this reason, we shall explore amperometric titrations with Cd^{2+} ions as an alternative in Section 1.8.

1.4. Thermodynamics of Ligand Adsorption

As in acid-base titrations, we can determine not only the amount of the NC surface, but also equilibrium constants of ligand adsorption. The simplest adsorption model, Langmuir

adsorption, neglects inter-particle interaction in the adsorbate. Cooperativity can be accounted for with the Hill equation or FFG isotherm. We do not, however, expect multilayer adsorption.

1.4.1. Langmuir adsorption

With the addition of every portion of the titrant, we create some initial concentration of the ligands in the solution, c_0. Part of the ligands adsorbs on the NC surface, and the remainder is free ligands in equilibrium with the adsorbate. We use an ion-selective electrode to probe the concentration of these free ligands, *c*, potentiometrically:

$$E = E^0 - s \cdot \log c \,.$$

With our notations, $(c_0 - c)$ moles of the ligands adsorb on the surface of the NCs per 1 L of the solution. If we denote with c_∞ the concentration of the ligands to cover exactly 100% of the NC surface provided that every ligand adsorbs on the surface, then the fraction of the occupied adsorption sites, θ, is given by:

$$\theta = \frac{c_0 - c}{c_\infty} \,.$$

Experimentally, we determine c_∞ from the equivalence point in the titration curve since it can be shown that the equivalence point coincides with the inflection point of the titration curve, *i.e.*:

$$\frac{d^2 E}{dc_0^{\,2}} = 0 \text{ at } c_0 = c_\infty \,.$$

As in acid-base titrations, we can extract equilibrium constants for ligand adsorption from a titration curve. The simplest model, which ignores ligand-ligand interaction in both the solution and the adsorbate, is Langmuir model. It is based on the equilibrium between free and occupied surface states.

$$\begin{array}{ccccc} \mathrm{L} + (\ ) & \leftrightarrow & (\mathrm{L}) \\ c \quad 1-\theta & & \theta \end{array}$$

The corresponding equilibrium constant is called Langmuir constant.

$$K_L = \frac{\theta}{c(1-\theta)}$$

At 50% coverage, $\theta = 1-\theta = 0.5$, the equilibrium concentration of the free ligand, $c = 1/K_L$. This way we calculate the value of the Langmuir constant by reading the cell potential half-way to the equivalence point and determining c from the calibration equation. Another way is to linearize Langmuir isotherm by inverting Langmuir equation. The slope of the $1/c$ as a function of $1/\theta$ graph is the reciprocal Langmuir constant.

$$\frac{1}{\theta} = 1 + \frac{1}{K_L c}$$

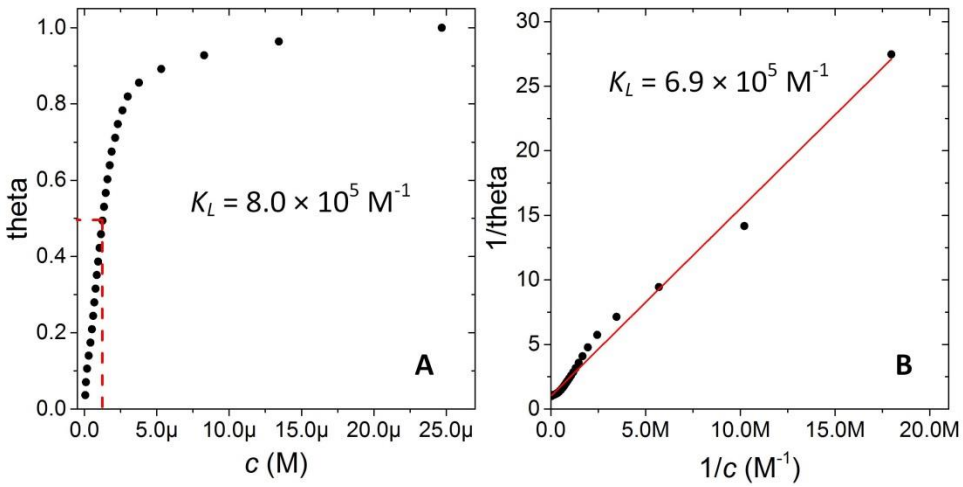

Figure 1.9. (A) Langmuir isotherm for adsorption of sulfide. (B) Linearized form to extract K_L.

The data and extracted values in Figure 1.9 are given for total sulfide: S^{2-} and SH^-. The value of the Langmuir constant is high, which makes sense, as sulfide, being a soft ligand, has a high affinity to surface Cd sites. Harder InP, in contrast, has a lower affinity to sulfide, and

therefore, demonstrates a shallower titration curve. Using Langmuir adsorption model, we computed titration curves for a few Langmuir constants (Figure 1.10 B).

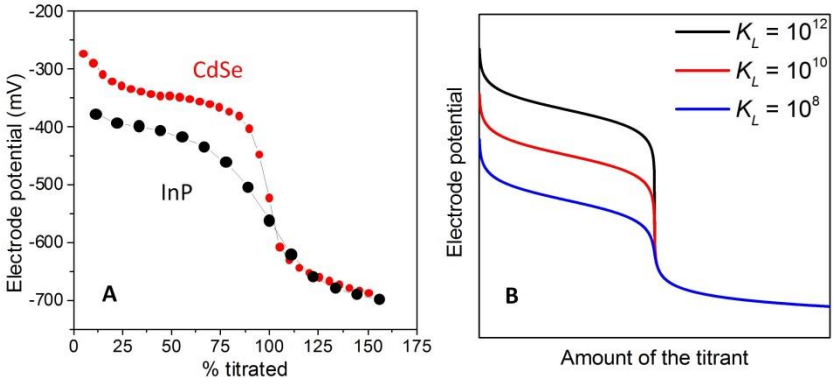

Figure 1.10. (A) Titration curves for titrations of CdSe and InP of a similar size. (B) Calculated titration curves for three different Langmuir constants. Adapted with permission from ref. 27. Copyright 2014, American Chemical Society.

Similarly, we extracted Langmuir constant for the adsorption of Cd^{2+} at the surface of $CdSe/S^{2-}$ QDs. The high value of the Langmuir constant indicates a high affinity of the ligand.

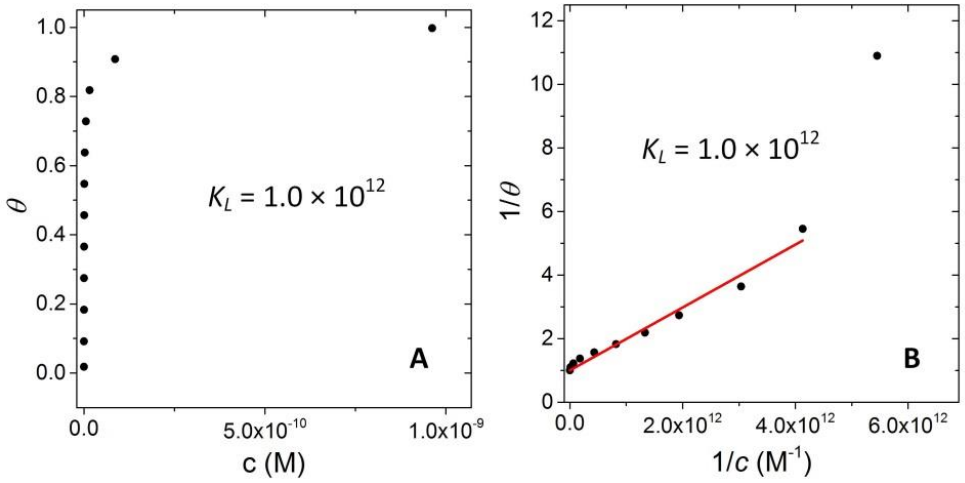

Figure 1.11. (A) Langmuir isotherm for adsorption of Cd^{2+}. (B) Linearized form to extract K_L.

1.4.2. Adsorption of charged ligands: Frumkin–Fowler–Guggenheim isotherm

Between charged sulfide ligands we expect a strong electrostatic repulsion. One model that introduces interactions between the adsorbate species results in Frumkin-Fowler-Guggenheim (FFG) isotherm, which is a modification to a Langmuir isotherm.[30]

$$\frac{\theta}{(1-\theta)c} = K_L \exp\left(-\frac{nU_p\theta}{k_BT}\right) = K_L \exp(\beta\theta),$$

where U_p is the interparticle potential energy of the ligand interaction and n is the number of the nearest neighbors of a ligand in a fully covered surface. At a given temperature, we combine 4 parameters/constants in a parameter β that is positive for inter-ligand attraction and negative for inter-ligand repulsion at the surface. We extract the adsorption parameters, K_L and β, from the linear fit to log-log plot of the FFG isotherm.

$$\log\frac{\theta}{(1-\theta)c} = \log K_L + \frac{1}{\ln 10}\beta$$

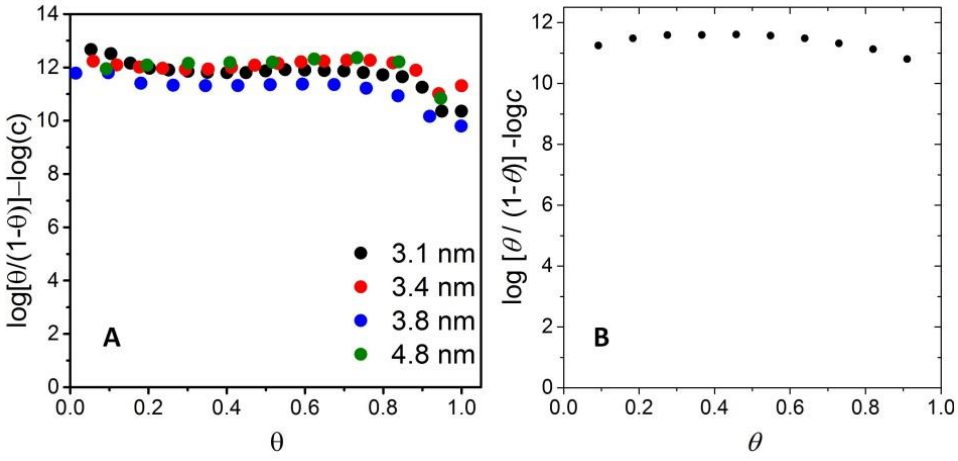

Figure 1.12. Linearized FFG isotherms of adsorption of (A) S^{2-} at the surface of "bare" CdSe QDs and (B) Cd^{2+} at the surface of CdSe/S^{2-} QDs. (A) is adapted with permission from ref. 27. Copyright 2014, American Chemical Society.

The value for K_L (~ 10^{12} M^{-1}) was independent of the QD size in the range from 3.1 nm to 4.8 nm. Parameter β was nearly zero for surface coverages up to 0.8, meaning that the inter-

ligand repulsion within the adsorbate was screened. This observation made sense because we dealt with a crystal layer growth and not physical adsorption. As a specific example, for 4.8 nm CdSe QDs, the electrode potential at the equivalence point of -523 mV corresponded to the equilibrium concentration of free S^{2-} of $1 \cdot 10^{-7}$ M and the surface coverage close to unity. The FFG isotherm of Cd^{2+} was similar, nearly constant at first and deviated downward at $\theta > 0.8$.

1.4.3. Is it possible to distinguish multiple facets potentiometrically?

In a titration of aminoacetate with acid, we observe two equivalence points: first due to the protonation of the amino group and second due to the protonation of the carboxylic group. We thus resolve two basic sites, one with a higher basicity and the other with a lower basicity. The surface of NCs (zb-CdSe for example) has multiple facets, from most Cd-rich (111) and less Cd-rich (100) to stoichiometric (110) and Se-rich (11-1). We expect different facets to have a different affinity to sulfide, and if the corresponding equilibrium constants differ by a few orders of magnitude, to resolve multiple equivalence points potentiometrically. Good candidates for such observations are anisotropic NCs, *e.g.*, NRs or NPLs because a substantial difference in the reactivity of facets is exactly the reason these structures grow anisotropically. If we learn to discriminate different facets, we will be able to synthesize complex anisotropic structures.

In a titration of CdSe/CdS core-shell NPLs, the electrode potential spanned a similar range of values as in titrations of QDs. We observed a kink in the titration curve *ca.* half-way to the equivalence point. We hypothesize that the large (001) facets of CdSe NPLs have higher affinity to S^{2-} ions. Indeed, for the highly anisotropic growth to occur during the NPL synthesis, these facets must be heavily passivated with carboxylate ligands, hence, Cd-rich. After removal of the carboxylate ligands with Me_3OBF_4, these facets expose the highest concentration of electrophilic metal sites and exhibit high reactivity. As a word of caution, our modeling shows

that to clearly resolve multiple equivalence points, the difference between K_L values should reach orders of magnitude with the smallest K_L at least of the order of 10^6 (Figure 1.13 B).[31]

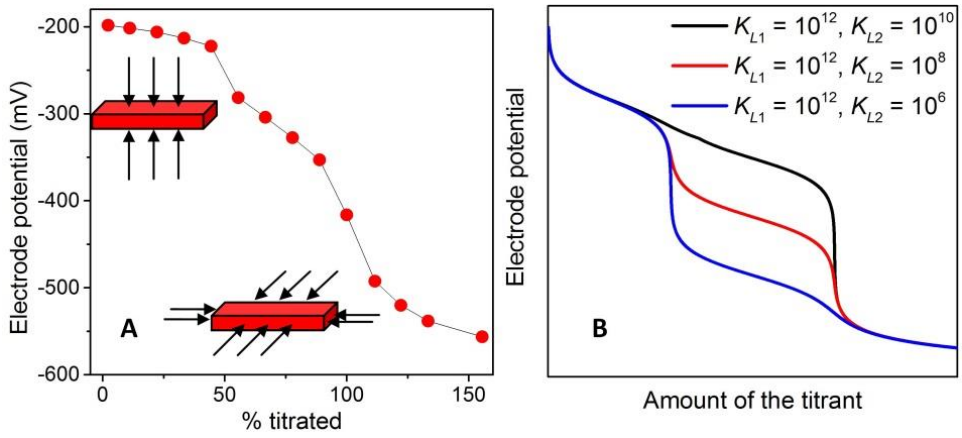

Figure 1.13. (A) A titration curve for a titration of CdSe/CdS NPLs (2 MLs CdS on each side). (B) Calculated titration curves for NCs with two types of facets. Adapted with permission from ref. 27. Copyright 2014, American Chemical Society.

The derivation of the equation that produced the curves is given in the supplementary section 1.10.

1.5. Kinetics of Ligand Adsorption

After the injection of every portion of the titrant, it took up to a few minutes for the reading of the potential to stabilize. Part of that was the electrode response, but the kinetics of ligands adsorption was an important contributor.

For a reversible reaction the differential rate equation is:

$$-\frac{dc}{dt} = -\frac{d\left(c - c_f\right)}{dt} = k_{eff}\left(c - c_f\right)^n,$$

where k_{eff} incorporates the rate constant as well as some power of the fraction of free surface sites $\left(1-\theta\right)$. We determine the effective rate constant and the reaction order from the log – log

plot of the differential rate equation. We analyze the last 4 injections before the equivalence point, as they showed the slowest kinetics.

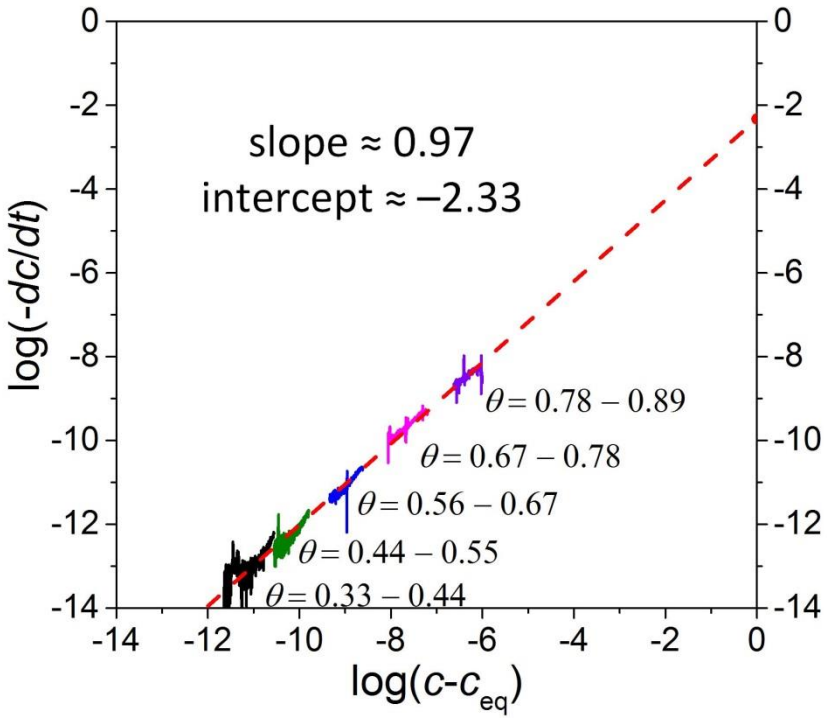

Figure 1.14. Linearized plot to extract the kinetics of the adsorption of S^{2-} at the InP QD surface. Adapted with permission from ref. 27. Copyright 2014, American Chemical Society.

The effective rate constant decreases as the surface coverage approaches 1, but clearly it does not follow the $\frac{1}{1-\theta}$ trend. Another observation is that the effective reaction order decreases from 1.25 to 0.5 over the 4 data sets. For an S_{N1} reaction:

$$S-X \longleftrightarrow S+X$$
$$S+Nu \xrightarrow{k2} S-Nu$$

the rate is given by:

$$r = \frac{k_1 k_2 [S][Nu]}{k_{-1}[X] + k_2[Nu]}$$

The concentration of sulfide, [Nu], decreases dramatically as we are tracking the adsorption kinetics after a single injection. X can be something like NMF or its anion, so its concentration is quite high and fairly constant. So the rate order in sulfide can change from 0 to 1 in the process of ion adsorption after every injection of the titrant. Another problem is that we are very sensitive to what we call c_f, especially in the plateaux of the time-potential curve.

The common linear fit to five data sets yielded the 1 for the reaction order and 4.7×10^{-3} s^{-1} for the rate constant. When the concentration of sulfide is the limiting factor, half of injected sulfide is adsorbed within 150 s after the injection. Ligand exchange is usually performed with excess ligand; therefore, a full coverage is achieved faster there. Halides, a more recent class of ligands, however, adsorb more slowly, so the kinetics analysis may be useful there, especially given silver – silver halide are good halide ion-selective electrodes for potentiometry.

1.6. Potentiometry in Non-Polar Solvents

The previous sections have established protocols for a deposition of chalcogen and cadmium layers on NCs in polar media. In contrast, the vast majority of syntheses and postsynthetic modifications of NCs occur in non-polar media like ODE or TOPO. A technique to monitor and control postsynthetic modifications and ultimately a synthesis of NCs from molecular precursors would be invaluable. The major obstacle is that potentiometry works only in conductive solutions. In non-polar media, the electrodes polarize indefinitely in open-circuit measurements. A number of ionic compounds (*e.g.*, tetraalkylammonium salts, $NR_4^+ X^-$) dissolve in non-polar solvents, but form tight ion pairs and do not conduct. One way to approach the problem is to perform the measurement at elevated temperatures and/or in aprotic solvents of intermediate polarity (*e.g.*, ethers, esters) to simultaneously disperse sterically stabilized NCs and dissociate the tight ion pairs. Another way is to run the reaction in a two-phase system: a non-

polar phase with NCs dispersed and the titrant added and a polar phase in contact in which the potential is measured.

1.6.1. Potentiometry directly in non-polar media

We titrated organic-capped CdSe NCs with freshly prepared oleylammonium sulfide (from OAm, aqeuous $(NH_4)_2S$, and molecular sieves, [Robinson]) in ODE. Pt plate served as a pseudo-reference; multiple Red-Ox pairs present in the system pinned its potential at a certain value. The signal, although noisy, clearly showed jumps due to addition of portions of the titrant. Traditional titration curve is not observed but the potential levels off past 140 μL, however.

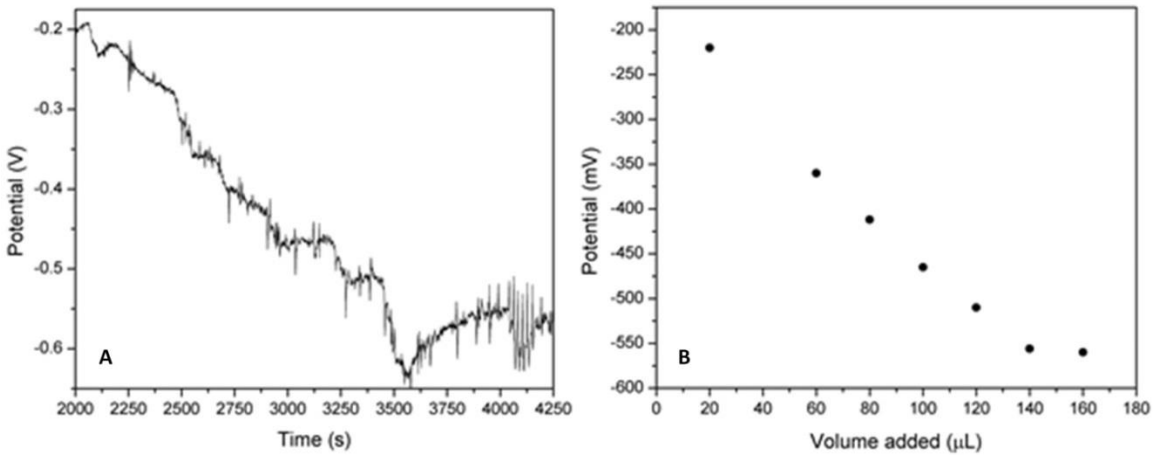

Figure 1.15. (A) Evolution of the electrode potential in a titration of organic-capped CdSe QDs at the room temperature in ODE. $Ag|Ag_2S$ was used as a working electrode and Pt plate was used as a pseudo-reference. (B) The corresponding "titration" curve.

Switching to a more polar solvent benzyl ether at 90°C yielded similar results. The cell potential drifted in benzyl ether, but stabilized after an injection of CdSe QDs. The electrode responded promptly and substantially to every injection of oleylammonium sulfide. The jump of the potential around the equivalence point was much smaller than in the case of titrations in polar solvents. The potential remained fairly stable past the injection of the titrant. An analogous

titration at the room temperature yielded similar results, but the response of the electrode was slower.

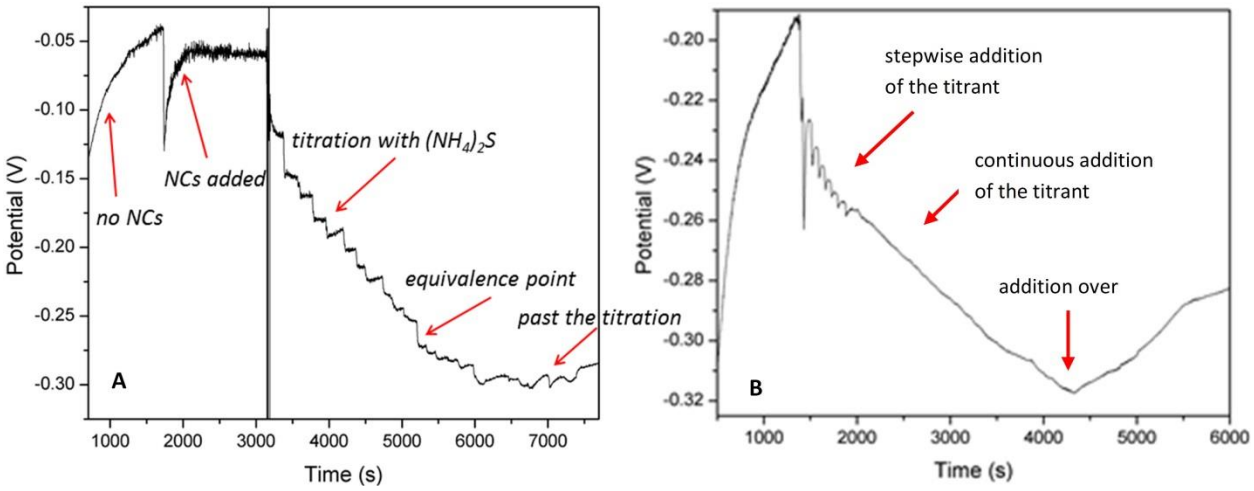

Figure 1.16. (A) Evolution of the electrode potential in a titration of organic-capped CdSe QDs in benzyl ether at 90°C. Ag|Ag_2S was used as a working electrode and Pt plate was used as a pseudo-reference. (B) Same at the room temperature.

A major disadvantage of the previous titrations is an uncertainty in the potential of the pseudo-reference electrode. The composition of the Red-Ox pair defining its potential (even the injected sulfide, for example) can change over the course of the titration. Our traditional Ag|AgCryp$^+$ electrode did not work because the NCs entered the membrane and clogged it. We used a commercial sulfide ion-selective electrode because it had a stable reference electrode (likely Ag|AgCl) in the inner compartment. We filled the outer compartment with 0.1 M NBu_4ClO_4/NMF and immersed the electrode directly into the hexane solution of CdSe QDs. The electrode showed a stable potential at the usual *ca.* -300 mV and responded to injected sulfide promptly. Past the equivalence point, the potential of the electrode did not vary with the injection of the titrant.

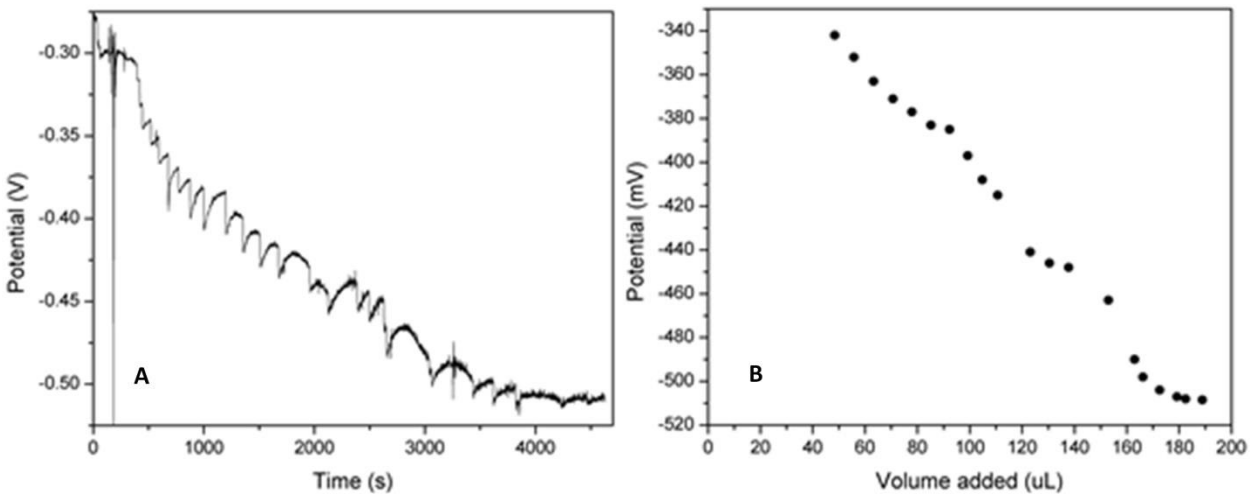

Figure 1.17. (A) Response of a commercial sulfide ion-selective electrode to the injected oleylammonium sulfide in a titration of zb-CdSe QDs in hexane. (B) The corresponding titration curve.

The titration curve somewhat shows two equivalence points; 70% of the titrant is consumed before the first one and 30% before the second one. Large zb-CdSe are close to a tetrahedral shape with the most Cd-rich (111)-type facet termination. Smaller zb-CdSe QDs have multiple facets, including less Cd-rich (100)-type and close to neutral (110)-type. It is likely that, in our batch of QDs, 70% of surface facets are (111)-type, producing the first equivalence point, and the remaining 30% are less Cd-rich facets, producing the second equivalence point. Calibration of the electrode would have helped us extract some quantitative information, but both home-made and commercial electrodes in non-polar solvents responded only in the presence of NCs.

1.6.2. Potentiometry in a two-phase system

To have a reliable electrode response, but still work with QDs in a non-polar medium, we ran potentiometric titrations in two-phase systems. The NCs were dispersed in the upper hexane phase, while the electrode(s) measured the potential in the lower NMF or FA phase. Ammonium sulfide was injected into the polar phase, or oleylammonium sulfide was injected into the non-

polar phase. Sulfide species in hexane established a trans-phase equilibrium with free S^{2-} in FA, so the electrode indirectly probed the concentration of the former.

$$(RNH_3^+)_2S^{2-} + 2\ NH_3 \rightarrow 2\ RNH_2 + 2\ NH_4^+ + S^{2-}$$

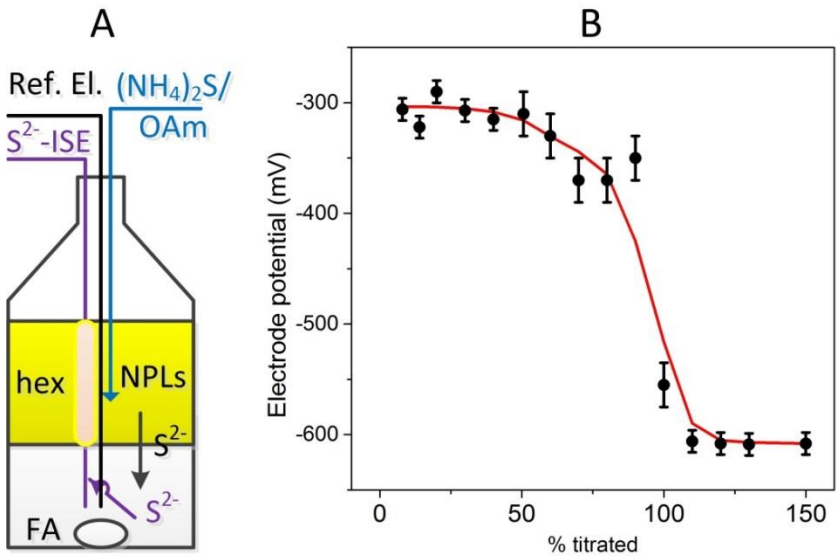

Figure 1.18. (A) A scheme of the set-up for a titration of zb-CdSe NPLs dispersed in the upper, hexane, phase by injection of $(NH_4)_2S$/OAm. The electrode potential is measured in the lower, FA, phase. (B) The corresponding titration curve; the error bars are defined by the uncertainty in the equilibrium electrode potential because of slow phase transfer of S^{2-}.

The electrode potential leveled off more slowly than in single-phase titrations because of the kinetics of the sulfide transfer across the phase boundary. The span of the potential was the usual -300 to -600 mV, but the amount of the titrant used was of the order of 10% of the amount of the NPL surface. Likely, the sulfide capped only the edges of the NPL forming a core-crown.

1.6.3. A probe to monitor systems *in situ*

This direction emerged as an extention of potentiometry in two-phase system without a phase transfer of NCs. We aimed to shrink the volume of the polar phase, where we probe the potential, in contact with the non-polar phase, where the titration of NCs occurs. For that we cut a small cup with a long handle out of a 12 ml glass vial. We sent a capillary across a septum, and put the tip into the cup. We filled the capillary and half of the cup with 0.01 M $LiClO_4$ in FA. At the top of the capillary we inserted the tip of the refernce electrode. Also, we placed the indicator electrode (a coil of Ag wire coated with Ag_2S) into the cup and sent the other end of the Ag wire across the septum. We tied the handle of the cup to the capillary. This way we obtained a probe that we inserted in the standard equipment for NC synthesis: a three-necked flask with a condenser and a temperature controller.

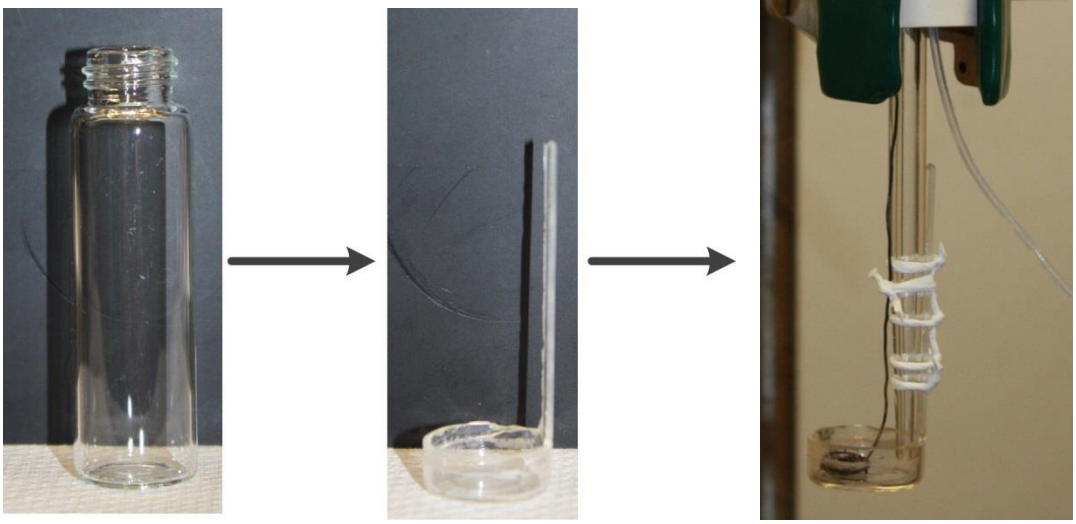

Figure 1.19. Fabrication of the probe for potentiometric monitoring *in situ*.

We established the following circuit: Ag|Ag_2S electrode | $LiClO_4$/FA on the bottom of the cup | $LiClO_4$/FA in the capillary | Ag|$AgCryp^+$ reference. TMS_2S served as a non-polar source of

sulfide. After the distribution of S^{2-} between the two phases had established, the concentration of free S^{2-} in the non-polar phase was proportional to that in the polar phase through the distribution constant: $\left[S^{2-}\right]_{hex} = K_{distr} \cdot \left[S^{2-}\right]_{FA}$. Logarithm of the distribution constant appeared as an offset in the electrode potential; therefore, although the titration curve was shifted vertically, its shape was not altered.

As a control experiment, we titrated 30 μmol of cadmium oleate with TMS_2S/ODE at 150°C. The titration in was complicated by the formation of bulk CdS precipitate that accumulated at the ODE-FA interface and on the surface of Ag/Ag_2S electrode. It negatively affected the signal-to-noise ratio of the electrode response and resulted in non-ideal shape of the titration curve (Figure 1.20). We did not notice these complications in titrations of NCs. We determined the exact concentration of ~0.2 M TMS_2S/ODE solution by a gravimetric analysis with $Pb(OAc)_2$. The true concentration of TMS_2S/ODE was 87% of the expected.

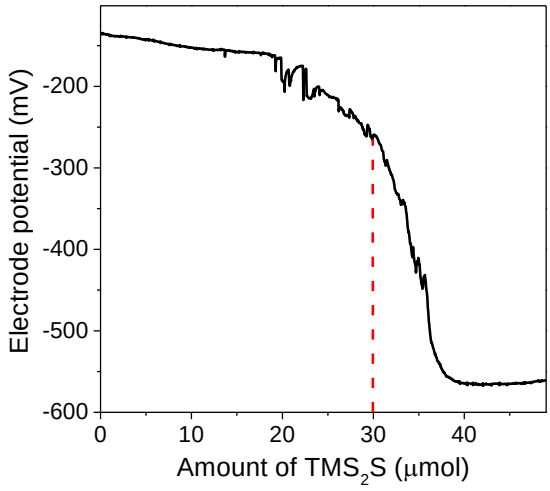

Figure 1.20. Titration of $Cd(oleate)_2$ with TMS_2S at 150°C in ODE. The dashed line indicates the expected equivalence point.

In a typical run we titrated an aliquot of w-CdSe QDs (Figure 1.21A) or zb-CdSe NPLs (Figure 1.21A) with TMS_2S in ODE. The equivalence point was clearly observable 10 minutes

from the beginning of the titration. The titration required 175 μL of the titrant to the equivalence point. From the first exciton position at 557 nm, we calculate the particle size using Donega's formula for w-CdSe[32] (for zb-CdSe one should use Hens's formula[33]):

$$E_g(\mathrm{eV}) = 1.858 + \frac{1}{0.220d^2 + 0.008d + 0.373}$$

– resulting in d = 3.25 nm. From the difference of absorbance A(350 nm) – A(700 nm) = 0.547, we calculate the concentration of the NCs in the cuvette using Hens's equation:[29]

$$c = \frac{A_{350}}{\varepsilon_{350} L} = \frac{0.547}{0.01685 d^3} = 0.9457\mu\mathrm{M}\,.$$

The amount of NCs in the cuvette is

$$0.9457\,\mu\mathrm{M} \cdot 3.030 \cdot 10^{-3}\,\mathrm{L} = 2.87 \cdot 10^{-3}\,\mu\mathrm{mol}\,.$$

For the spectrum, we used 30 μL of the stock solution, whereas for the titration we used 1 ml of the stock solution. So, the amount of NCs used for the titration was:

$$2.87 \cdot 10^{-3}\,\mu\mathrm{mol} \cdot \frac{1000}{30} = 0.0955\mu\mathrm{mol}\,.$$

The Cd-richest planes of the hexagonal wurtzite structure are (0001). These planes are 2-dimensional hexagonal lattices with the lattice constant of a = 0.430 nm. The area per Cd atom is then:

$$A_{Cd} = a^2\sqrt{3}/2 = 0.160\mathrm{nm}^2\,.$$

The area of a NC surface is:

$$A_{NC} = \pi d^2 = 33.2\mathrm{nm}^2\,.$$

Therefore, there are 207 Cd atoms on the NC surface. Henceforth, the amount of TMS_2S required is:

$$0.0955\mu mol \cdot 207 = 19.8\mu mol\ .$$

Because the concentration of TMS_2S was 0.087 M, it requires 19.8/0.087 = 230 μL of the titrant.

The experimentally determined value was 175 μL, so the prediction and the experimental results agreed. The fact that not all facets of w-CdSe NCs were (0001), as it was implied in the calculation, makes the required amount of the titrant lower than 230 μL. This information can be used to correct the amounts of precursors for SILAR and c-ALD techniques and prevent secondary nucleation, a typical problem in synthesis of core-shell nanostructures.

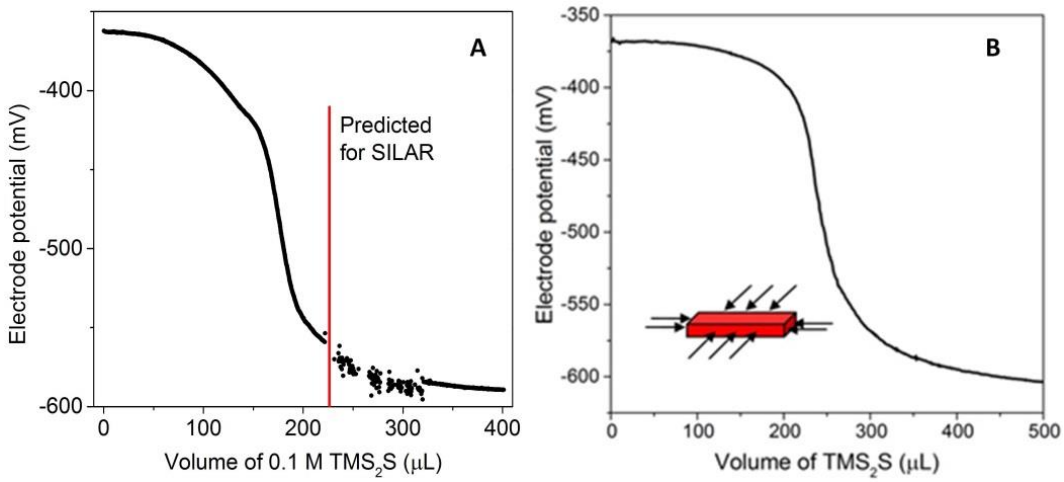

Figure 1.21. A titration of CdSe NCs with TMS_2S at elevated temperatures in ODE using the potentiometric probe. (A) w-CdSe QDs and (B) zb-CdSe NPLs were used for the titration. Adapted with permission from ref. 27. Copyright 2014, American Chemical Society.

In a titration of zb-CdSe NPLs we spent significantly lower amount of the titrant compared to the titrations of QDs in ODE or NPLs in polar media. We suspect that only adsorption at the thin edges appears as a clear equivalence point, but adsorption at ligand-passivated top and bottom faces is hidden in the tail of the titration curve. K_L must be at least 10^6 for us to see an equivalence point. In fact, the difference in reactivity of the large and narrow facets has been used to synthesize core/crown CdSe/CdS NPLs in a work by B. Dubertret and co-workers.[34]

Finally, we demonstrate a practical utility of potentiometry for the core-shell growth *via* controlled layer-by-layer deposition of CdS shell. In the previous experiment we noticed that the electrode potential at the equivalence point was between -450 and -500 mV, so in a typical titration experiment, we injected the equivalent amount of Cd oleate when the potential reached -450 mV. After the injection, the electrode potential grew sharply and then continued to follow a regular titration curve (Figure 3D). We controllably grew 3 layers of CdS. The resulting solution showed expected red shifts in the absorption and emission spectra and high photoluminescence efficiency. TEM images also showed no evidence of secondary nucleation of CdS (Figure 1.22).

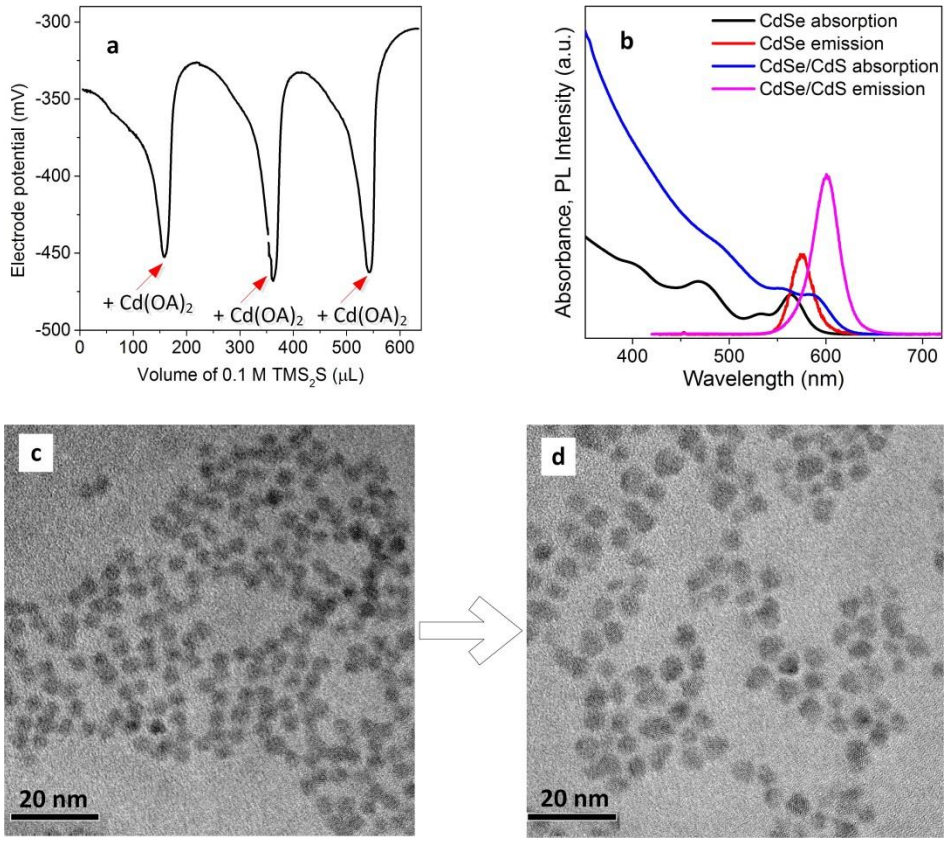

Figure 1.22. (a) Monitoring a growth of three layers of CdS over w-CdSe QDs *in situ*. (b) Absorption and emission spectra of CdSe before the growth and CdSe/CdS after the growth. (c) TEM image of CdSe NCs used for the core-shell growth. (d) TEM image of the resulting CdSe@CdS NCs with 3 layers of CdS. Adapted with permission from ref. 27. Copyright 2014, American Chemical Society.

1.7. Monitoring Syntheses of Semiconductor NCs *in Situ*

The true power of potentiometry would be in tracking a real hot synthesis of semiconductor NCs. zb-CdSe QDs is a good model system for a potentiometrically tracked synthesis because there is enough time to observe a slow nucleation and growth of the NCs during the heat-up of the system. In a typical synthesis, the precursors (cadmium myristate and SeO_2) are loaded in ODE and heated up rapidly to 240^{o}C. The electrode picked up a stable potential at 90^{o}C, followed by an upward drift up to 120^{o}C. There, when the nucleation became noticeable, the potential began to drift downward. At temperatures *ca.* 240^{o}C, when the QDs were 3 – 4 nm in diameter, the potential reached its minimum. It increased somewhat during the addition of oleic acid (to passivate the QDs) and then leveled off (Figure 1.23A). The resistivity of the reaction mixture increased by a factor of 5 from the nucleation event at 120^{o}C to the end of the synthesis at 240^{o}C (Figure 1.23 B). The resulting QDs showed typical absorption and PL spectra corresponding to *ca.* 4 nm CdSe QDs (Figure 1.23 C).

Two other tries were less successful. All three experiments shared a number of features. First, the potential of the electrode peaked right before or at the nucleation, decayed during the growth of the QDs, and leveled off when the growth was over. The variation of the electrode potential in a multi-hundred range corresponds to a multi-decade variation in the concentration of active sulfide species.

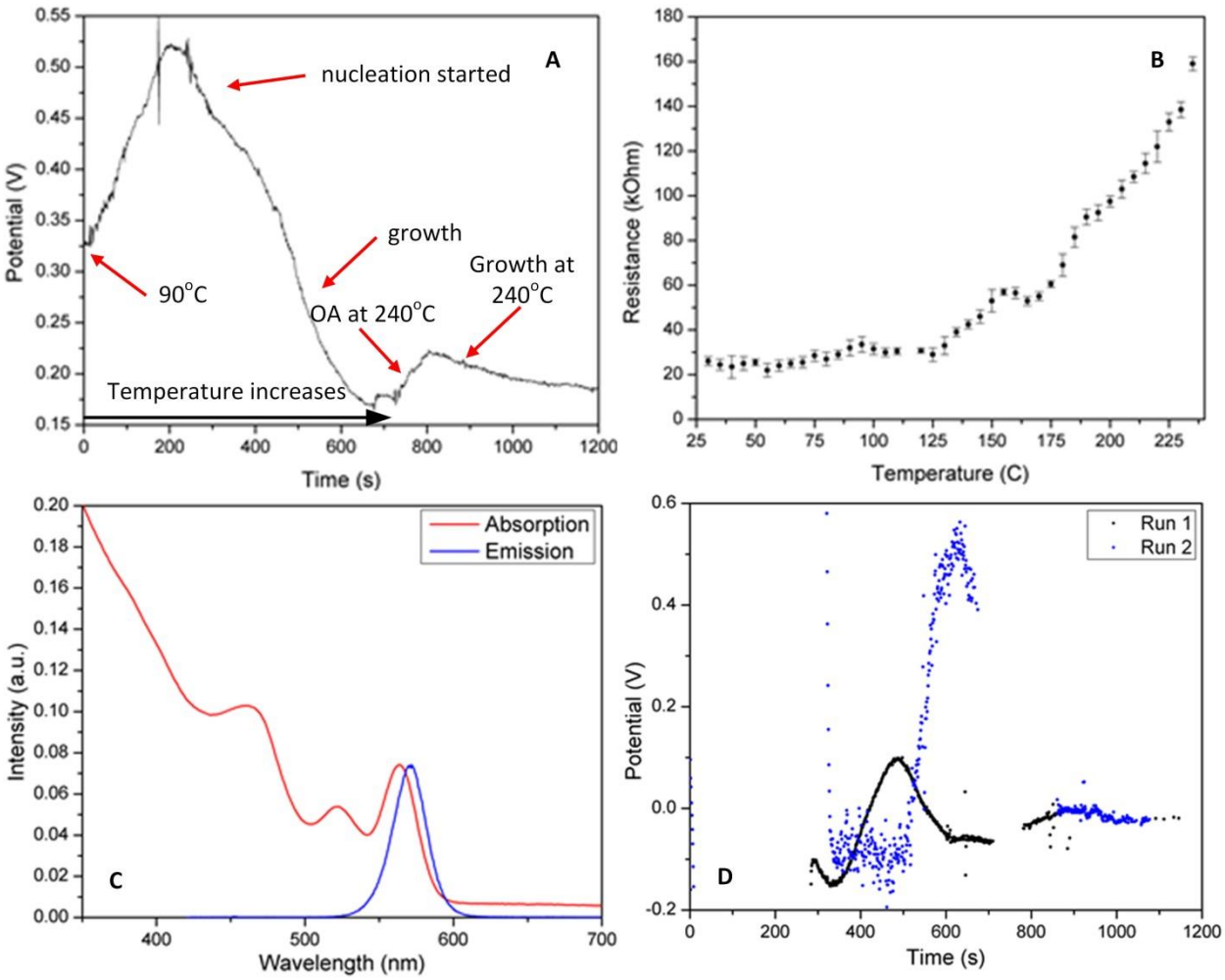

Figure 1.23. (A) Potentiometric tracking of a typical synthesis of zb-CdSe QDs at temperatures up to 240°C. The working electrode was home-made Ag|Ag_2S, and a Pt plate served a pseudo-reference. (B) Resistance of a volume (~ 1 cm^2 / 1 cm) of the reaction mixture during the synthesis. (C) Absorption and PL spectra of zb-CdSe QDs from the tracked synthesis. (D) Two other potentiometrically tracked syntheses of zb-CdSe QDs.

To eliminate unreliability of the Pt pseudo-reference, We switched to the potentiometric probe (Section 1.6.3). Polymerization of FA set 180°C as the temperature cap; therefore, syntheses occurring at lower temperature (*e.g.*, PbE QDs, E = S, Se) were ideal for this experiment. We tracked potentiometrically a twelve-fold scale-up of Scholes's synthesis of PbS. We dissolved PbO in OA and ODE at 150°C, cooled down the system, inserted the potentiometric probe, and heated the system to 80°C under nitrogen. Upon an injection of

TMS_2S/ODE into the reaction mixture, the temperature dropped to 70°C. The potential of TMS_2S, the potential of the electrode dropped dramatically likely due to an increase in the concentration of sulfide. When a visible nucleation appeared, the potential was recovering due to a consumption of TMS_2S. When the growth slowed down, the potential leveled off (Figure 1.24A).

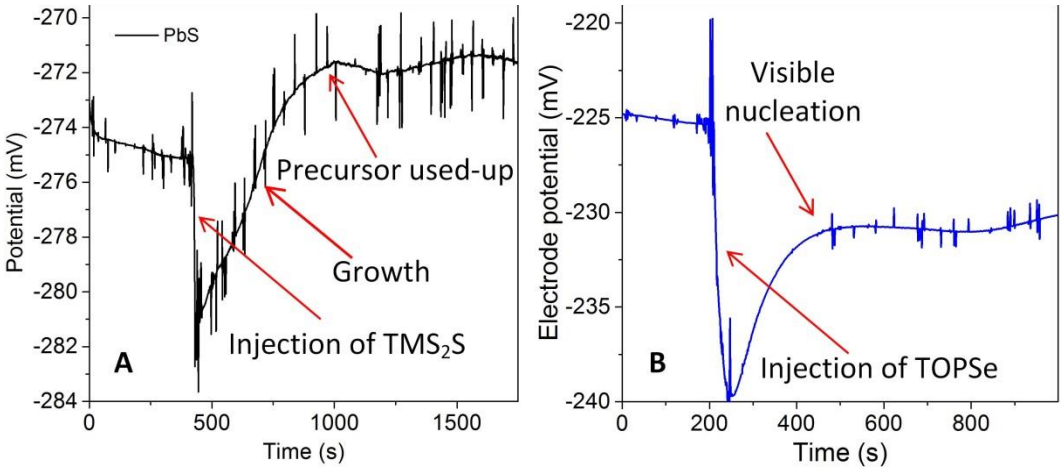

Figure 1.24. (A) A potentiometrically tracked synthesis of PbS QDs in ODE at 80°C using the potentiometric probe. (B) A potentiometrically tracked synthesis of PbSe QDs in ODE at 54°C using the potentiometric probe.

Another attractive model was a recipe for PbSe "magic-sized" clusters from lead oleate and technical-grade TOPSe/TOP in ODE by Krauss *et al.*[35] We prepared the Pb precursor in a 50 ml flask, installed the potentiometric probe, leveled the temperature at 54°C, and began the measurement. With the injection of TOPSe, the electrode potential dropped and then gradually recovered over 5 min (Figure 1A). The solution remained clear for 4 min after the injection, then turned brownish-yellow and was darkening in the 5th minute, and eventually turned dark brown past 5 min. That point was indicated that as the beginning of the nucleation, although no characteristic features in the electrode potential were observed. Over 3 hours of the reaction, the potential oscillated between -227 mV and -230 mV with no drift.

To eliminate the effect of the temperature drop upon the injection of TMS_2S or TOPSe, We ran a blank experiment in which we injected pure ODE or TOP into the lead precursor under similar conditions. The drop in the electrode potential did not exceed 1 mV in such case. Overall, the observed drops in the potential, although seem reliable, are too small, corresponding to a sub-decade variation in the concentration of active sulfide species.

1.8. Monitoring Cation Adsorption with Amperometry

In Section 1.3, we experienced difficulties with the calibration and use of commercial and home-made cadmium ion-selective electrodes. Briefly, a cadmium wire or plate responded poorly to intermediate concentration of Cd^{2+} in the solution. Nevertheless, capping the NCs with cations is the last step of the synthesis of the commercial bright core-shells, the step that passivates hole traps and makes the QDs luminescent. Understanding the completeness of metal coverage is therefore important in an economic use of the cadmium precursor.

1.8.1. Amperometry as a technique

The measured signal in amperometry is electric current due to an oxidation or reduction of a particular Red-Ox active species. The experiment is conducted in a steady state of the solution, without stirring. When a voltage is applied between two electrodes immersed in the solution, the cations roaming around the anode are reduced. The rate limiting step in this case is the electron transfer at the electrode and the measured current is essentially Faradaic current. Once the cationic cloud in the vicinity of the anode has been depleted, the rate limiting step is a diffusion of ions from the bulk of the solution to the electrode and the measured current is the diffusion current. The diffusion current at any point is proportional to the negative gradient of the concentration of cations at that point. If we assume an exponential depletion around the electrode with a characteristic length L:

$$c(x) = c_{\text{bulk}}\left(1 - e^{-x/L}\right)$$

– the diffusion current at the electrode is proportional to the concentration of the ions in the bulk of the solution.

$$J_{x=0} = -D\frac{dc}{dx}\bigg|_{x=0} = -\frac{Dc_{\text{bulk}}}{L}e^{-x/L}\bigg|_{x=0} = -\frac{D}{L}\cdot c_{\text{bulk}}$$

The measured signal is, therefore, proportional to the concentration of the species in the solution.

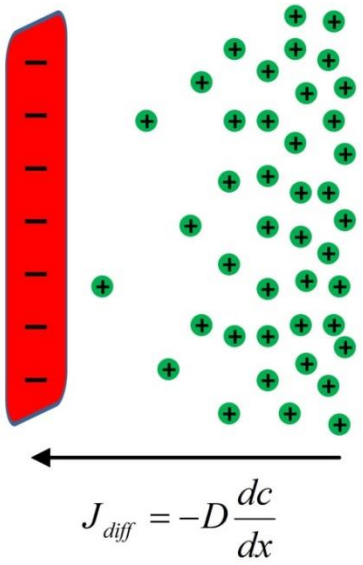

Figure 1.25. A schematic of amperometric measurement.

The depletion length L depends on the ionic strength of the solution. To minimize the contribution of the measure ions to the total ionic strength, the latter ought to be kept fairly high. We will run cyclic voltammetry scans on our system to determine the optimal bias for potentiometry, a bias that enables selective reduction of the desired cation.

1.8.2. Cyclic voltammetry

Cyclic voltammetry (CV) uses a three-electrode cell. The analysis-determining chemical reaction occurs at the working electrode (WE) – a platinum, gold, or glassy carbon disk. The

reference electrode (RE) is usually immersed in its own solution and is separated from the solution by a membrane. As in potentiometry, sometimes we shall use a pseudo-reference electrode, *e.g.*, a Pt plate. The counter electrode (CE) is a silver wire. The voltage is applied between the working and the reference electrodes, and current through the counter electrode is measured. Unlike potentiometry, CV is a non-equilibrium technique, so the signal is transient.

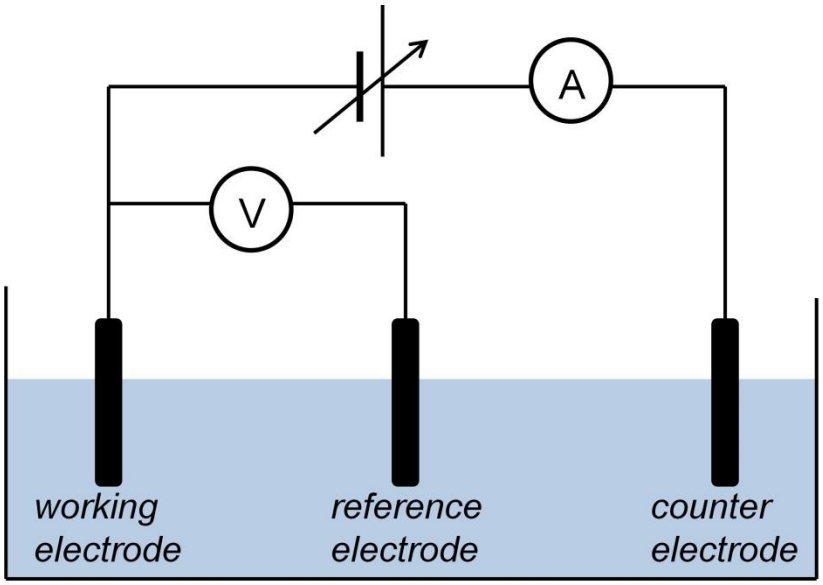

Figure 1.26. A schematic of the three-electrode cell for cyclic voltammetry and amperometry.

The first step is to choose the solvent and the electrolyte so that the Red-Ox pair of interest fits in the window. Next, we calibrate the cell with an established Red-Ox pair, ferrocene-ferrocenium couple. The reduction half-reaction is the following; Cp denotes cyclopentadienyl.

$$\overset{\text{III}}{\text{Fe}}(\text{Cp})_2^+ + e^- \rightarrow \overset{\text{II}}{\text{Fe}}(\text{Cp})_2$$

A CV scan of ferrocene shows an anodic and a cathodic peaks. At 0 V w.r.t. the RE, no oxidation or reduction occurs and measured current is nearly zero. At 400 mV, there is a spike of Faradaic current due to the oxidation of ferrocene into ferrocenium. The current then levels off

and is determined by the diffusion current. Again, the measured signal is not equilibrium but transient; it is not that the current is higher at 400 mV than at 600 mV. Rather, the current is higher at the time when the bias is 400 mV (and ferrocene around the electrode is not depleted yet) and lower at the time when the bias is 600 mV (when all ferrocene around the electrode is depleted).

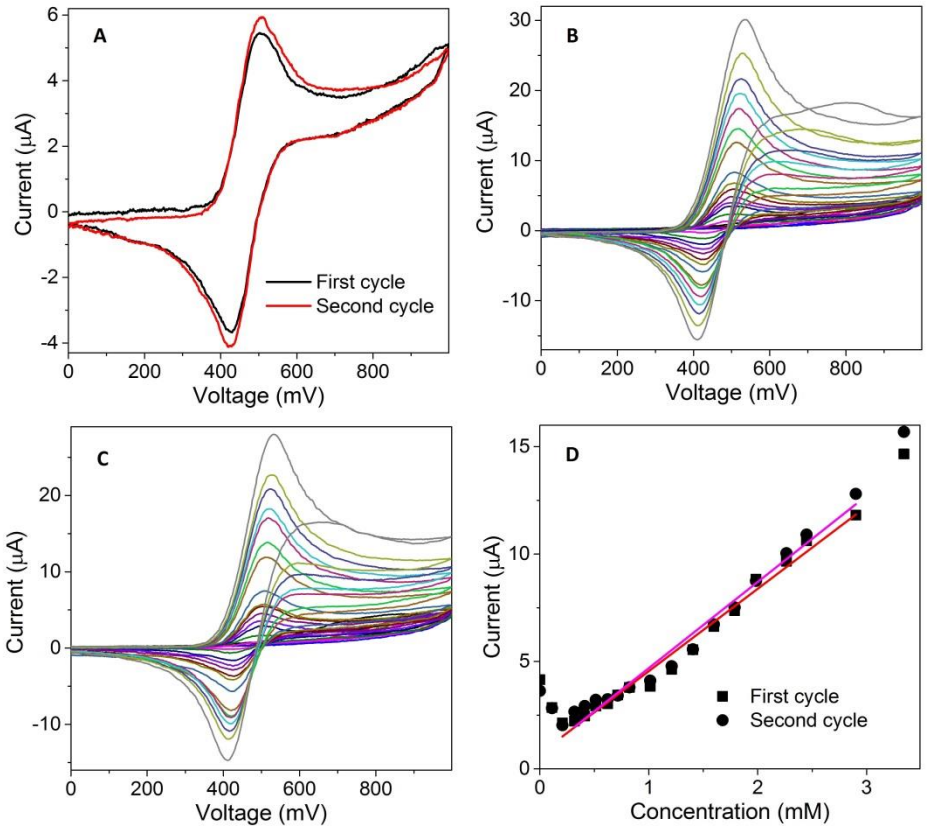

Figure 1.27. Calibration of the CV cell with ferrocene in 0.1 M NBu_4ClO_4 in NMF. WE: Pt disk, RE: Ag|AgCryp$^+$, CE: Ag wire. (A) The first and the second scans of CV of $FeCp_2$ coincide. (B) The first CV scan for different concentrations of ferrocene. (C) The second CV scan for different concentrations of ferrocene. (D) Current at 800 mV as a function of the concentration of ferrocene.

In the reverse scan, there is a spike of anodic Faradaic current due to a reduction of the formed ferrocenium to ferrocene and a level-off due to the depletion of the former. The arithmetic mean of the cathodic and anodic peak voltages is the standard Fc^+/Fc potential w.r.t.

the RE. Since the standard potential of Fc^+/Fc couple is tabulated for a number of solvents, we use this information to convert from potentials to energies measured from the vacuum level.

We extracted the anodic current at 800 mV, where it was determined by the diffusion current, for a number of concentrations of ferrocene. As expected, the diffusion current was proportional to the concentration of ferrocene for both the first and the second CV scans (Figure 1.27 D).

Methylene chloride is a good solvent of intermediate polarity: it can disperse sterically stabilized NCs, and at the same time, it can dissolve the supporting electrolyte to form conductive solutions. We calibrated the cell for potentiometric titrations with TMS_2S with Pt plate as a pseudo reference. The calibration curve started linear with a small offset, but then started to level off (Figure 1.28 C).

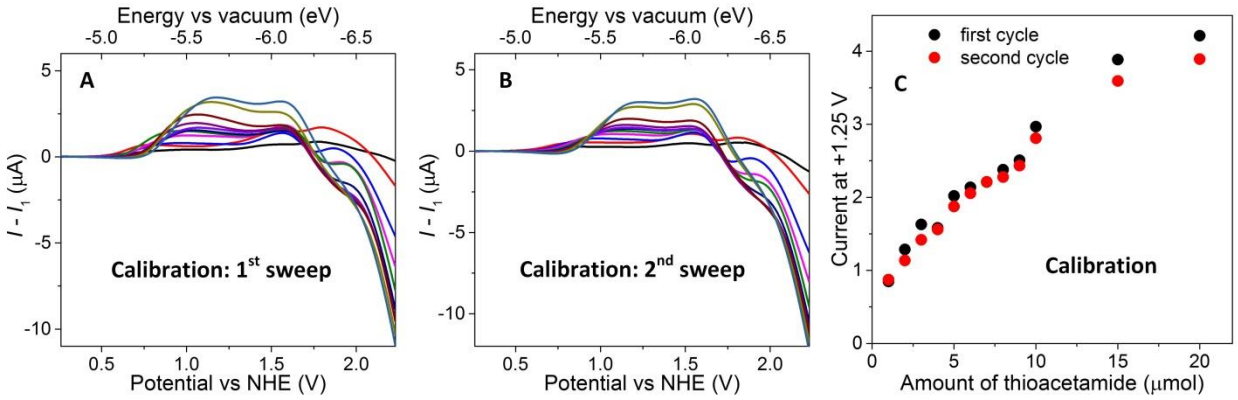

Figure 1.28. Calibration of a CV cell for amperometric titrations with TMS_2S in CH_2Cl_2. WE: Pt disk, QRE: Pt plate, CE: Ag wire. (A) The first forward sweep for a number of concentrations of TMS_2S with the blank subtracted. (B) Same with the second sweep. (C) Extracted current at +1.25 V.

1.8.3. Amperometric titrations

In titrations of NCs, we need to make sure the Red-Ox couple fits in the window (the band gap) of the semiconductor NC. The anodic peak in a CV of a colloidal solution of semiconductor NCs corresponds to the valence band and the cathodic peak to the conduction

band. Usually if a ligand is a hole trap (*e.g.*, S^{2-} for CdSe NCs), then its anodic peak will appear before that of the NC. We titrated a batch of sterically stabilized w-CdSe QDs with TMS_2S in CH_2Cl_2 in a slow continuous injection. For the first part of the titration curve, the current was low and nearly constant (0.8 μA is measured when no TMS_2S is added in the calibration run). At *ca.* 34 μmol TMS_2S, the current took off and became linear with the amount of the titrant added.

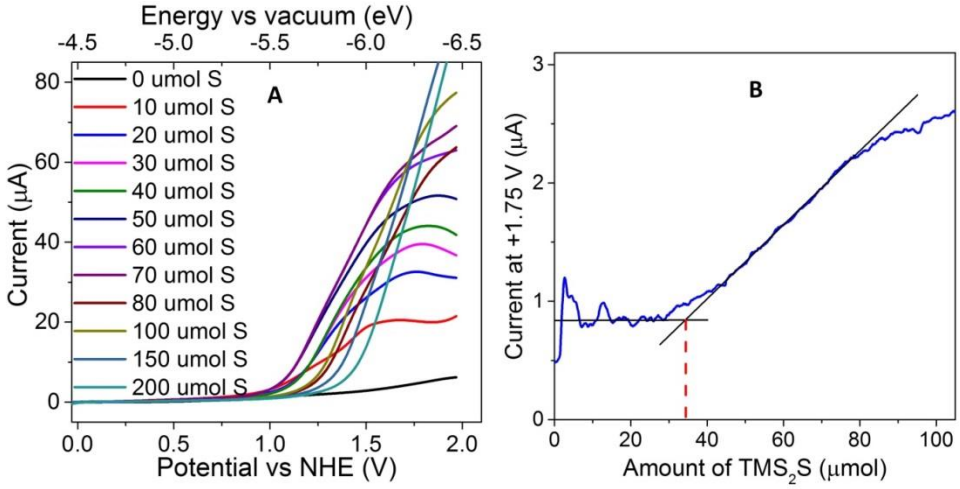

Figure 1.29. (A) Stepwise titration of w-CdSe QDs. (B) Continuous amperometric titration.

The true value of the technique will be in titrations of chalcogen-capped NCs with metal ions. In a cathodic CV scan of sulfide-capped CdSe NPLs, the $E_{1/2}$ of Cd during the titration was around -0.5 V, and was shifting to higher numbers slowly. The $E_{1/2}$ of Cd in the overtitrated sample occurred at -0.40 V (in water, $E^0_{Cd^{2+}/Cd} = -0.403\,V$).

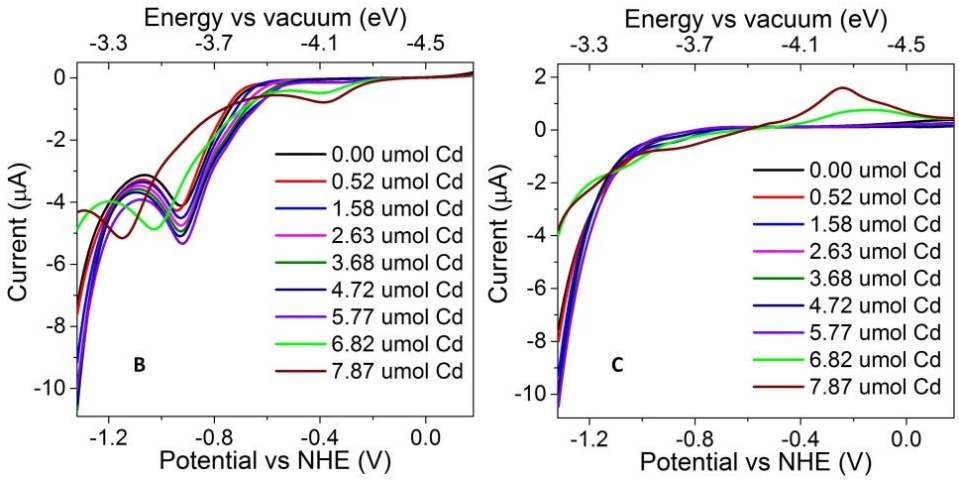

Figure 1.30. (B) Forward cathodic CV sweeps of $CdSe/S^{2-}$ NPLs with a series of injected amounts of $Cd(NO_3)_2$ in NMF. (C) Reverse cathodic CV sweeps of $CdSe/S^{2-}$ NPLs with a series of injected amounts of $Cd(NO_3)_2$ in NMF. WE: Pt disk, RE: $Ag|AgCryp^+$, CE: Ag wire.

During the titration, the anodic peak in the forward scan of the NPLs occurred at at – 0.9 V *vs* NHE. Past the equivalence point, a small anodic peak of free Cd^{2+} appeared at – 0.42 V and the anodic peak of the NCs shifted toward more negative voltages.

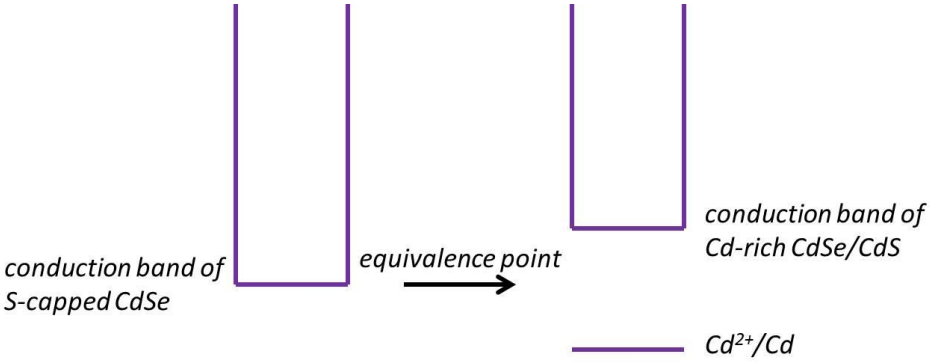

Figure 1.31. Band rearrangement at the equivalence point of $CdSe/S^{2-}$ NPLs titrated with Cd^{2+}.

One way to run an amperometric titration is to set the bias on the shoulder of the anodic peak and observe the decay of the current past the equivalence point due to the shift of the conduction band, followed by a growth of the current due to the accumulation of free Cd^{2+}. This jump occurs only when Pt disk used as the WE.

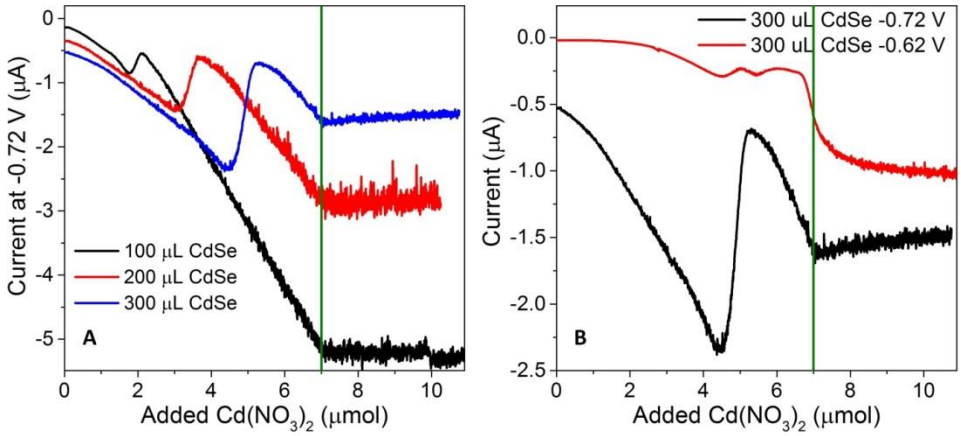

Figure 1.32. Amperometric titration curves for w-CdSe/S2- QDs titrated with $Cd(NO3)_2$ in NMF with stirring. 7 μmol $Cd(NO3)_2$ is injected in all cases, which is indicated with the vertical green line. (A) Three different aliquots titrated at the same bias. (B) The largest aliquot of the QDs titrated at two different biases. WE: Pt disk.

Gold working electrode yields a clean zero current during the titration. At the equivalence point, the current takes off and shows a slope similar to that in the calibration curve. Glassy carbon does not work for this application.

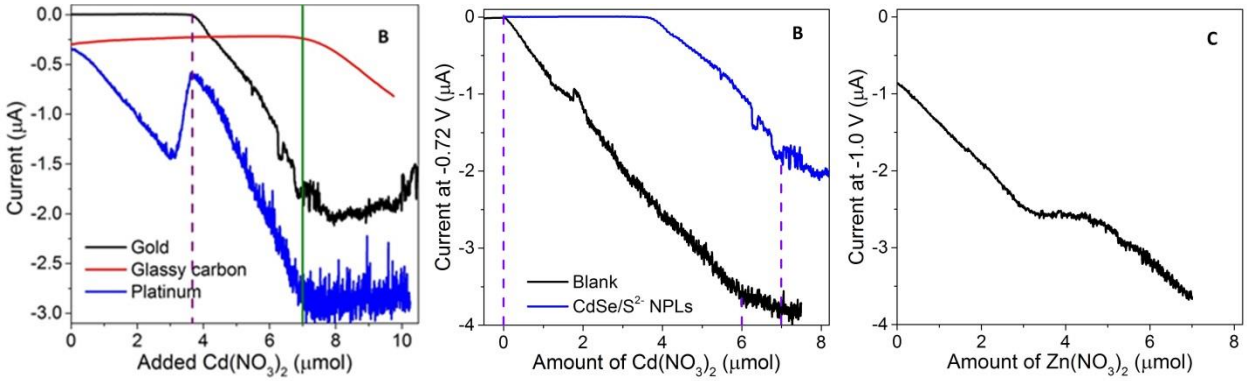

Figure 1.33. (A) Amperometric titrations of S-capped CdSe NPLs with $Cd(NO_3)_2$ in NMF with gold, glassy carbon, and platinum working electrodes. The dashed line shows the apparent equivalence point, and the solid green line shows the end of the addition of $Cd(NO_3)_2$. (B) Calibration of the set-up and an amperometric titration of $CdSe/S^{2-}$ NPLs with $Cd(NO_3)_2$. (B) Amperometric titration of $CdSe/S^{2-}$ NPLs with $Zn(NO_3)_2$. WE: Au disk, RE: $Ag|AgCryp^+$, CE: Ag wire.

1.9. Summary and Outlook

With potentiometry, we titrated "bare" CdSe and InP QDs and NPLs with K_2S, as well as CdSe/S^{2-} NCs with $Cd(NO_3)_2$ in polar solvents. We characterized the thermodynamics and kinetics of ligand adsorption. Steep titration curves resulted from high equilibrium constants of the ligand adsorption. We extended the technique to non-polar solvents, where we successfully titrated a batch of sterically stabilized QDs with a molecular source of sulfide TMS_2S. Potentiometry allowed us to controllably deposit 3 MLs of CdS over CdSe, resulting in improved PL and no secondary nucleation. With amperometry, we successfully titrated a batch of CdSe/S^{2-} NCs with $Cd(NO_3)_2$, showing that the technique can be extended to monitoring the deposition of other cations at the right cell potential.

Resolution of multiple equivalence points was challenging. Modeling showed that consecutive equilibrium constants would have to differ by more than two orders of magnitude, the lowest being at least 10^5. The number of type of facets our CdSe QDs had was likely too big, making the set of equilibrium constants closely spaced, and coalescing thus all equivalence points. Having reviewed the data and acquired some knowledge of CdSe NPLs, we suspect that we titrated preferentially side facets in titrations with TMS_2S in non-polar solvents. The goal can be achieved for NCs with well-defined types of facets with approximately equal fractions and very different stoichiometry, *e.g.*, PbSe NCs with stoichiometric and lead-rich facets.

One can combine potentiometrically-probed deposition of chalcogenides or halides with amperometrically monitored deposition of cations to construct a commercial probe for monitoring syntheses of core-shell materials. Finally, we the right design of the probe and choice of polar medium (ionic liquids), one can design a probe for monitoring hot syntheses.

1.10. Experimental Procedures and Supporting Information

In the synthesis of wurtzite CdSe QDs, we loaded a 100 ml three-necked flask with mix 2.4 g technical-grade TOPO, 2.25 ml of 0.5 M Cd oleate in oleic acid, and 12 ml ODE. We degassed the mixture at 70^{o}C for 1 hr. Then we refilled the flask with nitrogen and heated the up mixture to 300^{o}C. In a nitrogen-filled glove box, we filled a syringe with a mixture of 4 ml of 1 M TOPSe/TOP and 3 ml OAm. When the temperature in the flask reached 300^{o}C, we swiftly injected the Se precursor into the flask. We observed the temperature dropped down to 270^{o}C and allowed it to recover to 280^{o}C. We ran the reaction for 3 – 7 min depending on the desired QD size and quickly cooled down the flask to 150^{o}C and allowed it to slowly cool down to the room temperature. We ran 3 cycles of washing which included precipitation with ethanol and re-dispersion in hexane. To synthesize larger dots, we lowered the amount of TOPO (down to 1.2 g) and/or raised the injection and growth temperature.

To strip off organic ligands, we treated colloidal solutions of w-CdSe QDs or zb-CdSe NPLs in hexane heterogeneously with excess of solid Meerwein's salt, Me_3OBF_4. Then we collected the resulting thick suspension in a separate tube (to avoid Me_3OBF_4) and centrifuged it. To wash off Me_3OBF_4, we redispersed the NCs in DMF and precipitated them with toluene. Finally, we redispersed the NCs in 0.10 M NBu_4ClO_4 in NMF and used for the experiments. TEM images confirmed that the NPLs preserved their shape as a result of the treatment with Me_3OBF_4.

For the ligand exchange with K_2S, we used a protocol by Nag, A. *et al.*[36] with NMF as the polar solvent. For the ligand exchange with potassium formylmethylamide (K-NMF), we prepared a 0.3 M solution by dissolving 117 mg K in 10 ml NMF. We stirred 0.5 ml of a solution of CdSe NCs in hexane and 0.5 ml of the K-NMF solution to cause the phase transfer. NCs

transferred readily across the phase boundary and preserved the PL. We washed the polar phase with hexane, precipitated the NCs with toluene, and finally redispersed them in 0.01 M NBu_4ClO_4/NMF.

Electrodes. We prepared the silver sulfide electrode (a sulfide ion-selective electrode) as described by Dobcnik, D. *et al*.[37] A silver wire (Ø 0.5 mm, 99.9%) was immersed in HNO_3 (1:1 v/v) for 10 seconds, rinsed thoroughly with DI water, oxidized in 0.1 M solution of $(NH_4)_2S_2O_8$ for 15 min, immersed in an alkaline 0.1 M solution of Na_2S for 1 hour until the surface turned dark grey, rinsed thoroughly with DI water and dried. For NMF solutions, we prepared a silver-cryptate reference electrode,[26] which consisted of a glass tube filled with the solution containing 0.010 M $AgNO_3$, 0.020 M [2.2.2]-cryptand (Cryp) and 0.010 M NBu_4ClO_4 in NMF. The electrode was connected to the outer solution *via* a vycor membrane. The potential of this electrode was periodically cross-checked against a saturated calomel electrode in a saturated aqueous KCl solution. We also used commercial silver/sulfide and cadmium double junction BNC ISE electrodes manufactured by Cole Parmer. The interior of these electrodes was filled with 0.10 M NBu_4ClO_4/NMF. We polished the commercial platinum, gold, and glassy carbon working electrodes by rubbing them in a circular motion against a cloth with a few drops of a suspension of alumina.

Electrochemical measurements. Potentiometry was performed in a nitrogen-filled glove box. The cell was enclosed in a Faraday's cage. The two electrodes were connected to Agilent 34410A multimeter *via* BNC cables. The solution was delivered controllably using a syringe pump KDScientific 200. The multimeter and the syringe pump were driven by LabView programs. Cyclic voltammetry and amperometry were performed with a commercial potentiostat Gamry Reference 600.

Derivation of the equation for multiple adsorption constants. Let us assume two types of facets with Langmuir adsorption constants $K_{L1} > K_{L2}$ and capacities $c_{1\infty}$ and $c_{2\infty}$. Then the expressions for adsorption constants and the mass balance equation read:

$$\frac{\theta_1}{1-\theta_1} = K_{L1}c \Rightarrow \theta_1 = \frac{K_{L1}c}{1+K_{L1}c}$$
$$\frac{\theta_2}{1-\theta_2} = K_{L2}c \Rightarrow \theta_2 = \frac{K_{L2}c}{1+K_{L2}c}$$
$$c_0 = c + c_{1\infty}\theta_1 + c_{2\infty}\theta_2$$

θ_1 and θ_2 correspond to individual coverages of the two types of facets (for a fully covered surface, $\theta_1 = 1$ and $\theta_2 = 1$) From the set of equations, we arrive at a cubic equation in c:

$$K_{L1}K_{L2}c^3 + \left[K_{L1} + K_{L2} + \left(c_{1\infty} + c_{2\infty} - c_0\right)K_{L1}K_{L2}\right]c^2 + \left[1 - \left(c_0 - c_{1\infty}\right)K_{L1} - \left(c_0 - c_{2\infty}\right)K_{L2}\right]c - c_0 = 0$$

Let us assume N types of facets with Langmuir adsorption constants: $K_{L1} > K_{L2} > ... > K_{Lj} > ... > K_{LN}$. We write down the expressions for the adsorption constants and the mass balance equation as in the previous case. Now let us assume we are approaching jth equivalence point and make 2 approximations. First, all previous facets (with $K_{Li} > K_{Lj}$) are fully covered (θ_i = 1). Second, for all facets past the one being titrated, $K_{Li}c << 1$, which simplifies the denominators to 1.

$$\frac{\theta_1}{1-\theta_1} = K_{L1}c \Rightarrow \theta_1 = \frac{K_{L1}c}{1+K_{L1}c} \approx 1$$

$$\frac{\theta_2}{1-\theta_2} = K_{L2}c \Rightarrow \theta_2 = \frac{K_{L2}c}{1+K_{L2}c} \approx 1$$

...

$$\frac{\theta_{j-1}}{1-\theta_{j-1}} = K_{Lj-1}c \Rightarrow \theta_{j-1} = \frac{K_{Lj-1}c}{1+K_{Lj-1}c} \approx 1$$

$$\frac{\theta_j}{1-\theta_j} = K_{Lj}c \Rightarrow \theta_j = \frac{K_{Lj}c}{1+K_{Lj}c}$$

$$\frac{\theta_{j+1}}{1-\theta_{j+1}} = K_{Lj+1}c \Rightarrow \theta_{j+1} = \frac{K_{Lj+1}c}{1+K_{Lj+1}c} \approx K_{Lj+1}c$$

...

$$\frac{\theta_N}{1-\theta_N} = K_{LN}c \Rightarrow \theta_N = \frac{K_{LN}c}{1+K_{LN}c} \approx K_{LN}c$$

Then the mass balance with the approximations becomes simply a quadratic equation in *c*. We process each facet this way, and then overlay the obtained curves (Figure S4). With three equivalence points, even larger ratio between the consecutive K_L is required to clearly resolve multiple equivalence points.

$$c_0 = c + \sum_{i=1}^{N} c_{i\infty}\theta_i \approx c + \sum_{i=1}^{j-1} c_{i\infty} + c_{j\infty}\frac{K_{Lj}c}{1+K_{Lj}c} + \sum_{i=j+1}^{N} K_{Li}c$$

CHAPTER TWO

IMPROMEVENTS TO THE SYNTHESIS OF SEMICONDUCTOR NANOPLATELETS

2.1. Overview of the Synthesis of Semiconductor Nanoplatelets

2.1.1. Nanoplatelets of zincblende II – VI semiconductors

The first synthesis of CdSe nanoplatelets – colloidal quantum wells – by S. Ithurria and B. Dubertret in 2008 started a new direction in semiconductor NCs.[38] These nanoplatelets (NPLs) possess zincblende crystal structure. The faces are cadmium-terminated (001)-type facets of zincblende, and the planes of the edges are perpendicular to [110] direction.[39] Those may be true stoichiometric (110)-type facets or a combination of Cd-rich and Se-rich (111) and (11-1) facets.

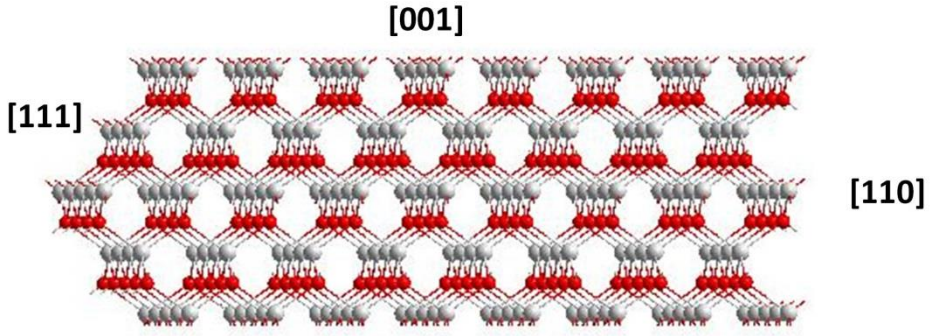

Figure 2.1. A ball-and-stick model of a CdSe 512 NPL.

The NPLs have atomically defined thickness between 0.6 and 2 nm and typical lateral dimensions bigger than the Bohr exciton diameter in CdSe. Therefore, the thickness alone determines the quantum confinement and spectra of NPLs. The position of the first exciton

(heavy hole – electron) in the absorption spectrum or the position of the PL peak (given the nearly zero Stokes shift) can serve as an identifier of the family of NPLs. We shall refer to them by the position of the first excitonic peak in the absorption spectrum or by the number of Se layers. For example, the most established family is CdSe 512 NPLs, or 4 ML CdSe NPLs (Table 2.1). For every thickness, a synthesis has been established that produces NPLs of only that particular thickness. Therefore, a batch of NPLs is potentially a homogeneous ensemble of NPLs.

Table 2.1. Five families of CdSe NPLs.

Family	Label	Number of Cd and Se layers	Formula	Number of unit cells	Thickness
397 nm*	2 ML	3 Cd and 2 Se	$[CdSe]_{2n}[Cd(OAc)_2L_{2-\delta}]_n$	One	0.61 nm (?)
462 nm	3 ML	4 Cd and 3 Se	$[CdSe]_{3n}[Cd(OAc)_2L_{2-\delta}]_n$	One and a half	0.92 nm
512 nm	4 ML	5 Cd and 4 Se	$[CdSe]_{4n}[Cd(OAc)_2L_{2-\delta}]_n$	Two	1.22 nm
550 nm	5 ML	6 Cd and 5 Se	$[CdSe]_{5n}[Cd(OAc)_2L_{2-\delta}]_n$	Two and a half	1.53 nm
576 nm*	6 ML	7 Cd and 6 Se	$[CdSe]_{6n}[Cd(OAc)_2L_{2-\delta}]_n$	Three	1.83 nm

Two distinct features set NPLs apart from QDs and make them an ideal system for photonic applications. First, extremely narrow (thermal, ~ 26 meV at the r.t.) emission bands will enable sharp color purity and minimize filtration losses in LCD pixels. Second, PL anisotropy will lower losses at the first polarizer of an LCD pixel if an array of NPLs is aligned properly. Dot-in-rod core-shells beat NPLs in the latter feature. NPLs with a tunable PL and high QY are desired for commercial applications.

Besides CdSe, there are other examples of zincblende II – VI NPLs. Four thicknesses of CdS NPLs have been independently synthesized by B. Dubertret's[7] and X. Peng's groups.[40] A number of thickness of CdTe NPLs have been made, and solid recipes for 3 ML, 4 ML, and 5

ML CdTe NPLs have been established by B. Dubertret's[41] and H. Demir's[42] groups. These families of NPLs were made by a direct hot synthesis. One thickness of HgSe and two thicknesses of HgTe NPLs have been synthesized by a cation exchange from the corresponding CdE NPLs by S. Ithurria *et al.*[16] These materials are especially valuable as narrow near-IR absorbers and emitters.

Table 2.2. Positions of the first excitonic peak in carboxylate-capped zincblende II – VI nanoplatelets.

# of ML	CdS	CdSe	CdTe	HgSe	HgTe
2 ML		397 nm*			
3 ML		462 nm	428 nm	766 nm**	~ 600 nm*
4 ML	328 / 340 nm	512 nm	500 nm		828 nm
5 ML	374 / 382 nm	550 nm	556 nm		
6 ML	407 / 414 nm	576 nm*	598 nm*		
7 ML	431 / 437 nm		622 nm*		

*This thickness of NPLs was mentioned only once without discussion.
**The value is given for amine-capped NPLs. The position of OA-capped NPLs would have been bluer. Capping with OAm shifts 4 ML HgTe from 828 to 882 nm, for example.

The series of CdSe and CdTe NPLs nicely demonstrate a stronger quantum confinement in CdTe (due to the lower effective mass of the carriers): 5 ML CdTe NPLs are redder than 5 ML CdSe NPLs, but 3 ML CdTe NPLs are bluer than 3 ML CdSe NPLs.

2.1.2. Typical synthetic procedures

In a typical synthesis of CdSe 512 NPLs, we degas and heat up 0.30 mmol Cd(myristate)$_2$ and 0.15 mmol Se powder in ODE. At 120 – 130^{o}C, the solution becomes dark green and then turns yellow, orange, and red. Se precursors formed *in situ* and Cd(myristate)$_2$ nucleate small

crystals of CdSe. When the solution turns orange-red (at 190 – 195^{o}C), we introduce 0.15 mmol $Cd(OAc)_2$. When the temperature reaches 240^{o}C, we allow the system to react for 1 to 5 min, then cool it down, and separate the NPLs from small QDs and unreacted precursors by centrifugation.

According to J. Owen *et al*., Se reacts with hydrocarbons forming H_2Se and episelenides or dehydrogenated hydrocarbons:[43]

$$C_{18}H_{36} + Se \rightarrow C_{18}H_{34}Se + H_2Se$$

$$C_{18}H_{36} + Se \rightarrow C_{18}H_{34} + H_2Se$$

The double bond in ODE matters, since running the reaction in squalane instead of ODE yielded different results. Likely Se adds to the double bond forming an episelenide. Our system hence has two types of Se precursors: the more reactive H_2Se and the less reactive selenoorganics – a desired combination in syntheses. H_2Se induces the nucleation.

$$(m+x)\ Cd(C_{13}H_{27}COO)_2 + m\ H_2Se \rightarrow [CdSe]_m[Cd(C_{13}H_{27}COO)_2]_x + 2x\ C_{13}H_{27}COOH$$

Earlier works suggested that the role of short acetate ligands was to bind tightly to (001) facets and block the growth in [001] direction (perpendicular to the faces of the NPLs), but allow the growth in the lateral dimensions. A work by D. Norris *et al*.[44] from March 2017 suggests that the role of cadmium acetate is to phase-segregate from ODE and maintain the reaction in concentrate solutions in small droplets of a separate phase. Nucleation of anisotropic structures is a fluctuation, according to the work. For thinner nuclei, the activation barrier to grow on side facets is lower than on the faces, which explains the growth in lateral dimensions. For thicker nuclei, however, there is no difference in the activation energy of growth on different facets and the growth is isotropic. The latter explains the maximum number of monolayers NPLs from a hot synthesis can have (6 ML for CdSe, for example).

There are a number of proposed mechanisms for the growth of the NPLs. The first hypothesis states that the growth is analogous to a radical polymerization: molecular cadmium carboxylates (R = CH_3 or $C_{13}H_{27}$ in the following reaction) and selenium precursors are attaching to a growing NPL.

$$[CdSe]_m[Cd(RCOO)_2]_x + Cd(RCOO)_2 + C_{18}H_{34}Se \rightarrow$$

$$\rightarrow [CdSe]_{m+1}[Cd(RCOO)_2]_x + (RCO)_2O + C_{18}H_{34}O$$

$$[CdSe]_p[Cd(RCOO)_2]_q + Cd(RCOO)_2 \rightarrow [CdSe]_p[Cd(RCOO)_2]_{q+1}$$

When the lateral dimensions of the NPLs become large, we can ignore the edges and assume the NPLs are nearly infinite. There is one X-type ligand per one surface Cd for charge balance. Carboxylates can act as bidentate ligands, the other denticity being L-type, so the general formula of a CdSe 512 NPLs is $[CdSe]_{4n}[CdX_2L_{2-\delta}]_n$.

$$[CdSe]_{4(n-1)}[Cd(OAc)_2]_{n-1} + 5\ Cd(OAc)_2 + 4\ C_{18}H_{34}Se \rightarrow$$

$$\rightarrow [CdSe]_{4n}[Cd(OAc)_2]_n + 4\ Ac_2O + C_{18}H_{34}O$$

This stoichiometry implies the density of cadmium atoms of 5.4 per nm^2 (0.185 nm^2/atom). A typical footprint of COO^- headgroup (~0.3 nm^2)[45,46] is larger than available area per surface atom, so some fraction of X-type ligands can be represented by small ions, *e.g.*, hydroxyl.[45,46]

Another hypothesis is that smaller nucleates of CdSe attach to a growing NPL:

$$[CdSe]_m[Cd(RCOO)_2]_x + [CdSe]_p[Cd(RCOO)_2]_q \rightarrow [CdSe]_{m+p}[Cd(RCOO)_2]_{x+q}.$$

In the above equation, $p << m$ and $q << x$. The merging NPL and nucleate must expel excess cadmium carboxylate from the merger plane.

As an extension, the final hypothesis is polycondensation of NPLs from smaller NPLs of a similar size. The process stops because it becomes harder to merge larger areas, but it is surprising that they grow to lateral dimensions like 10 nm × 40 nm at all.

The resulting NPLs are between 7 and 10 nm in width and between 20 and 40 nm in length. They tend to form stacks in some solvents (toluene) more than in others (hexane). Many NPLs appear twisted in TEM; the twist sometimes reaches 90°.

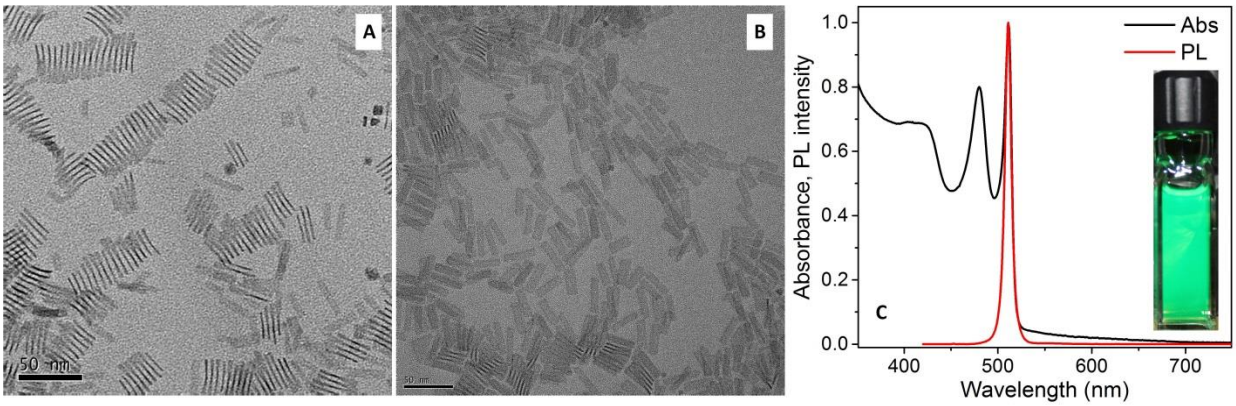

Figure 2.2. (A–B) TEM images of two batches of CdSe 512 NPLs. (C) Absorption and emission spectra of a solution of CdSe 512 NPLs in hexane. The inset shows a photograph of the PL of the NPLs under a UV irradiation.

In a typical synthesis of CdSe 550 NPLs, we degas and heat up 0.30 mmol $Cd(myristate)_2$ in ODE to 240°C. Then we inject 0.15 mmol Se powder suspended in ODE followed by 0.225 mmol $Cd(OAc)_2$ in 20 seconds. The higher reaction temperature affords thicker NPLs. Often, this family of NPLs has an impurity of particles that show triangular and square projections in TEM. The impurity can be separated by a size-selective precipitation.

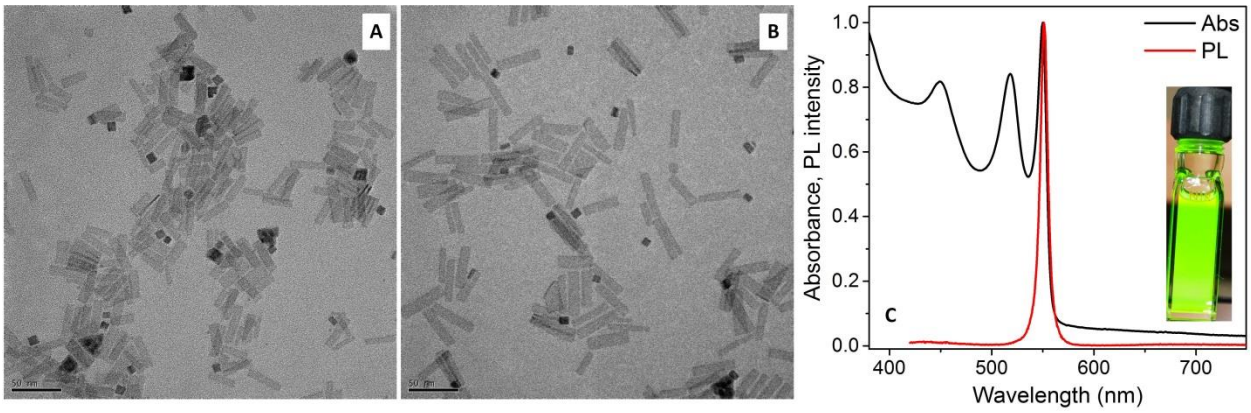

Figure 2.3. (A–B) TEM images of two batches of CdSe 550 NPLs. (C) Absorption and emission spectra of a solution of CdSe 550 NPLs in hexane. The inset shows a photograph of the PL of the NPLs under a UV irradiation.

In a typical synthesis of CdSe 462 NPLs, we degas 0.90 mmol $Cd(OAc)_2$ and 0.48 mmol oleic acid at 80°C for one hour. Up to 0.24 mmol $Cd(OAc)_2$ converts into oleate *in situ*. Then we heat up the system to 180°C under nitrogen and inject 0.15 mmol TOPSe. The NPLs slowly nucleate and grow over 20 min.

$$4n\ Cd(RCOO)_2 + 3n\ TOPSe \rightarrow [CdSe]_{3n}[Cd(RCOO)_2]_n + 3n\ TOPO + 3n\ (RCO)_2O$$

CdSe 462 NPLs are large in lateral dimensions and fold together in sterically stabilized solutions (Figure 2.4A). There is always trap emission coming from CdSe 462 NPLs, which increases over the storage of the NPLs (Figure 2.4C). As we shall see, one way to lower the trap emission is to disperse the NPLs in a good solvent like methylcyclohexane. Upon a ligand exchange or core-shell growth with sulfide, the NPLs unfold and show clear lateral dimensions in TEM (Figure 2.4B)

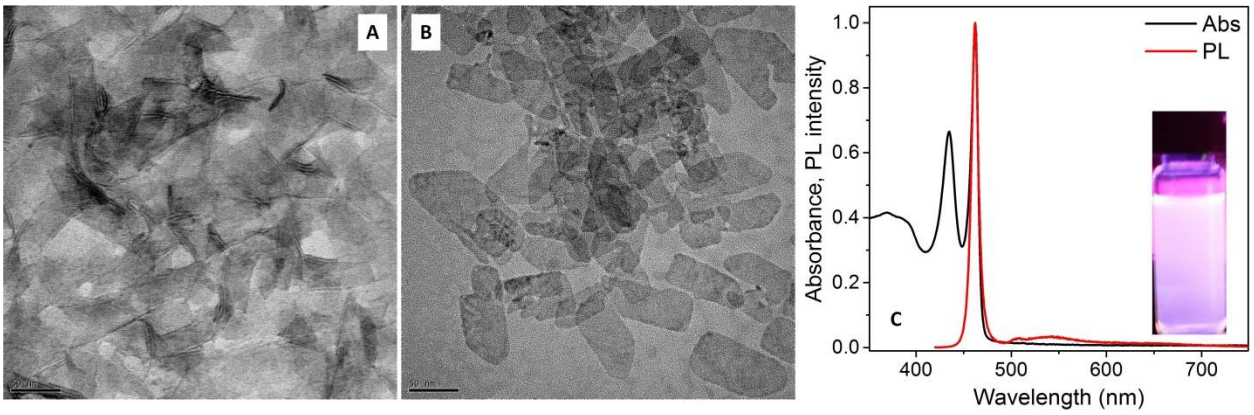

Figure 2.4. (A) TEM image of CdSe 462 NPLs. (B) TEM image of CdSe/CdS core-shell NPLs grown on 462 nm NPLs to demonstrate lateral dimensions of CdSe 462 NPLs. (C) Absorption and emission spectra of a solution of CdSe 462 NPLs in hexane. The inset shows a photograph of the PL of the NPLs under a UV irradiation. The color is purple and not blue because of the trap emission from the NPLs.

There are tworeports on a hot synthesis of CdSe 397 NPLs;[7,44] there are two reports of the synthesis of CdSe 576NPLs: one hot synthesis[47] and one shell growth over CdSe 512 NPLs.[48] Mercury chalcogenide NPLs have been a material of a great application potential. Likely, many researchers have tried a direct synthesis of it, but mercury precursors are very reactive. All my attempts to synthesize HgSe mimicking the synthesis of CdSe NPLs at various temperatures led to HgSe QDs. Only in August 2016, a recipe based on a cation exchange in CdSe and CdTe NPLs with $Hg(OAc)_2$ in amines was published.[16] The driving force is likely the high affinity of Cd^{2+} for amines. In 2014, B. Dubertret's group reported a cation exchange on CdS NPLs through a step of Cu_2S to produce zb-ZnS NPLs.[49]

Besides zincblende, other crystal structures of NPLs have been reported. Templated growth in amines yields w-CdSe and w-ZnSe NPLs.[50] These NPLs are likely terminated with stoichiometric faces. They often show weaker PL and behave differently in ligand exchange and core-shell growth compared to metal-rich zincblende NPLs. The mentioned cation exchange through CdS NPLs leads to rock-salt PbS NPLs. Lead chalcogenide NPLs have been also

prepared by oriented attachment.[51] The spectral features of NPLs from either route are very different from those of zincblende NPLs perhaps due to stoichiometric surface termination.

In a bigger scope, NPLs are a subgroup of 2D materials, but a very distinct one. Many 2D materials, *e.g.*, graphite, MoE_2, WE_2, *etc*. are layered materials, each layer being electrically neutral. This fact again implies that surface termination is either stoichiometric, or if one face is metal rich, the other is non-metal-rich. Surface chalcogenides often act as hole traps, so strong PL in such materials is challenging. Zincblende, in contrast, is not a layered material; every Cd atom on each face of a zb-CdSe NPL has two broken bonds, which must/can be passivated. This passivation is the key to a stable PL, but the broken bonds are a synthetic challenge. We suspect a major reason zb-InP NPLs have not been synthesized is the oxidation number of In being +3. The general formula of InP NPLs would be $[InP]_{4n}[InX_3L_{1-\delta}]$, so every surface indium atom would require one and a half X-type ligands to obey the charge neutrality. Such requirement may be hard to satisfy with carboxylate because of the steric hindrance (the lattice constant of InP is smaller than that of CdSe).

2.2. Control over the Dimensions of zb-CdSe NPLs in a Synthesis

2.2.1. Can we control the thickness of CdSe NPLs in a given synthesis?

One question that arises is do thicker NPLs grow from thinner ones during the synthesis. To find the answer, we took aliquots of the solutions of NPLs during the synthesis of CdSe 462, CdSe 512, and CdSe 550 NPLs and measured their UV-Vis and PL spectra, and TEM.

CdSe 462 NPLs acquired their first excitonic peak and the band-edge emission at least a minute and a half after the injection of TOPSe. The first aliquot showed a large trap emission, which decreased over the growth of the NPLs. We conclude that CdSe 462 NPLs acquire their

thickness immediately after the nucleation, grow in lateral dimensions over the course of the reaction, but do not convert into thicker NPLs over 30 min.

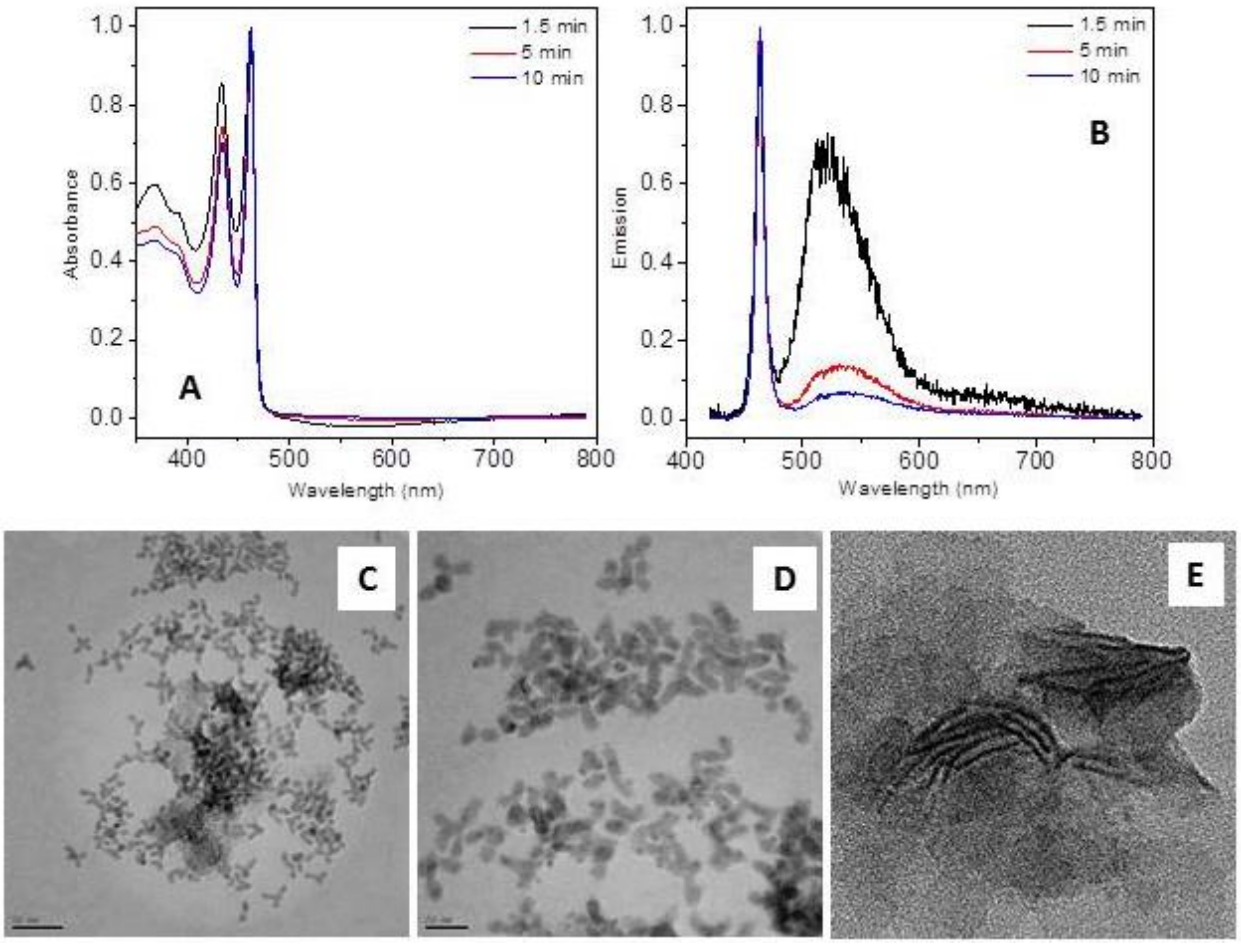

Figure 2.5. (A) UV-Vis spectra of three aliquots from a synthesis of CdSe 462 NPLs. (B) The corresponding PL spectra normalized at the main peak. (C – E) TEM images of aliquots from 1.5, 5, and 20 min of the reaction at 180^{o}C.

CdSe 512 NPLs showed their peak in the PL and UV-Vis already at 215^{o}C. There was no evidence of any thinner platelets in the spectra. With the increase of the temperature to 240^{o}C and over the course of the reaction there, the NPLs grew in lateral dimensions. The peak shifted from 506 nm to 512 nm over such growth. Therefore, this family of NPLs acquires its thickness soon after the introduction of cadmium acetate.

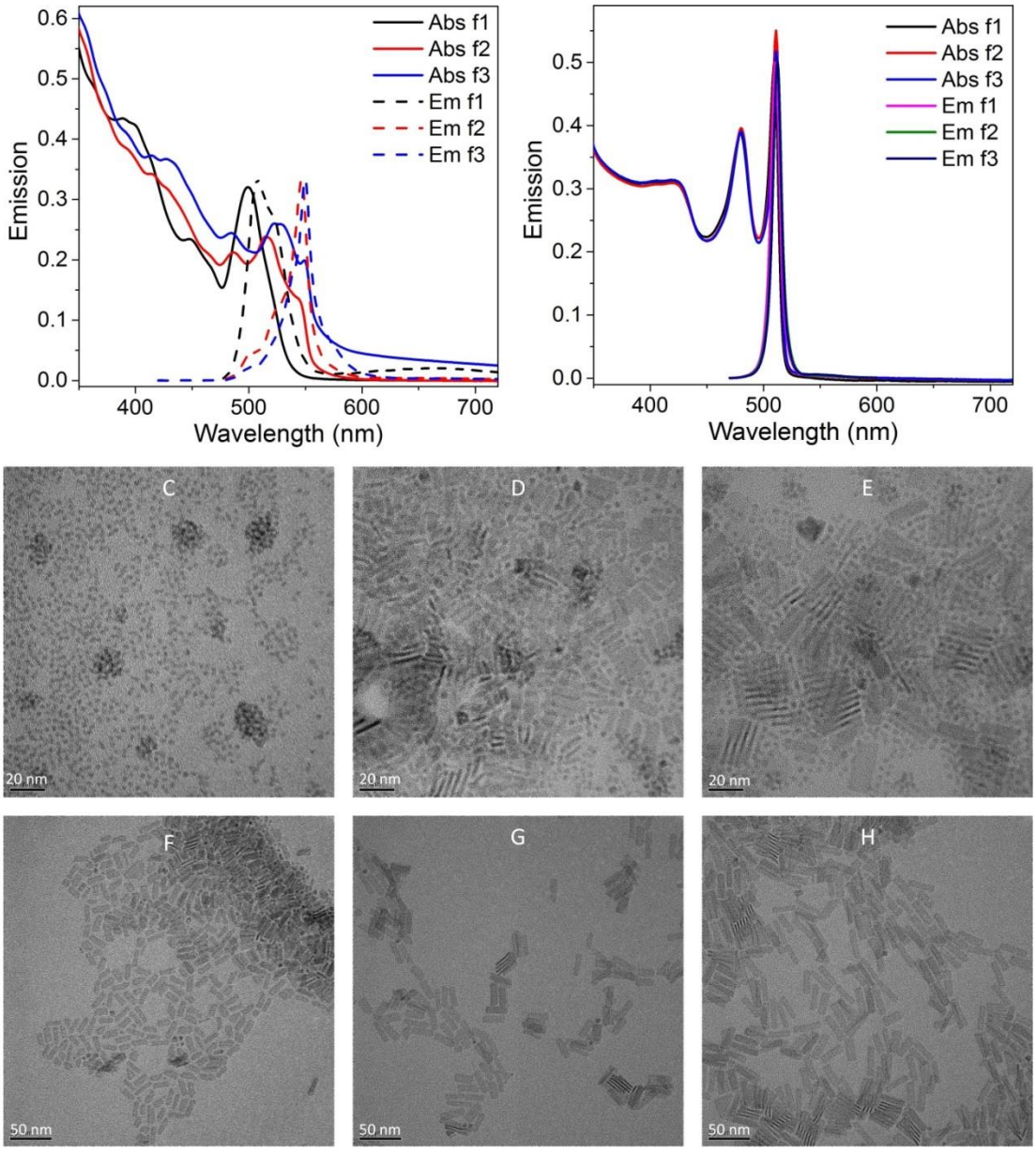

Figure 2.6. The difference in the growth of CdSe 512 and 550 NPLs. (A) UV-Vis and PL spectra of aliquots from a growth of CdSe 550 NPLs at 240^{o}C. (B) UV-Vis and PL spectra of aliquots from a synthesis of CdSe 512 NPLs taken at 225^{o}C, after 1 min at 240^{o}C, and after 5 min at 240^{o}C.

In contrast, aliquots from the growth of CdSe NPLs showed unusual for NPLs features in UV-Vis and PL spectra. For this thickness of NPLs, it required the full ten-minute course of

growth at 550 nm. TEM of aliquots showed small clusters at early times and a coexistence of clusters and NPLs at later times.

The coexistence of large NPLs and clusters contradicts a possible polycondensation mechanism for CdSe 550 NPLs. Likely, the mechanism of growth is polymerization of small clusters (the second mechanism discussed in Section 2.1). The absence of small clusters in aliquots of CdSe 512 NPLs suggests polymerization of the molecular precursors around a nucleus that already possesses the properties of a NPL as the growth mechanism. A similar growth mechanism applies to CdSe 462 NPLs.

As we can see, thicker platelets do not grow from thinner ones. Within a given protocol, we varied the amount of the short-chain ligand and tuned the chain length by one Carbon atom.

Table 2.3. Modifications to the recipes for CdSe 512 and 550 NPLs.

Recipe	Outcome
512 NPLs: 0 eq. Cd acetate, 1 eq. Cd formate	Bulk CdSe + zb-CdSe QDs (1^{st} exciton at 553 nm, FWHM of emission = 26 nm)
550 NPLs: 0 eq. Cd acetate, 1 eq. Cd formate	Bulk CdSe
512 NPLs: 1 eq. Cd acetate, 0.5 eq. Cd formate	A mix of 512 and 550 NPLs
512 NPLs: 1 eq. Cd acetate, 1 Cd formate	A mix of 512 and 550 NPLs
512 NPLs: 1.5 eq. Cd acetate	CdSe 512 NPLs
550 NPLs: 1 eq. Cd acetate, 1 Cd formate	Bulk CdSe, 550 NPLs

Shorter-chain formate competes with acetate and longer-chain carboxylates, but fails to block the growth and stabilize the resulting NPLs.

2.2.2. Control over the Lateral Dimensions of NPLs

We have seen that CdSe 462 and 512 NPLs of lateral dimensions smaller than standard can be grown by terminating the reaction prematurely. To obtain short CdSe 512 NPls, we stopped the reaction at 225^{o}C; to obtain intermediate CdSe 512 NPLs, we ran the reaction for 1 minute at 240^{o}C; and the standard 5 minutes at 240^{o}C followed by a natural cool-down led to big NPLs.[52]

Interestingly, we found another way to alter the lateral dimensions of CdSe 512 NPLs. Substitution of cadmium acetate with propionate led to longer (50 nm), but narrower 4 ML CdSe NPLs. The first excitonic peak was as blue as 502 nm, and the emission band peaked at 504 nm. The width of the NPLs became comparable to the exciton diameter, so polydispersity due to the NPL width appeared, which broadened the PL peak. Steric hindrance caused by propionate prevented the growth of a larger.

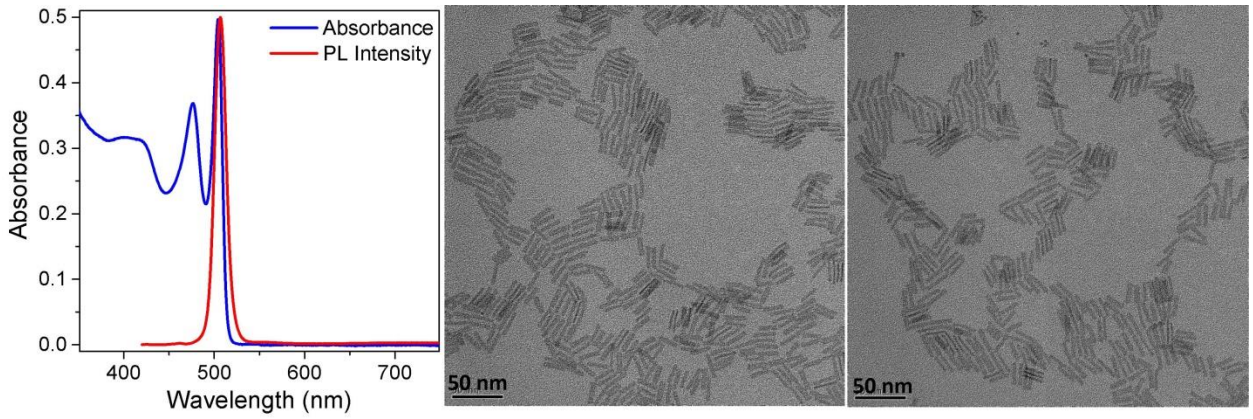

Figure 2.7. UV-Vis and PL spectra, and TEM of 4 ML CdSe NPLs grown in the presence of propionate.

As an extension, we used cadmium lactate as the short-chain ligand. The precipitate from the synthesis contained disk-like particles with the first exciton at 509 nm and the emission peak at 515 nm. Therefore, anisotropic growth occurred in the presence of lactate.

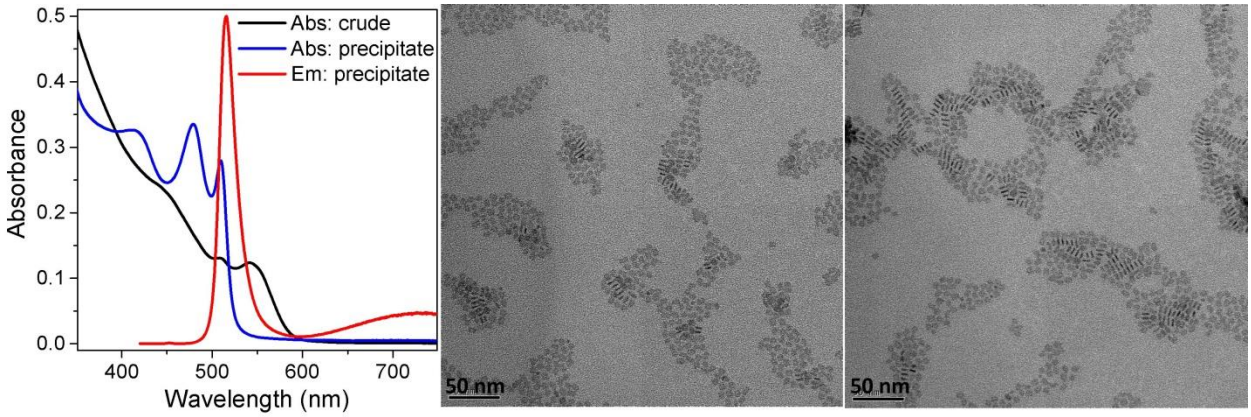

Figure 2.8. UV-Vis and PL spectra, and TEM images of CdSe NCs synthesized by the recipe for CdSe 512 NPLs with an equivalent amount of cadmium lactate instead of acetate.

We synthesize the cadmium precursor, cadmium myristate, from nitrate *via* metathesis. Even though we wash the precipitate five times, it was still important to see a possible effect of nitrate on NPL formation. We ran a synthesis with an equivalent amount of cadmium nitrate instead of acetate. The resulting solution consisted of a mix of spherical dots (the redder peak in spectra) and tiny rod-like NCs (two bluer peaks). The tiny rods likely transferred energy *via* FRET to the QDs. We conclude that cadmium nitrate added at 190^{o}C brings some anisotropy into the growth of NCs.

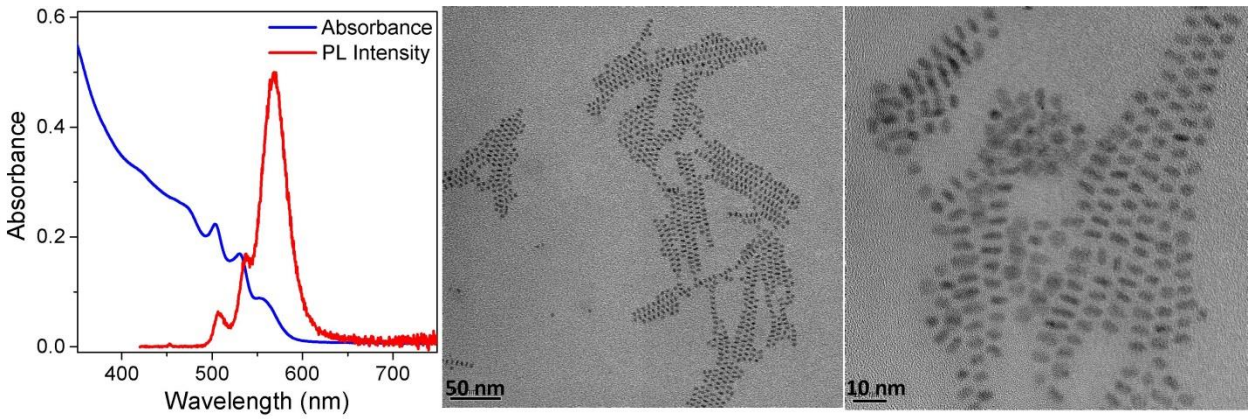

Figure 2.9. UV-Vis and PL spectra, and TEM images of CdSe NCs synthesized by the recipe for CdSe 512 NPLs with an equivalent amount of cadmium nitrate instead of acetate.

Unlike CdSe 462 or 512 NPLs, the 550 NPLs require the full course of reaction at 240°C for their features to appear. A premature termination of the synthesis does not yield shorter NPLs. Instead, we found a different route to longer CdSe 550 NPLs. We increased the injection temperature to 250°C, and injected 0.15 mmol Se suspended in 1 ml of 1 M solution of Se in ODE. One minute later, we introduced 0.45 mmol cadmium acetate and ran the reaction for 10 min. The resulting NPLs had a larger surface area. To obtain intermediate-size NPLs, we took an arithmetic mean of every numerical parameter in the standard and modified syntheses of CdSe 550 NPLs.

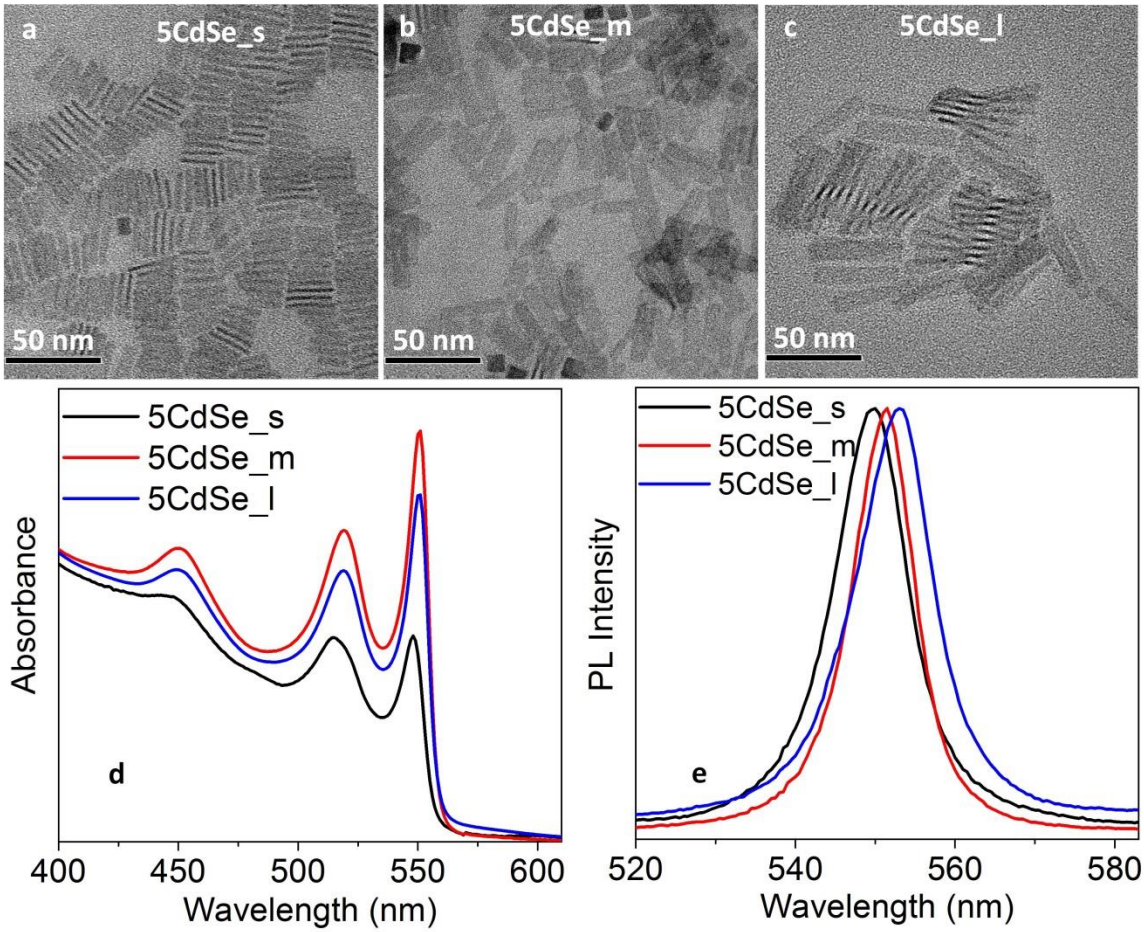

Figure 2.10. (a – c) TEM images of small, intermediate, and large CdSe 550 NPLs. (d) The corresponding UV-Vis spectra. (e) The corresponding PL spectra. Adapted with permission from ref. 52. Copyright 2015, American Chemical Society.

One common feature of CdSe 512 and 550 NPLs of different lateral dimensions is that the ratio of the intensity of the first exciton to the intensity of the second exciton increases with the increase in the NPL length (Figure 2.6B, 2.7A, and 2.8d).

2.2.3. Long-term stability of colloidal solutions of CdSe NPLs

Overall, sterically stabilized CdSe NPLs are less colloidally stable than CdSe QDs. The reason for that is a high face-to-face interaction. They require long and kinky oleate ligands for stabilization. From my observation, replacement of oleate for octanoate led to aggregation and precipitation of CdSe 512 NPLs. The choice of the solvent is important, too. While toluene and hexane are interchangeable dispersants for most QDs, NPLs are colloidally unstable in toluene. The dispersant must be a good solvent for oleate. Branched hydrocarbons like isooctane produce long-term stable suspensions of NPLs. A solvent that works particularly well is methylcyclohexane (MCH). Much fewer stacks are observed in TEM of NPLs cast from MCH than from hexane. Moreover, it is the only solvent we have found in which CdSe 462 NPLs do not show trap emission.

2.3. CdSe/CdS Core-Shell NPLs Grown by Colloidal Atomic Layer Deposition

In 2012, S. Ithurria and D. Talapin, developed a protocol for a shell growth over colloidal NCs by a series of self-limiting depositions with phase transfers.[19] Excess charged inorganic precursor is introduced, a layer is deposited, and the material is transferred into a different phase, leaving the excess precursor behind. The process is self-limiting because it is impossible to cover a layer of sulfide with another one, for example. The protocol was used by other groups for NPLs. Other room-temperature syntheses of core-shells on CdSe NPLs have been introduced. So far, there has been no single report on SILAR for CdSe NPLs, however.

2.3.1. The procedure of colloidal atomic layer deposition (*c*-ALD)

In our first core-shell growth, we precipitated a batch of CdSe 512 NPLs and re-dispersed them in hexane twice to remove excess $Cd(OAc)_2$ from the synthesis. We started with a typical ligand exchange in a two-phase system: NPLs in hexane as the top phase and NMF as the bottom phase. We added excess (*ca.* 5-fold w.r.t. the NPLs surface) of concentrate aqueous ammonium sulfide to the NMF phase, shook the system, and observed that the NPLs transferred into NMF leaving the organics back in the colorless hexane phase. The color of CdSe 512 NPLs changed from yellow to orange as a result according to the following reaction (R = CH_3, $C_{13}H_{27}$, or $C_{17}H_{33}$).

$$[CdSe]_{4n}[Cd(RCOO)_2]_n + 2n\ (NH_4)_2S \rightarrow [CdSe]_{4n}[CdS]_n[S^{2-}\ldots 2\ NH_4^+]_n + 2n\ RCOO^-NH_4^+$$

We removed excess sulfide by precipitating the NPLs with acetonitrile and toluene and re-dispersing them in NMF twice. Excess cadmium acetate, added to NMF, deposited a layer of cadmium on each side.

$$[CdSe]_{4n}[CdS]_n[S^{2-}\ldots 2\ NH_4^+]_n + 2nCd(OAc)_2 \rightarrow [CdSe]_{4n}[CdS]_{2n}[Cd^{2+}\ldots 2\ OAc^-]_n + 2nNH_4NO_3$$

We precipitated the NPLs with toluene, re-dispersed them in NMF, and phase-transferred them into hexane with 5% oleylamine (L) as the upper phase.

$$[CdSe]_{4n}[CdS]_{2n}[Cd^{2+}\ldots 2\ OAc^-]_n + (2-\delta)n\ L \rightarrow [CdSe]_{4n}[CdS]_{2n}[(Cd(OAc)_2L_{2-\delta}]_n$$

Acetate provides charge balance and OAm steric stabilization to NPLs in hexane. This step concludes one cycle of *c*-ALD, in which one layer of CdS is deposited on each face of NPLs.

We recorded UV-Vis and PL spectra. The PL bands were narrow (fwhm = 45 meV), Stokes shift was nearly zero, and the PL QY peaked at 3 ML. For this reason, we chose the 3 ML core-shell for amplified spontaneous emission and lasing.

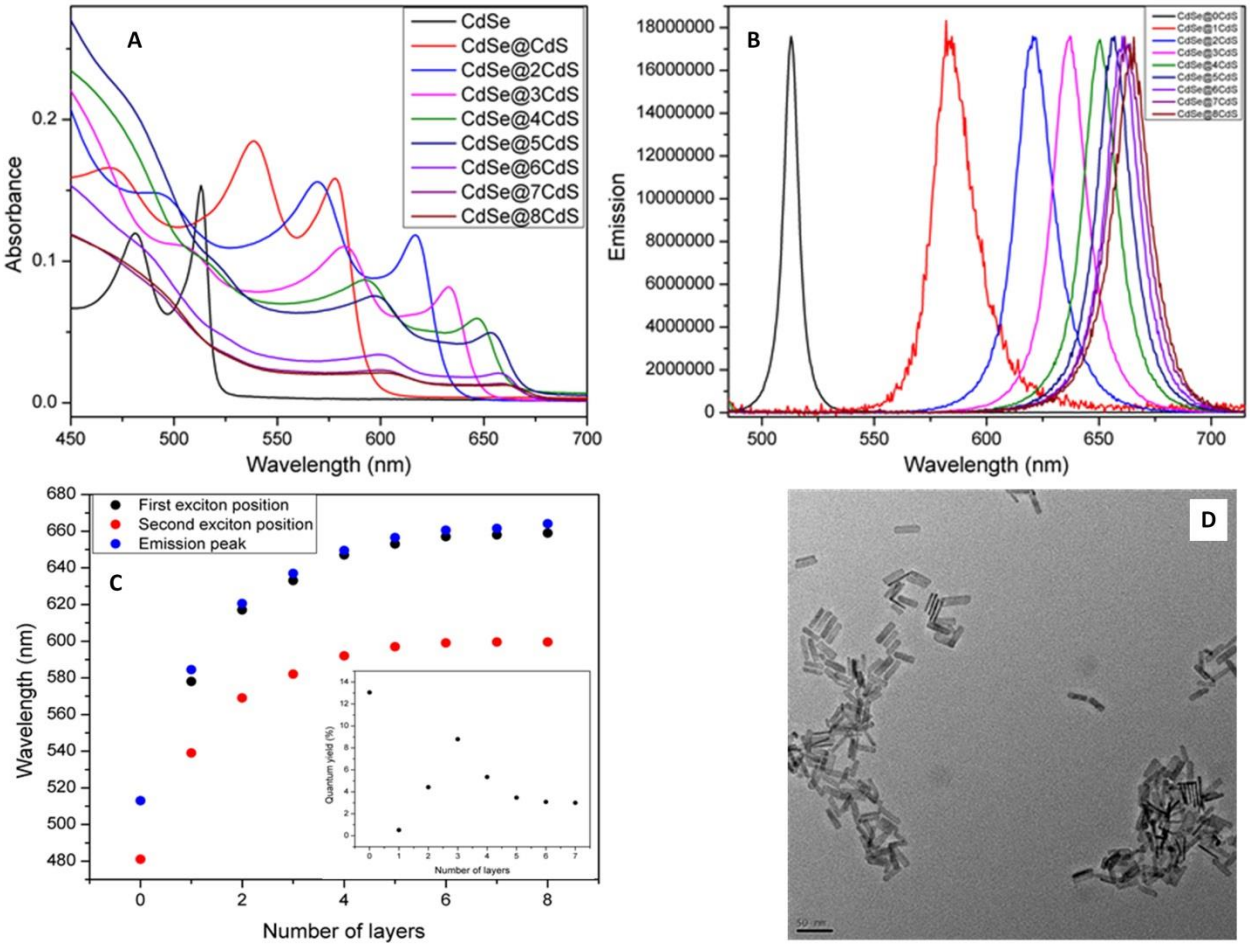

Figure 2.11. (A) UV-Vis spectra of CdSe 512 and CdSe/CdS NPLs for different numbers of MLs of CdSe. (B) The corresponding PL spectra. (C) Dependence of the HH – electron and LH – electron excitons, and the PL peak on the number of MLs of CdSe. The inset shows PL QY as a function of the number of MLs of CdS. (D) A TEM image of CdSe/CdS 512 – 3 ML NPLs.

We noticed that, even after two precipitations with ethanol, bare CdSe NPLs had a higher PL QY than a core-shell of any number of ML. For CdSe QDs, the opposite is true: shells are grown to passivate the surface and thus improve the PL. Improvements to *c*-ALD were required to achieve bright NPL core-shells.

2.3.2. CdSe/$Cd_{1-x}Zn_xS$ heterostacks

c-ALD provides a unique opportunity to deposit layers of semiconductors of a desired composition and synthesize thus complex heterostructures. The idea was to grow

CdSe/CdS/CdSe NPL heterostructures, where the electron would be delocalized across the entire structure and the hole localized in every CdSe NPL, or CdSe/$Cd_{1-x}Zn_xS$/CdSe structures with the hope to localize both carriers in CdSe layers. In the ideal case, if the wider-bandgap semiconductor isolated layers of CdSe from each other, we would obtain a system of individual coupled quantum wells with a fixed separation.

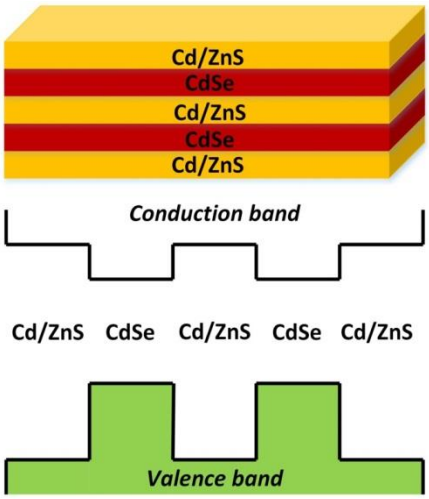

Figure 2.12. Proposed coupled-QW heterostructure of NPLs.

We grew 3 MLs of CdSe and the 2 MLs of CdS over CdSe/CdS 512 – 3 ML NPLs to form 2CdS/3CdSe/3CdS/4CdSe/3CdS/3CdSe/2CdS NPLs. UV-Vis and PL spectra showed no signature of couple QWs: those were ordinary spectra of CdSe/CdS core-shells. PL of secondary CdS nucleates appeared at *ca.* 400 nm, but TEM showed only NPLs. The washing cycle removes the secondary nucleates quite efficiently.

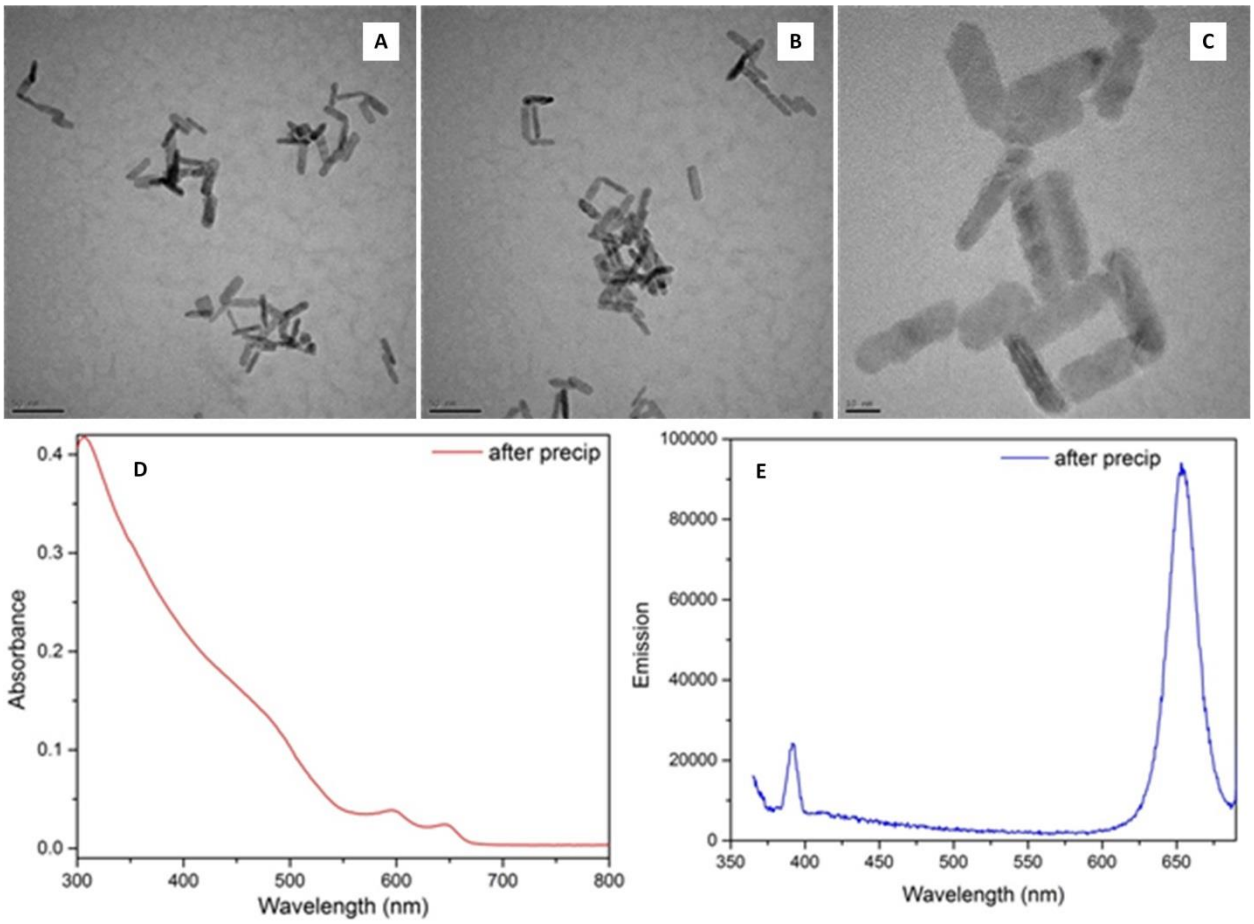

Figure 2.13. (A – C) TEM images of 2CdS/3CdSe/3CdS/4CdSe/3CdS/3CdSe/2CdS NPLs. (D) Absorption spectrum of the heterostructures. (E) PL spectrum of the heterostructure and secondary nucleates.

With the hope to isolate the CdSe NPLs from each other in the heterostructure, we grew layers of ZnS in between. First, we grew 3 MLs of ZnS over CdSe 512 NPLs using $Zn(OAc)_2$ as the precursor. *c*-ALD proceeded as usual, and the resulting solution was colloidally stable and showed orange emission (Figure 2.14 A,D). Next, we grew 2ZnS/3CdSe/3ZnS/4CdSe/3ZnS /3CdSe/2ZnS heterostructures. A regular shape of core-shells appeared in TEM (Figure 2.14 B,C). Absorption and emission spectra did not show any peculiar features, but the peaks were bluer than in the corresponding CdSe/CdS core-shells.

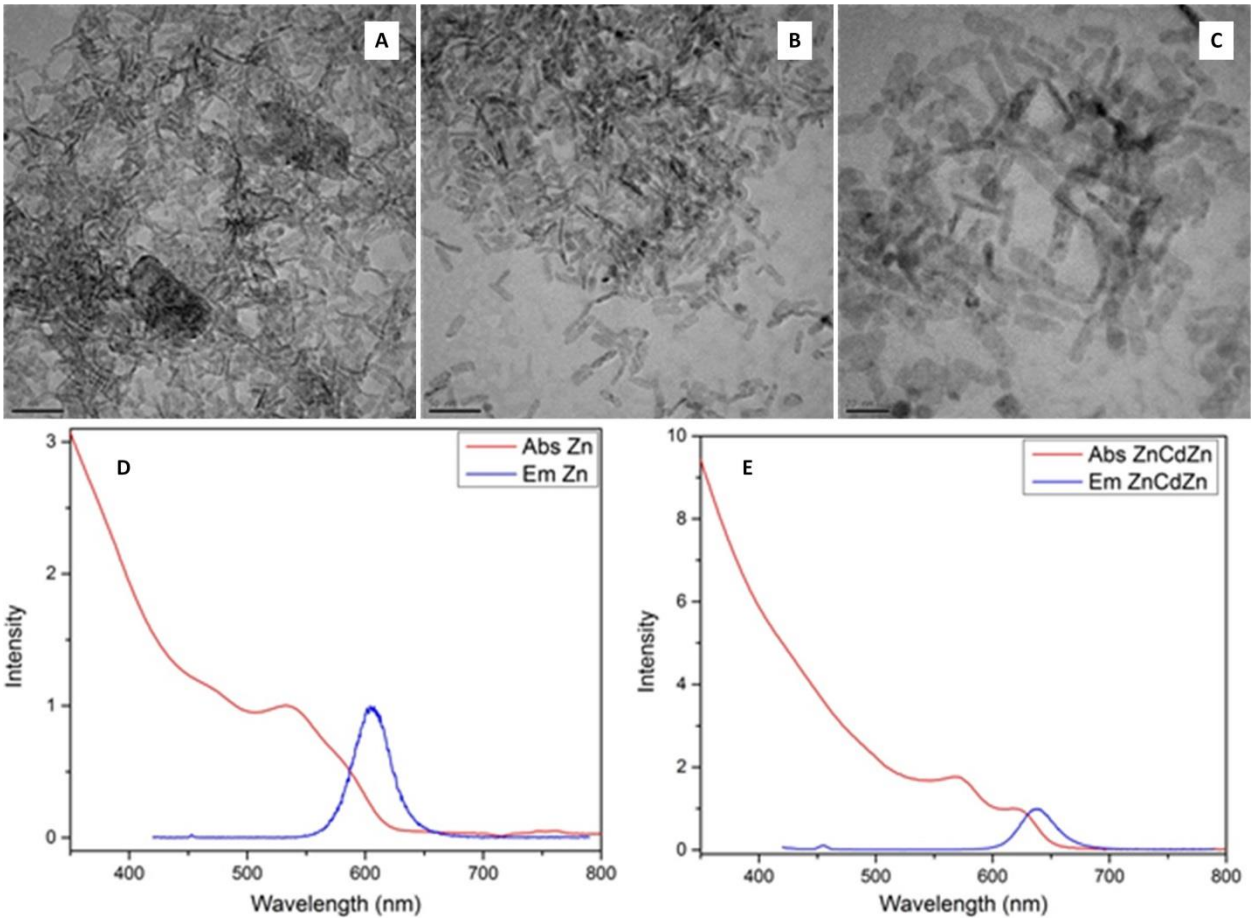

Figure 2.14. (A) TEM image of 3ZnS/4CdSe/3ZnS NPLs. (B–C) TEM images of 2ZnS/3CdSe/3ZnS/4CdSe/3ZnS/3CdSe/2ZnS NPLs. (D) Absorption and PL spectra of 3ZnS/4CdSe/3ZnS NPLs. (E) Absorption and PL spectra of 2ZnS/3CdSe/3ZnS/4CdSe/3ZnS /3CdSe/2ZnS NPLs.

We should view CdSe in these heterostructures as 3ZnS/3CdSe/3ZnS (CdSe/ZnS 462 – 3 ML NPLs) and 3ZnS/4CdSe/3ZnS (CdSe/ZnS 512 – 3 ML NPLs). Even those the position of the first exciton peak differs by 50 nm between 3 ML and 4 ML CdSe NPLs, this difference washes out as shells are grown. Therefore, it will be hard to resolve features of individual core-shells in these heterostructures by ordinary UV-Vis and PL spectroscopy.

Another note is that Na_2Se, used to grow CdSe layers, is insoluble in acetonitrile, so unwashed excess of it causes secondary nucleates of CdSe.

2.3.3. Improvements to the standard procedure of *c*-ALD

Methylcyclohexane (MCH) has proved to be equal to or better than hexane as a solvent for CdSe NPLs and core-shells. Therefore, we used MCH instead of hexane at all instances: to re-disperse CdSe NPLs after a precipitation, to transfer Cd-rich core-shells from NMF, *etc*.

There are a number of problems with the outlined protocol for the core-shell growth. The low QY of the core-shells grown by *c*-ALD is likely due to trap states that originate from crystal defects accumulated during the room-temperature growth and the numerous precipitation steps. In hope to improve the PL, we ran three cycles of *c*-ALD on CdSe 512 NPLs with phase transfers only and no precipitations. Namely, after the introduction of sulfide, we transferred the NPLs from NMF into MCH with didodecyldimethylammonium bromide (DDAB).

$$[CdSe]_{4n}[CdS]_n[S^{2-}\ldots 2NH_4^+]_n + 2n\ DDA^+Br^- \rightarrow [CdSe]_{4n}[CdS]_n[S^{2-}(DDA^+)_2]_n + 2n\ NH_4Br$$

DDA forms a tight ion pair with the surface sulfide and provides the steric colloidal stability to the NPLs in MCH. We discarded the bottom NMF phase with NH_4Br, introduced fresh NMF, and phase-transferred the NPLs from MCH into NMF with $Cd(OAc)_2$.

$$[CdSe]_{4n}[CdS]_n[S^{2-}(DDA^+)_2]_n + 2n\ Cd(OAc)_2 \rightarrow [CdSe]_{4n}[CdS]_{2n}[Cd^{2+}\ldots 2\ OAc^-]_n$$

After that, we proceeded as usual: a phase transfer from NMF to MCH with OAm and so on. The resulting core-shells showed the usual UV-Vis and PL spectra. From photoluminescence excitation (PLE) spectra, the sample of 3 ML core-shells was fairly monodisperse with a slight polydispersity on the blue side (likely due to the NPL width rather than thickness). The sample was fairly free of secondary nucleates with occasional islands thereof in TEM. The PL QY of the sample doubled compared to the previous growth, but there was still room for improvement.

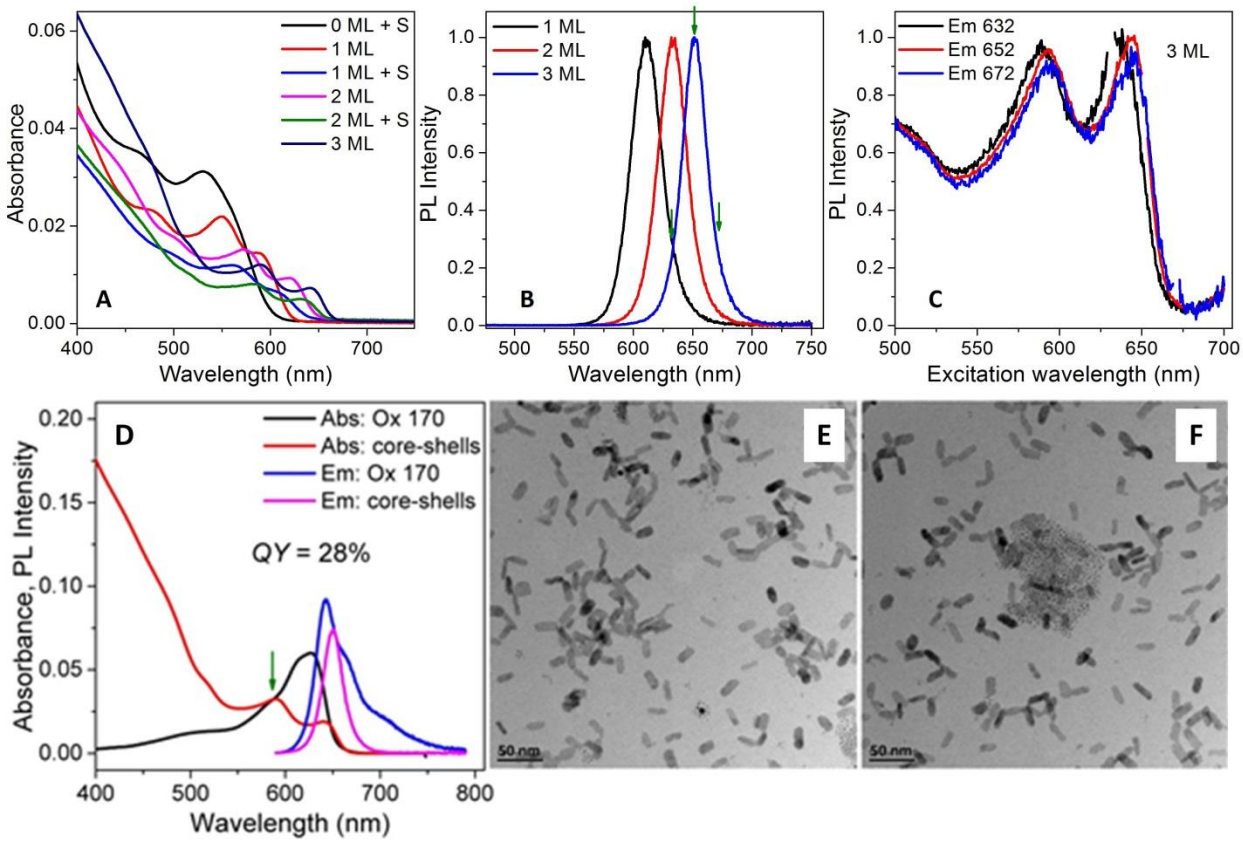

Figure 2.15. CdSe/CdS 512 – 3 ML NPLs grown by *c*-ALD with phase transfers only. (A) Absorption spectra after each layer. (C) PL spectra after each ML of CdS. (C) PLE spectra after each ML of CdS. (D) PL QY of the 3 ML core-shell measured against oxazine 170. (E, F) TEM images of the 3 ML core-shells.

The described method was possible with the introduction of MCH, as it dissolves DDAB and does not mix with NMF. Toluene – FA is an alternative pair, but FA is a worse solvent for electrostatically stabilized NCs than NMF. The method is valuable for systems with poor colloidal stability, as it avoids precipitations. Disadvantages include some secondary nucleation and a bigger loss of the material in phase transfers compared to precipitations.

We noticed that the core-shells improved their PL QY over some time after the addition of $Cd(OAc)_2$ in NMF or within a few hours after the phase transfer into hexane with OAm. Therefore, we eliminated the precipitation from NMF after the cadmium step and introduced a ten-minute lag here, a 6-hour lag after the phase transfer from NMF to MCH, and a 30-minute

lag after the precipitation with ethanol and re-dispersion in MCH. The latter precipitation is unavoidable because free cadmium acetate phase-transfers from NMF to MCH, forming a complex with OAm.

$$Cd^{2+} + 2\ OAc^{-} + 2\ C_{18}H_{35}NH_2 \rightarrow Cd(C_{18}H_{35})_2(OAc)_2$$

We also noticed that the supernatant was light green after the precipitation of sulfide-capped NPLs with acetonitrile and toluene to remove excess S^{2-}. It is known that ammonium polysulfides form trisulfide anion-radical ($S_3^{-\cdot}$, analogue of ozonide) stabilized in certain solvents like DMF or acetonitrile. This radical may get incorporated into the crystal structure and trap carriers. Inspired by a prompt reduction of Se by tributylphosphine, we found a way to reduce polysulfides in a two-phase system MCH – NMF. We dissolved yellow $(NH_4)_2S$ in the bottom in NMF phase and an equal volume of TBP in the top MCH phase, and vortexed the system. Eventually the yellow color of the NMF phase disappeared; the phase contained sulfide, free of polysulfides. The MCH phase with $TBP^{+}–S^{-}$ was discarded.

$$(n-1)\ TBP + S_n^{2-} \rightarrow (n-1)\ TBP^{+}–S^{-} + S^{2-}$$

The colorless $(NH_4)_2S$ successfully transferred and stabilized NPLs, and the supernatant was colorless after sulfide.

The improvements to the protocol raised the PL QY of the core-shells reproducibly up to *ca.* 40%. The PL QY peaked at 2 MLs of CdS for a number of samples. Long-term storage in MCH with 5% OAm v/v slowly raised the QY slightly. Annealing these core-shells in a sand bath at 100^{o}C for 24 hr improved the PL by a few percent. The NPLs were free of secondary nucleates in TEM (Figure 2.16 B).

Table 2.4. PL peak position and QY for CdSe 512 NPLs with a variable number of CdS shells.

Number of monolayers	PL peak position	PL QY
2 ML	634 nm	71%
3 ML	N/A (a different batch)	44%
4 ML	654 nm	38%
6 ML	662 nm	25%
8 ML	666 nm	11%

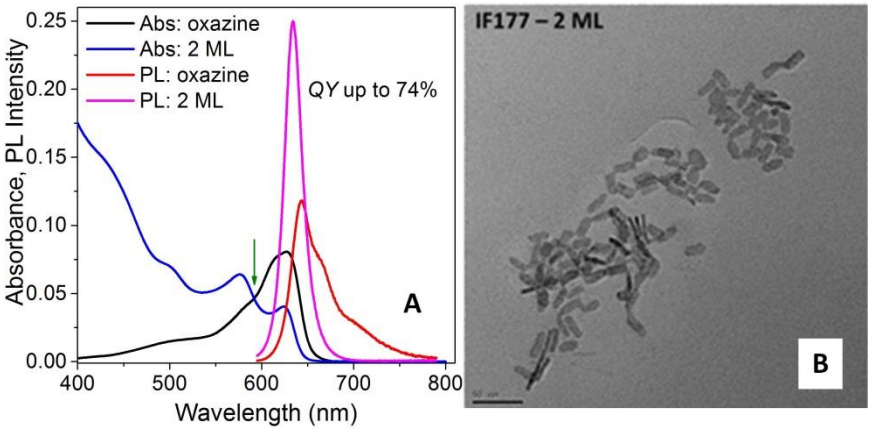

Figure 2.16. (A) PL QY of CdSe/CdS 512 – 2 ML NPLs measured against oxazine. (B) A TEM image of the sample.

We also introduced variable amounts of zinc in the shells. *c*-ALD allowed us to introduce any Cd:Zn ratio in the shell growth. The first layer was pure CdS, and the fraction of zinc increased in the consecutive $Cd_{1-x}Zn_xS$ layers. Examples of different core-shells are summarized in Table 2.5. Introducing zinc into the shells shifted the PL to slightly bluer wavelengths. For a given shell thickness, there is a slight variation in the PL position depending on the lateral dimensions of the NPLs. Remarkably, core-shells grown on needle-like CdSe NPLs (synthesized from cadmium propionate) showed a broad PL peak because of a polydispersity in the NPL width.

Table 2.5. Examples of the PL peak position and QY of different NPL core-shells.

Substance	Sample	Emission peak (nm)	FWHM (nm)	QY
CdSe/CdZnS	IF175 – 2 ML	637	21.7	49%
CdSe/CdZnS (annealed)	IF175 – 2 ML	636	22	18%
CdSe/CdS	IF175f2 – 1 ML	605	24	45%
CdSe/CdS	IF175f2 – 2 ML	636	21.5	33%
CdSe/CdS	IF177f1 – 2 ML	645	22	36%
CdSe/CdZnS	IF177f1 – 2 ML	639	23	31%
CdSe/CdS (smaller)	IF178 – 2 ML	630	27	26%
CdSe/CdS (regular)	IF180 – 2 ML	638	24	31%
CdSe/CdS (bigger)	IF171 – 2 ML	641	25	37%
CdSe/CdS (needles)	IF179 – 2 ML	620	35	37%

2.3.4. Thermal stability of the PL of CdSe/CdS nanoplatelets

Thermal stability of the chromophore is important for display applications. We dispersed CdSe/CdS 512 – 3 ML NPLs in ODE with 5% OAm, filled a 2 mm cuvette with the resulting solution, heated it up to *ca.* 130^{o}C, inserted the cuvette in the spectrometer, and measured the PL as the solution cooled down. Upon heating, NPL core-shells showed a red shift and broadening of the PL spectrum and a drop in the PL QY by a factor of 3 (Figure 2.17A). These features were reversible; after all the manipulations the absorption spectrum was unchanged as compared to the initial solution in hexane (Figure 2.17 B). CdSe/$Cd_{1-x}Zn_xS$ QD core-shells from QD Vision core-shells capped with carboxylic acids showed a similar effect but to a lesser extent (Figure 2.17C).

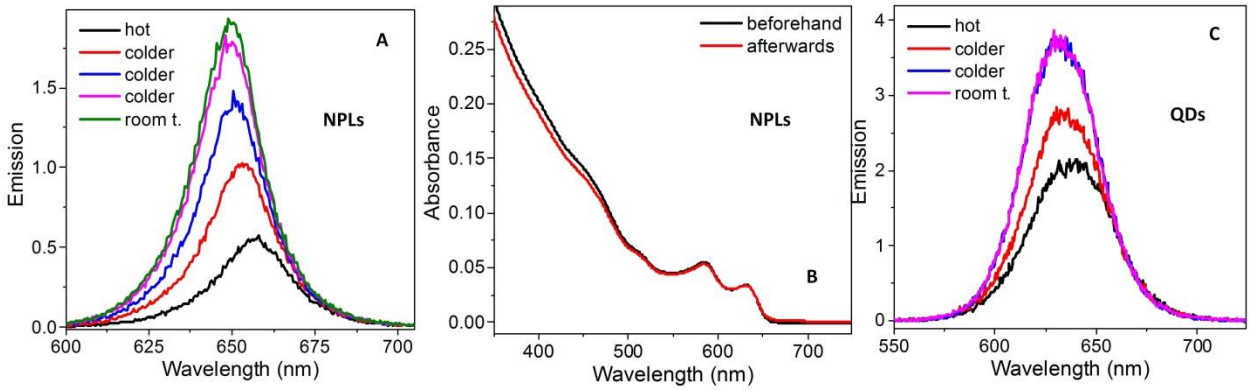

Figure 2.17. Thermal stability of the PL of core-shells. (A) A series of PL spectra of CdSe/CdS 512 – 3 ML NPLs upon cooling from 130°C to the room temperature. (B) UV-Vis spectra of the NPLs before and after thermal treatment. (C) A series of PL spectra of CdSe/$Cd_{1-x}Zn_xS$ QDs upon cooling from 130°C to the room temperature.

2.4. Summary and Outlook

We observed that CdSe 462 and 512 NPLs acquire their ultimate thickness soon after the nucleation, and therefore, developed protocols for NPLs of different lateral dimensions by taking aliquots. We also noticed that the use of cadmium propionate instead of acetate results in long needle-like NPLs. In contrast, CdSe 550 NPLs required a full course of growth at 240°C for the final thickness to establish, but they did not grow from thinner NPLs, however.

By fine-tuning *c*-ALD (*e.g.*, reduction of polysulfides in commercial $(NH_4)_2S$ with TBP), we grew core-shells with narrow emission lines with PL QY up to 74%.

The next goal will be to establish a protocol for 6 ML CdSe NPls, supposedly emitting at 576 nm.[47] Understanding of NPL growth will be very important in this achieving this goal, and *vice versa*, this synthesis can serve as a model system for testing current hypotheses on NPL growth. Thorough understanding of anisotropic growth may enable researchers to synthesize InP NPLs – a very ambitious goal, but a highly desired model system for colloidal InP NCs.

2.5. Experimental Details

CdSe 512 NPLs of three lateral dimensions. To synthesize regular 512 nm CdSe NPLs, we followed the recipe from the same source[53] with slight modifications. Namely, we degassed 170 mg Cd(myristate)$_2$ in 15 ml ODE at the room temperature for 30 min, then we added 12 mg of Se powder and degassed the system for 30 min at 90^{o}C. Then we rapidly heated up the reaction mixture to 240^{o}C under nitrogen. At 190^{o}C, when the solution turned orange-red, we introduced 40 mg of finely ground Cd(OAc)$_2$. We ran the reaction at 240^{o}C for 5 min, then quickly cooled down the reaction mixture to 150^{o}C and allowed it to further cool down. At 70^{o}C, we injected a solution of 2 ml of oleic acid in 10 ml ODE. When the system cooled down to the room temperature, we precipitated the NPLs by centrifugation and re-dispersed them in MCH.

To synthesize 512 nm short NPLs, we repeated the procedure until after the introduction of Cd(OAc)$_2$, but then at 225^{o}C collected the reaction mixture with a glass syringe and injected it through a septum into a vial containing 2 ml oleic acid in 10 ml MCH. (To lower the high pressure of compressed air and hexane vapors in the vial, we re-filled the 24 ml syringe with the atmosphere of the vial immediately after the injection). At the room temperature, we added 7 ml ethanol to the solution, precipitated the NPLs by centrifugation at 11000 rpm for 5 min, and re-dispersed them in hexane.

To synthesize 512 nm intermediate NPLs, we followed the standard procedure until we reached 240^{o}C and ran the reaction for 1 min. Then we injected the hot reaction mixture into 2 ml of oleic acid in ODE, let it cool down to the r.t., centrifuged at 11000 rpm without ethanol, and re-dispersed the NPLs in hexane.

CdSe 550 NPLs of three lateral dimensions. To synthesize regular 550 nm CdSe NPLs, we followed exactly the recipe from the source.[53] Namely, we degassed 170 mg Cd(myristate)$_2$

in 14 ml ODE at the room temperature, heated up the reaction mixture under nitrogen, at 240^{o}C injected 12 mg of Se powder pre-dispersed in 1 ml ODE by sonication, in 20 s introduced 60 mg of finely ground $Cd(OAc)_2$, ran the reaction for 10 min, cooled down the reaction mixture, and at 80^{o}C injected 2 ml of oleic acid in 15 ml ODE. When the suspension reached the room temperature, we centrifuged it without a non-solvent and re-dispersed the NPLs in MCH.

To synthesize 550 nm long NPLs, we degassed 170 mg $Cd(myristate)_2$ in 13.5 ml ODE at the room temperature, heated up the reaction mixture under nitrogen, at 250^{o}C injected 12 mg of Se powder pre-dispersed in 1.5 ml of 0.1 M Se-ODE by sonication, in 60 s introduced 120 mg of finely ground $Cd(OAc)_2$, ran the reaction for 10 min, cooled down the reaction mixture, and at 100^{o}C injected 2 ml of oleic acid in 15 ml ODE. When the suspension reached the room temperature, we centrifuged it without a non-solvent and re-dispersed the NPLs in MCH.

Synthesis of CdSe/CdS NPLs by *c*-ALD. We washed a standard batch of CdSe 512 NPLs by a precipitation with ethanol and re-dispersion in MCH twice. The final volume of the MCH phase was 4 ml. In a separate container, we prepared a two-phase system of 4 ml MCH (top) and 1 ml NMF (bottom). We dissolved 100 µl of 40 – 48% aqeous $(NH_4)_2S$ in the NMF and 100 µl in the MCH and vortexed the system until the yellow color disappeared. We then discarded the MCH phase, washed the NMF phase with fresh MCH, and introduced the washed NMF phase to the NPLs in MCH for a ligand exchange. After the phase transfer of the NPLs into NMF, we discarded the colorless MCH phase, washed the NMF phase with fresh MCH, and transferred it into a new vessel. We then added 2 ml toluene and 1 ml acetonitrile to the NMF phase and centrifuged the turbid suspension. We discarded the supernatant and re-dispersed the precipitate in 1 ml NMF. We then precipitated the solution again, now with 4 ml toluene. The supernatant was discarded and the precipitate re-dispersed in 0.25 ml NMF and transferred to a new

container. We added 1.75 ml of 0.20 M cadmium acetate in NMF, stirred the solution for 1 min, and let it rest for 10 min, until the PL improved. We then added 4 ml of 5% oleylamine in MCH and vertexed the system until the NPLs transferred into the upper, MCH phase. We allowed the PL to improve, discarded the NMF phase, and let the solution rest for a few hours, as the PL was slowly growing. We then precipitated the NPLs with ethanol containing 5% oleylamine, re-dispersed them in MCH, and either stored or used for the next cycle.

CHAPTER THREE

PHOTONICS OF CADMIUM SELENIDE NANOPLATELETS AND CORE-SHELLS

3.1. Optical Excitations in NPLs

3.1.1. Excitons in quantum wells

The length of a typical CdSe NPL is 2 – 5 times the exciton Bohr diameter in bulk CdSe; the width is comparable to the bulk exciton Bohr diameter; and the thickness is about one tenth of the bulk exciton Bohr diameter. We can say that the exciton is confined in the dimension of the NPL thickness and view the NPLs as quantum wells (QWs). There are, however, a few modifications to the excitons in NPLs compared to bulk CdSe. In dielectric-constant-matched (ε-matched) QWs, *e.g.*, epitaxially grown GaAs/$Al_{0.3}Ga_{0.7}As$, the exciton binding energy of 1S exciton is four times its value in the 3D case, the exciton diameter is half the value in the 3D case, and the coordinate of charge density maximum is one quarter of its value in the 3D case.[54] Furthermore, our CdSe NPL is a thin slab of semiconductor in a medium with a lower dielectric constant; therefore, the exciton binding energy is even bigger and the exciton is smaller than in a ε-matched QWs.[55] Based on these considerations and results of variational calculations, D. Miller assumed a nearly spherical rather than a "pancake" shape for the exciton in a QW.[56] According to him, a pancake shape would imply a high curvature, *i.e.*, a high second derivative of the wavefunction, at the edges of the exciton, and therefore, too high kinetic energy of the carriers. Recent studies on PbSe NRs (1D material, considerations similar to 2D)[57] and calculations on CdSe NPLs in a low-ε medium by A. Efros[58] indeed showed an increased exciton

binding energy in these structures. U. Woggon *et al*. showed a contraction of excitons in CdSe nanosheets in a low-ε medium compared to a high-ε medium as a result of the increased Coulombic interaction.[59]

For the purposes of this chapter, we shall assume an oblate spheroidal shape of excitons in NPLs. For example, in CdSe 512 NPLs, the smaller dimension of the exciton is 1.2 nm and the bigger is between 1.2 and 5 nm.

3.1.2. Nanoplatelets are an ideal candidate for amplified spontaneous emission

In amplified spontaneous emission (ASE), a spontaneous PL of a chromophore is amplified by a stimulated emission achieved in a resonant cavity (gain medium). ASE is a necessary condition for laser action (lasing). It implies population inversion in a two-level system. In the language of semiconductor NCs, population inversion is a biexciton[60] – a two-electron-two-hole bound state that can be obtained by absorption of two photons. We shall consider it within the two-state model system. A NC without excitons will absorb an incident photon and generate an exciton, showing a positive absorbance. A NC with one exciton can either absorb an incident photon to produce a biexciton or undergo a stimulated emission with 50% probability each, showing thus an optical transparency. Finally, a NC with a biexciton can only undergo a stimulated emission and have a negative absorbance.

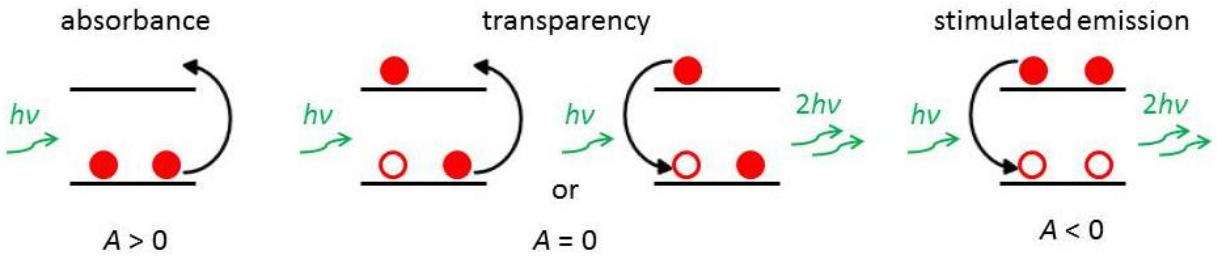

Figure 3.1. A schematic of optical absorbance, transparency, and stimulated emission in a two-level system populated with two electrons.

The biggest enemy of biexcitons (and ASE, as a result) is Auger recombination.[61] One electron-hole pair recombines, and the released energy is given to the other electron-hole pair. The carriers are excited to higher levels and quickly relax to the band edge (carrier cooling).

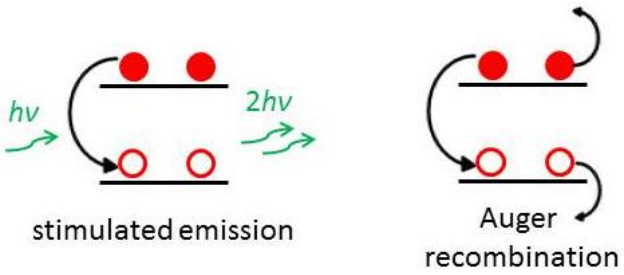

Figure 3.2. Auger recombination is a non-radiative recombination of biexcitons.

To achieve strong amplified spontaneous emission, we must suppress Auger recombination in the chromophore. Semiconductor NPLs are a suitable chromophore for ASE because, owing to its extended lateral dimensions, a NPL can afford multiple excitons with little overlap between them and thus lower the probability of Auger recombination.

To achieve gain in the medium, it is necessary that a molecule or particle of the chromophore be able to absorb a photon emitted by another molecule or particle. CdSe NPLs, showing nearly no Stokes shift, and CdSe/CdS NPLs, showing a small Stokes shift, are a good candidate for the demonstration of ASE.

3.2. Amplified Spontaneous Emission in Films of CdSe/CdS NPLs

3.2.1. Demonstration of ASE

I collaborated with our former postdoctoral fellow Dr. Chunxing She in this work. We deposited *ca.* 50 nm films of CdSe or CdSe/CdS NPLs out of hexane-octane (4:1, v/v) solutions onto glass substrates. Pulsed 400 nm laser light entered the films from the face, and we detected light coming from the edge of the film. At low excitation powers, regular PL was observed. The

PL peak was red-shifted in the film because NPLs were in a different dielectric environment compared to a dilute solution. At a certain pump power, a sharp narrow peak on the red side of the PL band emerged and grew with the pump power (Figure 3.3 A,B). This peak came from ASE. Its position was determined by two factors: the biexciton binding energy and the resonant wavelength of the film acting as a cavity.

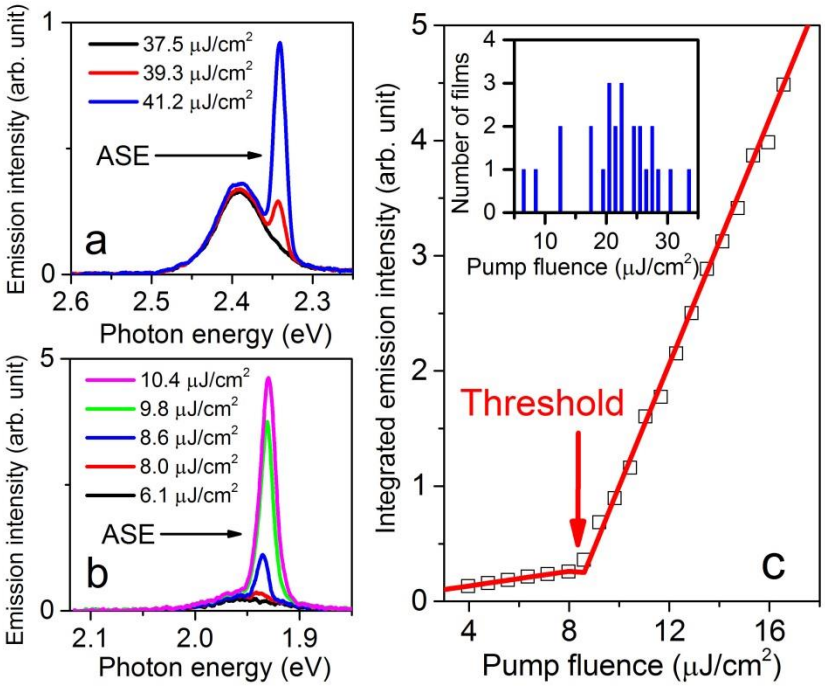

Figure 3.3. (a) A series of PL spectra from the edge of a film of CdSe 512 NPLs at different excitation powers, lower and higher than ASE threshold. (b) Same for a film of CdSe/CdS 512 – 3 ML NPLs. (c) Integrated intensity as a function of pump fluence clearly showing ASE threshold for the film in (b). The inset shows statistics of ASE thresholds from different batches of CdSe/CdS 512 – 3 ML NPLs. Adapted with permission from ref. 62. Copyright 2014, American Chemical Society.

The first figure of merit is the threshold of ASE – the lowest pump fluence at which ASE is observed. It is determined by the quality of the chromophore and the film. A high PL QY of the material and a slow Auger recombination lower ASE threshold. This parameter is also important because, multiplied with a NPL cross-section, ASE threshold tells us the average energy absorbed per NPL, *i.e.*, the average number of excitons per NPL at which ASE is

observed. As of 2014, we demonstrated the record-low ASE threshold 8 μJ/cm^2 with pulsed excitation.[62] We measured absorption cross-sections of a number of samples of CdSe and CdSe/CdS NPLs by measuring absorbance of an aliquot and then digesting it in nitric acid and measuring the amount of Se with ICP. Given the absorption cross-section of 1.1 × 10^{-13} cm^2 at 400 nm (3.1 eV, Figure 3.4) and the ASE threshold fluence of 8 μJ/cm^2, the average energy absorbed by a NPL was $1.1\cdot10^{-13}\text{cm}^2\times8\cdot10^{-6}\ {}^{\text{J}}\!/_{\text{cm}^2}=8.8\cdot10^{-19}\text{J}=5.5\,\text{eV}$. The average number of excitons per NPL was 5.5 eV / 3.1 eV = 1.8. Assuming Poissonian distribution of the excitons, 17% of NPLs did not have excitons, 30% of NPLs had exactly one exciton, and 53% of NPLs had two or more excitons. Therefore, our material operated in the biexcitonic regime.

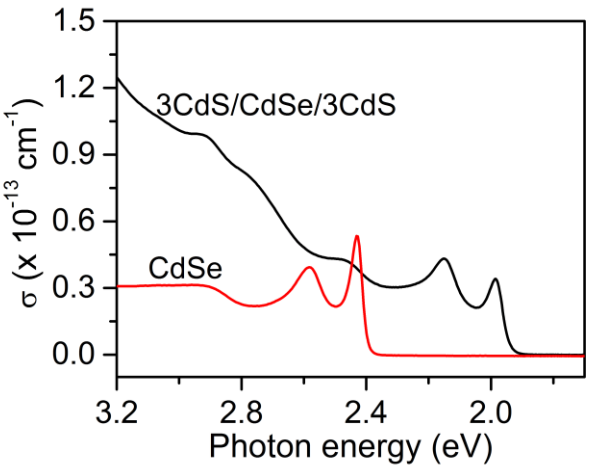

Figure 3.4. Absorption cross-sections of CdSe 512 NPLs with different numbers of monolayers of CdS. Adapted with permission from ref. 62. Copyright 2014, American Chemical Society.

3.2.2. Characterization of ASE

Another figure of merit describing the medium was the net optical gain – a relative increase of light intensity as a result of a passage of a unit length through the medium. The rate of increase of intensity, *I*, with the passed distance, *l*, is given by the following formula.

$$\frac{dI}{dl}=gI+I_s$$

I_s is the spontaneous luminescence intensity. We solve the equation for the intensity I.

$$I = \frac{I_s}{g}\left(e^{gl} - 1\right) + I_0$$

Experimentally, modal gain was measured by varying the stripe length of the excitation, l, at a constant stripe width and measuring the intensity coming out of the edge of the film in the direction of the stripe. Fitting the data to the above equation yielded values of g = 600 cm^{-1} (Figure 3.5a), a four-fold improvement compared to the values for QDs.[63]

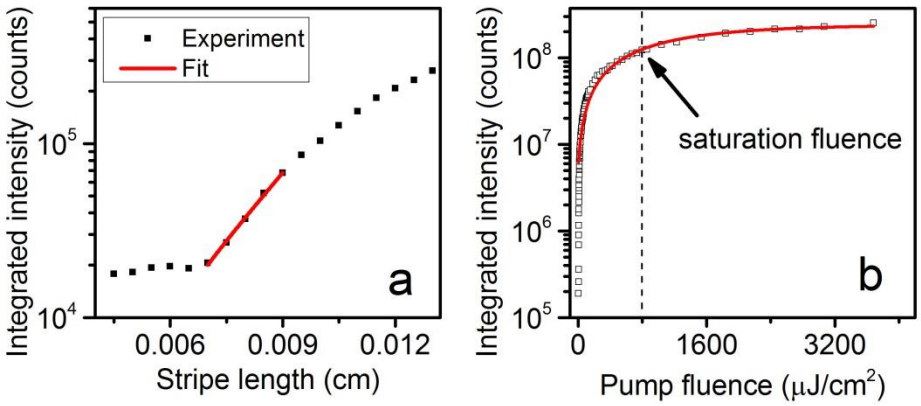

Figure 3.5. Modal gain and saturation fluence. (a) Total intensity of light coming out of the edge of a film as a function of the excitation stripe length in the direction toward the detector at a constant stripe width. Adapted with permission from ref. 62. Copyright 2014, American Chemical Society.

At high fluences, the intensity of the light coming out of the gain medium saturates because NPLs can accommodate only a certain number of excitons. The energy absorbed by a NPL with a cross-section σ and pump fluence J is given by the following formula.[64]

$$E = \frac{\sigma J}{1 + J/J_0}$$

As $J \rightarrow \infty$, $E \rightarrow \sigma J_0$; therefore, J_0 is the maximum energy that can be absorbed by a NPL of a unit cross-section. At $J = J_0$, the absorbed energy is half of its maximum value. We determined the saturation fluence of 800 μJ/cm^2 for our system, 100 times higher than the threshold.

Transient absorption (TA)[65] is a powerful technique to measure systems with multiexcitons. It is a pump-probe technique, in which an intense beam of laser light of a blue wavelength (400 nm or so, the pump) excites NCs in the volume of the sample through which it passes. A beam of polychromatic light is directed through the excited volume and measures the excited-state spectrum of the sample. NCs with one exciton generated by the pump are transparent to the probe. NCs with two excitons generated by the pump undergo a stimulated emission when probed and show a negative absorbance. Therefore, excited-state spectrum will show suppressed or negative excitonic peaks.

Table 3.1. A summary of parameters used in transient absorption.

# of excitons per NPL	Absorbance, α	Induced absorbance, $\Delta\alpha = \alpha - \alpha_0$	$-\Delta\alpha / \alpha_0$
0	α_0	0	0
$0 < N < 1$	$0 < \alpha < 1$	$-\alpha_0 < \Delta\alpha < 0$	$0 < -\Delta\alpha / \alpha_0 < 1$
1	0	$-\alpha_0$	1
> 1	< 0	$< -\alpha_0$	> 1

The spectral range, over which we achieve population inversion (negative absorbance) is called gain bandwidth. In our case it extended from 590 to 660 nm (Figure 3.6a). The time over which the average number of excitons per NPL is above 1 (the negative relative induced absorbance, $-\Delta\alpha / \alpha_0$, is above 1) is called gain lifetime. Our system measured a gain lifetime of 140 ps (Figure 3.6b). We shall compare this value with characteristic Auger times.

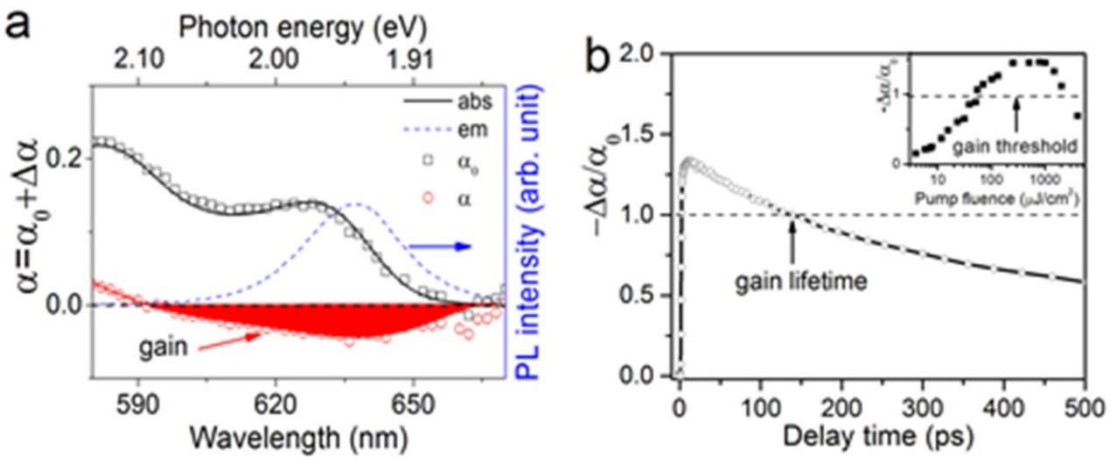

Figure 3.6. Gain bandwidth and gain lifetime. (a) Ground-state absorption (α_0), transient absorption (α), and PL spectra of a solution of CdSe 512 – 3 ML NPLs in hexane. (b) Decay of negative induced absorption with time. Adapted with permission from ref. 52. Copyright 2015, American Chemical Society.

Auger recombination is the major competing process of biexciton recombination. By measuring the decay of the negative induced absorbance in TA, we showed that ASE outpaces Auger recombination.

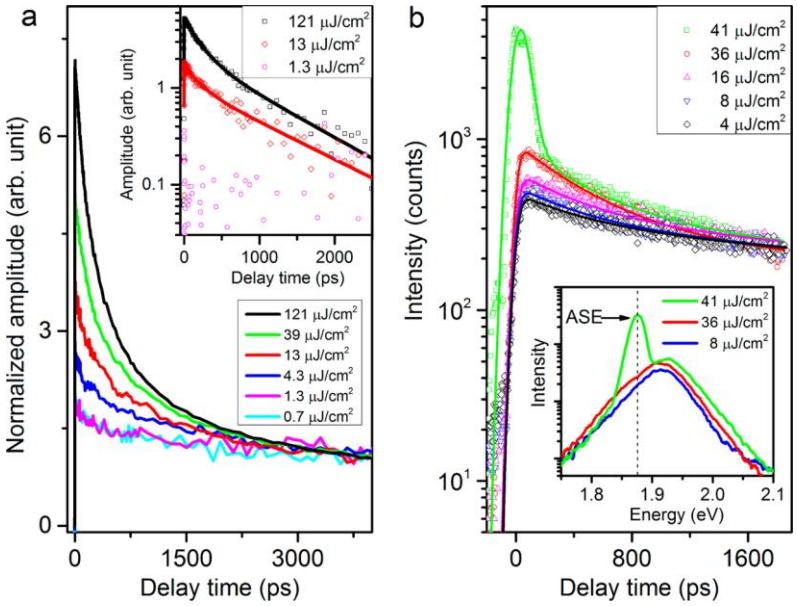

Figure 3.7. ASE outpaces Auger recombination. (a) TA spectra of a solution of CdSe/CdS 512 – 3 ML NPLs at a number of excitation fluences around the ASE threshold. (b) Time-resolved PL spectra of a film of the material at a number of excitation fluences around the ASE threshold. Adapted with permission from ref. 62. Copyright 2014, American Chemical Society.

3.3. Red, Yellow, Green, and Blue Amplified Spontaneous Emission and Lasing

3.3.1. ASE from films of CdSe NPLs

In addition to core-shells, we used pure CdSe 550, 512, and 462 NPLs to demonstrate ASE. Unlike core-shells, CdSe NPLs are more sensitive to the surrounding environment. One precipitation of a solution of NPLs is necessary to remove excess organics that makes films oily and opaque. Precipitation with ethanol lowers the PL QY of CdSe NPLs likely for two reasons. First, ethanol removes part of $Cd(OAc)_2$ from the surface, exposing hole-trapping Se sites. Second, ethanol induces stacking of NPLs, which lowers the PL QY due to a fast exciton diffusion *via* homo-FRET in a stack. We also aimed to explore the role of lateral dimensions on ASE, but small CdSe 512 NPLs required a non-solvent for precipitation from ODE (unlike regular CdSe 512 NPLs). We explored a number of non-solvents. Mild non-solvents like acetone and ethyl acetate precipitated NPLs, but together with organics. The PL QY of re-dispersed NPLs was high, but the cast films were opaque. Solvents like 1-propanol and 1-butanol washed the organics better, but did not impair the PL QY as much as ethanol. Therefore, we precipitated the crude solution of CdSe 512 short NPLs with acetone, re-dispersed the precipitate in a small volume of hexane, precipitated it with 1-propanol, and re-dispersed in hexane-octane for the film deposition.

Films of CdSe NPLs demonstrated low ASE threshold, the lowest being 17 $\mu J/cm^2$ for CdSe 512 NPLs, and the highest being 60 $\mu J/cm^2$ for CdSe 462 NPLs. The latter NPLs aggregated heavily and increased their trap emission after a precipitation with ethanol, which impaired their ASE threshold. Also, this thickness of NPLs showed a modal gain of 86 cm^{-1} – almost an order of magnitude lower than the other NPLs.

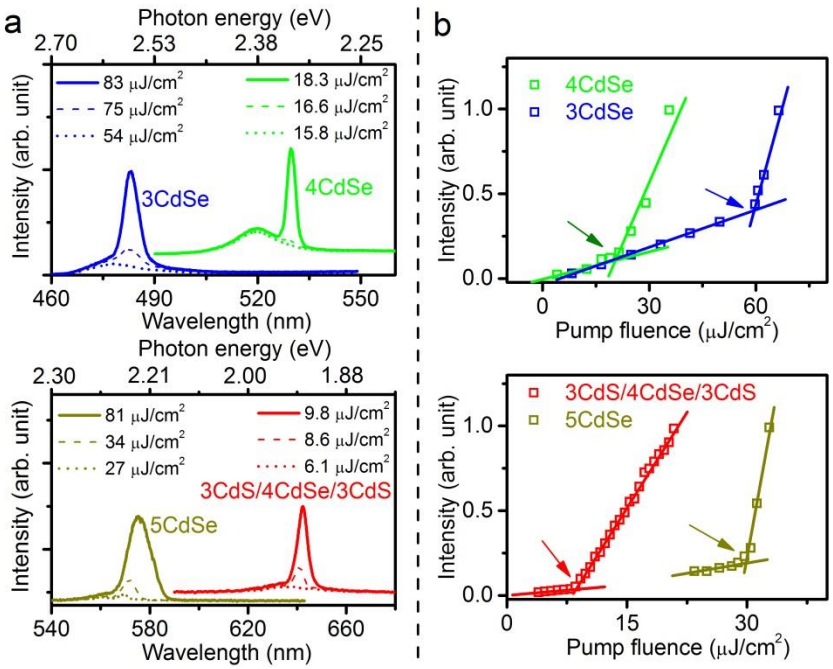

Figure 3.8. (a) Spectrum of the PL coming from the edge of the film for 3 ML, 4 ML, 5 ML CdSe, and 4 ML CdSe with 3 MLs CdS for different excitation powers. (b) Integrated intensities from (a) to find the ASE threshold. Adapted with permission from ref. 52. Copyright 2015, American Chemical Society.

3.3.2. Demonstration of lasing

The cavity consisted of two mirrors – the semitransparent output coupler, where the sample was deposited, and the parallel end mirror. A beam of excitation light was incident at the sample at an angle. Emitted light was bouncing between the mirrors, re-exciting the sample. Part of the light leaked through the output coupler and was detected by a CCD. CdSe NPLs of the three thicknesses and CdSe 512 – 3 ML core-shells demonstrated lasing in four different colors. To prove that we dealt with actual lasing, we increased the separation between the mirrors or turned one mirror by a small angle. Lasing decayed, but ASE (measured from the edge of the film) persisted. Therefore, the sharp peak on the red shoulder of every spectrum came from laser action.

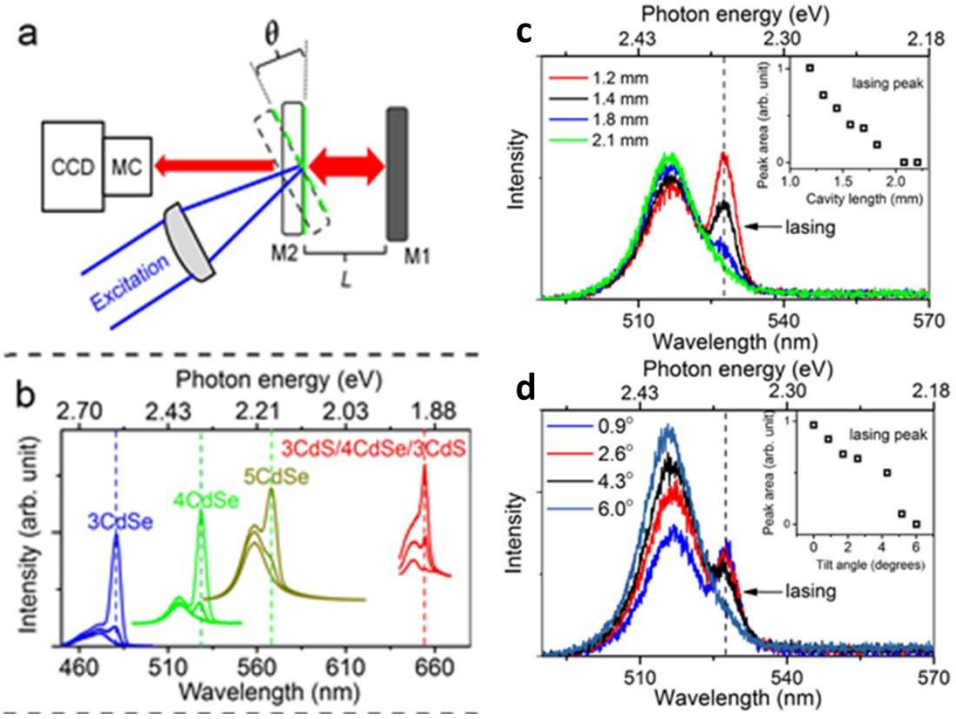

Figure 3.9. (a) A schematic of a laser cavity made up by two parallel mirrors. (b) Spectra of light coming out of the laser cavity for a number of samples. (c) Decay of lasing peak in CdSe 512 NPLs with the increase in the inter-mirror separation. (d) Same with turning one mirror. Adapted with permission from ref. 52. Copyright 2015, American Chemical Society.

Observation of yellow lasing at 570 nm is valuable because this wavelength sits in the middle of the wavelength gap of commercial lasers. There are a number of violet, blue, and green lasers available up to the wavelength of 532 nm. Many lasers operating at wavelengths above 600 nm are available as well. Demonstration of electrically pumped lasing on CdSe 550 (and 576) NPLs and commercialization thereof will fill the existing gap.

Whereas films of CdSe/CdS core-shell NPLs were stable during the measurement and long term afterwards, films of CdSe NPLs degraded during the measurement and soon afterwards. For a better operation, one will need to encapsulate these NPL in a matrix of a wide-bandgap materials like titania.

3.4. Multiexciton Dynamics in CdSe and CdSe/CdS NPLs

3.4.1. The average number of excitons per NPL

Radiative and non-radiative multiexciton lifetimes are essential for understanding multiexciton dynamics in ASE and Auger recombination in NCs. We measured time-resolved TA spectra of a solution of CdSe 512 NPLs and extracted a series of decay kinetics of the first excitonic bleach. The signal in TA corresponds to the lighter carrier (the electron in CdSe). Assuming no trion formation, we claim that the electron dynamics in TA reflects the exciton dynamics.

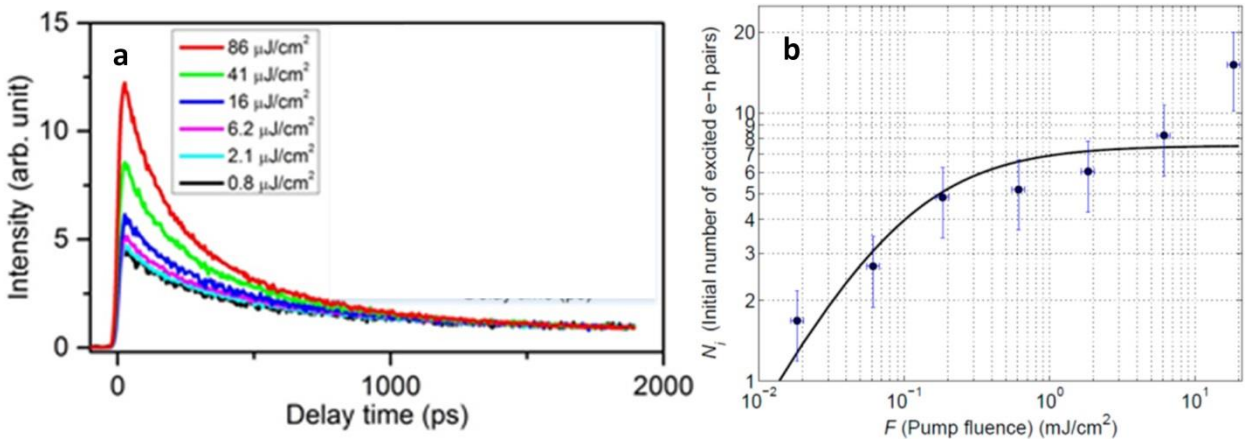

Figure 3.10. (a) Early-time pump fluence-dependent emission dynamics of 4CdSe NPLs. The dynamics are normalized at about 1.9 ns. (b) Determining the saturation fluence and the initial average number of excitons per NPL. (b) is adapted with permission from ref. 64. Copyright 2015, American Chemical Society.

The next step was to understand how many excitons per NPL we had on average. There are two ways to do so. First, we normalized the data for different pump powers by the decay tail (times > 1 ns). All multiexcitons had decayed by this time, so monoexcitonic kinetics should be identical for different runs. Normalized traces for the lowest pump fluences (0.8 and 2.1 μJ/cm^2) overlay even at early times (Figure 3.10a), meaning that they were purely monoexcitonic. As we increased the pump fluence, a faster decay at early times emerged from the normalized data. That

was a signature of a faster, multiexcitonic decay. This quick estimate is useful during the data collection, as it ensures the researcher collects data in the right range of powers, but does not tell us the exact average number of excitons per NPL, since there is a substantial biexcitonic dynamics even at one exciton per NPL on average.

The second way was to plot the tips of the TA decay data (the initial intensities) as a function of pump fluence, determine the saturation fluence, and calculate the initial average number of excitons per NPL given the absorption cross-section (Figure 3.10 b).[64]

$$\langle N \rangle_0 = \frac{(J/\hbar\omega)\sigma}{1+\left(J/J_0\right)}$$

The experimental results showed that saturation fluence in a batch CdSe 512 NPLs, J_0 = 90 μJ/cm^2, corresponded to 8 excitons per NPL. The average volume per one exciton was 30 nm^3 and the average area was thus 25 nm^2. If saturation implies tight packing of excitons, the lateral dimension of the exciton is *ca*. 5 nm, which is half of the exciton Bohr diameter in bulk CdSe and is consistent with the expected size of the exciton in QWs. The upward deviation from the fit at high fluences resulted from a formation of plasma of free carriers. Films of CdSe NPLs measured saturation fluences up to 500 μJ/cm^2.

The next step was to understand the exciton distribution among the NPLs. We assume that exciting a new exciton in a NPL is independent of the existing number of excitons. For $J << J_0$, it is a valid assumption. Let P be the total number of NPLs and E be the total number of excitons; $\langle N \rangle = E/P$. We pick one exciton and go over all NPLs one by one; the probability to put this exciton in a given platelet is $1/P$ and to not put it in this platelet is $1-1/P$. The fraction of NPLs that have exactly k excitons is given by the binomial distribution.

$$N_k = \binom{E}{k} \cdot \left(\frac{1}{P}\right)^k \left(1 - \frac{1}{P}\right)^{E-k}$$

The binomial distribution can be approximated by Poissonian distribution for $k << E$.

$$N_k \approx \frac{\langle N \rangle^k}{k!} e^{-\langle N \rangle}$$

The fraction of NPLs with no exctitons is $e^{-\langle N \rangle}$, with one exciton is $\langle N \rangle e^{-\langle N \rangle}$, *etc*. The most probable way to distribute 24 excitons among 12 NPLs, $<N> = 2$, is shown in Figure 3.11.

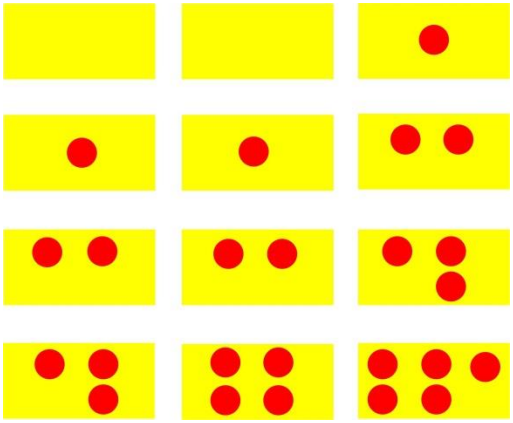

Figure 3.11. The most probable way to distribute 24 excitons among 12 NPLs.

There are two views at the multiexcitonic decay. The first view is a cascade of multiexctions: tetraexciton decays into triexciton, triexciton decays into biexciton, biexciton decays into monoexciton, monoexciton annihilates.[66] Within this view we can take a more exact approach and construct a set of differential equations describing the decay (approach one) or attempt to isolate a decay dynamics for every population of multiexcitons by a subtractive analysis (approach two). Another view is similar to chemical kinetics, where we deal with concentrations of carriers and excitons in cm^{-3} and try to analyze the decay as the first order, second order, third order, *etc.* (approach three).[64]

3.4.2. Approach one: cascade of multiexcitons

Monoexcitons annihilate and are produced from biexcitons. Biexcitons decay into monoexcitons and are produced from triexcitons. Triexcitons decay to biexcitons and are produced from tetraexcitons, *etc*.

$$\mathrm{Ex}_k \xrightarrow{\tau_k} \mathrm{Ex}_{k-1} \xrightarrow{\tau_{k-1}} \ldots \mathrm{Ex}_3 \xrightarrow{\tau_3} \mathrm{Ex}_2 \xrightarrow{\tau_2} \mathrm{Ex}_1 \xrightarrow{\tau_1} \text{no excitons}$$

We assume the decay of every multiexciton obeys the-first order kinetics.

$$\begin{aligned}
\frac{dn_1}{dt} &= -\frac{1}{\tau_1} n_1 + \frac{1}{\tau_2} n_2 \\
\frac{dn_2}{dt} &= -\frac{1}{\tau_2} n_2 + \frac{1}{\tau_3} n_3 \\
\frac{dn_3}{dt} &= -\frac{1}{\tau_3} n_3 + \frac{1}{\tau_4} n_4 \\
&\ldots
\end{aligned}$$

where n_k is the concentration of the k-fold multiexciton. The corresponding matrix:

$$\begin{bmatrix}
-\frac{1}{\tau_1} & \frac{1}{\tau_2} & 0 & 0\ldots \\
0 & -\frac{1}{\tau_2} & \frac{1}{\tau_3} & 0\ldots \\
0 & 0 & -\frac{1}{\tau_3} & \frac{1}{\tau_4}\ldots \\
0 & 0 & 0 & -\frac{1}{\tau_4}\ldots \\
\ldots & & &
\end{bmatrix}$$

– is a triangular matrix whose eigenvalues, therefore, are the diagonal elements. The general solution takes the following form.

$$n_1 = A_{11}e^{-t/\tau_1} + A_{12}e^{-t/\tau_2} + A_{13}e^{-t/\tau_3} + \ldots$$
$$n_2 = A_{21}e^{-t/\tau_1} + A_{22}e^{-t/\tau_2} + A_{23}e^{-t/\tau_3} + \ldots$$
$$n_3 = A_{31}e^{-t/\tau_1} + A_{32}e^{-t/\tau_2} + A_{33}e^{-t/\tau_3} + \ldots$$
$$\ldots$$

The columns are the eigenvectors corresponding to the eigenvalues. We, however, truncate the cascade at the *k*-fold exciton, *i.e.*, the *k*-fold exciton only decays into (*k* – 1)-fold exciton, but is not generated from anything. The solution then reads $n_k = n_{k0}e^{-t/\tau_k}$. We substitute for n_k into the differential equation for $n_{k\text{-}1}$ and work our way down the cascade. Having satisfied boundary conditions, we arrive at biexponential solutions for every multiexciton:

$$n_1 = (n_{10} + n_{20})e^{-t/\tau_1} - n_{20}e^{-t/\tau_2}$$
$$n_2 = (n_{20} + n_{30})e^{-t/\tau_2} - n_{30}e^{-t/\tau_3}$$
$$n_3 = (n_{30} + n_{40})e^{-t/\tau_3} - n_{40}e^{-t/\tau_4}$$
$$\ldots$$

where n_{10}, $n_{20}\ldots$ are the initial concentrations of multiexcitons. The experimentally measured magnitude is the total number of excitons, which is given by:

$$n = n_1 + 2n_2 + 3n_3 + \ldots = (n_{10} + n_{20})e^{-t/\tau_1} + (n_{20} + 2n_{30})e^{-t/\tau_2} + (n_{30} + 3n_{40})e^{-t/\tau_3} + \ldots$$

where the initial concentrations are calculated from the Poissonian distribution:

$$n_{10} = \frac{\langle n_0 \rangle^1}{1!}e^{-\langle n_0 \rangle}$$
$$n_{20} = \frac{\langle n_0 \rangle^2}{2!}e^{-\langle n_0 \rangle}$$
$$\ldots$$

The fitting strategy is the following. First, we fit the low-fluence, single-exciton decay to obtain τ_1. Then we fit a decay with a substantial contribution of biexcitons: we input fixed τ_1 and

distribute the initial amplitude between the two exponents according to the Poissonian distribution. Then we continue with higher multiexcitons likewise.

The monoexcitonic decay (both radiative and non-radiative) time was 410 ± 10 ps, which is faster than reported for NPLs. Nevertheless, it was long enough to not interfere with multiexciton analysis. The biexcitonic and triexcitonic decay times were 250 ± 10 ps and 100 ± 10 ps, respectively.

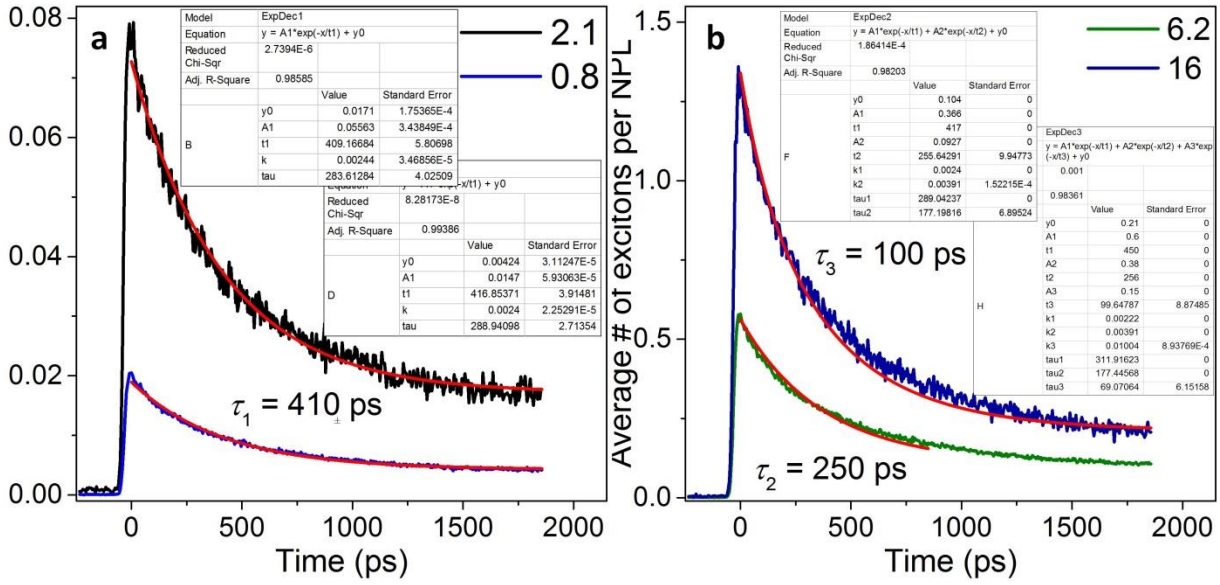

Figure 3.12. Analysis of the data in Fig. 3.10a. (a) Fitting low-fluence monoexcitonic decays. (b) Fitting higher-fluence multiexcitonic decays by inputting parameters from lower-excitonic decays.

3.4.3. Approach two: subtractive analysis

This approach was used by V. Klimov and M. Bawendi.[61] The data are normalized at late times (past 1 ns). Monoexcitonic decay time, τ_1, is extracted from averaged overlaying low-fluence data. Then we subtract the averaged monoexcitonic data from higher-fluence data to obtain τ_2 (as long as it remains biexcitonic and the slope does not diverge up at early times). After that we subtract biexcitonic data from higher-fluence data to extract τ_3 and so on. Here we present analysis of biexciton and triexciton dynamics for CdSe/CdS 512 – 3 ML NPLs from PL

decay measured with a streak camera. The monoexcitonic decay time is 1.0 ns – shorter than reported in the literature. The bi- and triexcitonic lifetimes are 490 ± 20 and 310 ± 20 ps, respectively (Figure 3.13). The ratio of consecutive multiexcitonic lifetimes was close to $\tau_1 : \tau_2 : \tau_3 = 1 : \frac{1}{2} : \frac{1}{3}$, which suggests a bimolecular kinetics in the total number of excitons: $-\frac{dn}{dt} = kn^2$.[66]

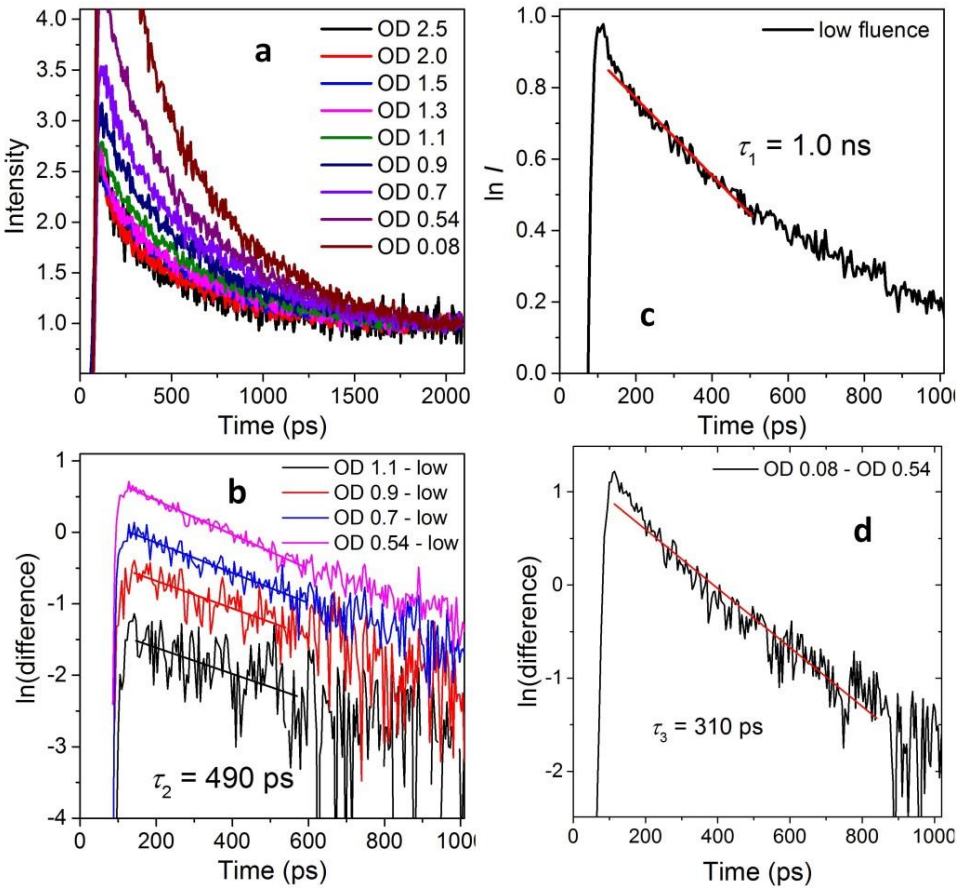

Figure 3.13. Subtractive analysis of multiexcitonic lifetimes on a solution of CdSe/CdS 512 – 3 ML NPLs. (a) PL decay measured by a streak camera for a number of fluences normalized at late times. (b) Averaged low-fluence data (OD 1.5 and OD 1.3) to extract monoexcitonic dynamics. (c) Differenced data to extract biexcitonic dynamics. (d) The difference of the data for the two highest fluences to extract triexcitonic dynamics.

3.4.4. Approach three: kinetics analysis of the concentration of excitons

Within this approach, we deal with the total concentration of excitons similarly to chemical kinetics. The rate of the excitonic decay, $-\frac{dn}{dt}$, can be first, second, third order in n, or a more complicated equation will describe the dynamics in the case of a multi-step processes like carrier trapping, trion formation, *etc*. Two considerations help us hypothesize the reaction order. First, exciton binding energy is high in NPLs; therefore, we deal with whole excitons rather than individual carriers. Second, Auger recombination implies interaction of one exciton with another. Therefore, we assume the second-order kinetics in *n*. The integrated rate equation for the second-order dynamics reads:

$$n = \frac{n_0}{1 + k n_0 t}$$

We can switch from the concentration of excitons to the average number of excitons per NPL given the volume of a NPL, *V*.

$$N = \frac{N_0}{1 + k_{\text{eff}} N_0 t}$$

The effective rate constant in the above equation is given by $k_{\text{eff}} = k/V$. Within this approach, the decay rate is independent of the history of the system and depends only on the current concentration of excitons. Therefore, we can shift raw lower-fluence data in time until they fall onto higher-fluence data (Figure 3.14).

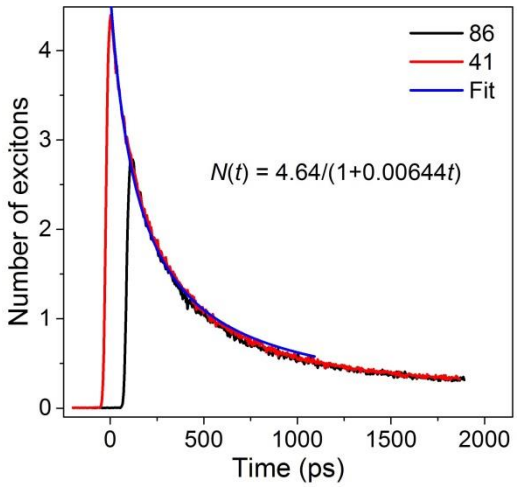

Figure 3.14. Second-order analysis of the exciton decay in CdSe 512 NPLs in hexane.

We analyzed two highest-fluence decays in Figure 3.10a. The value for k_{eff} was 0.00644/4.64 = 0.0014 exciton^{-1}s^{-1}, which is agrees with a published value of 0.00125 exciton^{-1}s^{-1}[1]. The lifetime in the second-order kinetics does depend on the initial number of excitons, and for the highest fluence, equals 267 ps. The two-exciton recombination rate (the slope of the curve at $\langle N \rangle = 2$), or $k \cdot 2^2$, is 5.55 excitons/ns.

The following experiment will be helpful in figuring the right approach to the exciton dynamics. Assume a solution of long NPLs pumped at a fluence to generate 4 excitons per NPL on average. If we cut every NPL in half, the average number of excitons per NPL will be 2. If it is the number of excitons per cm^3 that appears in the rate law, then the recombination rate will not change, but if it is the average number of excitons per NPL that matters, then the recombination rate will decrease.

3.4.5. Discussion of the biexcitonic dynamics

The decay of the bleach in TA and the PL decay in streak camera measurements originate from both radiative and non-radiative excitonic and multiexcitonic decays. It is even question whether we have a true biexciton (like H_2 molecule) or two excitons (like two H atoms). Our

hypothesis of the existence of biexciton is based on the position of the ASE peak on the red shoulder of the PL band. Such biexciton would have a binding energy of *ca.* 30 meV, slightly higher than k_BT at the room temperature. One can argue that the position of the ASE peak is also determined by the "resonant" conditions of the film; the counter argument is that the position of the ASE peak relative to the PL band is nearly independent of the film thickness or preparation conditions. In a two-dimensional system, the biexcitonic binding energy is expected to be about 20% of the hh – e monoexcitonic binding energy for any material.[67] Given the predicted 200 meV monoexcitonic binding energy in CdSe NPLs,[59] we estimate about 40 meV for the biexcitonic binding energy.

We also observed that biexcitonic lifetimes depended strongly on the thickness of the NPLs but not their lateral dimensions, staying between the values observed for NRs and QDs of a similar volume. The extracted biexcitonic lifetime, τ_2, combines both radiative and non-radiative biexcitonic lifetimes. We did not extract radiative lifetimes. It is possible to do so by measuring the multiexcitonic PL QY of the system and having a model for non-radiative recombination. The analysis is complicated by the fact that non-radiative monoexcitonic and radiative biexcitonic times are comparable. It is also possible to measure biexcitonic lifetimes and PL QY from time-correlated sngle-photon-counting spectroscopy.[68] We are currently collaborating with the group of M. G. Bawendi to measure biexcitonic PL QY and lifetime in CdSe/CdS NPLs, and the readers should search for the results in articles from 2017 – 2018.

3.5. Energy Transfer in Hetero-Stacks of CdSe NPLs

The PL band (e – hh) of CdSe 512 NPLs overlaps with the second exciton (lh – e) of CdSe 550 NPLs. Moreover, NPLs tend to form stable stacks with a large area contact and interplatelet separation determined by the surface ligands (*ca.* 2 nm). These are favorable

conditions for Förster (fluorescence, fast) resonance energy transfer (FRET). Together with radiative and non-radiative decays, FRET is one of the paths an exciton in a NC can undergo. The efficiency of FRET is given similarly to the PL QY.

$$\varepsilon = \frac{k_{\mathrm{FRET}}}{k_{\mathrm{r}} + k_{\mathrm{nr}} + k_{\mathrm{FRET}}}$$

Between two point chromophores, the efficiency of FRET decays rapidly with the separation between the chromophores.

$$\varepsilon = \frac{1}{1 + \left(r / R_0 \right)^6}$$

The sixth power of FRET radius (R_0, the separation that gives 50% FRET yield) is proportional to the spectral overlap between the FRET donor and acceptor. Given the high spectral overlap between CdSe 512 and 550 NPLs, and a plane-to-plane interaction rather than point-to-point interaction, we expect high rates of FRET in hetero-stacks of CdSe NPLs. FRET rates can be measured based on sensitization – an increase of the PL decay of the donor and a decrease of the PL decay of the acceptor.

Mixing a purified batch of CdSe 512 NPLs with a purified batch of CdSe 550 NPLs did not lead to sensitization: the PL decay rate of each chromophore in the mix was identical to that in a pure solution. This observation makes sense because the already existing stacks do not interpenetrate each other. We had to mix the NPLs hot, before they stacked. We ran two syntheses in parallel and adjusted the logistics so that the fifth minute of the growth of CdSe 512 NPLs at 240^{o}C coincided with the tenth minute of the growth of CdSe 550 NPLs at 240^{o}C. We collected the hot solution of CdSe 512 NPLs with a syringe, injected it into the flask with CdSe 550 NPLs, and slowly cooled down the system allowing the NPLs to form hetero-stacks. From

the difference in the appearance of CdSe 512 and 550 NPLs in TEM, we guessed the identity of the NPLs in a TEM image of the mix. CdSe 512 NPLs tend to twist, whereas CdSe 550 NPLs are more rigid (Figure 3.15).

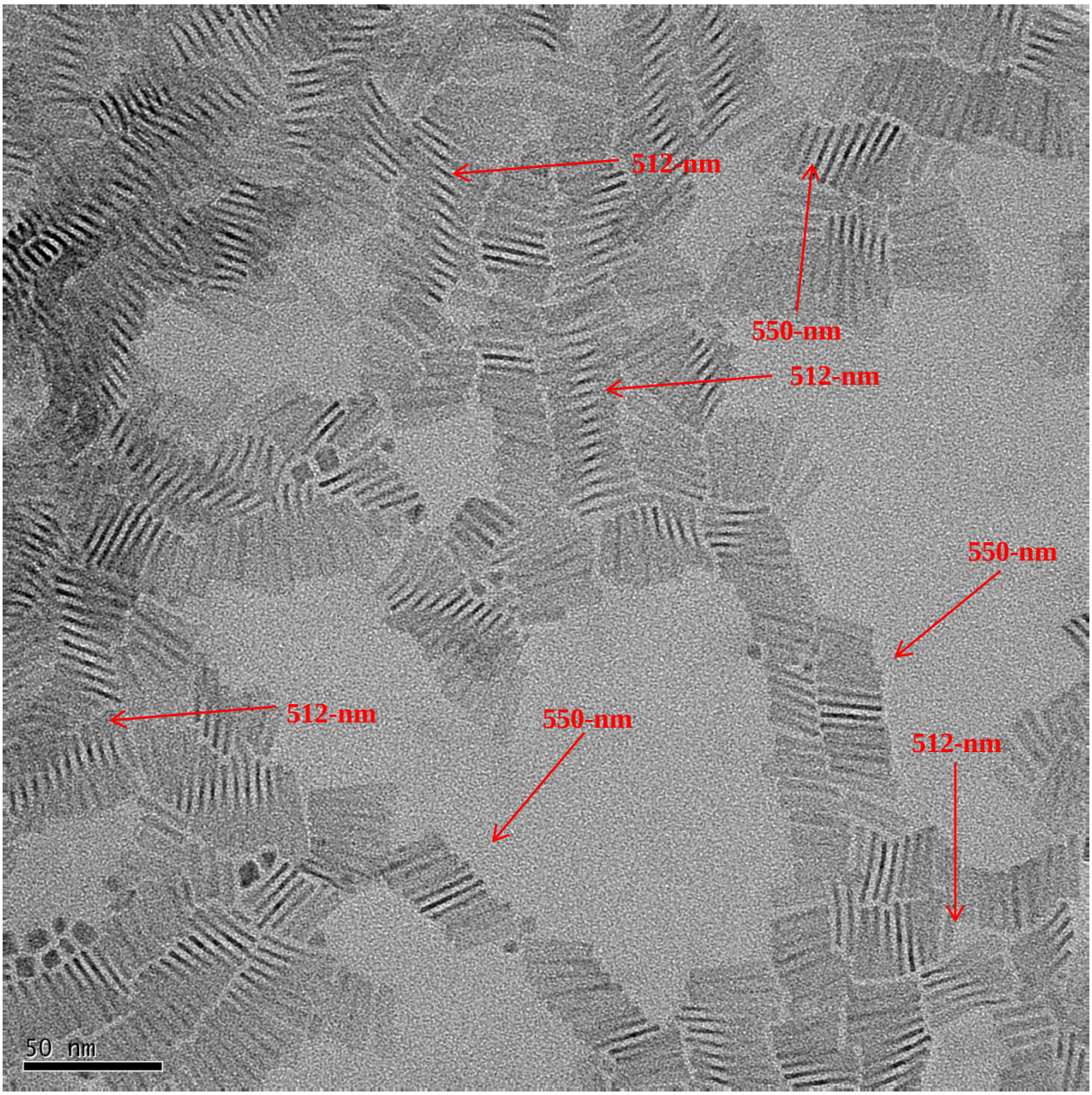

Figure 3.15. TEM image of a mix of CdSe 512 and 550 NPLs.

Our collaborators C. Rowland and R. Schaller performed a series of experiments demonstrating fast energy transfer from CdSe 512 to CdSe 550 NPLs within stacks in films of mixtures.[69] As an indirect observation first, PLE spectrum of a mix of the NPLs monitored at the PL peak of the acceptor (555 nm) resembled the absorption spectrum of the donor at high fractions of the latter (90 and 95%). The first excitonic peak of the donor in PLE had a clearly higher energy than the second excitonic peak of the acceptor. Therefore, it was the excitation of the donor and energy transfer to the acceptor that resulted in the PL of the acceptor at 555 nm for these two traces (Figure 3.16 d).

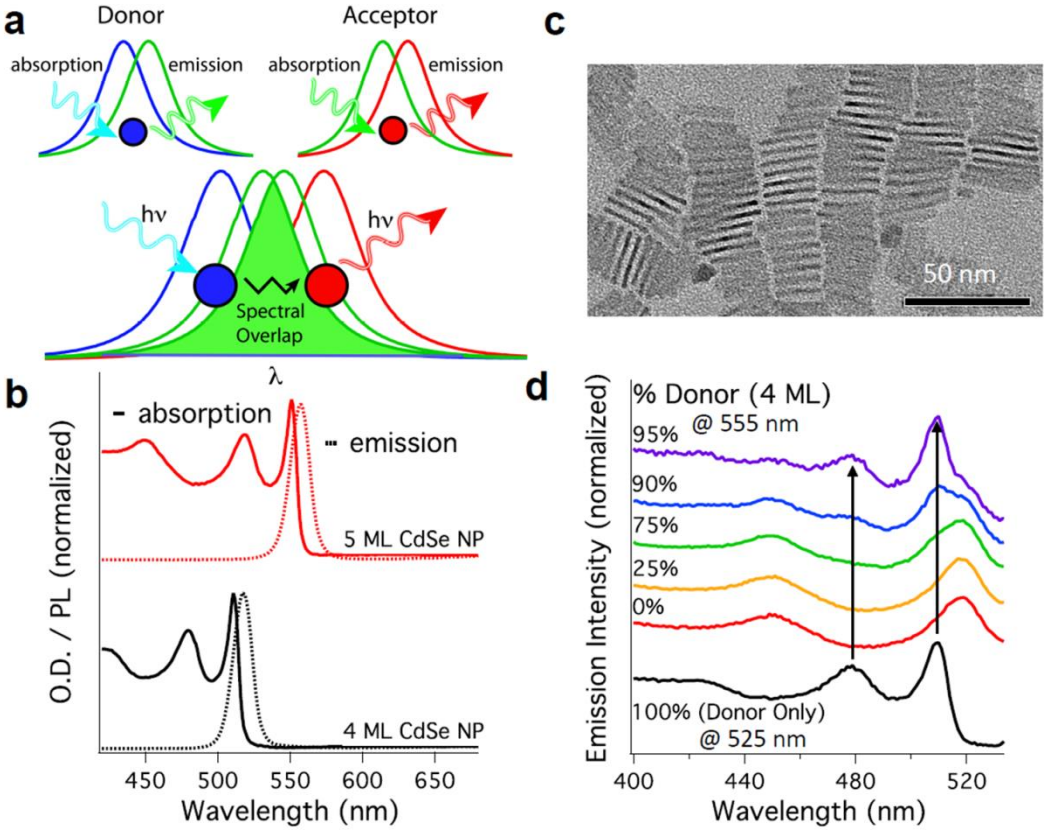

Figure 3.16. (a) A high spectral overlap between the donor and the acceptor is necessary for a high yield of FRET. (b) The PL band of CdSe 512 NPLs in the film has a high overlap with the second excitonic peak (lh – e) of CdSe 550 NPLs. (c) TEM image of stacks formed by CdSe 512 and 550 NPLs. (d) PLE spectra of a series of films of mixes of CdSe 512 and 550 NPLs monitored at 555 nm. Adapted with permission from ref. 69. Copyright 2015, Nature Publishing Group.

Streak camera measurements provided a more direct evidence for the fast energy transfer. The PL of the donor decayed faster in mixes with the acceptor than in the pure state, and the PL of the acceptor decayed more slowly in mixes with the donor than in the pure state, which a sign of sensitization (Figure 3.17). For a series of donor-to-acceptor ratios, the characteristic FRET time varied from 7.4 to 23.0 ps. For comparison, in 2015, B. Guzelturk *et al*. measured FRET times of 3 ps in homo-stacks of CdSe 512 NPLs.

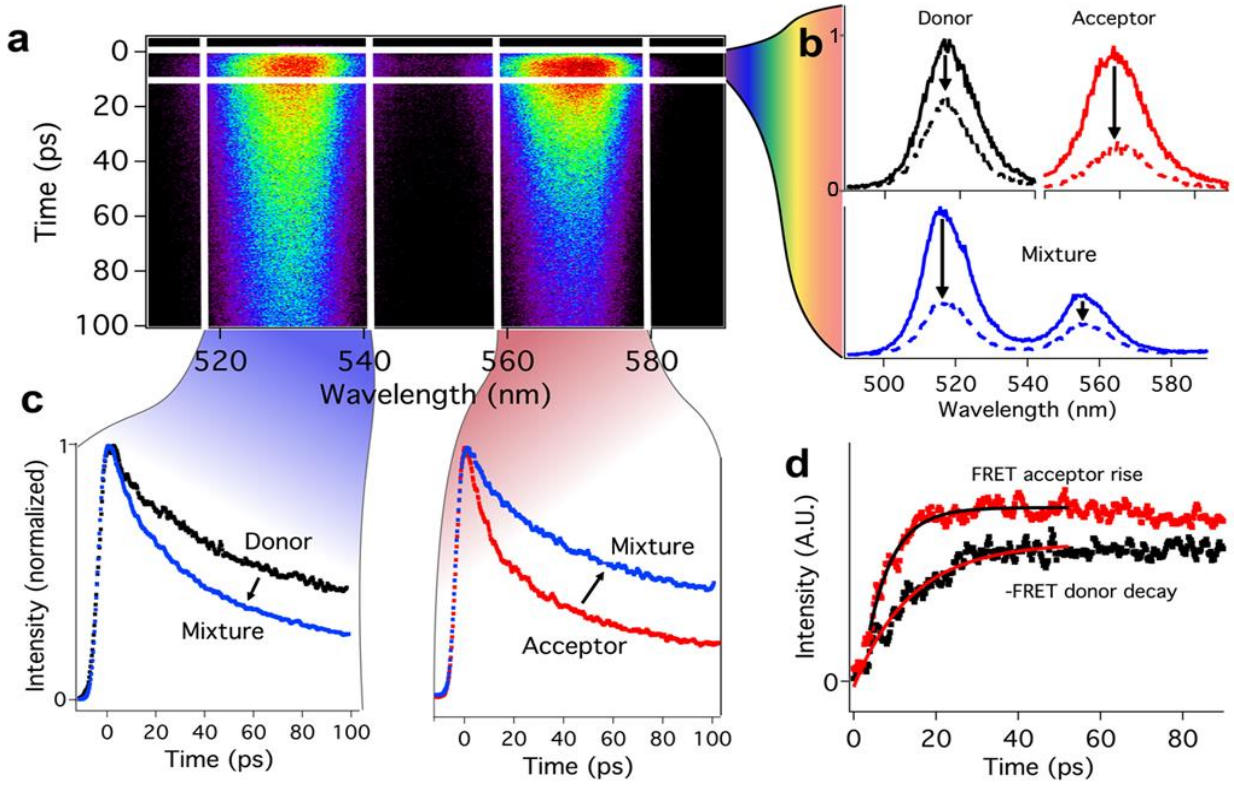

Figure 3.17. (a) Time-resolved PL of a film of a mix of CdSe 512 and 550 NPLs measured by a streak camera. (b) Integrated PL spectra of the donor, the acceptor and their mix at two different times. (c) Integrated intensity decays for the donor, the acceptor, and their mix. (d) The differenced data between a pure component and the mix for both the donor and the acceptor. Adapted with permission from ref. 69. Copyright 2015, Nature Publishing Group.

Finally, our collaborators showed that an acceptor platelet carrying an exciton can accept another exciton from a donor platelet, forming thus a biexciton. A series of fluence-dependent

PL data was measured for a pure acceptor to the start of the multiexcitonic regime. In a measurement of a mix of NPLs with the same set of fluences, higher-fluence PL decay deviated upward from lower-fluence data at early times – a signature of multiexcitons (Section 3.3). Acceptor platelets accumulated additional excitons from the donor (Figure 3.18).

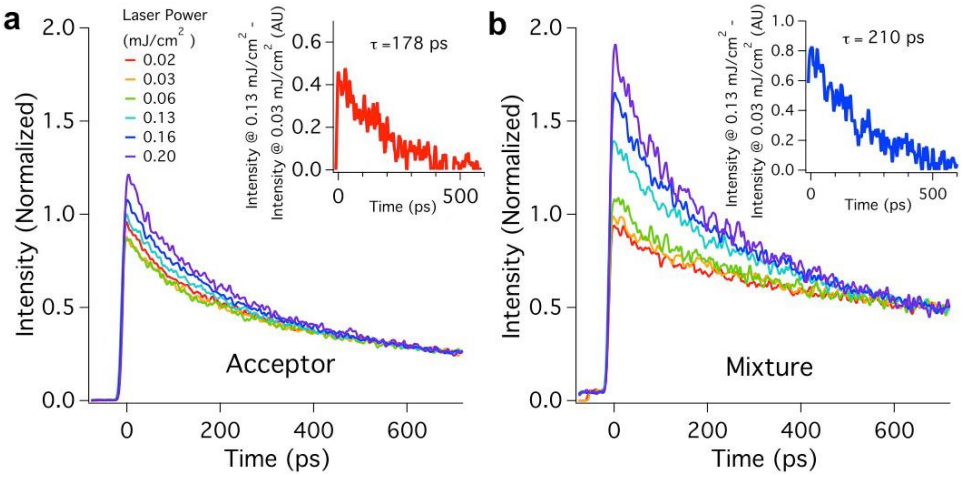

Figure 3.18. (a) A series of fluence-dependent integrated PL decay data normalized at late times for a film of pure acceptor. (b) Same for a mix of the donor and the acceptor. Adapted with permission from ref. 69. Copyright 2015, Nature Publishing Group.

3.6. Open Questions: Photoluminescence of NCs at Anti-Stokes Excitations

In our ordinary PL measurements, we excite samples to the blue of the anticipated emission peak. We shall call such excitation Stokes excitation. Dependence of the PL QY on the position of the Stokes excitation has been explored for QDs. How will the position and shape of the PL band, and the PL QY change with a shift of the excitation to the red of the emission peak (anti-Stokes excitation)? There are examples of so-called "up-conversion".[70,71,72] We measured the PL of NCs of different shapes and compositions at a number of excitation wavelengths (400 nm and anti-Stokes excitations) in Fluorolog. It was crucial to eliminate the blue double-frequency harmonic from the excitation with a long-pass filter because the absorbance of CdSe 512 NPLs, for example, at 260 nm is much higher than at 520nm, past the excitonic peak.

We observed an interesting correlation between the breadth of the PL peak and its behavior with the shift of the excitation peak. Narrow emitters (CdSe NPLs and perovskite $CsPbBr_3$ QDs) tended to retain their PL peak at the same position, whereas broad emitters shifted the PL peak with the excitation wavelength. In polydisperse samples, the anti-Stokes excitation excited primarily larger particles, causing the PL peak to shift with the excitation wavelengths. In homogeneous ensembles, the standard position of the band-edge PL was observed. The NCs used the energy of their phonons to make up for their band-gap energy.

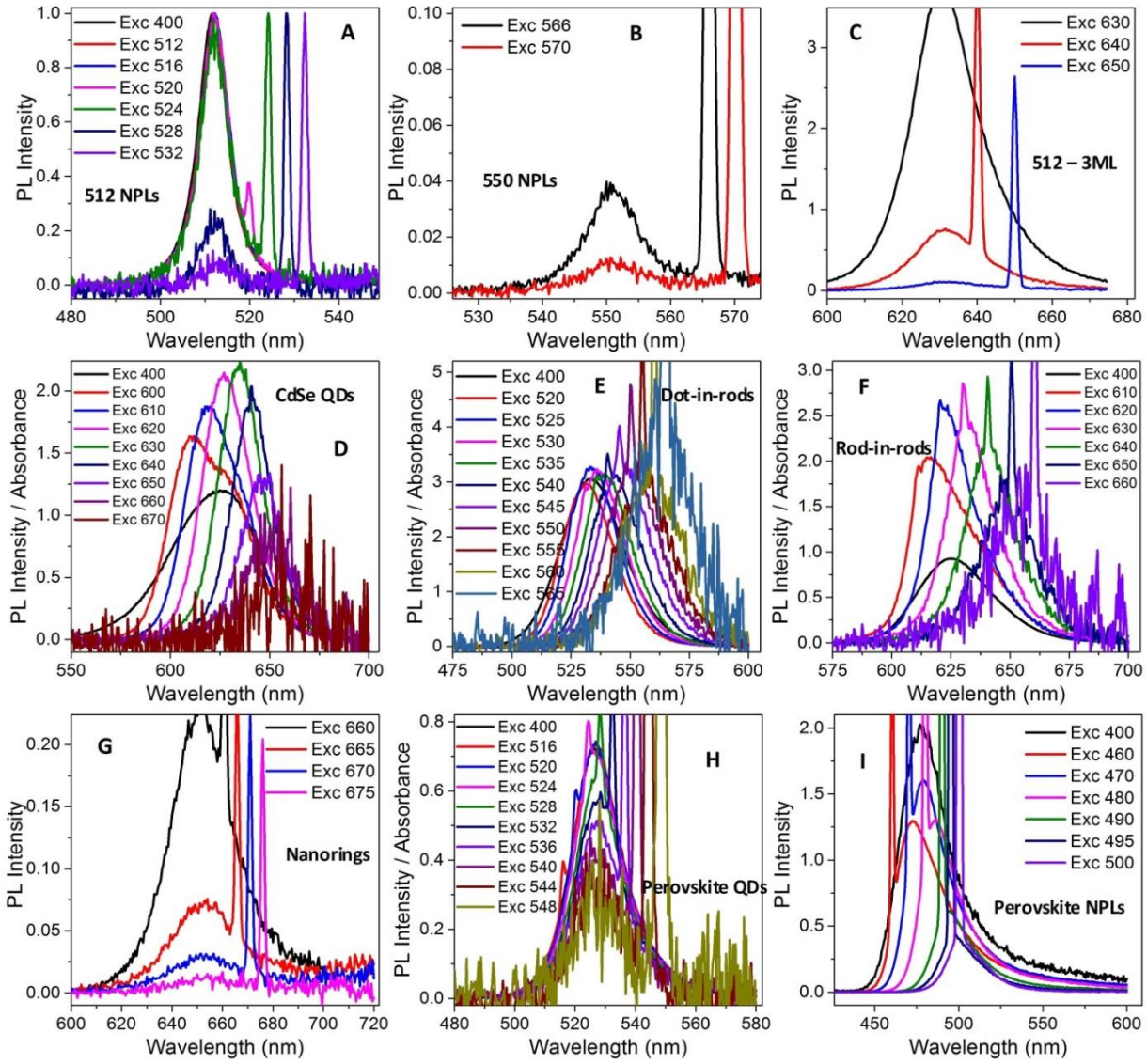

Figure 3.19. Series of PL spectra at different Stokes and anti-Stokes excitation wavelengths for (A) CdSe 512 NPLs, (B) CdSe 550 NPLs, (C) CdSe/CdS 512 – 3 ML, (D) CdSe QDs, (E) CdSe/CdS dot-in-rods, (F) CdSe/CdS rod-in-rods, (G) CdSe nanorings, (H) perovskite $CsPbBr_3$ QDs, (I) perovskite $CsPbBr_3$ NPLs. The sharp spikes show the position of the excitation.

Table 3.2. Summary of PL at anti-Stokes excitations for different systems.

Position of the PL peak	Systems	Comments
Identical for anti-Stokes and Stokes excitations.	CdSe 512 and 550 NPLs, perovskite $CsPbBr_3$.	High homogeneity of the ensemble: either high monodispersity (NPLs) or poor quantum confinement ($CsPbBr_3$).
A slight shift from blue to red excitations, stable anti-Stokes for red excitations.	CdSe/CdS NPLs.	High homogeneity as judged from PLE.
A shift with the excitation wavelength, always Stokes.	CdSe QDs, CdSe/CdS dot-in-rods, rod-in-rods, $CsPbBr_3$ NPLs.	Heterogeneity of the ensemble: high polydispersity of the NCs; only the red subpopulation is excited.

Results of measurements on another set of materials agreed with our hypothesis. The PL peak position did not shift with the excitation wavelength for perovskite formamidinium lead bromide NCs and CdSe 512 NPLs, but shifted with the excitation wavelength for commercial bright green CdSe based QDs. The latter happened likely due to the polydispersity of the sample, given the fact that the PL bands were narrower for red excitations than for 400 nm excitation.

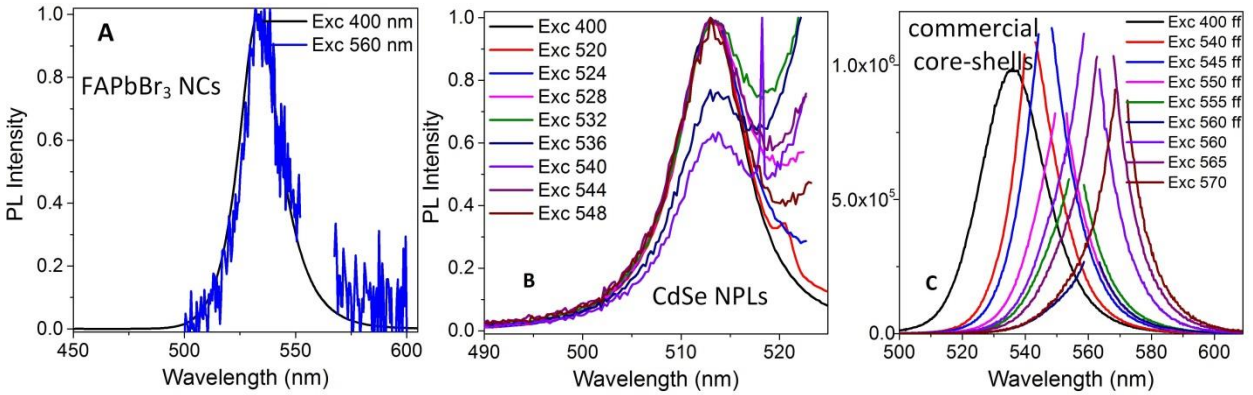

Figure 3.20. PL spectra with Stokes and anti-Stokes excitations for (A) perovskite $FAPbBr_3$, (B) CdSe 512 NPLs, and (C) commercial bright green QDs.

To eliminate a possible leak of the blue harmonic through the long-pass filter in Fluorolog, we measured a solution of CdSe 512 NPLs in a capillary under a confocal Raman

microscope using a 532 nm laser as the excitation source. We observed a PL peak at 513.6 nm and a weak trap-emission band. Interestingly, the relative intensity of the trap emission decreased with the increase of the laser power likely due to saturation of the traps.

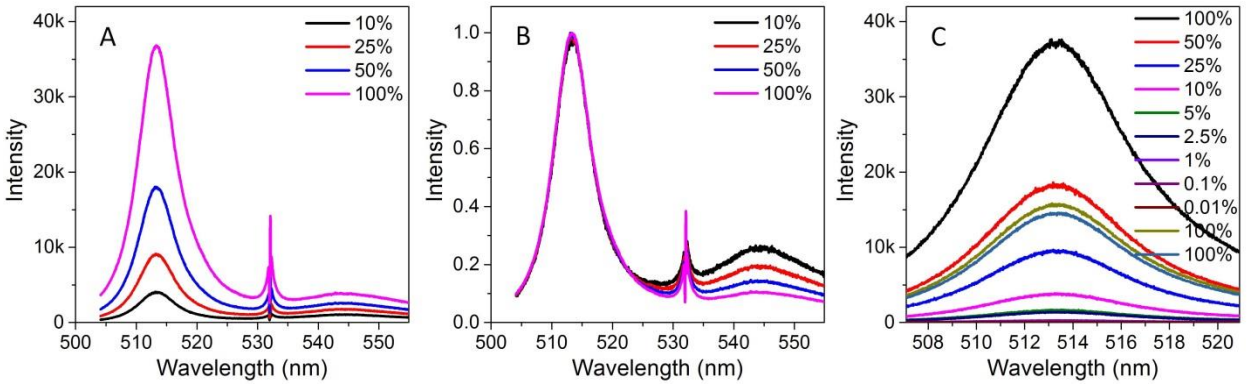

Figure 3.21. Photoluminescence of CdSe 512 NPls excited with a 532 nm laser, measured under a confocal Raman microscope. (A) PL at a series of laser powers. (B) PL data normalized by the band-edge peak. (C) PL data resolved with a high-resolution grating.

Observation of PL with anti-Stokes emission raises a question on the role of phonons in assisting such PL and the possibility of laser cooling of colloidal solutions of such materials. Assuming that every non-radiative recombination turns into heat, from a pure conservation of energy, to observe a net laser cooling of a sample, we must achieve a PL QY of at least $\lambda_{em}/\lambda_{exc}$.[73] In the case of a 532 nm excitation of CdSe 512 NPls, we will need a PLQY of 96.3%, for example, and no polydispersity in the sample. The reason net laser cooling has been demonstrated only for individual microparticles is that the above requirements for ensembles are very harsh. Nevertheless, increase in PL QY with the decrease of temperature in homogeneous ensembles of CdSe NPLs gives us an opportunity to demonstrate laser cooling in them.[74,75]

3.7. Summary and Outlook

We demonstrated a record-low threshold of ASE, 8 $\mu J/cm^2$, in films of CdSe/CdS NPLs. The system had a high saturation fluence (two orders of magnitude higher than the threshold), a high modal gain of 600 cm^{-1}, and a gain lifetime of 140 ps. From the average absorbed energy per NPL, it followed that was biexcitonic. Suppressed Auger recombination, likely due to extended lateral dimensions of NPLs, allowed for the superior performance of the system. We also demonstrated a low-threshold ASE in films of CdSe 462, 512, and 550 NPLs. In a cavity between two parallel mirrors, we demonstrated laser action from films of CdSe and CdSe/CdS NPLs. Interestingly, we demonstrated lasing at 575 nm – a wavelength gap in commercial lasers.

To build lasers from our materials, we will need to improve gain lifetime in them. One way to achieve it is to improve PL QY and stability of the material by encapsulating the MPLs in matrices of wide-bandgap materials, *e.g.*, titania. As an ambitious goal, an electrically pumped laser will be highly desired.

Our collaborators showed a fast energy transfer (10 – 15 ps) from CdSe 512 to CdSe 550 NPLs in heterostacks thereof. This high rate was attributed to the spectral overlap between the donor and the acceptor.

Finally, we observed a qualitative difference in the PL of different classes of materials under anti-Stokes excitation. In CdSe and CdSe/CdS NPLs, and perovskite $MPbBr_3$ (M = Cs, FA) NCs, the position of the PL band was independent of the excitation wavelength. These materials must make up for the bandgap energy with their internal energy (phonons). Therefore, these NCs are candidates for laser cooling in colloidal solutions.

3.8. Experimental Details

Film deposition. We rinsed glass substrates for film deposition with ethanol and blew them off. We precipitated colloidal solutions of CdSe/CdS NPLs of the standard concentration with ethanol (NPLs : EtOH = 4:1, v/v), making sure the supernatant is clear after the precipitation. We re-dispersed the precipitate in quarter of their original volume of hexane-octane (4:1, v/v), and filtered them through 0.2 μm PFTE membrane filters. We spread a variable volume of the solution (30 to 50 μL per cm^2), let it concentrate for 10 – 30 s, and span the substrate at 2000 rpm to make a uniform film.

Measurements of ASE were performed on set-ups built by Dr. Chunxing She and Dr. Peter Dahlberg in the laboratory of Prof. Gregory Engel. ASE, lasing, transient absorption, and streak camera measurements were performed by C. She on set-ups built by Dr. Richard Schaller at Argonne National Laboratory. The HRTEM image of the NPL was collected by Dr. Arnaud Demortière.

CHAPTER FOUR

COLLOIDAL CADMIUM SELENIDE QUANTUM RINGS

Cadmium selenide is an important model system in the field of nanoscale semiconductors. Generations of synthetic protocols have evolved to afford colloidal crystalline luminescent CdSe QDs, NPLs of controlled thickness and lateral dimensions, and NRs (NRs) of controlled diameter and aspect ratio. Precise control over the shape and dimensions of quantum-confined semiconductors gives rise to materials with desired optical properties (energy, bandwidth, and polarization of the PL, for example). One underrepresented topology for semiconductor NCs is quantum rings. Epitaxially grown toroidal InAs/GaAs NCs are interesting because they exhibit a variation in the allowedness of interband electronic transitions with the increase of the magnetic field penetrating the ring. A colloidal synthesis will be a cheaper, more scalable, and more reliable route toward semiconductor nanorings than epitaxy. Because of the challenging synthetic design, the toroidal topology is underrepresented among colloidal semiconductor NCs. Limited number of examples of colloidal nanorings include (1) rectangular nanorings of PbSe NCs *via* oriented attachment with quantum confinement in the thickness,[76] (2) perforated hexagonal-prismatic (nut-shaped) $CuInSe_2$ NCs,[77] (3) prolate nanorings of ZnSe with some effect of the topology on the electronic structure,[78] (4) colloidal nanorings of CdSe obtained by etching the cores of CdS/CdSe with hydrogen peroxide.[79] We report a synthesis of CdSe nanorings by a controlled etching of NPL faces.

4.1. Perforation of CdSe NPLs

X. Peng *et al.* reported an elegant way to raise the PL QY in CdSe QDs to unity.[80] The first step there was a treatment of CdSe QDs with Se in oleylamine at 140^{o}C. When we applied the same recipe to CdSe NPLs, we observed a subpopulation of perforated NPLs in TEM. The outcome, however, was sensitive to the experimental conditions: the initial sample of the NPLs, the amount of Se and the number of injections, the duration of the treatment, and the temperature of the treatment. In the optimized synthesis of toroidal nanorings, we precipitated an aliquot of a stock hexane solution CdSe 512 NPLs with ethanol twice. After the second precipitation and drying, the precipitated weighed 7.8 mg. We dispersed the precipitate into 3 ml ODE and 1 ml OAm in a three-necked flask. An easy way to do so was to disperse the NPLs in a small volume (50 μl) of MCH, dissolve the solution into the ODE and OAm, and heat the contents at 80^{o}C under nitrogen for 10 min to evaporate the MCH. We sonicated 7.9 mg Se in 1 ml OAm and added 0.2 ml of the resulting suspension into the flask. Then we degassed the contents of the flask at the room temperature for 10 min, heated them up to 140^{o}C under nitrogen and kept at this temperature for 10 min. Next, we injected 0.2 ml TBP, increased the temperature to 220^{o}C, removed the heat mantle, and allowed the solution to cool down to the room temperature. At 37^{o}C we added 10 mg of finely ground Cd formate and stirred the mixture for an hour.

The ratio of the amounts of the NPLs and Se is important. Absorption spectroscopy is a convenient way to estimate the amount of the NPLs. When a stock solution of the NPLs, diluted by a factor of 300, had absorbance of 0.2 at the first excitonic peak in a 1 cm cuvette, we used 1 ml of such stock solution for the perforation. During the ten-minute period at 140^{o}C, the color of the solution darkened and turned dark brownish-red. If the solution was red (the absorption

spectrum of an aliquot was clear past 600 nm), we made another 0.2 ml injection of Se/TBP and tracked time from the last injection.

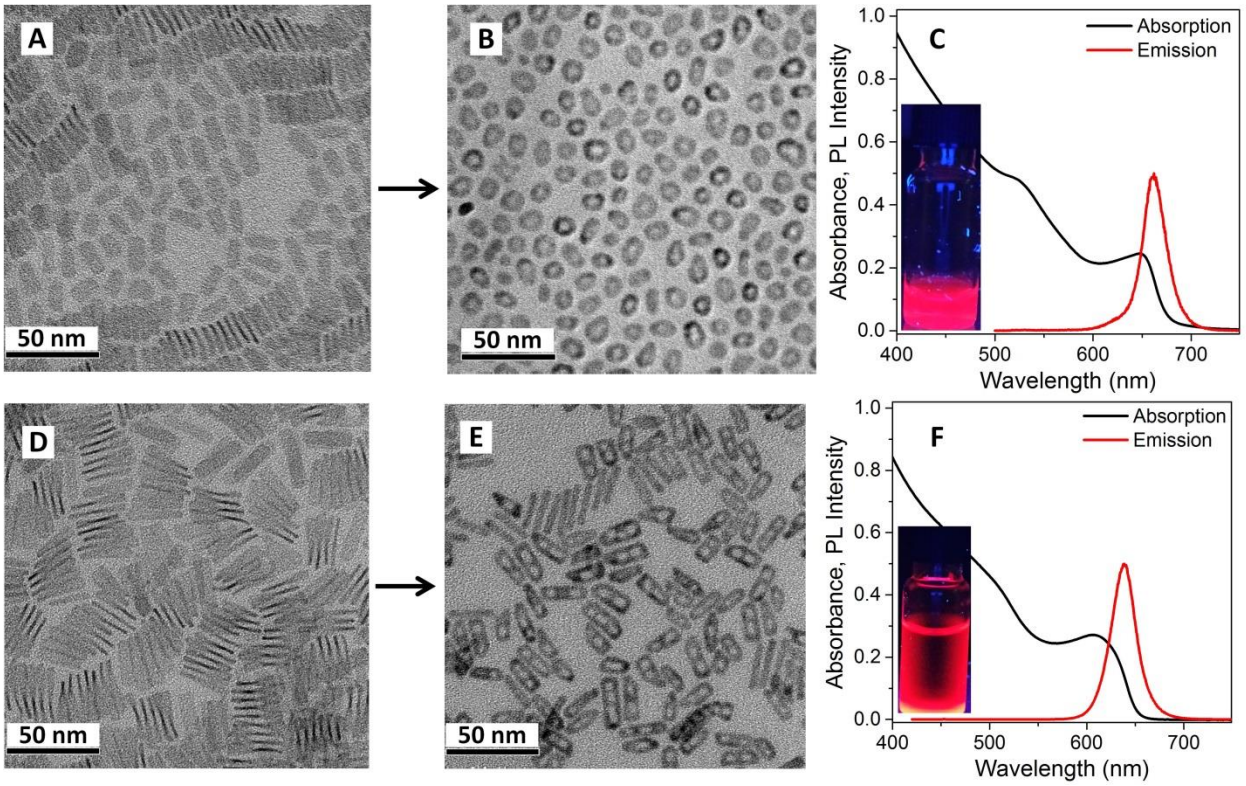

Figure 4.1. Perforation of CdSe NPLs. (A) TEM image of original intermediate-length NPLs used for perforation. (B) TEM image of the resulting nanorings. (C) Absorption and PL spectra of a colloidal solution of the nanorings. Inset is a photograph of the PL of the nanorings. (E) TEM image of original long NPLs used for perforation. (F) TEM image of the resulting double rings. (G) Absorption and PL spectra of a colloidal solution of the perforated NPLs. Inset is a photograph of the PL of double rings. Adapted with permission from ref. 85. Copyright 2016, American Chemical Society.

The nanorings showed clear excitonic peaks in the absorption spectra; their PL spectrum peaked at 661 nm with FWHM of 78 meV and the QY of 25% right after the synthesis (Figure 4.1C). Longer 512 NPLs transformed into double (and triple) rings upon the same treatment (Figure 4.1E). The PL of double rings peaked at 637 nm (fwhm = 91 meV), and the initial QY reached 50% (Figure 4.1F). For both nanorings and perforated NPLs, PLE spectra showed a homogeneous broadening in the red half of the PL spectrum and a moderate heterogeneous

broadening in the blue half of the PL spectrum (Figure 4.2A–B). PL anisotropy increased from 0.004 in zb-CdSe QDs undergone the treatment with Se powder and Cd formate to 0.04 in toroidal nanorings, and finally to 0.10 – 0.12 in perforated NPLs. (Figure 4.2C) Such increase agrees with the growing anisotropy of the particles. Whereas transition dipole moment can point in any direction in a spherical QD, it is confined to planes close to the plane of a nanoring, and is likely to lie in the plane of a perforated NPL.

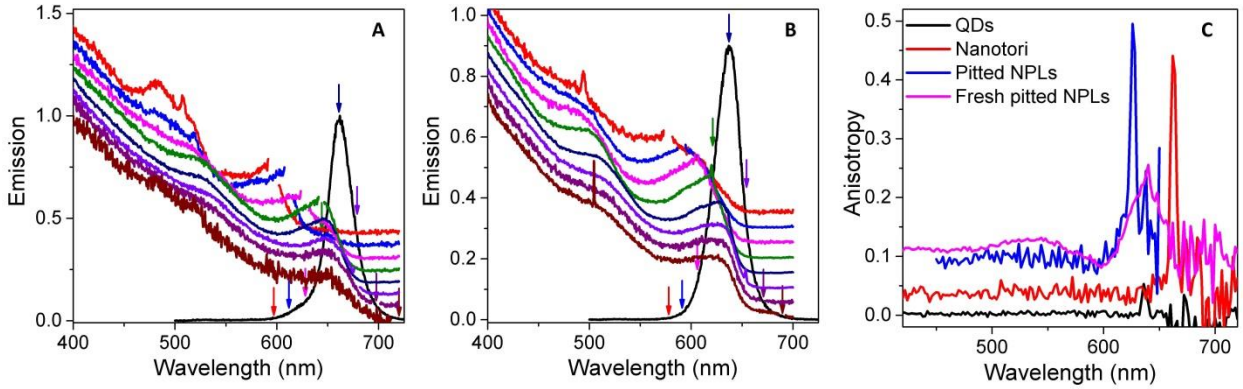

Figure 4.2. (A) PLE spectra of CdSe nanorings. (B) PLE spectra of CdSe perforated NPLs. (C) PL anisotropy of CdSe QDs, nanorings, and perforated NPLs.

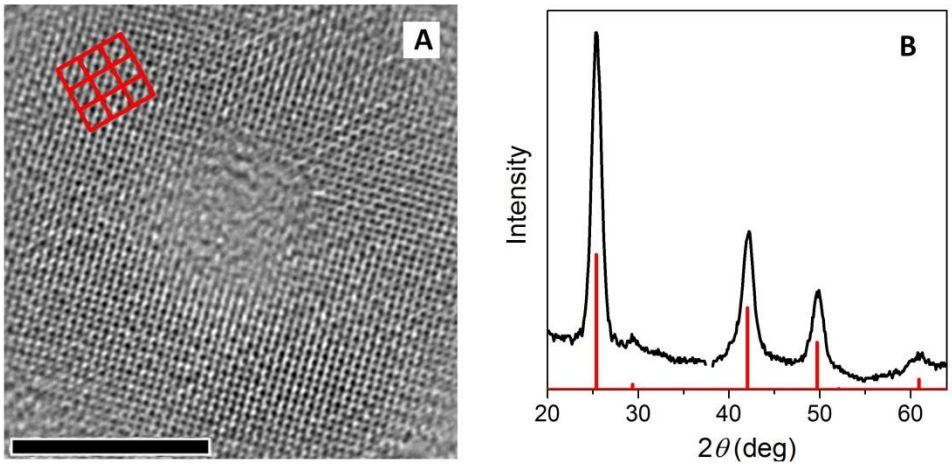

Figure 4.3. (A) HRTEM image of a CdSe nanoring. The scale bar indicates 5 nm. The red grid shows 3×3 unit cells of zincblende. (B) Powder X-ray diffraction pattern of a film of CdSe nanorings. Adapted with permission from ref. 85. Copyright 2016, American Chemical Society.

Nanorings preserved the zinclblende crystal structure of the maternal NPLs (Figure 4.3B). HRTEM clearly resolves lattice planes of zincblende (Figure 4.3A). From a square of 10×10 unit cells around the ring, we measured the lattice constant to be 6.0 – 6.1 Å, which agreed with the reported values of 6.05 – 6.08 Å for zb-CdSe.

4.2. Understanding the Mechanism of Perforation

The next step was to understand the chemical processes involved in the perforation. In blank experiments, we observed that selenium without OAm did not perforate NPLs, nor did OAm and TBP without Se. According to J. Owen *et al.*,[43] elemental Se transforms primary amines into selenoamides according to $RCH_2NH_2 + Se \rightarrow RC(Se)NH_2 + H_2Se$. To bring chemical rigor into the procedure, we performed an experiment with thioacetamide, $CH_3C(S)NH_2$, which resulted in perforation. OAm was still necessary for the perforation.

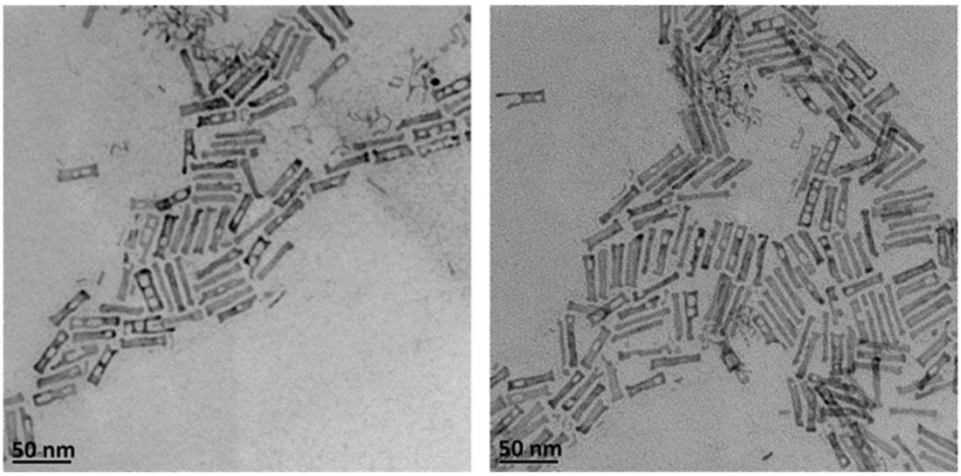

Figure 4.4. Examples of CdSe 512 NPLs perforated with thioacetamide at 140^{o}C.

Next, our goal was to track the perforation with selenium and OAm. We took aliquots of the mixture as the reaction progressed at 140^{o}C and after the injection of TBP as the system was heated up to 220^{o}C. The perforation had not begun before the temperature reached 140^{o}C. After the first minute, Se grew crowns around NPLs. At the fourth minute the NPLs were in the middle

of the perforation, which was nearly over at the end of the eighth minute. No visible change of the nanostructures (both in absorption spectra and not shown here TEM) happened after the injection of TBP at 10 min and heating the system to 220^{o}C, likely due to lowering Se reactivity by forming TBPSe.

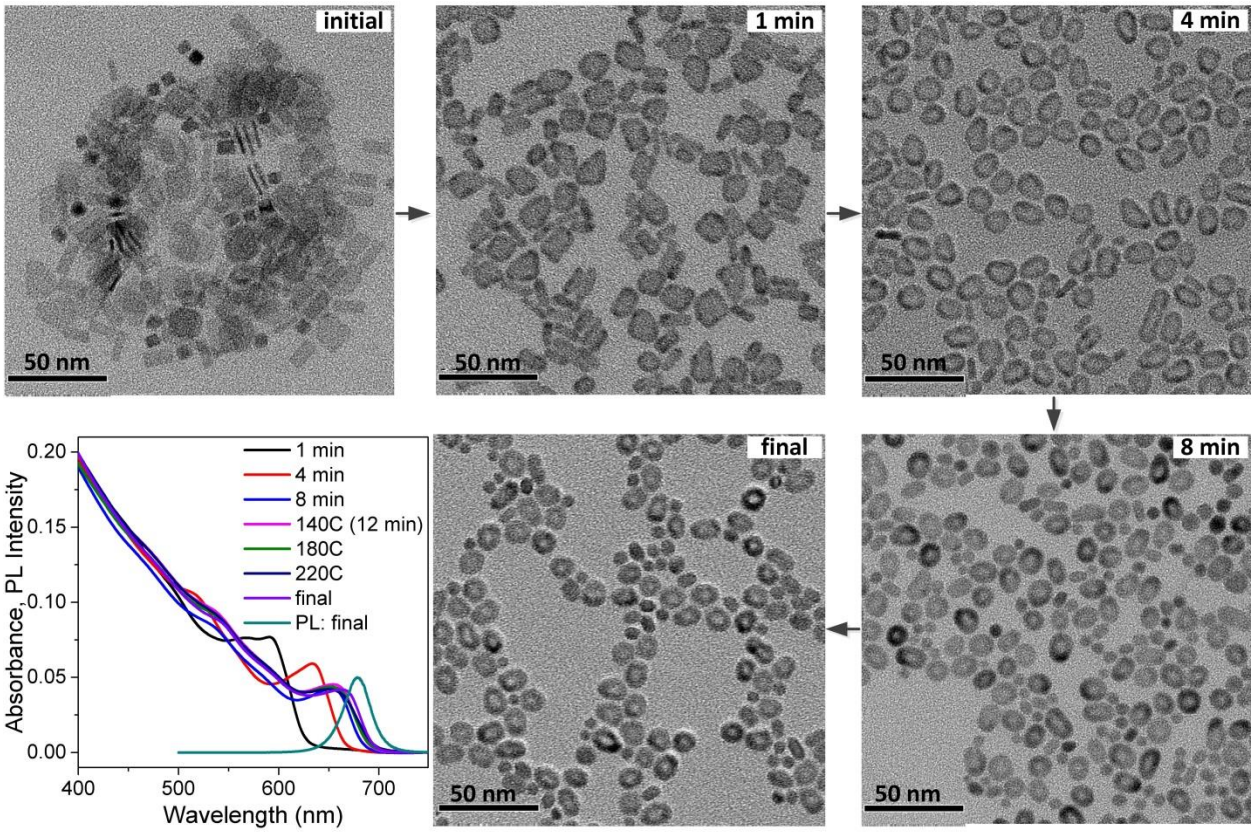

Figure 4.5. TEM images spectra of aliquots taken in a typical treatment. The labels indicate the time elapsed at 140^{o}C.

In the case of a lack of Se, perforated NPLs are transient between the second and the sixth minutes. They collapse into dumbbell-like structures by the tenth minute. Selenium begins to dissolve in ODE at 120 – 130^{o}C, which sets 140^{o}C close to the lower boundary for the perforation reaction. We attempted several reactions at higher temperatures (150^{o}C and 160^{o}C) and observed issues with run-to-run reproducibility of the ring formation.

Section 2.1 describes the surfaces of CdSe 512 NPLs. Briefly, the faces are Cd-terminated (001) facets, where every Cd atom has two bonds with the crystal and two broken bond, one of which must be passivated with an X-type ligand. The side facets are perpendicular to the [110] direction: either true (-1-10) facets, perpendicular to the faces, or a combination of Cd-rich (111) facets and Se-rich (11-1) facets. In either case, every surface atom makes three bonds with the crystal and has one dangling bond.

We propose the following mechanism of the counterintuitive[81] perforation. First, oleylselenoamide deposits a layer of Se on the side facets of a NPL, forming a rim of Se. We observed such structures in TEM of an aliquot taken after 1 min at 140^{o}C, and this hypothesis is consistent with the synthesis of CdSe/CdS[82], CdSe/CdTe[83], and CdS/CdSe[84] core-crown NPLs under somewhat similar experimental conditions. Next, we hypothesize that, at 140^{o}C, in the presence or absence of Se, molecules of CdX_2 depart from the surface, forming a complex with oleylamine (L).

$$[CdSe]_{4m}[CdX_2]_m + 2\ L \leftrightarrow [CdSe]_{4m}[CdX_2]_{m-1} + CdX_2L_2$$

We do not observe such behavior in syntheses of NPLs because excess cadmium precursor shifts the equilibrium left and there is no amine in the system to stabilize CdX_2 in ODE. Removing one Cd from a (001) facet implies breaking two Cd – Se bonds, but removing a Cd atom from a side (110) or (111) facet implies breaking three Cd – Se bonds. Therefore, side facets are more susceptible to growth but less susceptible to dissolution than faces in CdSe NPLs. A released CdX_2L_2 molecule can either land back at the desorption site or land at the side of the NPL. Even if the two affinities are equal, the sides have a much larger area. Therefore, the law of mass action will drive cadmium from the face to the edges, growing a layer of cadmium over the rim of selenium.

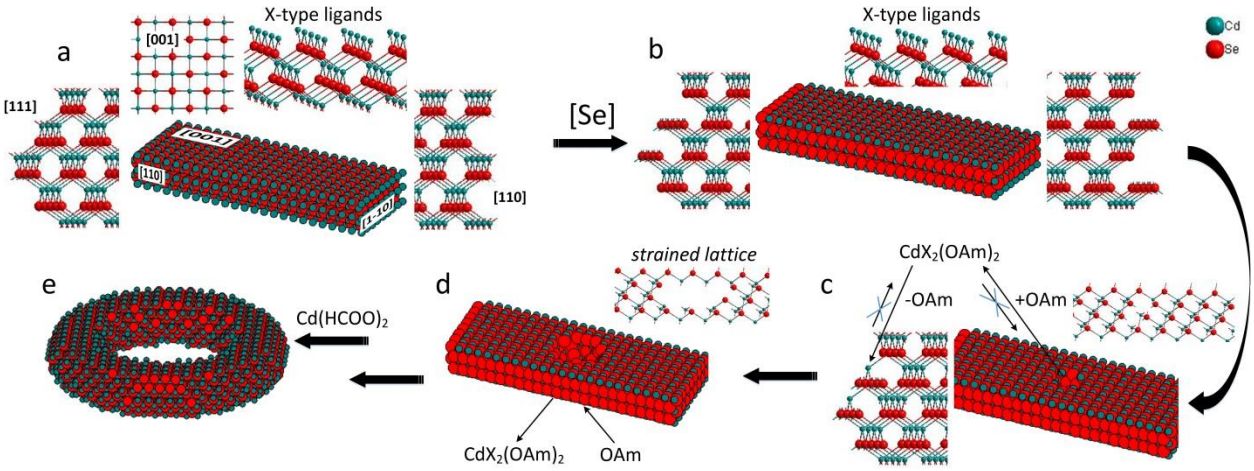

Figure 4.6. Proposed mechanism of the transformation of CdSe NPLs into nanorings. (a) Initial CdSe NPL is a thin slab of zb-CdSe lattice terminated by (001) top and bottom facets and side facets represented by either (110)- or (111)-type facets. The atomic structure of the corresponding surfaces is shown. (b) Treated with a Se precursor, the side facets get Se-terminated while the top and bottom facets remain Cd-terminated and ligated by X-type ligands. (c) Cd atoms can depart (001) facet via the Z-type ligand displacement reaction promoted by an L-type ligand oleylamine. The removed Cd atoms can deposit at the side facets. (d) The etch-pit developed in CdSe NPL generates strain that distorts crystal lattice and may activate the etching of the bottom facet. (e) Final CdSe nanoring. Adapted with permission from ref. 85. Copyright 2016, American Chemical Society.

The removal of CdX_2L_2 leaves neighboring Cd and Se atoms unsaturated, destabilizing the structure locally and making it susceptible to further etching and developing an etch pit. CdSe units, stabilized by amine, can depart the site and land at the edge, forming a cavity behind. Development of the cavity causes a strain in the lattice and makes atoms on the opposite face prone to desorption. A pit develops and grows into a bigger hole. Eventually, the structure transforms into a toroidal particle. If the initial NPL has a large face area, formation of two or more pits may run in parallel. Further studies will be necessary to confirm the mechanism.

4.3. Growth of CdS and $Cd_{1-x}Zn_xS$ Shells over CdSe Nanorings and Double Rings

With help of *c*-ALD, a mild shell-growth technique, we deposited 3 MLs of $Cd_{1-x}Zn_xS$ over nanorings and 2 MLs over double rings. We introduced Cd only in the first monolayer, Cd

and Zn (7:3) in the second monolayer, and for single rings only, Cd:Zn (1:1) in the third monolayer. There was a red shift in UV-Vis and PL spectra compared to the parent core structures. The PL of single-ring core-shells peaked at 685 nm (fwhm = 66 nm).

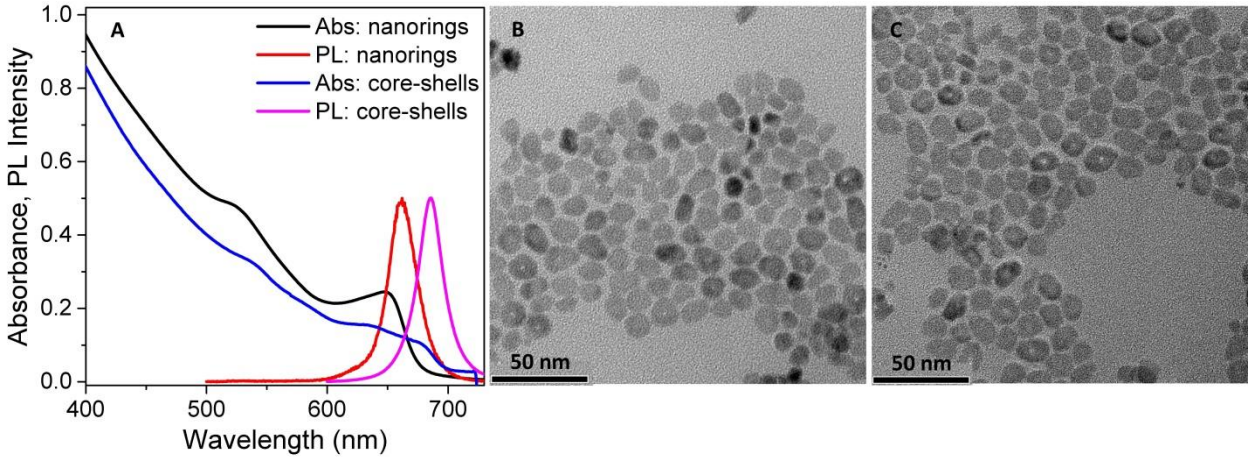

Figure 4.7. UV-Vis and PL spectra, and TEM images of CdSe nanorings with 3 MLs of $Cd_{1-x}Zn_xS$ shells. Adapted with permission from ref. 85. Copyright 2016, American Chemical Society.

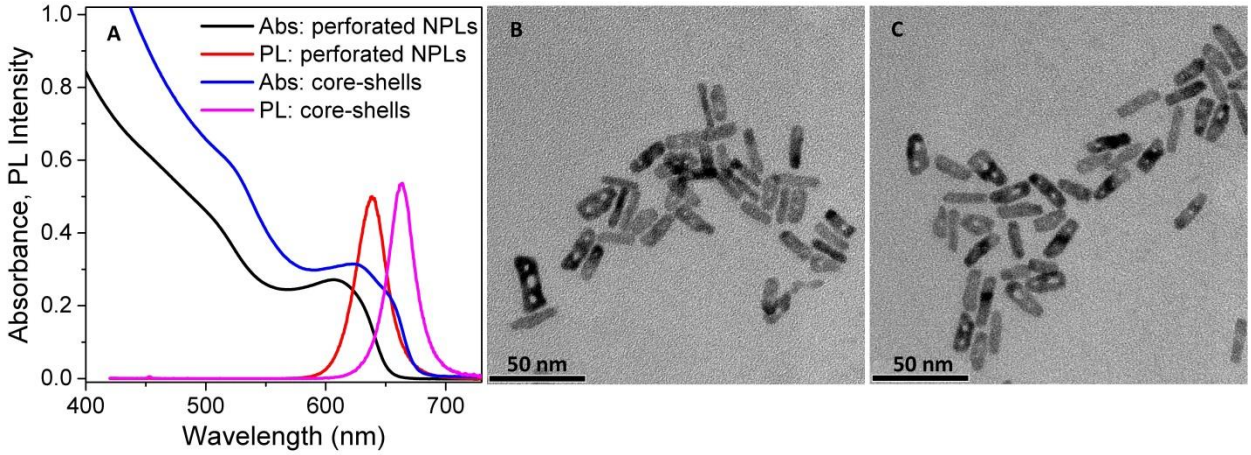

Figure 4.8. UV-Vis and PL spectra, and TEM images of CdSe double nanorings with 2 MLs of $Cd_{1-x}Zn_xS$ shells. Adapted with permission from ref. 85. Copyright 2016, American Chemical Society.

The resulting core-shell structures have a high crystallinity.

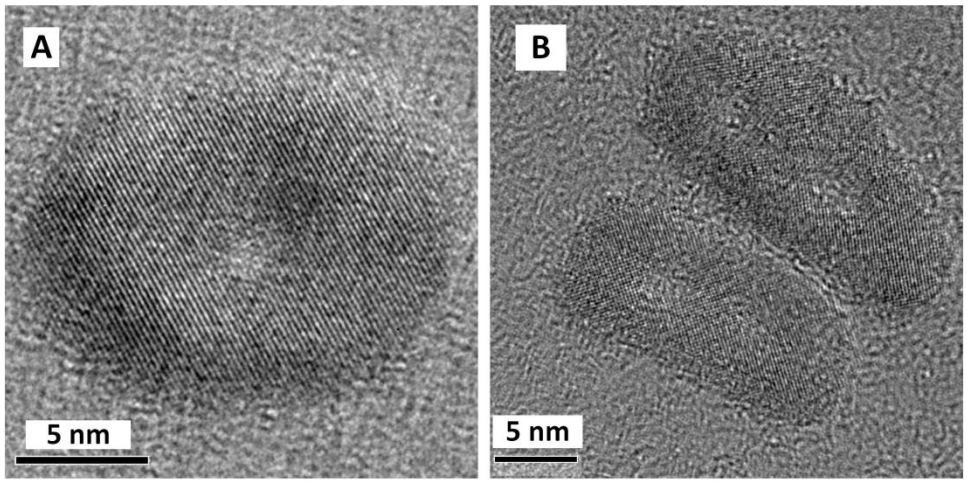

Figure 4.9. (A) HRTEM image of an individual CdSe/$Cd_{1-x}Zn_xS$ nanoring. (B) HRTEM image of an individual CdSe/$Cd_{1-x}Zn_xS$ double rings. Adapted with permission from ref. 85. Copyright 2016, American Chemical Society.

4.4. Miscellaneous

The perforation applies to other cadmium chalcogenide NPLs. CdS and CdTe NPLs, like CdSe 462 NPLs, have large lateral dimensions and are sheet-like structures. Se powder introduced to CdS 386 NPLs[49] created holes that grew and caused some NPLs to tear into stripe-like fragments. CdTe 500 NPLs behaved similarly (Figure 5.10). Quantum rings of other semiconductors, *e.g.*, Cu_2Se, Ag_2Se, can be synthesized from CdSe *via* cation exchange.

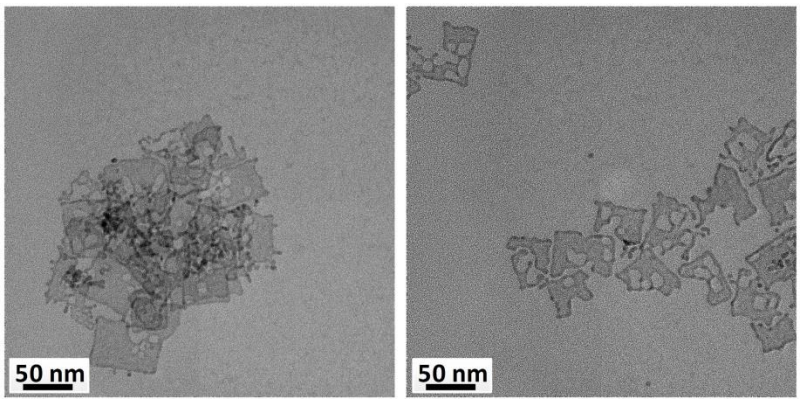

Figure 4.10. TEM images of perforated CdTe 500 NPLs.

CdSe double rings are the first example of semiconductor double rings, colloidal or epitaxial. It is not only the geometry but also the topology that influences electronic properties of the material.[86,87] QDs, NRs, NPLs, and their core-shells are topologically equivalent to polyhedra and have a topological genus (maximum number of cuts without rendering disintegration), $g = 0$, and the Euler characteristic (for convex polyhedra: $V - E + F$), $\chi = 2$.[88] For quantum rings, $g = 1$ and $\chi = 0$; for double rings, $g = 2$ and $\chi = -2$. Senyuk *et al.* described nontrivial behavior of topological colloids (rings and double rings) in a nematic liquid crystal, leading to topological defects and new memory effects in the liquid crystals,[89] calling for new explorations of topology-determined colloidal phenomena.

There are other potential interesting properties of semiconductor quantum rings. Epitaxially grown InAs/GaAs nanorings demonstrated a stepwise translation of the angular momentum quantum number, l, from zero to higher values, and as a result, oscillations of the bandgap with an increasing magnetic field perpendicular to the ring.[90,91,92] The system oscillated between bright ($l_e = 0$, $l_h = 0$; $l_e = -1$, $l_h = +1$; *etc.*) and dark ($l_e = 0$, $l_h = +1$; $l_e = -1$, $l_h = +2$, *etc.*) excitons[93] — an optical manifestation of the Aharonov–Bohm effect.[94] Given the radius of our rings, it will require a magnetic field of 50 T to change l by 1. If we generate, for example, a pentaexciton in a nanoring the minimum required magnetic field will drop by a factor of 5 to an accessible value of 10 T.[95]

CHAPTER FIVE

SEMICONDUCTOR NANOCRYSTALS FOR FIELD-EFFECT TRANSISTORS

Field-effect transistors (FETs) are a convenient model system to probe charge transport in granular semiconductor solids. They are more forgiving than solar cells or light-emitting diodes, and their operation relies only on one carrier type (the electron or the hole) at a time. This model system is suitable for studying the effect of inorganic ligands on the electronic properties of semiconductor NCs in solids.

Currently, II – VI and III – V semiconductors are complementary in the bulk and the nanocrystalline phase. CdSe QDs are the most studied and best understood system in semiconductor NCs. Syntheses produce homogeneous ensembles of CdSe emitters. CdSe QDs capped with composition-matched ligands sinter into solids that show carrier mobility up to 1/3 of the bulk values. Quantum confinement in HgE (E = Se, Te) opens up a tunable bandgap and enables their use in IR materials. Quantum-dot displays of CdSe/$Cd_{1-x}Zn_xS$ NCs are available for purchase. Bulk III – V semiconductors, on the other hand, have superior electronic properties (low carrier effective mass and high carrier mobility) in the bulk, but have not opened up their potential in the nanocrystalline state. Syntheses often produce polydisperse batches of QDs (InP) or are challenging at all (GaAs, InSb). Higher covalency tolerates crystal defects better, which impair electronic properties. Poor surface passivation leads to lower PL QY. Absence of sintering upon annealing means carrier hopping will be the only transport mechanism in annealed films of solution-processed InP or InAs.

Improving crystallinity, elimination of defects, and surface passivation with electron-rich ligands should improve transport of electrons in arrays of III – V QDs. We plan to probe the electron in such arrays of InP QDs by fabricating *n*-type FETs thereof.

5.1. Synthesis of InP and InAs QDs

5.1.1. Synthesis of the Micic InP and InAs QDs

One of the first recipes for InP was proposed by O. Micic and A. Nozik in 1994.[3] The synthesis is based on a reaction of indium chloride or carboxylates with *tris*(trimethylsilyl)phosphine (TMS_3P). The reaction is driven by a high tendency of silicon to chlorine or oxygen. We used a slightly modified recipe, where we dissolved 4.66 mmol $InCl_3$ and 2.33 mmol TOPO in excess TOP, degassed the solution at 80°C, and injected 3.00 mmol TMS_3P under vacuum. We ramped up the temperature to 270°C. The system slowly changed colors to yellow, orange, red, dark red, and black. We allowed the QDs to grow for 16 hours.

$$m\ InCl_3 + m\ TMS_3P + l\ TOPO \rightarrow [InP]_m(TOPO)_l + 3m\ TMSCl \uparrow$$

Chemistry is less defined for InP than CdSe. The only ligand there to sterically stabilize InP is an L-type ligand TOPO, coordinating to surface indium with oxygen. Given no excess X-type ligands, the NCs must be stoichiometric, which necessarily implies there are phosphorus atoms at the surface. Uncoordinated non-metal atoms at the surface carry lone pairs of electrons and are hole traps, which impairs the PL of the NCs. Additionally, non-metal-rich surfaces make ligand exchange with anionic ligands impossible. One can passivate non-metal surface atoms with Lewis-acidic species like $AlCl_3$, but the latter will be aggressive to ligands capping metal sites. Side reactions can occur in the synthesis of InP; TOP can be a source of phosphorus at high temperatures, making the surface terminated with dialkylphosphide.

$$[InP]_m + n\ InCl_3 + 3n\ Oct_3P \rightarrow [InP]_m[In(POct_2)_3]_n + 3n\ OctCl$$

Two octyl groups originate from a surface P atom, which is a part of the crystal structure. Such NCs are P-rich and possess the problems discussed above.

The synthesis yielded a polydisperse batch of non-luminescent InP QDs. Size-selective precipitation produced 20 fractions with reasonable excitonic features (Figure 5.1A).

We synthesized InAs from $InCl_3$ and home-made TMS_3As. To synthesize the latter, we first prepared $(Na/K)_3As$ from the elements in dimethoxyethane over 24 hr. After that, we added TMSCl to the reaction mixture and refluxed the suspension for another 16 hr. The suspension changed color from black to brown to orange. After removing the precipitate and DME, we isolated TMS_3As from the reaction mixture by a distillation in vacuum.

$$(Na/K)_3As + 3\ TMSCl \rightarrow TMS_3As + 3\ (Na/K)Cl$$

To synthesize InAs, we dissolved $InCl_3$ and TMS_3As in room-temperature TOP. The resulting solution turned orange. Then we did 3 injections of the reaction mixture into hot (270^oC) pre-degassed TOP. QDs of InAs grew over a few hours.

$$m\ InCl_3 + m\ TMS_3As + l\ TOP \rightarrow [InAs]_m(TOP)_l + 3m\ TMSCl \uparrow$$

Size selection of the resulting polydisperse ensemble yielded 20 fractions with a decent excitonic resolution (Figure 5.1B).

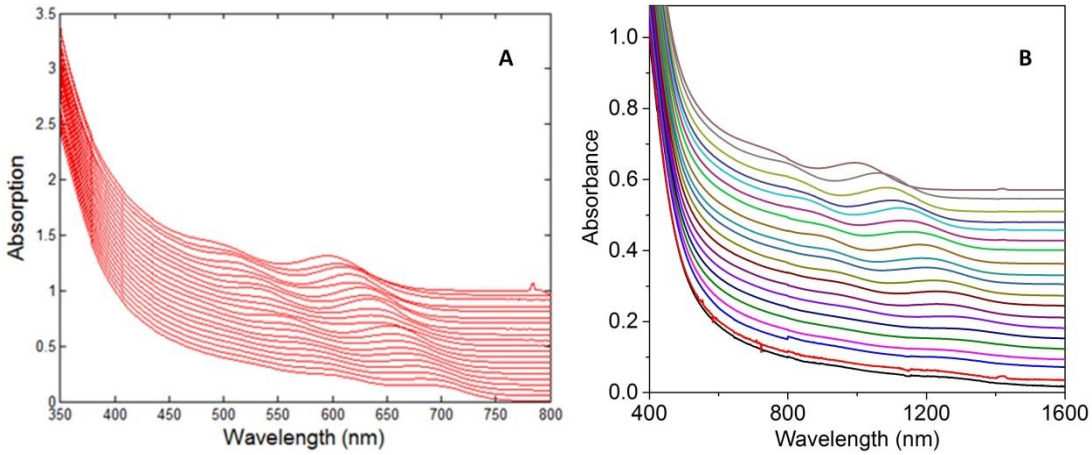

Figure 5.1. (A) Absorption spectra of 21 size-selected fractions of one batch of the Micic InP QDs. (B) Absorption spectra of 20 size-selected fractions of one batch of InAs QDs. The spectra are shifted vertically for clarity.

It turned out that size-selection into 20 fractions was unnecessary for a good size distribution. We optimized the procedure to obtain 5 fractions of comparable amounts of InP with a decent size distribution (Figure 5.2). Experimental details are in Section 5.7.

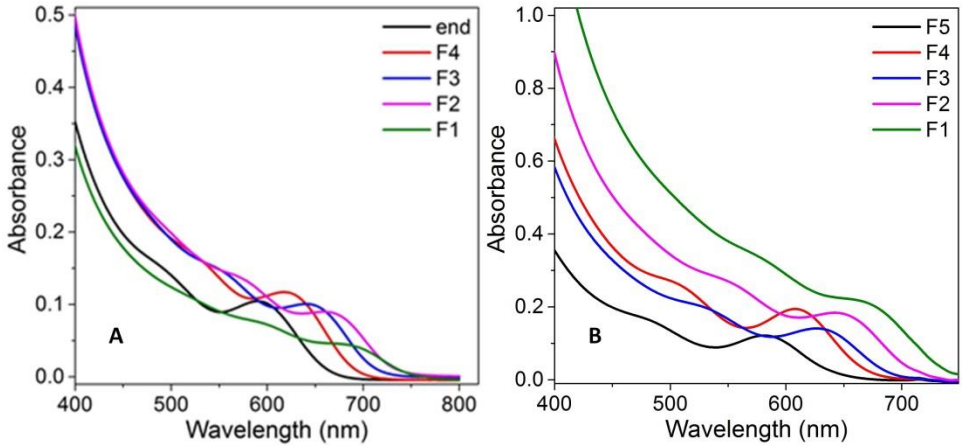

Figure 5.2. Size-selection of two batches of the Micic InP into five fractions each. Equal aliquots were taken for each absorption spectrum.

5.1.2. Synthesis of the Peng InP

Poor surface passivation, absence of PL, and polydispersity of as-synthesized the Micic InP QDs prompted the community to use precursors capable of producing well-passivated

indium-rich InP QDs. Carboxylates are an example of such precursors. In 2007, X. Peng developed a recipe for InP from indium acetate, myristic acid, and TMS_3P in ODE.[96] Our goal was to optimize the recipe to obtain large QDs, desired for electronics. We combined 0.4 mmol $In(OAc)_3$, 1.54 mmol myristic acid, and 5 ml ODE the mixture to 188°C under nitrogen flow without prior evacuation. Eventually the suspension turned into a transparent yellowish solution indicating a possible completion of the metathesis reaction:

$$In(CH_3COO)_3 + (3 - x)\ C_{13}H_{27}COOH \rightarrow In(C_{13}H_{27}COO)_{3-x}(OAc)_x + (3 - x)\ CH_3COOH \uparrow$$

We injected 0.2 mmol TMS_3P and 2.4 mmol octylamine in 1 ml ODE into the flask at 188°C and observed a swift color change from yellow through orange to red. Ten minutes after the injection, the NCs revealed a clear excitonic peak at 512 nm in the absorption spectrum, indicating small size and good size distribution. Only weak PL from trap states appeared in the emission spectrum. The NCs did not grow significantly overnight, but their size distribution broadened and a band-edge PL appeared (Figure 5.3 A).

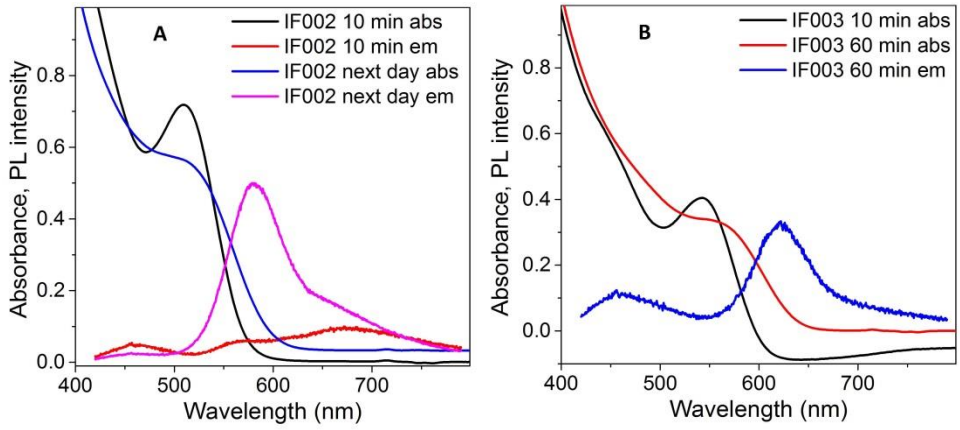

Figure 5.3. (A) Absorption and emission spectra of InP NCs synthesized in ODE using octylamine. (B) Same using oleylamine.

When we replaced octylamine with OAm, the size of the QDs increased somewhat (Figure 5.3B). We conclude that a swift nucleation leads to a large number of nucleates and a

rapid use-up of the precursors, leading to small particles. For example, when we evacuated the flask with indium precursor for an hour, the nucleation upon the injection was instant and led to a polydisperse batch of tiny particles. If our goal is to synthesize large monodisperse particles, must control the nucleation rate. Moisture and acid were essential for a slower nucleation of large particles. The rate of the color change after the injection of TMS_3P, was an indicator of the size of the QDs at the end of the synthesis: a slow color change meant large QDs at the end.

According to X. Peng, an increase in the amount of myristic acid increases the QD size. We confirmed it when we increased the amount of myristic acid to 1.65 mmol: 7 min after the injection, we observed a clear first exciton at 623 nm. After 50 min of growth, there was a clear exciton at 675 nm (Figure 5.4B). To further increase the QD size, we held indium acetate with myristic acid under nitrogen flow at 188^{o}C for an hour, replaced octylamine with OAm, and maintained the temperature at 188^{o}C after the injection of TMS_3P. Ten minutes after the injection, we observed the first excitonic peak at 682 nm. This batch was of comparable quality to the corresponding size-selected fraction of the Micic InP.

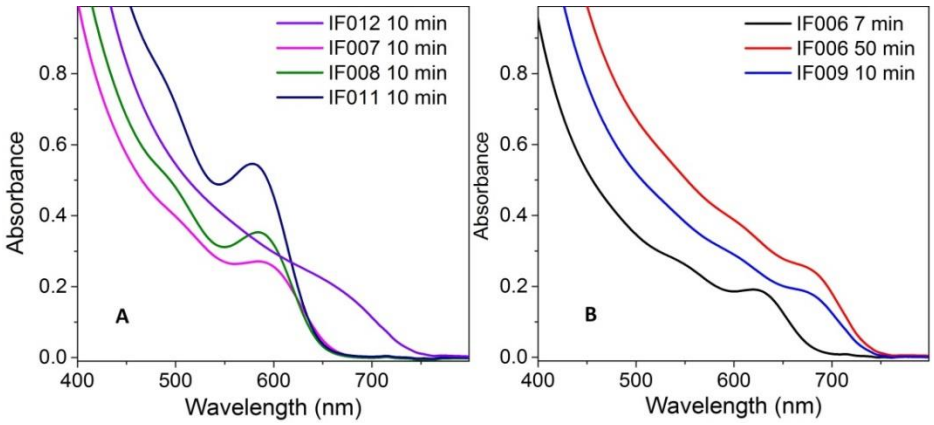

Figure 5.4. Absorption spectra of a few batches of InP.

Table 5.1. Summary of synthesis parameters for the Peng InP.

Batch	Evacuate?	N_2?	Amine	Myristic acid	Inject. temp.	Rxn temp.	Nucleation	Size	Size distr.
IF002	No	Yes	Oct, Ald	1.54 mmol	188°C	178°C	rapid	small	good
IF003	No	Yes	Ol, Ald	1.54 mmol	188°C	178°C	fast	med.	good
IF004	Yes	Yes	Ol, Ald	1.54 mmol	188°C	178°C	rapid	tiny	poor
IF006	No	Yes	Oct, Ald	1.64 mmol	188°C	178°C	slow	big	good
IF007	No	No	Ol, Ald	1.64 mmol	188°C	178°C	slow	big	fair
IF008	No	Yes	Ol, Ald	1.64 mmol	178°C	178°C	slow	big	good
IF009	No	Yes	Oct, Ald	1.64 mmol	188°C	188°C	slow	huge	good
IF011	No	Yes	Oct, AA	1.64 mmol	188°C	178°C	slow	big	good
IF012	No	Yes	Ol, Ald	1.64 mmol	188°C	178°C	slow	huge	poor

5.1.3. Synthesis of InP QDs from pure indium myristate and TMS_3P

A source of uncertainty was the completeness of the transformation of indium myristate to acetate and the amount of free acetic acid in the system. For that reason, we synthesized indium myristate *ex situ* by a metathesis of indium nitrate and sodium myristate in boiling methanol. Simply replacing indium acetate and myristic acid for indium myristate led to small InP QDs (first excitonic peak bluer than 500 nm). Table 5.2 summarizes the results; x = 0.40 mmol, y = 0.55 mmol.

Table 5.2. Summary of syntheses of InP from indium myristate and TMS_3P.

Batch	$In(myristate)_3$	$In(OAc)_3$	Myristic acid	TMS_3P	Octylamine
the Peng InP	0	x	$3y$	$x/2$	$6x$
IF013	x	0	$3(y - x)$	$x/2$	$6x$
IF014	x	0	0	$x/2$	$6x$
IF015	x	$y - x$	0	$x/2$	$6x$

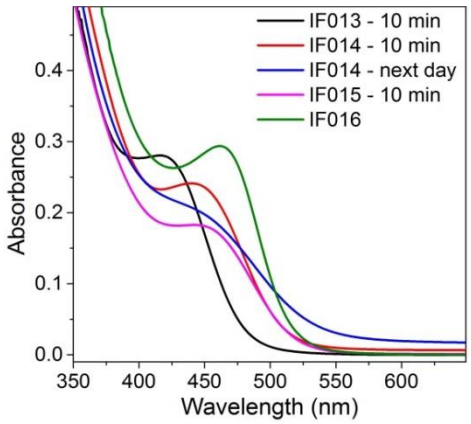

Figure 5.5. Absorption spectra of a few batches of InP QDs synthesized from pure indium myristate.

In another attempt, we mimicked Cao's recipe for zb-CdSe QDs.[97] We dissolved 0.40 mmol of indium myristate in hot ODE, cooled down the solution to the room temperature, and injected 0.2 mmol TMS_3P and 1.2 mmol octylamine. We rapidly heated up the solution to 178^{o}C. The solution remained clear first, then it turned yellow at 40^{o}C, and finally it turned orange at 55^{o}C. Remarkably, running the reaction overnight at 178^{o}C did not cause Ostwald ripening. The first exciton was at 462 nm (IF016). These QDs were too small for electronics application, but may be valuable for a core-shell growth for further PL applications.

Presence of the band-edge PL in InP QDs after the synthesis suggests the surface of the QDs is passivated. The use of indium carboxylates as precursors favors indium-rich surfaces. R stands for $C_{13}H_{27}$ (or CH_3) and L for octylamine or OAm in the following equation.

$$(m + n)\ \mathrm{In(RCOO)_3} + m\ \mathrm{TMS_3P} + n(1 - \delta)\ \mathrm{L} \rightarrow [\mathrm{InP}]_m[\mathrm{In(RCOO)_3L_{1-\delta}}]_n + 3m\ \mathrm{RCOOTMS}$$

5.2. Modification of the Surface of InP and InAs QDs

5.2.1. Treatment of the Micic InP QDs with electrophilic agents

As we have seen, the Micic InP QDs are at best stoichiometric if not phosphorus-rich, and thus are unable to undergo a ligand exchange with inorganic ligands. Nevertheless, these QDs may be more desirable for electronics given their bigger size and potentially better crystallinity owing to the higher-temperature synthesis as compared to the Peng InP QDs. An elegant photoetching of InP QDs with HF was described by D. Talapin *et al*. in 2002.[98] In that process, a surface P atom traps the photogenerated hole and gets fluorinated by HF. The electron reduces oxidants like trace molecules of O_2 or TOPO. The simplified reaction is the following.

$$[\mathrm{InP}]_{(m+n)} + 3n\ \mathrm{HF} + 1.5n\ [\mathrm{O}] \rightarrow [\mathrm{InP}]_m[\mathrm{InF_3}]_n + 3n\ \mathrm{PF_3} + 1.5n\ \mathrm{H_2O}$$

PF_3 hydrolyzes in traces of water; TOPO, which provides sterical stabilization, is not shown.

Band-edge PL from InP QDs appears as a result of the treatment: the QDs become indium-rich and their general formula is $[\mathrm{InP}]_m[\mathrm{InX_3L_{1-\delta}}]_n$. X is F, OH, or phosphonate from TOPO. L is TOPO. In some experiments, we replaced TOPO with oleic acid or TOP, but the result was similar. These In-rich QDs could undergo a ligand exchange with inorganic ligands.

Other electrophilic agents indium and gallium triflate and chloride first brought PL to InP QDs, but then precipitated InP and InAs QDs and made them dispersible in polar solvents like DMF (Figure 5.6A,B). We made sure to remove all mobile protons (traces of alcohols) by dispersing the QDs in hexane and evaporating the solvent twice to prevent a hydrolysis of the

salts and formation of acid. This chemical transformation is similar to ligand stripping with Me_3OBF_4. The QDs became indium-rich and capable of ligand exchange with inorganic ligands.

$$[InP]_m[TOPO]_l + n\ In(OTf)_3 \rightarrow [InP]_m[In^{3+}\ldots(OTf^-)_3]_n + l\ TOPO$$

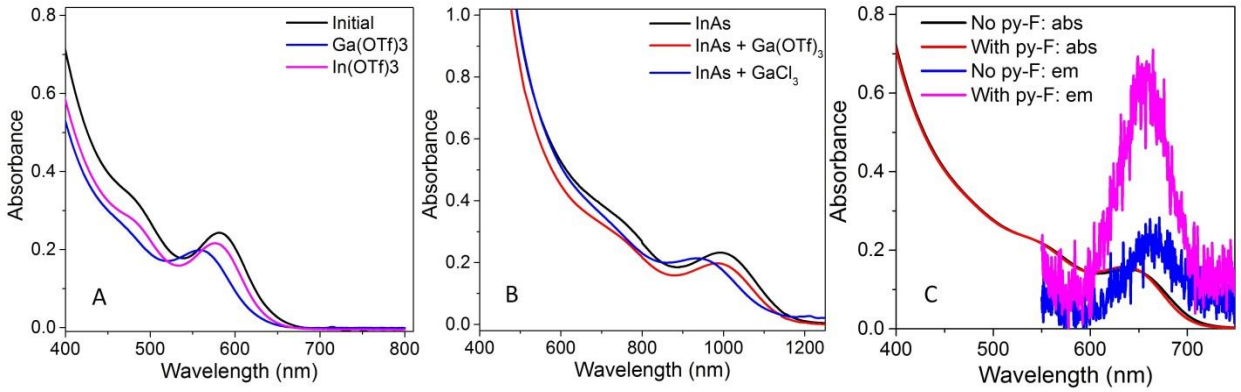

Figure 5.6. (A) Absorption spectra of InP QDs treated with gallium and indium triflates. (B) Absorption spectra of InAs QDs treated with gallium triflate and chloride. (C) Absorption and emission spectra of InP QDs treated with N-fluoropyridinium tetrafluoroborate.

A combination of a trapped hole and F^- ion can be viewed as electrophilic fluorine. In organic chemistry, there are clean sources of the latter, for example, N-fluoropyridinium. A gentle treatment of a fraction of InP QDs with $pyF^+BF_4^-$ improved their PL without etching or impairing size distribution (Figure 5.6 C).

5.2.2. Ligand exchange with inorganic ligands

InAs, the Peng InP, and electrophile-treated Micic InP QDs underwent a ligand exchange with a variety of metal-chalcogenide complexes (MCCs) like $(N_2H_5)_2In_2Se_4$, $(N_2H_5)_4Sn_2S_6$, and $N_2H_5Cu_7S_4$ forming electrostatically stabilized colloidal solutions in hydrazine. The excitonic features in UV-Vis preserved.

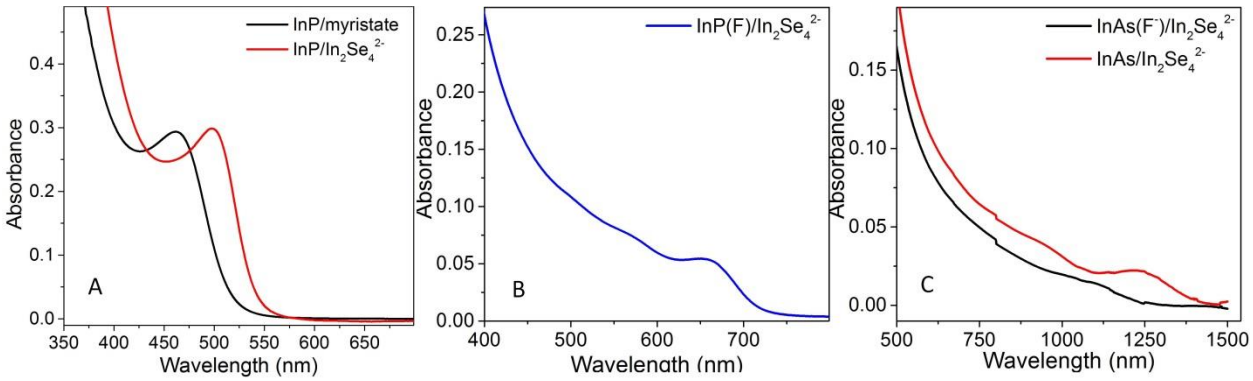

Figure 5.7. Absorption spectra of (A) the Peng InP, (B) the Micic InP, and (C) InAs QDs capped with $(N_2H_5)_2In_2Se_4$ in hydrazine.

We deposited films of these QDs and annealed them. InP and InAs QDs do not sinter, but the ligands transformed into a matrix around the NCs.

$$[InP]_m[In^{3+}/(In_2Se_4^{2-})_{3/2}]_n \rightarrow [InP]_m@[In_2Se_3]_{2n}$$

In one experiment, we aimed to avoid oxygen-containing ligands on InP during the synthesis and photo-etching to eliminate a possibility of formation of a shell of indium oxide. Therefore, we performed a synthesis in pure TOP and used TOP as the ligand in etching wit HF. After washing, the resulting QDs seemed very clean: the ligand exchange occurred easily and there were no signs of excess organics during the post-exchange washing. FETs, however, were highly insulating. We hypothesize that, in the absence of TOPO, TOP acts as a source of P during the QD growth. As a result, there are octyl groups, covalently bound to surface P atoms, that persist after the ligand exchange.

5.3. Field-Effect Transistors of InP and InAs

5.3.1. Introduction to the operation of FETs

In a field-effect transistor, passage of carriers in the channel is controlled by a bias on the gate. We fabricated FETs with the bottom-gate geometry. A heavily-doped conductive silicon wafer served as the bottom gate. A 100 nm layer of silica grown on the wafer served as the gate

dielectric. We deposited a layer of semiconductor onto a clean and hydrophilized substrate and evaporated two aluminum electrodes (source and drain) on top. The short space between the electrodes (L = 30 μm) was the FET channel.

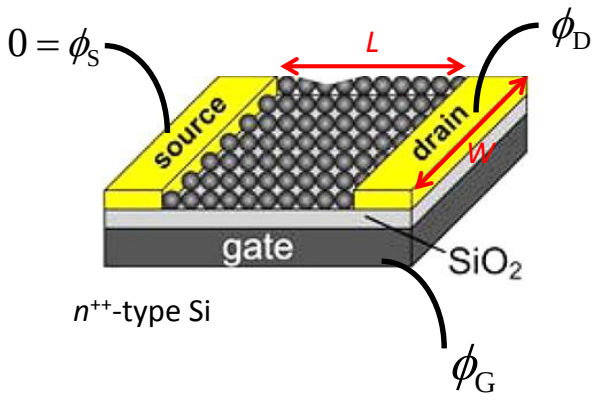

Figure 5.8. Schematic of a bottom-gate field-effect transistor.

A very simplified way to view an FET is to view it as a capacitor with a layer of dielectric between the plates and charge transport along one of the plates. When a voltage is applied between the "plates", they will carry opposite and equal charges. For example, when the potential of the gate is positive, the layer of silicon will carry a positive charge density near the interface with silica. The "other plate" – the semiconductor will carry a negative charge density near the interface with the dielectric. Therefore, positive gate biases will attract electrons into the channel. If we apply a small voltage between the source and drain electrodes (a potential difference along the "plate"), the accumulated electrons will conduct electricity. Therefore, if the electron is the carrier in the semiconductor (an *n*-type FET), positive biases on the gate will attract carriers and amplify the current in the channel. Negative gate biases will repel electrons from the channel and ideally set current to zero. The described phenomenon is a transistor action.

In our set-up, the source electrode was grounded, and the source-gate voltage, V_{GS}, and the source-drain voltage, V_{DS}, were controlled. Sweeps of the gate voltage at a fixed source-drain

bias generated transfer characteristics. Sweeps of the source-drain voltage at a fixed source-gate bias generated output characteristics. All electron mobility values were extracted from the forward-gate voltage sweep (V_{GS} from −30 V to 30 V), which provides a conservative estimate for electron mobility. In the gradual channel approximation, the current in the FET channel can be analytically described for two different regimes of operation. At $V_{DS} << V_{GS} - V_t$, the channel current, I_D, increases linearly with the gate voltage.

$$I_D = \frac{W}{L} C \mu_{lin} \left(V_{GS} - V_t - V_{DS}/2 \right) V_{DS}$$

Here C is the capacitance per unit area of the insulating layer (30 nF/cm^2), V_t is the threshold (turn-on) voltage, and μ_{lin} is the linear field-effect mobility. μ_{lin} is calculated from the transconductance (the slope of the transfer curve in the region with $V_{GS} - V_t >> V_{DS}$):

$$\left. \frac{\partial I_D}{\partial V_{GS}} \right|_{V_{DS}} = \frac{W}{L} C V_{DS} \cdot \mu_{lin}$$

For $V_{DS} >> V_{GS} - V_t$, I_D tends to saturate due to pinch-off of the accumulation layer (saturation regime). This case is approximately described by:

$$I_D = \frac{1}{2} \frac{W}{L} C \mu_{sat} \left(V_{GS} - V_t \right)^2$$

The saturation mobility can be calculated from the slope of $\sqrt{I_D}$ as a function of V_{GS}:

$$\left. \frac{\partial \sqrt{I_D}}{\partial V_{GS}} \right|_{V_{DS}} = \sqrt{\frac{1}{2} \frac{W}{L} C V_{DS} \cdot \mu_{sat}}$$

The extracted mobility values serve as a measure of the properties of our NCs (surface passivation) and film morphology.

5.3.2. FET performance of InAs

The optimal ligand for InAs QDs was thiocuprite, $N_2H_5Cu_7S_4$. FETs demonstrated linear mobilities up to 2.6 cm^2/Vs, saturation mobilities up to 2.2 cm^2/Vs, and on-off ratios up to 10^3. The behavior was comparable to the previously observed for InAs.[99]

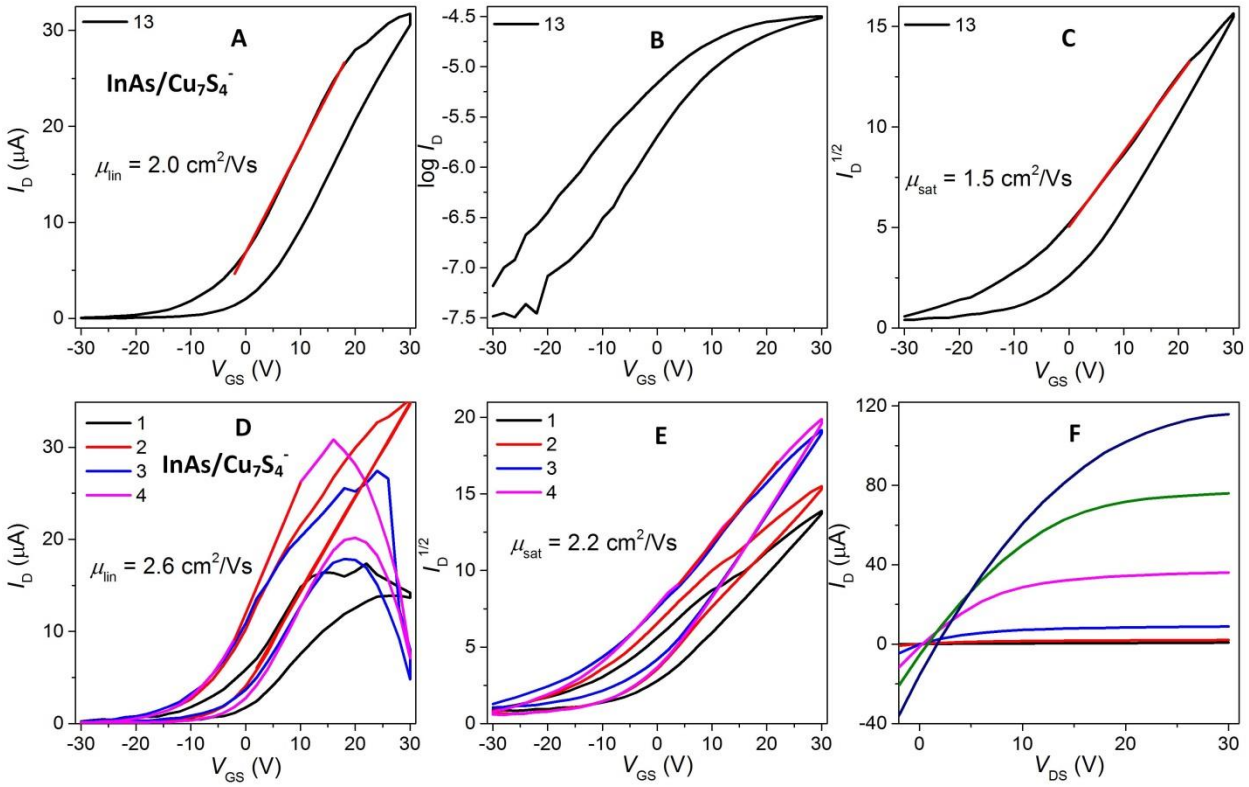

Figure 5.9. Transfer and output characteristics of FETs from two batches InAs/$N_2H_5Cu_7S_4$. (A) Transfer characteristics of an FET from the first batch in the linear regime. (B) Logarithm of current in (A) to extract the on-off ratio. (C) Transfer characteristics of an FET from the first batch in the saturation regime. (D) Transfer characteristics of FETs from the second batch in the linear regime. (E) Transfer characteristics of FETs from the second batch in the saturation regime. (F) Output characteristics of an FET from the second batch.

5.3.3. Performance of InP FETs

The optimal ligand for InP was selenoindate, $(N_2H_5)_2In_2Se_4$. Colloidal solutions in hydrazine deposited smooth dense films, but FET performance was lower than in the case of InAs: carrier mobility reached only 0.016 cm^2/Vs and the on-off ratio did not reach 10^2.

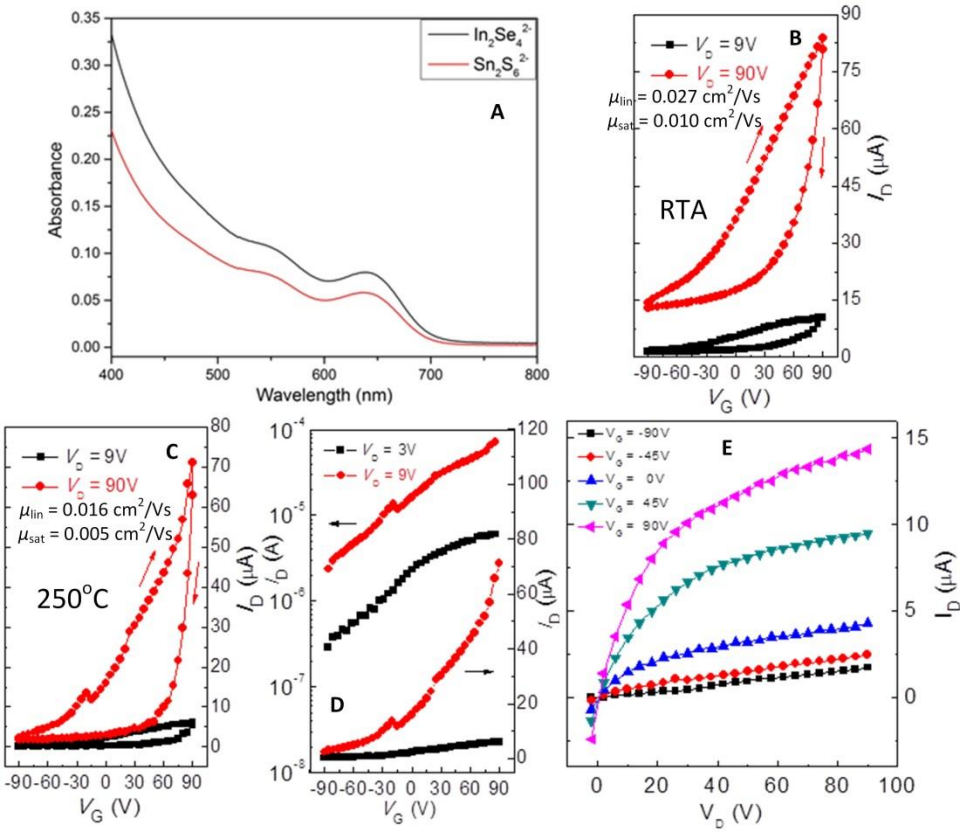

Figure 5.10. (A) Absorption spectra of InP QDs capped with metal-chalcogenide complexes. (B) Transfer characteristics of an FET of InP/$In_2Se_4^{2-}$ annealed by RTA. (C – E) Transfer and output characteristics of FETs of InP/$In_2Se_4^{2-}$ annealed at 250°C for 30 min.

We varied a number of material processing parameters. For example, we performed photo-etching of InP in the presence of oleic acid to introduce a controllable amount of X-type ligand that is easier to exchange for inorganic ligands (as opposed to unknown amounts of phosphonates in TOPO). There was no improvement from this modification, however. We also explored rapid thermal annealing as an alternative to 30 minute annealing on a hot plate. This modification improved the mobility but impaired the on-off ratio somewhat. Nevertheless, the performance of FETs remained poor overall.

Table 5.3. Summary of the performance of FETs of InP/$In_2Se_4^{2-}$ with different organic ligands used in photoetching and different annealing conditions for the films.

Material – annealing	μ_{lin}, cm^2/Vs	μ_{sat}, cm^2/Vs	On-off ratio
InP/TOPO – 250°C	0.012	0.007	> 10
InP/TOPO – RTA	0.027	0.010	< 10
InP/OA – 250°C	0.011	0.007	> 10
InP/OA – RTA	0.011	0.003	< 10

5.3.4. Improvements to FETs of InP

We suspected the devices worked poorly because the Fermi level of our InP lay too low to make it a true *n*-type material and accumulated electrons were trapped during transport. Our aim was to raise the Fermi level above the trap states by doping the material. In one experiment, we evaporated thin layers (0.1 – 1 nm) of indium onto silica before the deposition of the semiconductor. The mobility of the resulting devices did not improved and did not depend on the thickness of the indium layer; the on-off ratio degraded. The devices, therefore, contained a high concentration of ungated carriers, but the Fermi level was not raised above the trap states.

In the next step, we decided to deposit a layer of electron-rich species like In (I) between the dielectric and the semiconductor. When we added hydrazine to InCl, the solution turned black and insoluble powder (of $InCl_3$ likely) and shiny pieces of metallic indium accumulated. In (I) underwent disproportionation according to the following reaction.

$$3\ InCl \rightarrow InCl_3 + 2\ In$$

We filtered the solution and prepared a sample for TEM in the GB. We observed NCs of elemental indium were observed in TEM (Figure 5.11). The absorption spectrum showed no

excitonic or plasmonic peaks. No PL was observed from the solution. The most likely mechanism of stabilization was electrostatic, with Cl^- ions.

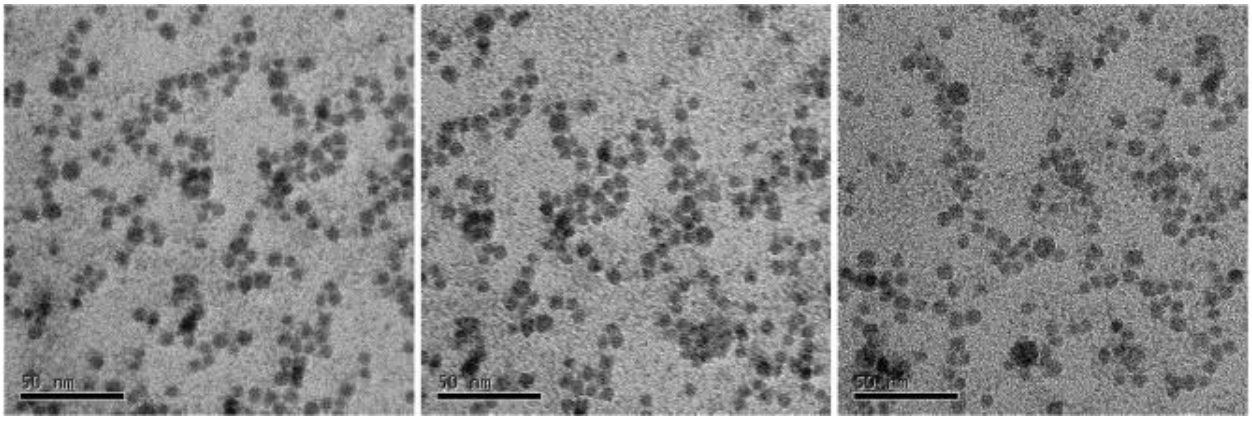

Figure 5.11. TEM images of NCs of indium.

We spin-coated this diluted filtered solution of In NCs on the substrate before the deposition of InP. Higher annealing temperatures increased the mobility. For the samples annealed at 300°C, the thin layer of indium improved the mobility by a factor of 3.

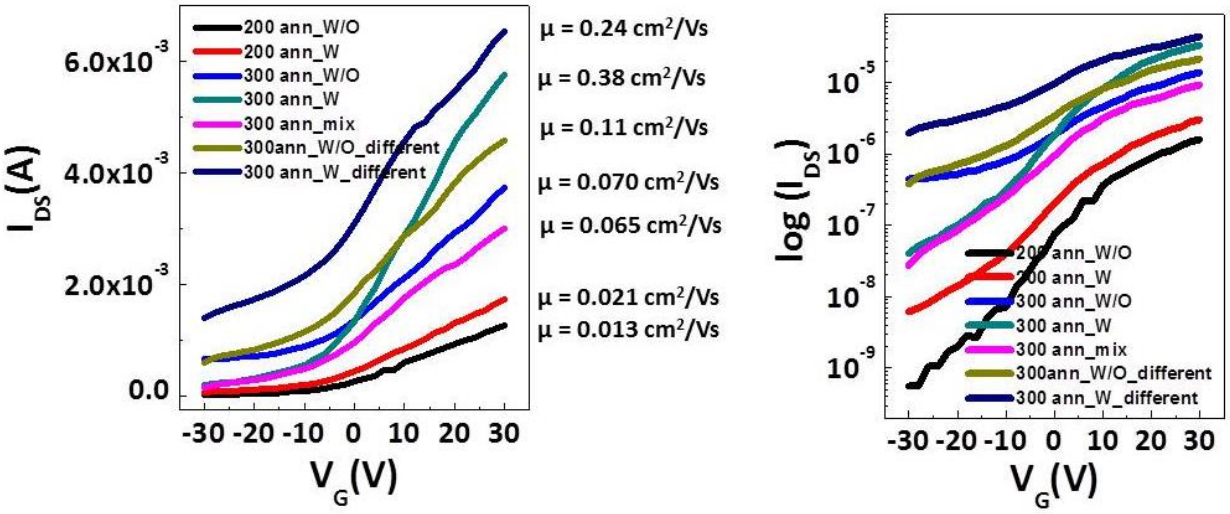

Figure 5.12. Transfer characteristics of FETs of InP/$In_2Se_4^{2-}$ with and without a thin layer of indium at different annealing temperatures.

Overall, a thin layer of indium improved the performance of FETs. Intermediate thicknesses (< 5 nm) of indium NC films were optimal. Thicker films of indium impaired the on-

off ratio, and thinner films impaired the mobility. Larger InP QDs (from earlier size fractions) worked better than smaller InP QDs. Even in devices without indium, we noticed an improvement in performance compared to previous experiments. We attributed it to extensive washing of the QDs with after the photo-etching with HF and after the ligand exchange. Also, when we centrifuged the electrostatically stabilized solution of InP/$(N_2H_5)_2In_2Se_4$ right after the ligand exchange, about half QDs precipitated. The re-dispersed QDs in hydrazine were much purer from organics and made smooth films at the end.

5.4. Understanding the Poor Performance of InP QDs in FETs

5.4.1. Film morphology

Even the highest value of mobility observed in doped InP (0.38 cm^2/Vs) is far below the bulk value 5000 cm^2/Vs. Our goal was to understand this discrepancy. First, we studied the morphology of the film with SEM. The channel area generally appeared smooth (Figure 5.13 B), with occasional islands of two-micrometer-long cracks (or grooves). Nevertheless, we did not attribute the poor performance to such occasional cracks, especially given how smooth the film was around them (Figure 5.13 C, D). Likely, the problem rooted in the surface passivation of individual dots in the film (matrix of In_2Se_3) and a high density of electron traps there.

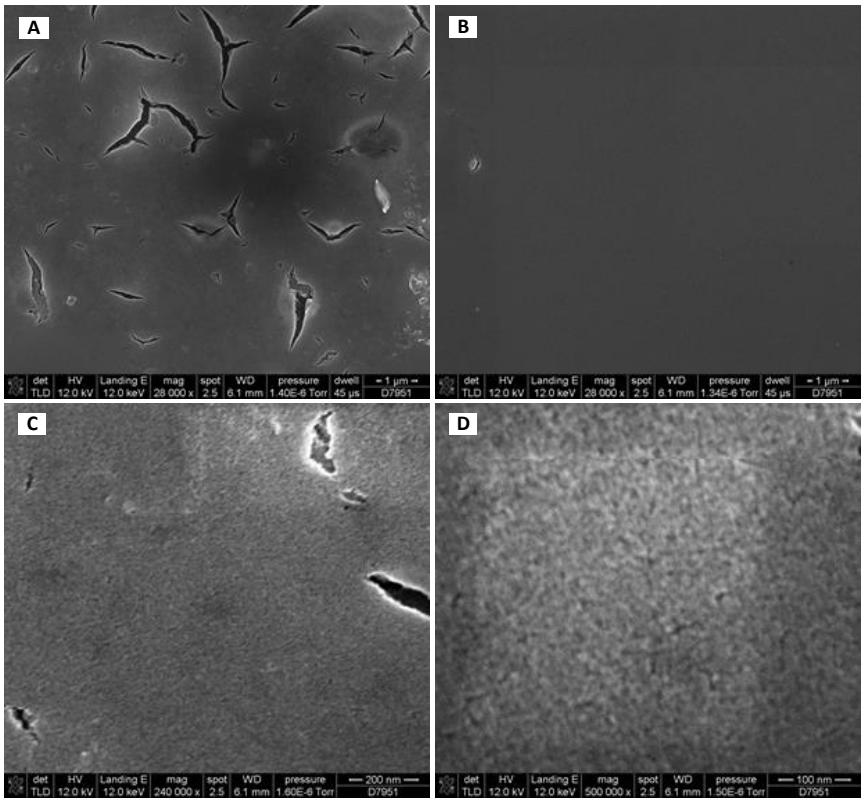

Figure 5.13. SEM images of the channel of an FET. Films of InP/$(N_2H_5)_2In_2Se_4$ were deposited onto pre-evaporated 1 Å of indium and annealed. (A, B) Magnification = 28 kx, (C) magnification = 240 kx, (D) magnification = 500 kx.

5.4.2. Will embedded InP QDs impair the FET performance a matrix of CdSe with composition-matched ligands?

w-CdSe QDs, capped with composition-matched $Na_2Cd_2Se_3$ ligands and annealed into a matrix, demonstrated electron mobilities up to 1/3 of the value for bulk CdSe. Our goal was to see whether embedding InP QDs into a matrix of CdSe would lower the performance of the latter. We grew shells of CdSe over etched Micic InP QDs and performed a ligand exchange with $Na_2Cd_2Se_3$. We processed the material as if it had been w-CdSe/$Na_2Cd_2Se_3$. The resulting FETs showed the electron mobility of 0.003 cm^2/Vs, five orders of magnitude lower than that for CdSe. Clearly, the presence of InP QDs affected the performance of CdSe matrix.

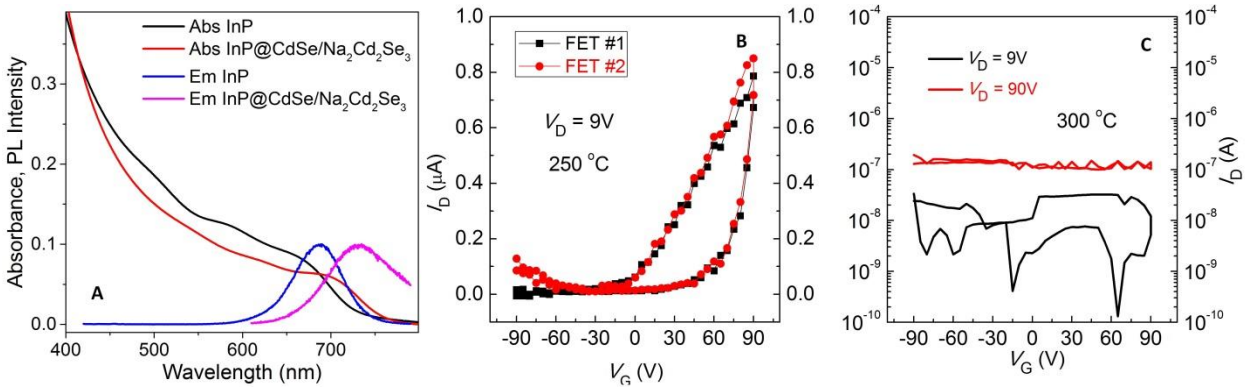

Figure 5.14. (A) UV-Vis and PL spectra of etched Micic InP QDs and InP/CdSe/$Na_2Cd_2Se_3$ QDs. (B) Transfer curves of FETs from InP/CdSe/$Na_2Cd_2Se_3$ QDs annealed at 250°C. (C) Same, but annealed at 300°C.

5.4.3. Transient absorption of solutions and films of InP QDs.

Since we expected the FETs to be *n*-type, it was important to study the lifetime of the electron by transient absorption in organic-capped InP QDs in toluene and inorganic-capped InP QDs in hydrazine. We performed a ligand exchange on a batch of etched InP QDs. Thiol preserved the PL, but MCCs ruined it. The lifetime of the electron in all samples was nanoseconds, the shortest being in InP/$(N_2H_5)_2In_2Se_4$ (6 ns) and the longest being in etched InP. Given he long lifetimes of the electron, the loss of the PL in MCC-capped InP likely happened due to hole trapping. The lifetimes were comparable to those in other semiconductors (CdSe), so did not explain the poor performance of FETs.

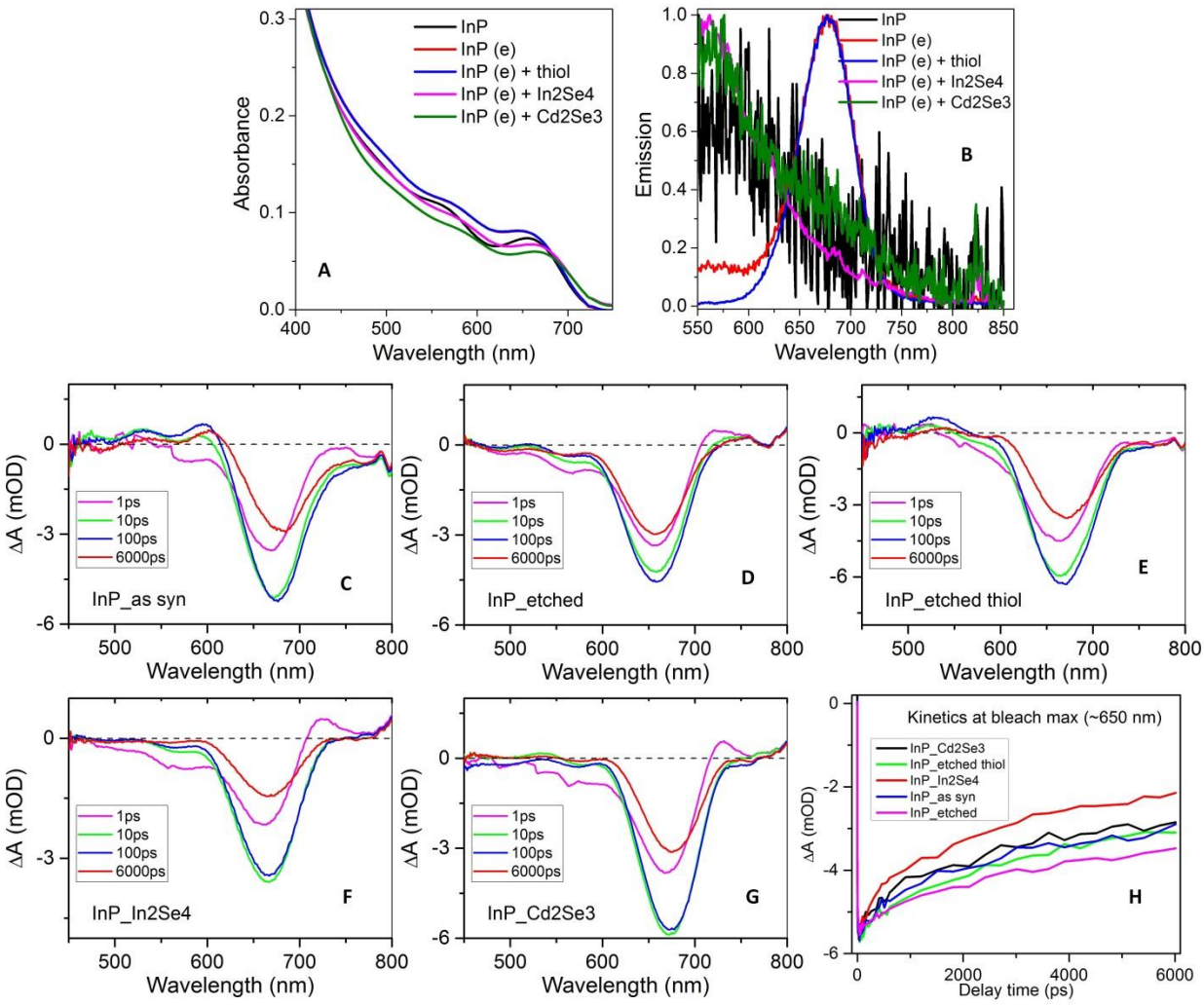

Figure 5.15. (A) UV-Vis spectra of InP QDs capped with organic and inorganic ligands. (B) The corresponding PL spectra. (C – G) Snapshots of the first excitonic bleach of the samples in transient absorption. (H) Electron dynamics in the samples obtained by integrating the bleach signals at different times.

Long lifetimes of the electron from solution TA is a necessary but not sufficient condition for a good mobility of electrons. In films, the dielectric environment around the NCs is different than in dilute solutions. We prepared a film of InP on glass under conditions identical to FET fabrication and sealed it in the glove box to prevent degradation by air during the measurement. The lifetime of the electron in the film is of InP/$In_2Se_4^{2-}$ was 220 ± 50 ps, which is 30 times as short as in the solution.

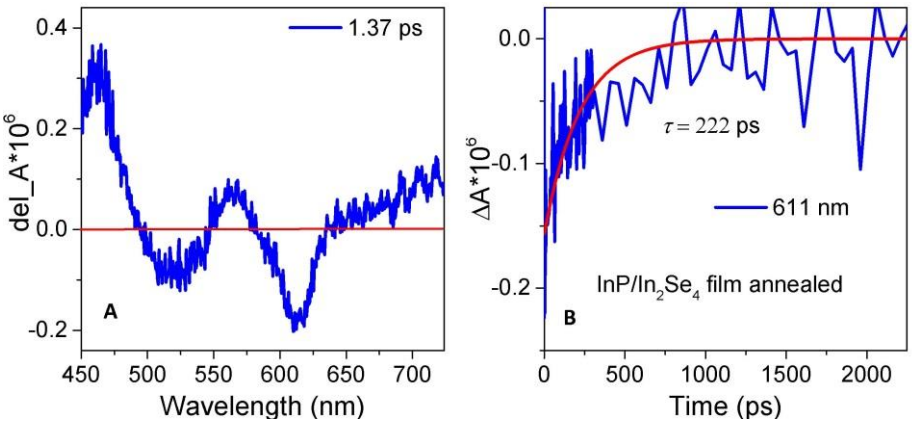

Figure 5.16. (A) A TA spectrum of a film of $InP/In_2Se_4^{2-}$ QDs on glass, prepared and annealed as in FET fabrications. (B) Dynamics of the first excitonic bleach.

5.4.4. How is InP different from CdSe or InP?

The difference between CdSe and InP is substantial. First, Cd^{2+} is a soft acid and therefore has affinity to soft bases like chalcogenides or MCCs. CdSe will not form a crust of CdO around a NC. In^{3+}, in contrast, is a hard acid and therefore is highly oxophilic. Ligand exchange of carboxylates or phosphonates for MCCs will be incomplete. Oxygen-containing ligands form a crust of insulating indium oxide or phosphate upon annealing. The crust will be a barrier to charge transport and may be one of the reasons for absence of sintering in indium oxide upon annealing. Absence of sintering implies carrier hopping between QDs, which is another problem for transport. Second, under identical conditions, NCs of InP will tend to be more stoichiometric than NCs of CdSe. Every excess Cd atom comes with two X-type ligands in CdSe, $[CdSe]_m[CdX_2]_n$, but every excess In will bring three X-type ligands in InP, $[InP]_m[InX_3]_n$ which causes steric hindrance. The surface of InP is not susceptible to ligand exchange, and electrophilic treatments, which enable ligand exchanges, grow insulating crusts. Last but not least, InP is a more covalent semiconductor than CdSe; therefore, it tolerates crystal disruptions like anti-site defects more so. These defects can serve as carrier traps.

The difference between InP and InAs is more challenging to explain. Indeed, FETs of InAs QDs show carrier mobilities of the order of 10^1 cm^2/Vs, two orders of magnitude higher than our best results for InP. InAs NCs are susceptible to ligand exchange right after the synthesis, without electrophilic treatments. One could explain it by the fact that the bigger dielectric constant allows for a better passivation of excess In atoms at the surface. The lattice constant of InAs (6.06 Å) is only slightly higher than that of InP (5.87 Å).

5.5. Electronic Properties of Photopatterned Materials

One niche of applications of solution-processed semiconductors is fabrication of patterned materials. A photosensitive agent is added to the "ink" of dielectric, semiconductor, or metallic NCs, and a film of the material is spin-casted. When parts of the film are exposed to UV light, the photosensitive agent undergoes chemical transformations that alter the surface chemistry and thus solubility of the exposed parts. The film is then washed with a certain solvent, and either the photo-treated or unphoto-treated parts of it dissolve and the remainder forms a desired pattern.

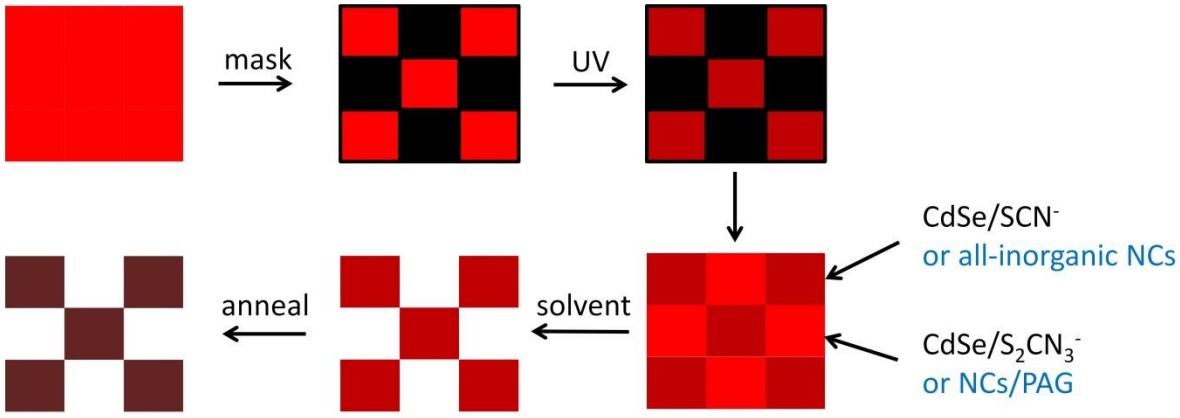

Figure 5.17. A schematic of photo-patterning of NC films with embedded photosensitive agents.

I collaborated with our postdoctoral fellow Dr. Yuanyuan Wang in this work. We used two types of photosensitive agents: anionic 1,2,3-thiatriazole-5-thiolate ($S_2CN_3^-$, TTT), and

cationic triarylsulfonium (Ar_3S^+) and diaryliodonium (Ar_2I^+) photoacid generators (PAG). TTT decomposes into thiocyanate, nitrogen, and sulfur under UV illumination, and the resulting thiocyanate acts as an inorganic ligand.

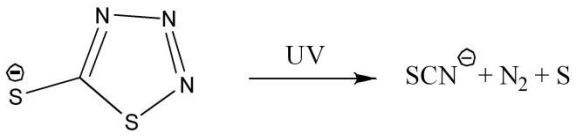

PAGs generate acid (H^+) from mobile protons (alcohols, amines) or even from their own phenyl rings in the absence of the latter.

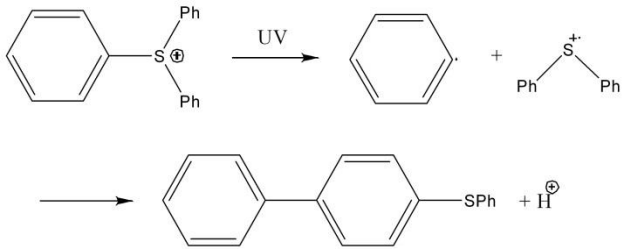

The photo-generated acid strips organics similar to Me_3O^+ or other electrophilic agents. The resulting NCs thus become all-inorganic and insoluble in non-polar solvents, so the untreated NCs and byproducts of the treatment are washed away with solvents like toluene.

We tested the electronic properties of the photo-treated materials: the dielectric constant of oxides, the conductivity of metals, and the carrier mobility in semiconductors. We measured capacitance of 125-nanometer-thick films of alumina deposited onto 100-nanometer-thick silica with an RLC meter SR 720 in the frequency range from 100 Hz to 100 kHz. The equivalent capacitance for the two capacitors in series was the following.

$$C = \varepsilon_0 A \Big/ \left(\frac{d_1}{\varepsilon_1} + \frac{d_2}{\varepsilon_2} \right)$$

We calculated the dielectric constant of alumina to be 6.9. The discrepancy with the value for bulk alumina (9.3) comes from the porosity of the film.

Films of Au/$S_2CN_3^-$ NCs were deposited onto 1.5 cm × 1.5 cm glass substrates, irradiated, developed, and annealed at 150 °C. We measured conductivity of a 60-nanometer-thick film of gold by the four-probe Van der Pauw method with a parametric analyzer Keysight B1500A. First, we drove current between two adjacent electrodes, I_{12}, and measured the voltage between the other two electrodes, V_{43} (black trace). Then we rotated the assignment of the electrodes by one position and drove current between electrodes 2 and 3, I_{23} while measuring the voltage between electrodes 4 and 1, V_{14} (red trace). The two traces overlay, as expected for the square geometry. We calculated sheet resistivity from Van der Pauw's theorem as $R_s = \frac{\pi}{\ln 2} R$, R being the slope of the $V - I$ curve. Resistivity of the film was then $\rho = R_S h = 5.2 \cdot 10^{-8}$ Ω m. The value is only 2.14 times as high as for bulk gold.

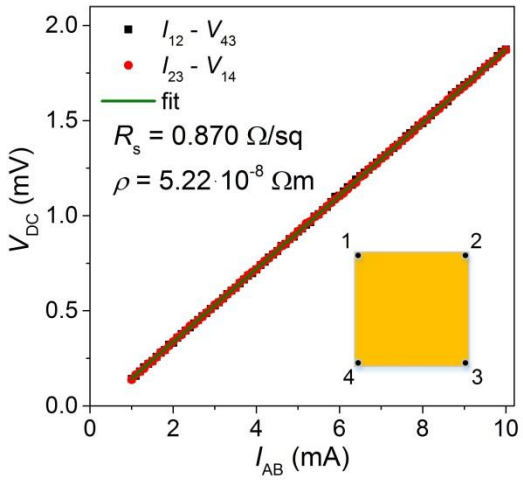

Figure 5.18. The Van der Pauw measurement on a phototreated film of gold.

Finally, we characterized photo-treated semiconductors by FET measurements. Sol-gel indium gallium zinc oxide (IGZO) treated with PAG produced films with linear carrier mobilities up to 11.6 cm^2/Vs and nearly no hysteresis in transfer curves.

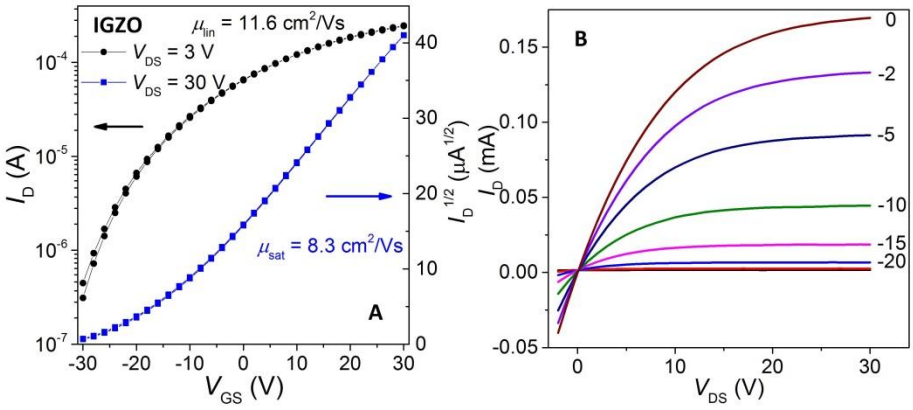

Figure 5.19. (A) Transfer and (B) output characteristics of an FET on a photo-patterned slightly over-doped IGZO film.

CdSe NCs treated with TTT measured mobilities up to one half of the values reported for $CdSe/SCN^-$ [Kagan] (Figure 5.20 A,B). CdSe NCs treated with $(Ar_3S)_2CdCl_4$ in pyridine showed hysteresis-free transfer curves with mobilities half of the reported values for $CdSe/CdCl_3^-$ QDs [Hao] (Figure 5.20 C,D). The PAG chemistry was also applicable to hydrazine-based ligands like $(N_2H_5)_2In_2Se_4$ (Figure 5.20 E,F). Electronic donors in the aryl groups (inset in Figure 5.20 D) make the PAG less susceptible to nucleophilic attacks by hydrazine.

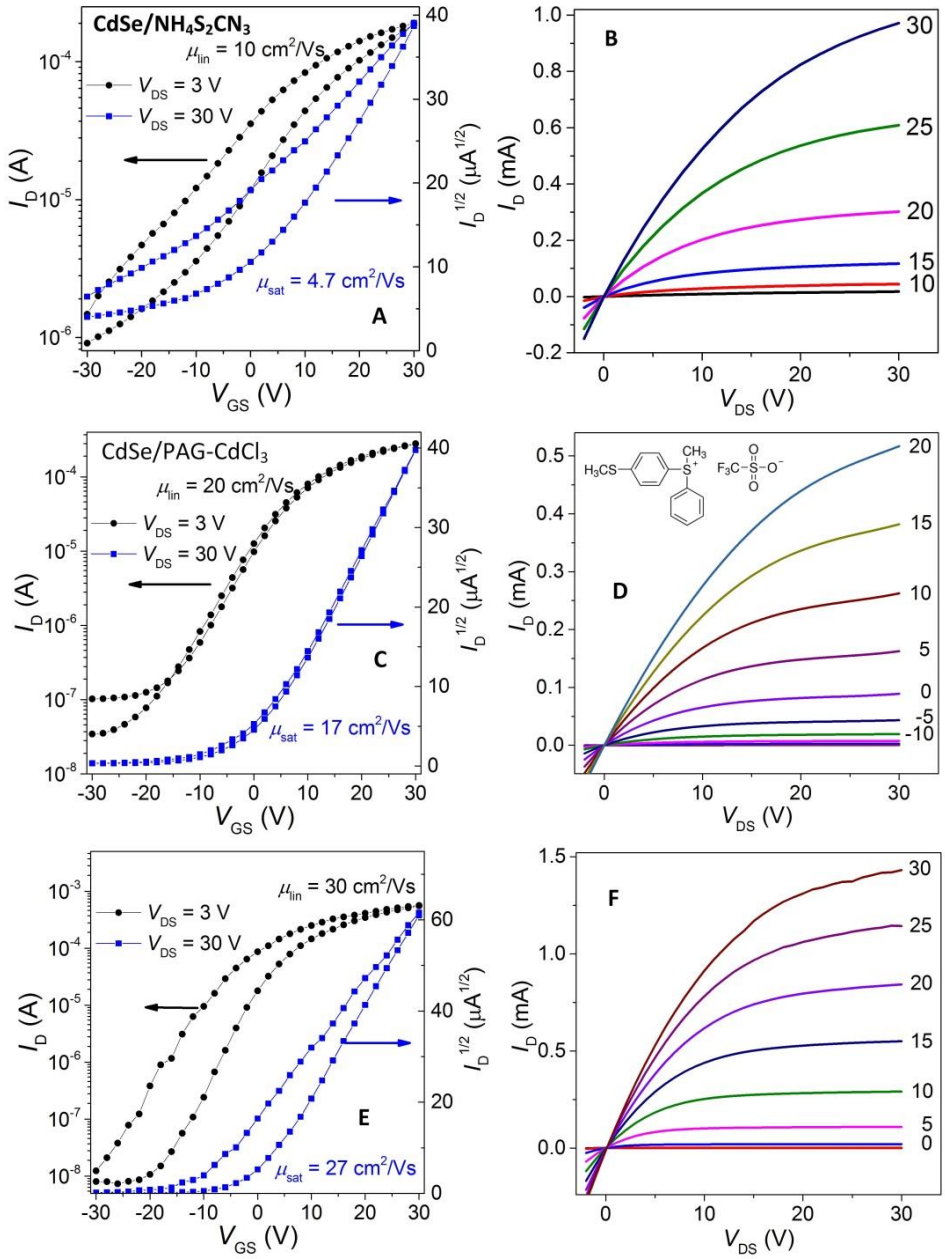

Figure 5.20. (A) Transfer and (B) output characteristics of an FET of photopatterned and partially sintered CdSe/$NH_4S_2CN_3$ NCs. (C) Transfer and (D) output characteristics of FET of CdSe/NH_4CdCl_3 NCs photopatterned with a PAG whose formula is shown in the inset. (E) Transfer and (F) output characteristics of FET of photopatterned and partially sintered CdSe NCs with $In_2Se_4^{2-}$ ligand and (4-methylthiophenyl)(methyl) (phenyl)sulfonium triflate.

5.6. Summary and Outlook

FETs of InP showed a poor performance in both the carrier mobility and the on-off ratio. Doping films of InP/$In_2Se_4^{2-}$ with improved the performance somewhat. Our best devices showed mobilities up to 0.38 cm^2/Vs, and on-off ratios up to 10^3. These values are a record for solution-processed InP, but the mobility is four orders of magnitude lower than the bulk value. Transient absorption, however, showed relatively high lifetime of the elctron (6 ns in the solution and 220 ps in the film). Possible reasons for the poor performance include high density of defects due to poor crystallinity and poor surface passivation. Another possible reason is formation of crusts of insulating In_2O_3 around the QDs, which prevents them from sintering and impedes charge transport.

A niche for applications of solution-processed semiconductors is photopatterning. FETs of IGZO and CdSe phototreated with PAGs showed high carrier mobilities, high on-off ratios, and little hysteresis.

5.7. Experimental Details

In the synthesis of the Micic InP QDs, in a glove box, we dissolved 1.030 g $InCl_3$ in 9.8 g TOP (slight heating may be necessary) and filtered the resulting solution through a 0.2 μm filter into a three-necked flask. We added 0.9 g TOPO to the solution and degassed the contents of the flask at 80°C on a Schlenk line until TOPO dissolved. After that, we injected 0.75 g TMS_3P and ramped up the temperature to 270°C. The color of the solution transformed from yellow to orange, red, dark red, and black. We ran the reaction for at least 16 hr. We took the cooled-down flask to the glove box, added 12 ml toluene, and performed size selection.

Size-selective precipitation. We added a certain volume of ethanol to the solution of QDs, centrifuged it, re-dispersed the precipitate and stored it as a fraction, and continued the procedure on the supernatant. The following parameters yielded 5 fractions of about equal mass of InP.

Table 5.4. Parameters for size-selective precipitation of InP.

Starting solution	Volume of ethanol	Centrifugation rate	Duration	Precipitate	Supernatant
crude (24 ml)	none	5000 rpm	10 min	discard	proceed
supernatant	18 ml	10000 rpm	5 min	F1	proceed
supernatant	+ 6 ml	10000 rpm	5 min	F2	proceed
supernatant	+ 6 ml	10000 rpm	5 min	F3	proceed
supernatant	+ 12 ml	10000 rpm	5 min	F4	proceed
supernatant	+ 30 ml	4500 rpm	10 min	F5	discard

Photochemical etching with HF. In a plastic centrifuge tube (no glass), we dissolved 1.4 g TOPO in 14 ml hexane, and added 1 ml of a solution of InP QDs in toluene. To the stirring solution, we added between 0.5 and 1 ml of 4% HF in butanol (prepared by mixing butanol and 48% aqueous HF, 11:1) drop by drop. We put a long-pass filter in front of a xenon lamp to excite only the first exciton of InP (we used FGL 610 or 550) and focused the light onto the tube with the stirred solution. After 4 hr of etching, when PL appeared, we precipitated the QDs with an equal volume of acetonitrile, re-dispersed the precipitate in 2 ml toluene, and precipitated it with an equal volume of ethanol, leaving the supernatant slightly colored. We re-dispersed the precipitate in 3 ml toluene and used it for a ligand exchange.

Ligand exchange. In a 6 ml vial, we added 1 ml hydrazine and 3 ml of etched InP in toluene, creating a two-phase system. We added 0.25 ml × 0.25 M $(N_2H_5)_2In_2Se_4$ in hydrazine and stirred the mixture overnight. When the ligand exchange has occurred, we discarded the

toluene phase, moved the hydrazine phase into a clean vial, and did a series (up to 7) of two-phase washes with toluene, hexane, and MCH. We moved the hydrazine phase to a centrifuge tube and precipitated it with acetonitrile, leaving a slightly colored supernatant. Upon the addition of acetonitrile, the suspension must be black; if white or grey clouds are observed, the solution is not washed from organics. We re-dispersed the precipitate in 300 µl hydrazine, filtered it through a 0.2 µm PFTE filter and used it for the film deposition.

Fabrication of FETs. Si wafers (heavily *n*-doped, $\rho < 0.005$ Ωcm, QL) with 100 nm SiO_2 dielectric were used as the bottom gate and a substrates for FET fabrication. The substrates, 1 cm × 1 cm in size, were immersed in piranha (conc. H_2SO_4 and 30% aqueous H_2O_2, 5:3 by volume) and heated for 10 min until the oxygen stopped bubbling. Once the substrates cooled down, we rinsed them with water multiple times. Colloidal solutions of inorganic materials with photosensitive ligands (Section IV) were spin-coated out of N_2H_4, NMF, or DMF (spread: 600 rpm, 6 s; spin: 2000 rpm, 40 s) onto freshly cleaned substrates to produce 30–100 nm thick NC films. The NC films were irradiated under DUV in the glovebox and developed in corresponding solvents (Section V). After drying at 100 °C for 30 min to evaporate the solvent, the film was then annealed at 350 °C for 30 min to decompose the ligand and to promote NC grain growth. A 70 nm thick Al source and drain electrodes were deposited through a shadow mask using a thermal evaporator to complete a top-contact, bottom-gate FET structure (channel width and length were 180 µm and 30 µm, respectively). In this work we used thermally grown SiO_2 as the gate dielectric, which is known to give somewhat lower mobility and higher operating voltages compared to FETs with high-ε dielectric layers.

Transient absorption was performed on set-ups built by Dr. Richard Schaller and Dr. David Gosztola at Argonne National Laboratory.

REFERENCES

1. Murray, C. B.; Norris, D. J.; Bawendi, M. G., SYNTHESIS AND CHARACTERIZATION OF NEARLY MONODISPERSE CDE (E = S, SE, TE) SEMICONDUCTOR NANOCRYSTALLITES. *Journal of the American Chemical Society* **1993,** *115* (19), 8706-8715.

2. McDonald, S. A.; Konstantatos, G.; Zhang, S. G.; Cyr, P. W.; Klem, E. J. D.; Levina, L.; Sargent, E. H., Solution-processed PbS quantum dot infrared photodetectors and photovoltaics. *Nature Materials* **2005,** *4* (2), 138-142.

3. Micic, O. I.; Curtis, C. J.; Jones, K. M.; Sprague, J. R.; Nozik, A. J., SYNTHESIS AND CHARACTERIZATION OF INP QUANTUM DOTS. *Journal of Physical Chemistry* **1994,** *98* (19), 4966-4969.

4. Protesescu, L.; Yakunin, S.; Bodnarchuk, M. I.; Krieg, F.; Caputo, R.; Hendon, C. H.; Yang, R. X.; Walsh, A.; Kovalenko, M. V., Nanocrystals of Cesium Lead Halide Perovskites (CsPbX3, X = Cl, Br, and I): Novel Optoelectronic Materials Showing Bright Emission with Wide Color Gamut. *Nano Letters* **2015,** *15* (6), 3692-3696.

5. Owen, J. S.; Park, J.; Trudeau, P. E.; Alivisatos, A. P., Reaction chemistry and ligand exchange at cadmium-selenide nanocrystal surfaces. *Journal of the American Chemical Society* **2008,** *130* (37), 12279-+.

6. Wang, W.; Banerjee, S.; Jia, S. G.; Steigerwald, M. L.; Herman, I. P., Ligand control of growth, morphology, and capping structure of colloidal CdSe nanorods. *Chemistry of Materials* **2007,** *19* (10), 2573-2580.

7. Ithurria, S.; Tessier, M. D.; Mahler, B.; Lobo, R.; Dubertret, B.; Efros, A., Colloidal nanoplatelets with two-dimensional electronic structure. *Nature Materials* **2011,** *10* (12), 936-941.

8. Yoffe, A. D., Semiconductor quantum dots and related systems: electronic, optical, luminescence and related properties of low dimensional systems. *Advances in Physics* **2001,** *50* (1), 1-208.

9. Hines, M. A.; Guyot-Sionnest, P., Synthesis and characterization of strongly luminescing ZnS-Capped CdSe nanocrystals. *Journal of Physical Chemistry* **1996,** *100* (2), 468-471.

10. Yu, D.; Wang, C. J.; Guyot-Sionnest, P., n-type conducting CdSe nanocrystal solids. *Science* **2003,** *300* (5623), 1277-1280.

11. Dolzhnikov, D. S.; Zhang, H.; Jang, J.; Son, J. S.; Panthani, M. G.; Shibata, T.; Chattopadhyay, S.; Talapin, D. V., Composition-matched molecular "solders" for semiconductors. *Science* **2015,** *347* (6220), 425-428.

12. Rosen, E. L.; Buonsanti, R.; Llordes, A.; Sawvel, A. M.; Milliron, D. J.; Helms, B. A., Exceptionally Mild Reactive Stripping of Native Ligands from Nanocrystal Surfaces by Using Meerwein's Salt. *Angewandte Chemie-International Edition* **2012,** *51* (3), 684-689.

13. Zhang, H.; Kurley, J. M.; Russell, J. C.; Jang, J.; Talapin, D. V., Solution-Processed, Ultrathin Solar Cells from CdCl3--Capped CdTe Nanocrystals: The Multiple Roles of CdCl3-Ligands. *Journal of the American Chemical Society* **2016,** *138* (24), 7464-7467.

14. Li, H.; Zanella, M.; Genovese, A.; Povia, M.; Falqui, A.; Giannini, C.; Manna, L., Sequential Cation Exchange in Nanocrystals: Preservation of Crystal Phase and Formation of Metastable Phases. *Nano Letters* **2011,** *11* (11), 4964-4970.

15. De Trizio, L.; Gaspari, R.; Bertoni, G.; Kriegel, I.; Moretti, L.; Scotognella, F.; Maserati, L.; Zhang, Y.; Messina, G. C.; Prato, M.; Marras, S.; Cavalli, A.; Manna, L., Cu3-xP Nanocrystals as a Material Platform for Near-Infrared Plasmonics and Cation Exchange Reactions. *Chemistry of Materials* **2015,** *27* (3), 1120-1128.

16. Izquierdo, E.; Robin, A.; Keuleyan, S.; Lequeux, N.; Lhuillier, E.; Ithurria, S., Strongly Confined HgTe 2D Nanoplatelets as Narrow Near-Infrared Emitters. *Journal of the American Chemical Society* **2016,** *138* (33), 10496-10501.

17. Nedelcu, G.; Protesescu, L.; Yakunin, S.; Bodnarchuk, M. I.; Grotevent, M. J.; Kovalenko, M. V., Fast Anion-Exchange in Highly Luminescent Nanocrystals of Cesium Lead Halide Perovskites (CsPbX3, X = Cl, Br, I). *Nano Letters* **2015,** *15* (8), 5635-5640.

18. Li, J. J.; Wang, Y. A.; Guo, W. Z.; Keay, J. C.; Mishima, T. D.; Johnson, M. B.; Peng, X. G., Large-scale synthesis of nearly monodisperse CdSe/CdS core/shell nanocrystals using air-stable reagents via successive ion layer adsorption and reaction. *Journal of the American Chemical Society* **2003,** *125* (41), 12567-12575.

19. Ithurria, S.; Talapin, D. V., Colloidal Atomic Layer Deposition (c-ALD) using Self-Limiting Reactions at Nanocrystal Surface Coupled to Phase Transfer between Polar and Nonpolar Media. *Journal of the American Chemical Society* **2012,** *134* (45), 18585-18590.

20. Neave, J. H.; Joyce, B. A.; Dobson, P. J.; Norton, N., Dynamics of film growth of GaAs by MBE from Rheed observations. *Applied Physics A* **1983,** *31* (1), 1-8.

21. Tuinenga, C.; Jasinski, J.; Iwamoto, T.; Chikan, V., In Situ Observation of Heterogeneous Growth of CdSe Quantum Dots: Effect of Indium Doping on the Growth Kinetics. *ACS Nano* **2008,** *2* (7), 1411-1421.

22. Dagtepe, P.; Chikan, V.; Jasinski, J.; Leppert, V. J., Quantized Growth of CdTe Quantum Dots; Observation of Magic-Sized CdTe Quantum Dots. *The Journal of Physical Chemistry C* **2007,** *111* (41), 14977-14983.

23. Coronado, J. M.; Kataoka, S.; Tejedor-Tejedor, I.; Anderson, M. A., Dynamic phenomena during the photocatalytic oxidation of ethanol and acetone over nanocrystalline

TiO2: simultaneous FTIR analysis of gas and surface species. *Journal of Catalysis* **2003,** *219* (1), 219-230.

24. Hens, Z.; Martins, J. C., A Solution NMR Toolbox for Characterizing the Surface Chemistry of Colloidal Nanocrystals. *Chemistry of Materials* **2013,** *25* (8), 1211-1221.

25. Polte, J.; Ahner, T. T.; Delissen, F.; Sokolov, S.; Emmerling, F.; Thünemann, A. F.; Kraehnert, R., Mechanism of Gold Nanoparticle Formation in the Classical Citrate Synthesis Method Derived from Coupled In Situ XANES and SAXS Evaluation. *Journal of the American Chemical Society* **2010,** *132* (4), 1296-1301.

26. Izutsu, K.; Ito, M.; Sarai, E., Silver-Silver Cryptate(2,2) Ion Electrode as a Reference Electrode in Nonaqueous Solvents. *Analytical Sciences* **1985,** *1* (4), 341-344.

27. Fedin, I.; Talapin, D. V., Probing the Surface of Colloidal Nanomaterials with Potentiometry in Situ. *Journal of the American Chemical Society* **2014,** *136* (32), 11228-11231.

28. Izutsu, K. s., -, *Electrochemistry in nonaqueous solutions*. Wiley-VCH: Weinheim, Germany, 2002.

29. Gomes, R.; Hassinen, A.; Szczygiel, A.; Zhao, Q.; Vantomme, A.; Martins, J. C.; Hens, Z., Binding of Phosphonic Acids to CdSe Quantum Dots: A Solution NMR Study. *The Journal of Physical Chemistry Letters* **2011,** *2* (3), 145-152.

30. Butt, H.-J. r., *Physics and chemistry of interfaces*. Array ed.; Wiley-VCH: Weinheim, 2006.

31. Additional details are provided in Supporting Information.

32. de Mello Donegá, C.; Koole, R., Size Dependence of the Spontaneous Emission Rate and Absorption Cross Section of CdSe and CdTe Quantum Dots. *The Journal of Physical Chemistry C* **2009,** *113* (16), 6511-6520.

33. Karel Čapek, R.; Moreels, I.; Lambert, K.; De Muynck, D.; Zhao, Q.; Van Tomme, A.; Vanhaecke, F.; Hens, Z., Optical Properties of Zincblende Cadmium Selenide Quantum Dots. *The Journal of Physical Chemistry C* **2010,** *114* (14), 6371-6376.

34. Tessier, M. D.; Spinicelli, P.; Dupont, D.; Patriarche, G.; Ithurria, S.; Dubertret, B., Efficient Exciton Concentrators Built from Colloidal Core/Crown CdSe/CdS Semiconductor Nanoplatelets. *Nano Letters* **2013,** *14* (1), 207-213.

35. Evans, C. M.; Guo, L.; Peterson, J. J.; Maccagnano-Zacher, S.; Krauss, T. D., Ultrabright PbSe Magic-sized Clusters. *Nano Letters* **2008,** *8* (9), 2896-2899.

36. Nag, A.; Kovalenko, M. V.; Lee, J. S.; Liu, W. Y.; Spokoyny, B.; Talapin, D. V., Metal-free Inorganic Ligands for Colloidal Nanocrystals: S2-, HS-, Se2-, HSe-, Te2-, HTe-, TeS32-,

OH-, and NH2- as Surface Ligands. *Journal of the American Chemical Society* **2011,** *133* (27), 10612-10620.

37. Dobcnik, D.; Gros, I.; Kolar, M., A silver/ silver sulphide selective electrode prepared by means of chemical treatment of silver wire. *Acta Chim. Slov.* **1998,** *45*, 209-216.

38. Ithurria, S.; Dubertret, B., Quasi 2D Colloidal CdSe Platelets with Thicknesses Controlled at the Atomic Level. *Journal of the American Chemical Society* **2008,** *130* (49), 16504-+.

39. Bouet, C.; Mahler, B.; Nadal, B.; Abecassis, B.; Tessier, M. D.; Ithurria, S.; Xu, X. Z.; Dubertret, B., Two-Dimensional Growth of CdSe Nanocrystals, from Nanoplatelets to Nanosheets. *Chemistry of Materials* **2013,** *25* (4), 639-645.

40. Li, Z.; Qin, H.; Guzun, D.; Benamara, M.; Salamo, G.; Peng, X., Uniform thickness and colloidal-stable CdS quantum disks with tunable thickness: Synthesis and properties. *Nano Research* **2012,** *5* (5), 337-351.

41. Pedetti, S.; Nadal, B.; Lhuillier, E.; Mahler, B.; Bouet, C.; Abecassis, B.; Xu, X.; Dubertret, B., Optimized Synthesis of CdTe Nanoplatelets and Photoresponse of CdTe Nanoplatelets Films. *Chemistry of Materials* **2013,** *25* (12), 2455-2462.

42. Kelestemur, Y.; Olutas, M.; Delikanli, S.; Guzelturk, B.; Akgul, M. Z.; Demir, H. V., Type-II Colloidal Quantum Wells: CdSe/CdTe Core/Crown Heteronanoplatelets. *Journal of Physical Chemistry C* **2015,** *119* (4), 2177-2185.

43. García-Rodríguez, R.; Hendricks, M. P.; Cossairt, B. M.; Liu, H.; Owen, J. S., Conversion Reactions of Cadmium Chalcogenide Nanocrystal Precursors. *Chemistry of Materials* **2013,** *25* (8), 1233-1249.

44. Riedinger, A.; Ott, F. D.; Mule, A.; Mazzotti, S.; Knusel, P. N.; Kress, S. J. P.; Prins, F.; Erwin, S. C.; Norris, D. J., An intrinsic growth instability in isotropic materials leads to quasi-two-dimensional nanoplatelets. *Nat Mater* **2017,** *advance online publication*.

45. Boles, M. A.; Ling, D.; Hyeon, T.; Talapin, D. V., The surface science of nanocrystals. *Nat Mater* **2016,** *15* (2), 141-153.

46. Zherebetskyy, D.; Scheele, M.; Zhang, Y.; Bronstein, N.; Thompson, C.; Britt, D.; Salmeron, M.; Alivisatos, P.; Wang, L.-W., Hydroxylation of the surface of PbS nanocrystals passivated with oleic acid. *Science* **2014,** *344* (6190), 1380-1384.

47. Tessier, M. D.; Biadala, L.; Bouet, C.; Ithurria, S.; Abecassis, B.; Dubertret, B., Phonon Line Emission Revealed by Self-Assembly of Colloidal Nanoplatelets. *Acs Nano* **2013,** *7* (4), 3332-3340.

48. Lhuillier, E.; Pedetti, S.; Ithurria, S.; Heuclin, H.; Nadal, B.; Robin, A.; Patriarche, G.; Lequeux, N.; Dubertret, B., Electrolyte-Gated Field Effect Transistor to Probe the Surface

Defects and Morphology in Films of Thick CdSe Colloidal Nanoplatelets. *Acs Nano* **2014,** *8* (4), 3813-3820.

49. Bouet, C.; Laufer, D.; Mahler, B.; Nadal, B.; Heuclin, H.; Pedetti, S.; Patriarche, G.; Dubertret, B., Synthesis of Zinc and Lead Chalcogenide Core and Core/Shell Nanoplatelets Using Sequential Cation Exchange Reactions. *Chemistry of Materials* **2014,** *26* (9), 3002-3008.

50. Wang, F. D.; Wang, Y. Y.; Liu, Y. H.; Morrison, P. J.; Loomis, R. A.; Buhro, W. E., Two-Dimensional Semiconductor Nanocrystals: Properties, Templated Formation, and Magic-Size Nanocluster Intermediates. *Accounts of Chemical Research* **2015,** *48* (1), 13-21.

51. Koh, W. K.; Dandu, N. K.; Fidler, A. F.; Klimov, V. I.; Pietryga, J. M.; Kilina, S. V., Thickness-Controlled Quasi-Two-Dimensional Colloidal PbSe Nanoplatelets. *Journal of the American Chemical Society* **2017,** *139* (6), 2152-2155.

52. She, C.; Fedin, I.; Dolzhnikov, D. S.; Dahlberg, P. D.; Engel, G. S.; Schaller, R. D.; Talapin, D. V., Red, Yellow, Green, and Blue Amplified Spontaneous Emission and Lasing Using Colloidal CdSe Nanoplatelets. *Acs Nano* **2015,** *9* (10), 9475-9485.

53. Pelton, M.; Ithurria, S.; Schaller, R. D.; Dolzhnikov, D. S.; Talapin, D. V., Carrier Cooling in Colloidal Quantum Wells. *Nano Letters* **2012,** *12* (12), 6158-6163.

54. Schmitt-Rink, S.; Chemla, D. S.; Miller, D. A. B., Linear and nonlinear optical properties of semiconductor quantum wells. *Advances in Physics* **1989,** *38* (2), 89-188.

55. Keldysh, L. V., COULOMB INTERACTION IN THIN SEMICONDUCTOR AND SEMIMETAL FILMS. *Jetp Letters* **1979,** *29* (11), 658-661.

56. Miller, D. A. B., Optical Physics of Quantum Wells.

57. Tischler, J. G.; Kennedy, T. A.; Glaser, E. R.; Efros, A. L.; Foos, E. E.; Boercker, J. E.; Zega, T. J.; Stroud, R. M.; Erwin, S. C., Band-edge excitons in PbSe nanocrystals and nanorods. *Physical Review B* **2010,** *82* (24).

58. Benchamekh, R.; Gippius, N. A.; Even, J.; Nestoklon, M. O.; Jancu, J. M.; Ithurria, S.; Dubertret, B.; Efros, A.; Voisin, P., Tight-binding calculations of image-charge effects in colloidal nanoscale platelets of CdSe. *Physical Review B* **2014,** *89* (3).

59. Achtstein, A. W.; Schliwa, A.; Prudnikau, A.; Hardzei, M.; Artemyev, M. V.; Thomsen, C.; Woggon, U., Electronic Structure and Exciton-Phonon Interaction in Two-Dimensional Colloidal CdSe Nanosheets. *Nano Letters* **2012,** *12* (6), 3151-3157.

60. Klimov, V. I., Spectral and dynamical properties of multilexcitons in semiconductor nanocrystals. In *Annual Review of Physical Chemistry*, 2007; Vol. 58, pp 635-673.

61. Klimov, V. I.; Mikhailovsky, A. A.; Xu, S.; Malko, A.; Hollingsworth, J. A.; Leatherdale, C. A.; Eisler, H. J.; Bawendi, M. G., Optical gain and stimulated emission in nanocrystal quantum dots. *Science* **2000,** *290* (5490), 314-317.

62. She, C.; Fedin, I.; Dolzhnikov, D. S.; Demortière, A.; Schaller, R. D.; Pelton, M.; Talapin, D. V., Low-Threshold Stimulated Emission Using Colloidal Quantum Wells. *Nano Letters* **2014,** *14* (5), 2772-2777.

63. Malko, A. V.; Mikhailovsky, A. A.; Petruska, M. A.; Hollingsworth, J. A.; Htoon, H.; Bawendi, M. G.; Klimov, V. I., From amplified spontaneous emission to microring lasing using nanocrystal quantum dot solids. *Applied Physics Letters* **2002,** *81* (7), 1303-1305.

64. Baghani, E.; O'Leary, S. K.; Fedin, I.; Talapin, D. V.; Pelton, M., Auger-Limited Carrier Recombination and Relaxation in CdSe Colloidal Quantum Wells. *Journal of Physical Chemistry Letters* **2015,** *6* (6), 1032-1036.

65. Klimov, V. I., Optical nonlinearities and ultrafast carrier dynamics in semiconductor nanocrystals. *Journal of Physical Chemistry B* **2000,** *104* (26), 6112-6123.

66. Htoon, H.; Hollingsworth, J. A.; Dickerson, R.; Klimov, V. I., Effect of zero- to one-dimensional transformation on multiparticle Auger recombination in semiconductor quantum rods. *Physical Review Letters* **2003,** *91* (22).

67. Singh, J.; Birkedal, D.; Lyssenko, V. G.; Hvam, J. M., Binding energy of two-dimensional biexcitons. *Physical Review B* **1996,** *53* (23), 15909-15913.

68. Beyler, A. P.; Bischof, T. S.; Cui, J.; Coropceanu, I.; Harris, D. K.; Bawendi, M. G., Sample-Averaged Biexciton Quantum Yield Measured by Solution-Phase Photon Correlation. *Nano Letters* **2014,** *14* (12), 6792-6798.

69. Rowland, C. E.; Fedin, I.; Zhang, H.; Gray, S. K.; Govorov, A. O.; Talapin, D. V.; Schaller, R. D., Picosecond energy transfer and multiexciton transfer outpaces Auger recombination in binary CdSe nanoplatelet solids. *Nature Materials* **2015,** *14* (5), 484-489.

70. Paskov, P. P.; Holtz, P. O.; Monemar, B.; Garcia, J. M.; Schoenfeld, W. V.; Petroff, P. M., Photoluminescence up-conversion in InAs/GaAs self-assembled quantum dots. *Applied Physics Letters* **2000,** *77* (6), 812-814.

71. Rakovich, Y. P.; Donegan, J. F.; Filonovich, S. A.; Gomes, M. J. M.; Talapin, D. V.; Rogach, A. L.; Eychmuller, A., Up-conversion luminescence via a below-gap state in CdSe/ZnS quantum dots. *Physica E-Low-Dimensional Systems & Nanostructures* **2003,** *17* (1-4), 99-100.

72. Dantas, N. O.; Qu, F. Y.; Silva, R. S.; Morais, P. C., Anti-Stokes photoluminescence in nanocrystal quantum dots. *Journal of Physical Chemistry B* **2002,** *106* (30), 7453-7457.

73. Sheik-Bahae, M.; Epstein, R. I., Can laser light cool semiconductors? *Physical Review Letters* **2004,** *92* (24).

74. Epstein, R. I.; Buchwald, M. I.; Edwards, B. C.; Gosnell, T. R.; Mungan, C. E., OBSERVATION OF LASER-INDUCED FLUORESCENT COOLING OF A SOLID. *Nature* **1995,** *377* (6549), 500-503.

75. Ha, S.-T.; Shen, C.; Zhang, J.; Xiong, Q., Laser cooling of organic–inorganic lead halide perovskites. *Nat Photon* **2016,** *10* (2), 115-121.

76. Cho, K. S.; Talapin, D. V.; Gaschler, W.; Murray, C. B., Designing PbSe nanowires and nanorings through oriented attachment of nanoparticles. *Journal of the American Chemical Society* **2005,** *127* (19), 7140-7147.

77. Guo, Q.; Kim, S. J.; Kar, M.; Shafarman, W. N.; Birkmire, R. W.; Stach, E. A.; Agrawal, R.; Hillhouse, H. W., Development of CuInSe2 Nanocrystal and Nanoring Inks for Low-Cost Solar Cells. *Nano Letters* **2008,** *8* (9), 2982-2987.

78. Jia, G.; Sitt, A.; Hitin, G. B.; Hadar, I.; Bekenstein, Y.; Amit, Y.; Popov, I.; Banin, U., Couples of colloidal semiconductor nanorods formed by self-limited assembly. *Nat Mater* **2014,** *13* (3), 301-307.

79. Naskar, S.; Miethe, J. F.; Sánchez-Paradinas, S.; Schmidt, N.; Kanthasamy, K.; Behrens, P.; Pfnür, H.; Bigall, N. C., Photoluminescent Aerogels from Quantum Wells. *Chemistry of Materials* **2016**.

80. Gao, Y.; Peng, X., Photogenerated Excitons in Plain Core CdSe Nanocrystals with Unity Radiative Decay in Single Channel: The Effects of Surface and Ligands. *Journal of the American Chemical Society* **2015,** *137* (12), 4230-4235.

81. Sangwal, K., *Etching of Crystals: Theory, Experiment, and Application*. North-Holland Physics Publishing: Amsterdam, 1987.

82. Tessier, M. D.; Spinicelli, P.; Dupont, D.; Patriarche, G.; Ithurria, S.; Dubertret, B., Efficient Exciton Concentrators Built from Colloidal Core/Crown CdSe/CdS Semiconductor Nanoplatelets. *Nano Letters* **2014,** *14* (1), 207-213.

83. Pedetti, S.; Ithurria, S.; Heuclin, H.; Patriarche, G.; Dubertret, B., Type-II CdSe/CdTe Core/Crown Semiconductor Nanoplatelets. *Journal of the American Chemical Society* **2014,** *136* (46), 16430-16438.

84. Delikanli, S.; Guzelturk, B.; Hernandez-Martinez, P. L.; Erdem, T.; Kelestemur, Y.; Olutas, M.; Akgul, M. Z.; Demir, H. V., Continuously Tunable Emission in Inverted Type-I CdS/CdSe Core/Crown Semiconductor Nanoplatelets. *Advanced Functional Materials* **2015,** *25* (27), 4282-4289.

85. Fedin, I.; Talapin, D. V., Colloidal CdSe Quantum Rings. *Journal of the American Chemical Society* **2016,** *138* (31), 9771-9774.

86. Zhang, Y.; Tan, Y.-W.; Stormer, H. L.; Kim, P., Experimental observation of the quantum Hall effect and Berry's phase in graphene. *Nature* **2005,** *438* (7065), 201-204.

87. Zhang, T. Y.; Cao, J. C., Optical absorption in semiconductor nanorings under a lateral terahertz electric field. *Journal of Applied Physics* **2005,** *97* (2), 024307.

88. Massey, W. S., *Algebraic Topology: An Introduction*. Harcourt, Brace & World, Inc.: 1967.

89. Senyuk, B.; Liu, Q.; He, S.; Kamien, R. D.; Kusner, R. B.; Lubensky, T. C.; Smalyukh, I. I., Topological colloids. *Nature* **2013,** *493* (7431), 200-205.

90. Lorke, A.; Luyken, R. J.; Govorov, A. O.; Kotthaus, J. P.; Garcia, J. M.; Petroff, P. M., Spectroscopy of nanoscopic semiconductor rings. *Physical Review Letters* **2000,** *84* (10), 2223-2226.

91. Grochol, M.; Grosse, F.; Zimmermann, R., Optical exciton Aharonov-Bohm effect, persistent current, and magnetization in semiconductor nanorings of type I and II. *Physical Review B* **2006,** *74* (11), 115416.

92. Grochol, M.; Zimmermann, R., Noncircular semiconductor nanorings of types I and II: Emission kinetics in the excitonic Aharonov-Bohm effect. *Physical Review B* **2007,** *76* (19), 195326.

93. Govorov, A. O.; Ulloa, S. E.; Karrai, K.; Warburton, R. J., Polarized excitons in nanorings and the optical Aharonov-Bohm effect. *Physical Review B* **2002,** *66* (8).

94. Aharonov, Y.; Bohm, D., Significance of Electromagnetic Potentials in the Quantum Theory. *Physical Review* **1959,** *115* (3), 485-491.

95. Kim, H. D.; Okuyama, R.; Kyhm, K.; Eto, M.; Taylor, R. A.; Nicolet, A. L.; Potemski, M.; Nogues, G.; Dang, L. S.; Je, K.-C.; Kim, J.; Kyhm, J.-H.; Yoen, K. H.; Lee, E. H.; Kim, J. Y.; Han, I. K.; Choi, W.; Song, J., Observation of a Biexciton Wigner Molecule by Fractional Optical Aharonov-Bohm Oscillations in a Single Quantum Ring. *Nano Letters* **2015**.

96. Xie, R.; Battaglia, D.; Peng, X., Colloidal InP nanocrystals as efficient emitters covering blue to near-infrared. *Journal of the American Chemical Society* **2007,** *129* (50), 15432-+.

97. Chen, O.; Chen, X.; Yang, Y. A.; Lynch, J.; Wu, H. M.; Zhuang, J. Q.; Cao, Y. C., Synthesis of Metal-Selenide Nanocrystals Using Selenium Dioxide as the Selenium Precursor. *Angewandte Chemie-International Edition* **2008,** *47* (45), 8638-8641.

98. Talapin, D. V.; Gaponik, N.; Borchert, H.; Rogach, A. L.; Haase, M.; Weller, H., Etching of colloidal InP nanocrystals with fluorides: Photochemical nature of the process resulting in high photoluminescence efficiency. *Journal of Physical Chemistry B* **2002,** *106* (49), 12659-12663.

99. Liu, W.; Lee, J.-S.; Talapin, D. V., III–V Nanocrystals Capped with Molecular Metal Chalcogenide Ligands: High Electron Mobility and Ambipolar Photoresponse. *Journal of the American Chemical Society* **2013,** *135* (4), 1349-1357.